



**SISSA**

INTERNATIONAL SCHOOL FOR ADVANCED  
STUDIES

Department of Astrophysics and Cosmology

PHD THESIS

# Stellar Evolution with Rotation in **PARSEC v2.0**: Tracks and Isochrones for Low- and Intermediate-mass Stars

*Supervisors:*

**Prof. Alessandro BRESSAN**

*Candidate:*

**Chi Thanh NGUYEN**

*Co-Supervisors:*

**Dr. Léo GIRARDI**

**Dr. Guglielmo COSTA**

---

Academic Year 2021-2022

# *Abstract*

Rotation is always known as an important ingredient in stellar models. Studying the impacts of rotation on stellar structure and evolution is the goal of my thesis. PARSEC models is being widely used in the astronomical community over the last decade. Nevertheless, for the first time, the PARSEC rotating stellar tracks and isochrones are provided to the community, with a suitable range of masses and metallicities. Specifically, we consider the models from very low mass up to  $14M_{\odot}$ , and the metallicity ranges from 0.004 to 0.017. The PARSEC V2.0 code is used to perform the calculations, and the dedicated sites are created for delivering them to users.

The concurrence between rotation and the convective core overshooting phenomenon has been carefully calibrated in previous works. In this project, I inherit this result and adopt the maximum value of core overshooting efficiency parameter  $\lambda_{\text{ov,max}} = 0.4$ . A linear growth from zero of stars that do not develop a convective core to this maximum value where stars already have a fully convective core is adopted for stars with masses in the transition region. The shellular rotation is treated as a purely diffusive process under the assumption of Roche model. Seven initial rotation rates are considered from zero to the extremely close critical velocity (namely,  $\omega_i = 0 - 0.99$ ). The mass loss process is now applied during the evolution of stars due to the enhancement caused by rotation, with the suitable adopted rates that depend on the mass range. In this project, the low-mass ( $0.8 \lesssim M \lesssim 2M_{\odot}$ ) and intermediate-mass ( $2 \lesssim M \lesssim 14M_{\odot}$ ) are the main targets of the analysis in this thesis. The effects of geometrical distortion and rotational mixing are clearly seen in the Hertzsprung-Russell diagram of our tracks. We have seen the rotating stars spend their time longer in the Main-Sequence phase with respect to their non-rotating counterparts. Also, the higher core mass they would have at the post-main-sequence phases. Especially in the case of intermediate-mass stars, where the CNO-cycles are the main channel of

nuclear burning during the main-sequence, the enhancement (depletion) of surface nitrogen and helium (carbon and oxygen) are the most evidence of rotational mixing. Indeed, the faster stars rotate the more enhancement/depletion. As a consequence, with our new models, we can reproduce very well the hook feature of the open cluster M67, as well as the “global” fitting. Furthermore, we also see a hint of at least two populations that harbour in the open cluster NGC 6633 to explain the extended main-sequence and the position of the three He-clump stars. Finally, this new collection of stellar tracks and corresponding isochrones are available online at the dedicated websites, and most suitably used for studies of young and intermediate-age open clusters.

# *Acknowledgement*

First of all, I would like to give the biggest thank to my supervisor, Prof. Alessandro Bressan who guides me step by step to this point, who I learn so many things from. A huge thank to my other supervisor Dr. Léo Girardi who gives me precious corrections and knowledge. And Dr. Guglielmo Costa who gives me constant supports and discussions. Without your helps I would not be able to complete my PhD. More than many thanks I would like to give to my collaborators: Yang Chen, Xiaoting Fu, Guglielmo Volpato, Paola Marigo, who help me to complete part by part of my works.

I would like to thank the SISSA staffs of Astrophysics and Cosmology group, without them giving me the opportunity to start in the first place I would never be able to stand here. And my colleagues of these four years who I have got a chance to meet, even just a “hello” in the corridor, it lights my day, thank you. I would like to express my gratitude to the SISSA administrative, especially Riccardo Iancer and Marco Marin for your constant helps and kindness that sometimes it’s hard to find on these days.

And my friends, Natalia, Matteo, Lotte, Anto, Francesco (A., G.), Farida, Tommaso, Gabriele, Mina, Cesar, Raul, Khuyen, Hang, Phuong (and many others!!!). With your appearance, my life becomes more beautiful and less tedious. Thank you deeply for the time we spent together. And Giulio for dragging me out as much as possible, for wandering with me under the burning Sun of summer days or the delicious meals of only vegetables, thank you truly! And Hasti, Kevin for making me feel shame whenever I compare the things you have done for me and the things I did for you, you know how much I owe you for all the laughter, the cries and the fun we had, thank you!

My family, the molecular cloud of my tiny Universe. Without you I am but nothingness. Thank you for having me and thank you for being there wherever I go, whenever I need, whoever I become. My live is worthy and meaningful because of you guys.

# Contents

<b>1</b>	<b>Introduction</b>	<b>1</b>
<b>2</b>	<b>Stellar Structure and Evolution</b>	<b>4</b>
2.1	Equations of stellar structure and evolution . . . . .	4
2.2	Equation of state, opacity and energy sources . . . . .	7
2.3	Mixing-length theory and convective overshooting . . . . .	11
2.3.1	Mixing-length theory for convective flux . . . . .	11
2.3.2	Convective overshooting . . . . .	13
2.4	Treatment of turbulent mixing and nuclear network . . . . .	15
2.5	Boundary conditions . . . . .	16
2.5.1	The inner region . . . . .	16
2.5.2	The atmosphere region . . . . .	17
2.5.3	The envelope region . . . . .	18
<b>3</b>	<b>Stellar Model with Rotation</b>	<b>20</b>
3.1	Basic assumptions . . . . .	20
3.2	The Roche model and stellar surface . . . . .	21
3.3	Hydrostatic equilibrium . . . . .	24
3.4	Continuity equation . . . . .	26
3.5	Energy conservation . . . . .	26
3.6	Transport of energy . . . . .	27
3.6.1	Radiative transfer . . . . .	27
3.6.2	Convective transport . . . . .	28
3.7	Stellar structure equations with rotation . . . . .	29
3.7.1	Equations for stellar envelope . . . . .	30
3.7.2	Equations for stellar atmosphere . . . . .	31
3.8	Calculation of the form factors . . . . .	33
3.8.1	Surface of an isobar . . . . .	33

3.8.2	Average effective gravity . . . . .	34
3.8.3	Volumetric radius . . . . .	35
3.8.4	Computing the form factors . . . . .	36
3.9	The Von Zeipel theorem and the surface temperature . . . . .	37
<b>4</b>	<b>Angular Momentum Transport</b>	<b>40</b>
4.1	Meridional circulation . . . . .	41
4.2	Shear instability . . . . .	44
4.3	Transport of angular momentum . . . . .	45
4.4	Chemical mixing and the calibration of parameters . . . . .	47
4.5	The transition from non rotating to rotating, low-mass stars . . . . .	49
4.6	Mass loss . . . . .	51
4.6.1	Low-mass stars . . . . .	52
4.6.2	Intermediate-mass and massive stars . . . . .	53
4.7	Self-consistent physical mass loss rate . . . . .	55
4.7.1	Theoretical description . . . . .	55
<b>5</b>	<b>PARSEC V2.0: stellar tracks</b>	<b>65</b>
5.1	Motivation and aims . . . . .	65
5.2	Input physics . . . . .	67
5.2.1	Solar metallicity, opacities, nuclear reactions, mixing length, equation of state . . . . .	67
5.2.2	Convective Overshooting . . . . .	69
5.2.3	Mass Range for Core and Envelope Overshooting . . . . .	69
5.2.4	Rotation . . . . .	71
5.2.5	Transport of angular momentum and chemical mixing . . . . .	72
5.2.6	Mass loss rates . . . . .	74
5.3	Evolutionary tracks . . . . .	76
5.3.1	Very-low-mass stars . . . . .	77
5.3.2	Low-mass stars . . . . .	78
5.3.3	Intermediate-mass and massive stars . . . . .	88
5.4	Comparison with PARSEC V1.2S and other databases . . . . .	93
<b>6</b>	<b>PARSEC V2.0: Isochrones with rotation</b>	<b>98</b>
6.1	Production of isochrones . . . . .	99
6.2	Discussion and conclusions . . . . .	102
6.3	Web-interfaces . . . . .	107

<b>7</b>	<b>Globular cluster M92</b>	<b>112</b>
7.1	General background . . . . .	112
7.2	Chemical mixtures . . . . .	113
7.3	Calibration with M92 . . . . .	116
7.3.1	Input physics . . . . .	116
7.3.2	Mass-Radius relation . . . . .	117
7.3.3	Preliminary track and isochrones fitting . . . . .	121
7.4	Preliminary conclusions, remarks and next steps . . . . .	125
<b>8</b>	<b>Conclusion</b>	<b>129</b>
<b>A</b>	<b>Self-consistence mass loss rate</b>	<b>132</b>
A.1	Hot coronal Mass Loss . . . . .	134
A.1.1	Mechanical energy flux . . . . .	136
A.1.2	Conductive energy flux . . . . .	138
A.2	Cold-wave driven Mass Loss . . . . .	139
A.3	Combining hot and cold mass loss rate . . . . .	143

# List of Figures

2.1	Sketch of three regions in PARSEC models: inner part, envelope and atmosphere . . . . .	19
3.1	Shape of rotating stars' surface . . . . .	23
3.2	The angle $\xi$ between the effective gravity and the radius on an isobar of rotating stars . . . . .	33
3.3	Ratio of effective temperature between rotating model and its non-rotating counterpart . . . . .	38
4.1	Circulation current of a rotating star . . . . .	42
4.2	Distribution of diffusion coefficients . . . . .	46
4.3	Distribution of angular momentum velocity with stellar masses . . . . .	49
4.4	Illustration of transition region in cool star . . . . .	57
4.5	Distribution of $P_{\text{MS}}$ with effective temperature . . . . .	62
4.6	Mass loss rate as function of luminosity . . . . .	64
5.1	Transition masses ( $M_{\text{O1}}$ , $M_{\text{O2}}$ , $M_{\text{HeF}}$ ) as a function of metallicity in the case of no rotation . . . . .	70
5.2	HRD of rotating-stars . . . . .	78
5.3	Ratio between the MS lifetimes of rotating and non-rotating models of the same mass . . . . .	80
5.4	Time evolution of the mass of the convective core during the H-burning phase . . . . .	81
5.5	Evolution of surface tangential velocity at the equator . . . . .	82
5.6	Mass-loss rate as a function of time . . . . .	83
5.7	Total mass lost until the TRGB . . . . .	84
5.8	Difference in He-core mass at the TRGB phase between the rotating models and their non-rotating counterparts . . . . .	85



5.9	Internal distribution of angular velocity . . . . .	86
5.10	He-burning phase of LMSs . . . . .	87
5.11	Evolution of the mass of the convective core . . . . .	89
5.12	Evolution of $\log L$ , $\log T_{\text{eff}}$ , rotation rate, $\omega$ , and surface abundances of N, C, O, and He at the surface for many initial rotation rates . . . . .	91
5.13	As in Figure. 5.12 but for the case of $9M_{\odot}$ stars. . . . .	92
5.14	Maximum mass at which the star burns He in the central region under a strongly degenerative condition, $M_{\text{HeF}}$ , versus the initial rotation rates . . . . .	92
5.15	HRD comparing tracks between PARSEC v2.0 and the previous version for non-rotating stars . . . . .	93
5.16	Luminosity at the TRGB as a function of initial mass for the tracks produced in this work and others . . . . .	95
5.17	Comparison on HRD of rotating tracks between this work and STAREVOL . . . . .	96
6.1	Theoretical isochrones calculated with the TRILEGAL code . . . . .	99
6.2	Theoretical isochrones of rotating models . . . . .	100
6.3	CMD of open cluster M67 and the fits . . . . .	104
6.4	CMD of the open cluster NGC 6633 and the fits . . . . .	105
6.5	Web-interface for stellar tracks that are presented in this work. . . . .	108
6.6	Stellar tracks from previous version PARSEC V1.2S. . . . .	109
6.7	Web-interface for isochrones. . . . .	110
7.1	Maps of Rosseland mean opacities in the $\log T$ - $\log R$ plane . . . . .	118
7.2	Same as Fig. 7.1 but for “H-rich” table . . . . .	119
7.3	Mass-radius relation . . . . .	120
7.4	HRD of tracks for FG and SG-mixtures . . . . .	122
7.5	Preliminary CMD fit of M92 . . . . .	124
7.6	Evolution of surface chemical abundances . . . . .	127

# List of Tables

2.1	Summaried values of $\alpha_{\text{MLT}}$ in different stellar evolution codes.	13
3.1	The dimensionless quantities as function of rotation rate $\omega$ . In which, $S'$ is the surface, $V'$ is volume, $f_P$ , $f_P$ are the form factors and the product $V'\omega^2$ .	37
4.1	Values of rotational mixing efficiency parameters, $f_c$ and $f_\mu$ .	48
4.2	The values of $\omega_{\text{max}}$ at different initial masses.	51
4.3	Adopted coefficients.	61
5.1	Values of core and envelope overshooting efficiency parameters	77
7.1	Adopted chemical abundances of GC M92.	114
7.2	Metallicity, $[\alpha/\text{Fe}]$ ratio and helium abundance of M92.	116

# List of abbreviations

<b>HRD</b>	Hertzsprung-Russell Diagram
<b>CMD</b>	Colour-Magnitude Diagram
<b>MLT</b>	Mixing-Length Theory
<b>EOS</b>	Equation Of State
<b>VLMS</b>	Very Low-Mass Star
<b>LMS</b>	Low-Mass Star
<b>IMS</b>	Intermediate-Mass Star
<b>PMS</b>	Pre-Main-Sequence
<b>MS</b>	Main-Sequence
<b>ZAMS</b>	Zero-Age Main-Sequence
<b>TAMS</b>	Terminal-Age Main-Sequence
<b>RGB</b>	Red-Giant-Branch
<b>RGBB</b>	Red-Giant-Branch Bump
<b>TRGB</b>	Tip of Red-Giant-Branch
<b>HB</b>	Horizontal Branch
<b>ZAHB</b>	Zero-Age Horizontal Branch
<b>AGB</b>	Asymptotic-Giant-Branch
<b>TP-AGB</b>	Thermal-Pulse Asymptotic-Giant-Branch
<b>JPDF</b>	Join Probability Density Function
<b>TR</b>	Transition Region
<b>LMC</b>	Large Magellanic Cloud
<b>COV</b>	Core Overshooting
<b>EOV</b>	Envelope Overshooting
<b>BC</b>	Bolometric Correction
<b>GC</b>	Globular Cluster
<b>FG</b>	First Generation
<b>SG</b>	Second Generation

# Chapter 1

## Introduction

In general, stars can be divided into three classes based on their initial masses: low-mass stars (LMSs), intermediate-mass stars (IMSs), and massive stars. Low-mass stars are usually defined as stars that develop a strong degenerate He-core after the H-burning phase and thus undergo a so-called He-flash. These stars are generally having masses below  $\sim 2M_{\odot}$  depending on metallicity. A transition mass  $M_{\text{HeF}}$ , is then introduced to distinguish LMS and its next class (IMS), which is defined as the maximum mass at which the star ignites He in the central region under a strongly degenerative condition. Stars with masses below this limit are called low-mass stars. Besides that, in this class stars with very low mass ( $\lesssim 0.8M_{\odot}$ , depend on  $Z$ ) so that the time they spend in the MS phase burning hydrogen is much larger than the age of the Universe ( $\sim 13.7$  Gyr). They are usually subdivided and called by very-low-mass stars (VLMS). Moreover, the lowest mass that is required for hydrogen burning to occur is about  $0.08M_{\odot}$ , hence it sets the lower limit for VLMS classification.

In contrast, intermediate-mass stars (IMSs) undergo a so-called quiet He-burning phase after the MS, i.e., their He-core remains non-degenerate after the H-burning phase and ignites He in a stable condition. After the central He-burning phase, IMSs also develop a carbon-oxygen core that becomes degenerate. Therefore, the second mass limit,  $M_{\text{up}} \sim 8M_{\odot}$ , is then introduced to distinguish the IMSs and massive stars, which is the maximum mass at which a star ignites carbon in a strongly degenerative condition. In another word, stars with mass above  $M_{\text{HeF}}$  and below  $M_{\text{up}}$  are defined as intermediate-mass stars. Both  $M_{\text{HeF}}$  and  $M_{\text{up}}$  depend on metallicity.

Therefore, by definition stars with mass above the limit  $M_{\text{up}}$  are called

massive stars. The upper mass limit for massive stars is still uncertain. However, a rough value can be relied on is about  $\sim 300M_{\odot}$  (Crowther et al., 2010) and rather be Z-dependent (Vink, 2018). At this point, it is worth to note that we consider stars up to  $14M_{\odot}$  only in this thesis.

Simulations of stellar evolution have been pursued since decades ago (e.g., Schwarzschild et al., 1957). The methodology to solve the system of nonlinear partial equations of stellar structure and evolution was first introduced by Henyey et al. (1964) and further improved by Kippenhahn et al. (1967). Since then, many stellar evolutionary codes base on this approach to model the evolution of stars and consequently provide knowledge of their internal structure have been published until today. For example, the Dartmouth Stellar Evolution Program (DSEP, Dotter et al., 2008), the Geneva stellar evolution code (GENEC, Eggenberger et al., 2008), the Frascati Raphson Newton Evolutionary Code (FRANEC, Chieffi and Limongi, 2013), the Modules for Experiments in Stellar Astrophysics (MESA, Paxton et al., 2011) and the PAdova and tRieste Stellar Evolutionary Code (PARSEC, Bressan et al., 2012).

The PARSEC code was first implemented in Bressan et al. (2012) and then used in several works, aimed at producing large grids of stellar evolutionary tracks and isochrones. For instance, Chen et al. (2014) extended the calculation to very low-mass star models, Tang et al. (2014) and Chen et al. (2015) pursued massive stars up to  $350 M_{\odot}$ , and Fu et al. (2018) studied the evolution with  $\alpha$ -enhanced compositions. Extended sets of isochrones using PARSEC tracks were described in Bressan et al. (2012) and Marigo et al. (2017). More recently, a significant development was presented in Costa et al. (2019b), where *rotation*, for the first time, was included in the PARSEC code.

The concept of star's rotating is simply understood under the conservation of angular momentum,  $\Omega r^2 = \text{const}$ ; for example, a star with radius of  $\sim 10^{11}$  cm, born from a slow-rotating molecular cloud with a typical radius of  $\sim 10^{17}$  cm, after the collapsing process should rotates very fast. In 1909 Schlesinger observed the rotation of stars by measuring the limb-effect in the eclipsing variables  $\delta$ -Librae and  $\lambda$ -Tauri. In 1922, Hellerich provided further evidence with observations during the time of eclipse in a number of Algol-type variables, (see Shajn and Struve, 1929). Several studies from both theoretical (e.g, von Zeipel, 1924a,b; Kippenhahn et al., 1970; Zahn, 1992; Meynet and Maeder, 1997; Endal and Sofia, 1981) and observational (e.g., Oke and Greenstein, 1954; Abt et al., 1972; Mora et al., 2001) side show that rotation can not be ignored in stellar evolutionary codes.

Rotating stars evolve in a different way than non-rotating ones. In general, they become more luminous and cooler, they spend longer time in the MS phase, enrich the surface chemical abundances with products from internal H-burning regions, and built-up a heavier core. The key points to explain these differences in rotating stars can be counted by the effects of centrifugal force and the extra-mixing, induced by rotation.

In this thesis, I will focus on the case of low- and intermediate-mass range, and target the effects of rotation on these stellar models. This thesis will be structured and organised in six chapters, as follow.

The classical model of stellar structure and evolution is described in Chapter. 2, in which I will recall the standard equations of stellar structure and evolution under the assumption of spherical symmetry of stars, i.e., non-rotating.

In Chapter. 3, the stellar structure equations are re-derived for rotating stars. The effects of geometrical distortions due to rotation are shown and the methodology that is used in PARSEC is delineated.

In Chapter. 4, the treatment of angular momentum transport in rotating stars is discussed. The effects of meridional circulation and shear instabilities are explicitly studied in this chapter, as well as the chemical mixing caused by rotation. The mass loss process is also described in this chapter.

In Chapter. 5, the intensive calculations of stellar evolutionary tracks with PARSEC v2.0 code are presented. Several updates on the convective overshooting, treatment of turbulent mixing, and nuclear reaction networks are included, as well as rotation. The computed tracks are then studied in view of the degree of initial rotation. The comparison with previous version PARSEC v1.2S and other databases will also be shown in this chapter.

In Chapter. 6, the corresponding isochrones from the computed tracks are shown. A briefly summary of the methodology of obtaining isochrones from TRILEGAL code will be shown, before presenting the full sets of isochrones accompanied by preliminary tests on the CMD of two open clusters, M67 and NGC 6633. For easy use of the new collection of tracks and isochrones from the community, a dedicated web-interfaces has been built and it will be described in the last section of this chapter.

In Chapter. 7, I will present a synthesis of my future work on the enhancement of  $\alpha$ -elements in the low metallicity domain. In particular, the collection of chemical abundances estimates for the globular cluster M92, and calculations of evolutionary tracks with these abundances. Preliminary tests of the corresponding isochrones on this cluster will be also presented.

# Chapter 2

## Stellar Structure and Evolution

The basic standard system of equations that used to model stellar structure and its evolution will be introduced in this chapter. The assumption of spherical symmetry is remained throughout this chapter, which means no rotation is yet considered. The methodology to solve these partial derivative equations to obtain the properties of stars as implemented in our PARSEC code (Bressan et al., 2012) will be the main target of this chapter. In Sect. 2.1, the system of partial derivative equations which are used to model the structure and evolution of a star is introduced. The EOS and opacity will be discussed in Sect. 2.2. Section. 2.3 focuses on the energy transfer in convective regions. In Sect. 2.4, the update of treatment of turbulent mixing and nuclear network in PARSEC v2.0 code will be described. Finally, the boundary conditions which are used to solve the structure equations will be explained in Sect. 2.5.

### 2.1 Equations of stellar structure and evolution

The structure of a star is determined, in the assumptions of spherical symmetry (non-rotating) and complete equilibrium (thermal and mechanical),

by solving the four equations for:

$$\text{mass conservation: } \frac{\partial m}{\partial r} = 4\pi r^2 \rho, \quad (2.1)$$

$$\text{hydrostatic equilibrium: } \frac{\partial P}{\partial r} = -\rho \frac{Gm}{r^2}, \quad (2.2)$$

$$\text{thermal conservation: } \frac{\partial L}{\partial r} = 4\pi r^2 \rho q, \quad (2.3)$$

$$\text{radiative transfer: } \frac{\partial T}{\partial r} = -\frac{3}{4ac} \frac{\kappa \rho}{T^3} \frac{L}{4\pi r^2} \quad (2.4)$$

in which, the independent variable is the radial coordinate,  $r$ . Besides chemical composition  $X_i$ , the functions stellar mass ( $m$ ), pressure ( $P$ ), luminosity ( $L$ ), and temperature ( $T$ ), characterise the structure of the star. Other parameters that are related to these quantities are: density  $\rho = \rho(P, T, X_i)$ , nuclear energy generation rate  $q = q(\rho, T, X_i)$ , and opacity  $\kappa = \kappa(\rho, T, X_i)$  (see sections below for a detailed discussion of opacities and nuclear generation rate). The values of the physical constants that appear in the above equations adopted in this work are  $G = 6.6738 \times 10^{-11} \text{m}^3 \text{kg}^{-1} \text{s}^{-2}$  (gravitational constant),  $a = 7.5657 \times 10^{-16} \text{Jm}^{-3} \text{K}^{-4}$  (radiation constant),  $c = 2.9979 \times 10^8 \text{ms}^{-1}$  (light speed).

In practise, it is often more useful to use the Lagrangian formalism where  $m$  is the independent variable, instead of the Euler formalism where  $r$  is the independent variable. This is because, during evolution, the mass of stars almost doesn't change except for the red-giant-branch (RGB) and asymptotic-giant-branch (AGB) of low and intermediate-mass and the massive ones. In contrast, the radius of stars changes dramatically during their evolution. Therefore, it is convenient to re-write the four structure equations above in  $m$ -coordinate:

$$\frac{\partial r}{\partial m} = \frac{1}{4\pi r^2 \rho}, \quad (2.5)$$

$$\frac{\partial P}{\partial m} = -\frac{Gm}{4\pi r^4}, \quad (2.6)$$

$$\frac{\partial L}{\partial m} = \epsilon_n - \epsilon_\nu + \epsilon_g, \quad (2.7)$$

$$\frac{\partial T}{\partial m} = -\frac{T}{P} \frac{Gm}{4\pi r^4} \nabla_{\text{rad}}, \quad \text{with } \nabla_{\text{rad}} = \frac{3}{16\pi acG} \frac{\kappa LP}{mT^4}, \quad (2.8)$$

where  $m$  varies from 0 to the total mass of the star and  $\nabla_{\text{rad}}$  is the radiative temperature gradient. Note that in the Eq. 2.7 the energy generation rate on



the right-hand side is now having contribution not only from nuclear reactions ( $\epsilon_n$ ), but also from *neutrino loss* ( $\epsilon_\nu$ ) and gravitational work -contraction or expansion- ( $\epsilon_g$ ).

Energy can be transported also by convection. In this case, the actual gradient  $\nabla$  will replace  $\nabla_{\text{rad}}$  in the Eq. 2.8,

$$\frac{\partial T}{\partial m} = -\frac{T}{P} \frac{Gm}{4\pi r^4} \nabla. \quad (2.9)$$

The expression of  $\nabla$  is rather complicated: i) in the deep interior, where a negligible excess of  $\nabla$  over the adiabatic value is sufficient to transport the whole luminosity,  $\nabla = \nabla_{\text{ad}}$ , ii) in the upper part of the outer convective envelope, the value of  $\nabla$  will be somewhere between  $\nabla_{\text{ad}}$  and  $\nabla_{\text{rad}}$ , with an exact solution provided by solving the equations of the mixing length theory (See Sect. 2.3.1). The adiabatic temperature gradient is written as,

$$\nabla_{\text{ad}} = \frac{P\delta}{T\rho c_P}, \quad (2.10)$$

where  $\delta = -\left(\frac{\partial \ln \rho}{\partial \ln T}\right)_P$  is the thermo-dynamical derivative and  $c_P$  is the specific heat capacity at constant pressure.

The stability of the medium against convection depends on  $\nabla_{\text{rad}}$  and a critical gradient,

$$\nabla_{\text{cr}} = \nabla_{\text{ad}} + \frac{\phi}{\delta} \nabla_\mu, \quad (2.11)$$

where  $\phi = \left(\frac{\partial \ln \rho}{\partial \ln \mu}\right)_{P,T}$  is a thermo-dynamical derivative and  $\nabla_\mu = \frac{\partial \ln \mu}{\partial \ln P}$  is the molecular weight gradient. In particular, if  $\nabla_{\text{rad}} > \nabla_{\text{cr}}$ , then small perturbations will increase to finite amplitude until the whole region becomes interested, by convective motions. In this case, the local flux is carried by convection. In contrast, if the layer is stable which means  $\nabla_{\text{rad}} < \nabla_{\text{cr}}$ , there will be no convective motions occur, and hence the transportation is driven by radiation. This is known as the *Ledoux criterion* for dynamical stability. Specifically, in the case where the layer is stable and chemically homogeneous ( $\nabla_\mu = 0$ ) one has the *Schwarzschild criterion* for dynamical stability where the condition  $\nabla_{\text{rad}} < \nabla_{\text{ad}}$  reaches. Therefore, in the deep stellar interiors, the equation of energy transport is then usually written as,

$$\frac{\partial T}{\partial m} = -\frac{T}{P} \frac{Gm}{4\pi r^4} \min [\nabla_{\text{ad}}, \nabla_{\text{rad}}]. \quad (2.12)$$

In more external convective layers, where convection may be inefficient, the actual temperature gradient may be as high as  $\nabla = \nabla_{\text{rad}}$ .

The chemical composition directly affects the properties of stars, for example, through the absorption of radiation or the generation of energy by nuclear reactions. These reactions, in turn, alter the chemical composition. Therefore, the variation of chemical composition with time is an essential ingredient that must be known with high accuracy. If we can neglect diffusion, in radiative regions the evolution of chemical composition of a star is given by,

$$\frac{\partial X_i}{\partial t} = \frac{A_i}{\rho} (\Sigma r_{ji} - \Sigma r_{ik}), \quad (2.13)$$

where  $X_i = X_i(m, t)$  is the mass fraction of any element  $i = 1 \dots I$  and  $I$  is the total number of elements that are considered in the nuclear network.  $r_{lm}$  is the nuclear reaction rate, that is the number of reactions per unit volume and time that transform nuclei from type  $l$  into type  $m$ , and  $A_i$  is the atomic mass of element  $i$ .

## 2.2 Equation of state, opacity and energy sources

The stellar structure is determined by the  $4 + I$  variables such as  $r$ ,  $P$ ,  $T$ ,  $L$ ,  $X_1, \dots, X_I$ , obtained from the left-hand side of Eqs. 2.5-2.8 and 2.13, while the properties of it are contained in the right-hand side of these equations. An equation of state of the stellar matter describes the relation of each these quantities as a function of the structure's parameters which means a number of thermodynamic relations:

$$\rho = \rho(P, T, X_i), \quad (2.14)$$

$$c_P = c_P(P, T, X_i), \quad (2.15)$$

$$\delta = \delta(P, T, X_i), \quad (2.16)$$

$$\nabla_{\text{ad}} = \nabla_{\text{ad}}(P, T, X_i), \quad (2.17)$$

$$(2.18)$$

In PARSEC, the sets of EOS are computed by using the FREEEOS code (Irwin, 2012) which is freely available at <sup>1</sup>. The FREEEOS package is fully

---

<sup>1</sup><http://freeeos.sourceforge.net/>

implemented in the code and it may be used as “on-the-fly” or by interpolating between the pre-computed tables. The comparison between the two methods gives a negligible difference on the HR diagram (see [Bressan et al., 2012](#)). Since the pre-computed tables are sufficiently accurate for most of our purposes, the second method is then used as the standard option. The contribution of several elements from hydrogen to nickel is taken into account, and many values of metallicity ( $Z$ ) for any specified distribution of heavy elements  $\{X_i/Z\}$  are considered. The EOS tables are different between the “H-rich” regime and the “H-free” regime. Namely, the “H-rich” set contains 10 tables that characterised by different values of H-abundance for the H-burning phase, and the “H-free” set contains 31 tables which are used for the advanced phases such as He-burning. For each desired initial metallicity, a set of EOS tables are computed with this exact metallicity and partitions. This set is then inserted into the EOS database for interpolation purpose when the global- $Z$  changes during the evolution.

We also need equations for the opacity, the reaction rates, the nuclear energy generation rate, and the rate of neutrino losses:

$$\kappa = \kappa(P, T, X_i), \quad (2.19)$$

$$r_{lm} = r_{lm}(P, T, X_i), \quad (2.20)$$

$$\epsilon_n = \epsilon_n(P, T, X_i), \quad (2.21)$$

$$\epsilon_\nu = \epsilon_\nu(P, T, X_i), \quad (2.22)$$

$$\epsilon_{\text{grav}} = \epsilon_{\text{grav}}(P, T, \delta t, X_i). \quad (2.23)$$

The opacity is a physical quantity that characterises the degree to which the radiation intensity is reduced by the presence of matter. It determines the rate at which the energy that is going out of a star, hence it determines the value of luminosity. Therefore, opacity plays a key role in stellar properties. In thermodynamic equilibrium, the opacity  $\kappa$  is deduced from the diffusive flux of radiation, which is a mean value over all frequencies  $\nu$  and is given as,

$$\frac{1}{\kappa} = \frac{\pi}{acT^3} \int_0^\infty \frac{1}{\kappa_\nu} \frac{\partial B}{\partial T} d\nu, \quad (2.24)$$

which is also known as *Rosseland mean* opacity. In the equation above,  $B$  is the Planck function for the intensity of black-body radiation, and  $\kappa_\nu$  is the frequency-dependent opacities.

It is clear that we need to know  $\kappa_\nu$  to calculate the Rosseland mean  $\kappa$ . Depending on physical processes that contribute to the stellar opacity,  $\kappa_\nu$  has different forms, they mainly are from:

- **Electron scattering:** Namely, the free electrons exchange momentum with radiation (photons); this is also known as “Thomson scattering”. This effect become important at high temperatures, roughly  $T > 10^8$  K (depending on density), (see [Kippenhahn et al., 2013](#)). In this case,  $\kappa_\nu$  is frequency-independent and is written as,

$$\kappa_\nu = 0.2(1 - X), \quad (2.25)$$

where  $X$  is the mass fraction of hydrogen.

- **Free-free absorption:** This process happens when a free electron passes sufficiently close to an ion, they are can absorb or emit radiation. The absorption coefficient has been classically derived by Kramers and has a form,

$$\kappa_\nu \sim Z^2 \rho T^{-1/2} \nu^{-3}, \quad (2.26)$$

where  $Z$  is the charge number of the ion. If this process is the only source, the opacity is the so-called “Kramers opacity”. It is most effective at high densities and intermediate temperatures (matter must be ionized).

- **Bound-free transition:** A neutral atom (or ion) might be ionised by a photon and releases an electron. In this case, the relative number of atoms in the different stages of excitation  $n_{\text{ion}}$  and the absorption coefficient of each ion  $a_\nu$  are needed to know before obtaining the frequency-dependent opacity,

$$\kappa_\nu = \frac{a_\nu n_{\text{ion}}}{\rho}. \quad (2.27)$$

A special case in which the ion is negative hydrogen ion. In this case, the number of  $H^-$  ion is given by the Saha formula.

- **Bound-bound transition:** the absorbed photon has just enough energy to excite the electron from a lower level to a higher level. This is the case of bound-bound transition. The absorption coefficient  $\kappa_\nu$  is therefore written as the sum over all transitions  $nn'$  and elements  $j$ ,

$$\kappa_\nu(j) = \sum_j \sum_{nn'} \kappa_{\nu,nn'}(j). \quad (2.28)$$

- **Molecular opacities:** For low temperatures ( $< 10^4$  K) the formation of molecules in the envelopes of cool stars becomes important since they are important absorbers due to their rich system of energy levels. Molecular opacities depend on atomic abundances, on the formation and stability of the various molecules, and on their energy level spectrum. The calculations including all these processes rather be complicated, however, the largest sets of such tables have been provided by Alexander and Ferguson (Alexander and Ferguson, 1994; Ferguson et al., 2005) and more recently by Marigo and Aringer (2009).

In PARSEC, the opacities at a given chemical abundance distribution are obtained by interpolating the pre-computed tables of Rosseland mean opacities as a function of density, temperature, and composition in a wide range of parameters to cover up all values that we meet in the stellar structure, during the evolution. The tables are computed with different programs:

- In the high temperature regime,  $4.2 \leq \log(T/K) \leq 8.7$ , the opacity tables are provided by the Opacity Project At Livermore (OPAL; see Iglesias and Rogers, 1996).
- In the low temperature regime,  $3.2 \leq \log(T/K) \leq 4.1$ , we generate the opacity tables with the AESOPUS tool (Marigo and Aringer, 2009).
- In the transition region,  $4.1 \leq \log(T/K) \leq 4.2$ , the opacities are linearly interpolated between the OPAL and AESOPUS values.
- At high densities also conduction becomes important. The contribution from conduction is computed following Itoh et al. (2008).

In practice, at a given metallicity distribution  $\{X_i/Z\}$ , the tables are constructed into two sets as mentioned above, which are “H-rich” and “H-free” opacities. For both sets, each opacity table includes a rectangular region defined by the interval of temperature ( $3.2 \leq \log(T/K) \leq 8.7$ ) and interval of the quantity  $R = \rho/T_6$ , ( $-8 \leq \log R \leq 1$ ), where  $T_6 = T/10^6$  K. These tables are loaded alongside with the EOS tables before the computation of evolutionary tracks. A number of tables with different values of  $Z$  are loaded preliminarily in order to cover in detail any changes in the local metal content due to, for example, mixing processes by convection, diffusion, and rotation.

## 2.3 Mixing-length theory and convective overshooting

This section deals with the contribution of convection to the energy transport and mixing. We discuss the adopted value of the mixing-length coefficient used in PARSEC and the overshooting efficiency, i.e. the efficiency of extra-mixing beyond the formal borders of convective regions.

### 2.3.1 Mixing-length theory for convective flux

The total energy of a star is partially transported by convective motions, besides radiation which is always present. The model that is commonly used to describe this process is the so-called “mixing-length theory” (MLT) (Böhm-Vitense, 1958). The mass elements are assumed to move an average vertical distance  $l_{\text{MLT}}$  which is called by the mixing length before they dissolve into their surroundings and deliver their excess energy content. Both the hotter upward moving elements and the cooler downward moving elements contribute to the outward transport of energy. Usually, the mixing length is computed by

$$l_{\text{MLT}} = \alpha_{\text{MLT}} H_{\text{P}} \quad \text{with} \quad H_{\text{P}} \equiv -\frac{dr}{d \ln P}, \quad (2.29)$$

where  $\alpha_{\text{MLT}}$  is the MLT coefficient, and  $H_{\text{P}}$  is pressure scale height which has dimension of length.

The average flux that resulted from convective motions of elements which have an average velocity  $\bar{v}$  and an average temperature excess  $\overline{\Delta T}$  over their surrounding can be written as,

$$F_{\text{con}} = \rho C_P \bar{v} \overline{\Delta T}. \quad (2.30)$$

Assume that at first, all elements start with a very small perturbation, and thus  $\overline{\Delta T}$  and  $\bar{v}$  are zero. The  $\overline{\Delta T}$  and  $\bar{v}$  increase when the elements rise (or sink) until they break after a distance  $l_{\text{MLT}}$ . The average excess temperature is then defined as

$$\frac{\overline{\Delta T}}{T} = \frac{1}{T} \left( \frac{dT_{\text{int}}}{dr} - \frac{dT}{dr} \right) \frac{l_{\text{MLT}}}{2} = (\nabla - \nabla_{\text{int}}) \frac{1}{H_{\text{P}}} \frac{l_{\text{MLT}}}{2}, \quad (2.31)$$

with  $T_{\text{int}}$ ,  $T$  are the internal and external temperatures of the elements. The average velocity is obtained by assuming half of the work done by radial buoyancy force goes into the kinetic energy while the other half is transferred to the surroundings (viscosity):

$$\bar{v}^2 = g\delta(\nabla - \nabla_{\text{int}})\frac{l_{\text{MLT}}^2}{8H_P}, \quad (2.32)$$

where  $g$  is gravity and  $\delta = -\left(\frac{\partial \ln \rho}{\partial \ln T}\right)_P$  is the thermo-dynamical derivative. Hence, with the expressions of  $\Delta \bar{T}$  and  $\bar{v}$ , the convective flux becomes,

$$F_{\text{con}} = C_P \rho T (g\delta)^{1/2} (\nabla - \nabla_{\text{int}})^{3/2} \frac{l_{\text{MLT}}^2}{4\sqrt{2}H_P^{3/2}}. \quad (2.33)$$

Besides that, the change of the temperature  $T_{\text{int}}$  inside the elements is caused by the adiabatic expansion<sup>2</sup> (or compression) and by the radiative exchange of energy to their surroundings. Considering the total change of temperature per unit length leads to an equation that links  $\nabla$ ,  $\nabla_{\text{int}}$  and  $\bar{v}$ ,

$$\frac{\nabla_{\text{int}} - \nabla_{\text{ad}}}{\nabla - \nabla_{\text{int}}} = \frac{6acT^3}{\kappa\rho^2 C_P l_{\text{MLT}} \bar{v}}. \quad (2.34)$$

Putting together, the Eqs. 2.32, 2.33, 2.34 with the total and radiative flux,

$$F_{\text{rad}} + F_{\text{con}} = \frac{4ac}{3} \frac{G}{\kappa P r^2} \frac{T^4 m}{\kappa P r^2} \nabla_{\text{rad}}, \quad F_{\text{rad}} = \frac{4ac}{3} \frac{G}{\kappa P r^2} \frac{T^4 m}{\kappa P r^2} \nabla, \quad (2.35)$$

gives a solution for  $F_{\text{rad}}$ ,  $F_{\text{con}}$ ,  $v$ ,  $\nabla_{\text{int}}$  and  $\nabla$ , if the local properties of matter are known:  $P$ ,  $T$ ,  $\rho$ ,  $l_{\text{MLT}}$ ,  $m$ ,  $C_P$ ,  $\nabla_{\text{ad}}$ ,  $\nabla_{\text{rad}}$  and  $g$ .

As shown above, the mixing-length contains a free parameter  $\alpha_{\text{MLT}}$ . It is worth to note that the adopted value of  $\alpha_{\text{MLT}}$  is slightly different in different stellar evolutionary codes. This is due to the solar model calibration needed to constrain such free parameter, in which each stellar evolutionary code uses different input physics such as the adopted solar-scaled mixtures, EOSs, opacities, and the nuclear reaction rates. Some examples of  $\alpha_{\text{MLT}}$  value are displayed in Table. 2.1. It is also interesting to mention that Viani et al. (2018) suggests a dependency of  $\alpha_{\text{MLT}}/\alpha_{\text{MLT}\odot}$  on gravity, effective temperature and metallicity. Another study in FGK stars, Song et al. (2020), mainly

Table 2.1: Summaried values of  $\alpha_{\text{MLT}}$  in different stellar evolution codes.

Name	Chemical mixture	$\alpha_{\text{MLT}}$	EOS	Opacities	Nuclear reaction rate	Reference
STAREVOL	AGSS09	1.973	Modified PTEH95	OPAL F05	NACRE II	<a href="#">Amard et al. (2019)</a>
DSEP	GS98	1.938	CK95	OPAL F05	Adelberger+98	<a href="#">Dotter et al. (2008)</a>
FRANEC	AS05	1.68	FreeEOS4	OPAL F05	BP92	<a href="#">Tognelli et al. (2011)</a>
MESA	AGSS09	1.82	OPAL+SCVH95	OPAL F05	LUNA	<a href="#">Choi et al. (2016)</a>
PARSEC	Caffau+11	1.74	MDM12	OPAL F05	JINA REACLIB	<a href="#">Bressan et al. (2012)</a>
			FreeEOS	OPAL	JINA REACLIB	
			AESOPUS			

AGSS09: [Asplund et al. \(2009\)](#); GS98: [Grevesse and Sauval \(1998\)](#); AS05: [Asplund et al. \(2006\)](#); Caffau+11: [Caffau et al. \(2011\)](#)

PTEH95: [Pols et al. \(1995\)](#); CK95: [Chaboyer and Kim \(1995\)](#); OPAL06: [Rogers and Nayfonov \(2002\)](#);

SCVH95: [Saumon et al. \(1995\)](#); MDM12: [MacDonald and Mullan \(2012\)](#); OPAL: [Iglesias and Rogers \(1996\)](#);

F05: [Ferguson et al. \(2005\)](#); NACRE II: [Xu et al. \(2013\)](#); Adelberger+98: [Adelberger et al. \(1998\)](#);

BP92: [Bahcall and Pinsonneault \(1992\)](#); LUNA: [Bemmerer et al. \(2006\)](#); JINA REACLIB: [Cyburt et al. \(2010\)](#).

focuses on the dependence on metallicity. These new suggestions could certainly be inspirations for future works on this important problem.

In PARSEC the calibration of solar model had been done in [Bressan et al. \(2012\)](#), with the adopted input physics shown in Table. 2.1. The calibration gives  $\alpha_{\text{MLT}} = 1.74$ , this value of the mixing-length efficiency parameter is used for the calculations of stellar tracks in this thesis that will be presented in Chapter 5.

### 2.3.2 Convective overshooting

The convective unstable region is defined in the framework of Schwarzschild criterion, [Schwarzschild \(1958\)](#). This condition however is a local condition, i.e., defined using quantities computed locally:  $\nabla_{\text{rad}}$ ,  $\nabla_{\text{ad}}$ ,  $\nabla_{\mu}$ . As such, the Schwarzschild (or Ledoux) condition defines the acceleration field and not the velocity field. In reality, convective elements can travel beyond the formal border where the acceleration becomes null, up to a certain point at which their velocity drops to zero. This phenomenon is called convective overshooting.

- **Core overshooting:** The determination of the edge of the true convective core was described in [Bressan et al. \(1981\)](#). The velocity in overshooting region is computed by a ballistic approximation,  $v^2(r) \propto \int_{r_i}^r g \Delta\rho / \rho dr$ , where densities  $\rho$  and  $\Delta\rho$  are expressed as in [Maeder](#)

<sup>2</sup>the moving mass elements do not exchange heat or mass with their surroundings, and pressure remains balanced as long as motions are subsonic.



(1975) and Bressan et al. (1981). The integral limits are bounded by condition,  $r - r_i \leq 0.5l_{\text{ov}}$ , which is defined as the mean free path of the convective element's bubbles *in presence of a convective border*, so that they can travel a further distance before their velocity drops to zero. The core overshooting length is expressed in units of the pressure scale height  $H_P$ , namely,  $l_{\text{ov}} = \frac{1}{2}\lambda_{\text{ov}}H_P$ , with  $\lambda_{\text{ov}}$  is the core overshooting efficiency parameter. In general,  $\lambda_{\text{ov}}$  is a calibrated parameter and depends on stellar masses, (see Claret and Torres, 2016, 2017, 2018, 2019). In PARSEC, the overshooting efficiency parameter may depend on the star's initial mass. A detailed review of the adopted  $\lambda_{\text{ov}}$  in this thesis will be discussed below.

- **Envelope overshooting:** The existence of a downward overshoot at the base of the convective envelope was introduced to explain the observations of the location of Red-Giant-Branch bump (RGBB) in low-mass stars and to explain the extension of blue loops in intermediate-mass stars. In particular, Alongi et al. (1991) was the first to consider the effects of envelope overshooting where they found that only models with envelope overshooting length  $\Lambda_e \sim 0.7H_P$  could well fit the location of the RGBB in the HR diagram of globular clusters. Latter on, Cassisi et al. (2002) provided a lower limit of  $\Lambda_e \geq 0.5H_P$ , after computing several stellar models with varying values of  $\Lambda_e = 0.1 - 0.75H_P$ . However, the comparison with helioseismic data by Christensen-Dalsgaard et al. (2011) favoured a value of convective overshooting for solar models of about  $0.37H_P$ . Furthermore, Tang et al. (2014) claimed that in order to reproduce the observed blue-loop of IMSs, the EOV required a mixing length scale of  $2H_P-4H_P$  which is extremely large in comparison with other estimates. Shortly after, Fu et al. (2015) showed that the Li-abundance in the pre-main-sequence (PMS) phase and the observed Spite plateau and its falling branch at low temperatures could be very well reproduced by the models of low-mass stars with a wide range of extra-mixing scale length. However, by calibration with the globular cluster 47 Tuc, Fu et al. (2018) concluded that the model with  $\Lambda_e = 0.5H_P$  produces a very good agreement with the observational data. The adoption of  $\Lambda_e$  at a given mass model in this thesis will be described detail in Chapter 5.

Concerning the changes in the core overshooting distance,  $l_{\text{ov}}$ , we have to say that it directly impacts on the amount of mixing of chemical elements

and thus on the evolution of stars. Many approaches are used to constrain the core overshooting efficiency parameter  $\lambda_{\text{ov}}$ , such as the colour-magnitude diagrams (CMDs) of star clusters (Woo et al., 2003; Rosenfield et al., 2017), bump Cepheids (Keller and Wood, 2006), asteroseismology of red clump stars (Bossini et al., 2017), or detached double-lined eclipsing binaries (DLEBs Claret and Torres, 2018; Constantino and Baraffe, 2018; Higl et al., 2018). A series of works (e.g., Demarque et al., 2004; Pietrinferni et al., 2004; Bressan et al., 2012; Mowlavi et al., 2012) suggest that there is a transition region of the overshooting efficiency, namely, a growth from 0 for stars with radiative core ( $M_i \sim 1 - 1.2M_\odot$ ) to a constant value for stars that have well developed fully convective cores ( $M_i \sim 1.5 - 2M_\odot$ ).

A detailed analysis to investigate the possible combined effects of the core overshooting and rotation performed on observed DLEBs (Costa et al., 2019b) of well known masses, provides an insightful reference, especially when rotation is involved such as the case of this thesis. By using the Bayesian method to treat the binary data using the PARAM code (see da Silva et al., 2006; Rodrigues et al., 2014, 2017), the 2D joint probability density function (JPDF) for age and  $\lambda_{\text{ov}}$ , at a given metallicity, is obtained for each binary system. The same methodology is adopted for rotation rate with a fixed value of  $\lambda_{\text{ov}}$ . The analysis is performed for 38 DLEBs in total. The results show that a mild value of  $\lambda_{\text{ov}} = 0.4$ , in combination with rotation rates from  $0 \leq \omega \leq 0.8$  (1 is the critical value) is the solution that better reproduces the observed as a function of the initial mass  $M_i \gtrsim 1.9M_\odot$  (Costa et al., 2019b). It is convenient to notice here that in this thesis, we will use this calibrated value of  $\lambda_{\text{ov}} = 0.4$  as the maximum efficiency of core overshooting when the stars already develop a full convective core, as we will see in Chapter. 5.

## 2.4 Treatment of turbulent mixing and nuclear network

In the previous version PARSEC v1.2S, the nuclear reaction networks and the transport of elements were solved separately. First, all the abundances changes by nuclear reactions were solved with a semi-implicit extrapolation scheme (see Marigo et al., 2001), and then the mixing of elements by microscopic diffusion or by the turbulent convection was added. In the latest version PARSEC v2.0, nuclear reactions and the mixing are solved at the

same time. The variation of elements  $i$  is given by,

$$\frac{\partial Y_i}{\partial t} = \frac{1}{\rho r} \frac{\partial}{\partial r} \left( r^2 \rho D \frac{\partial Y_i}{\partial r} \right) \pm \Sigma_j Y_j \lambda_k(j) \pm \Sigma_{j \geq k} Y_j Y_k [jk], \quad (2.36)$$

where  $Y_i = X_i/A_i$  with  $X_i$  and  $A_i$  being the mass fraction and atomic mass of element  $i$ ;  $D$  is turbulent diffusion coefficient which is computed in the MLT framework, i.e.,  $D = D_{\text{MLT}} = \frac{1}{3} v l_{\text{MLT}}$  with  $v$  being the velocity of the convective mass elements, and  $Y_j Y_k [jk]$  describes the two body reactions. As we will see later, the diffusion coefficient can also contain the effects of rotational mixing. The fully implicit method is used to solve this equation.

The nuclear reaction network has been recently updated and now contains 32 isotopes from hydrogen to zinc. It includes the p-p chains, CNO tri-cycle, Ne-Na and Mg-Al chains, and the  $\alpha$ -capture reactions. In total, 72 reaction rates are considered. These have been updated from JINA REACLIB database [Cyburt et al. \(2010\)](#), with their 6th April, 2015 recommendations, from which the rates and the reaction energy  $Q$  were provided. The electron screening factors are from [Dewitt et al. \(1973\)](#) and [Graboske et al. \(1973\)](#).

## 2.5 Boundary conditions

The boundary conditions at the centre and surface of the star are required to solve the structure equations, Eqs. 2.5-2.8. They are simply set, at the centre region,  $m = 0$ , and at the surface,  $m = M$ . In reality, there is a gradual and rather extended transition to the values of  $P$  and  $T$  at the outer regions of the star. Therefore, in practice, the star is sub-divided into three regions: 1) the inner region is solved all the structure equations; 2) the envelope, where no reactions are allowed to occur and the luminosity is kept constant ( $\epsilon_n=0$ ,  $\epsilon_\nu=0$ ,  $\epsilon_{\text{grav}}=0$ ); 3) the atmosphere where the mass is equal to the total mass, and the luminosity is kept constant.

### 2.5.1 The inner region

At the centre, the mass, radius and luminosity are null. Therefore, in order to obtain the central pressure and density, we need to use an approximation by expanding the formulas in power of  $m$ , in which  $m \rightarrow 0$ . The structure equations that describe the quantities at the surface of central small sphere

of mass  $m$  (where  $P, T, r, L$  are defined) then become,

$$P - P_c = -\frac{G}{2} \left( \frac{4\pi}{3} \right)^{1/3} \rho_c^{4/3} m^{2/3}, \quad (2.37)$$

$$r = \left( \frac{3m}{4\pi\rho_c} \right)^{1/3}, \quad (2.38)$$

$$L = \epsilon_c m, \quad (2.39)$$

$$T^4 - T_c^4 = -\frac{\kappa\epsilon_c}{2ac} \left( \frac{3}{4\pi} \right)^{1/3} \rho_c^{4/3} m^{2/3}, \quad (2.40)$$

$$\ln T - \ln T_c = -\left( \frac{\pi}{6} \right)^{1/3} \frac{G}{P_c} \rho_c^{4/3} m^{2/3} \nabla_{\text{ad}}, \quad (2.41)$$

where  $\epsilon_c$  is the total energy generation rate at the centre. The last two equations are for either the radiative case or convective case.

### 2.5.2 The atmosphere region

The atmosphere is supposed to begin at infinity where gas density falls to zero. It ends at the photosphere where  $R$ =stellar radius and  $L$ = stellar luminosity. It is supposed to give a negligible contribution to the total mass so that also  $M$ =constant. Then, from the hydrostatic equilibrium, the pressure and temperature are deduced from,

$$\frac{\partial P}{\partial r} = -\rho g, \quad (2.42)$$

where  $\rho$  is the density of the material and  $g$  is the gravity of the star at the atmosphere region. Combining this equation with the definition of optical depth,  $d\tau = \rho\kappa dr$ , we obtain the relation,

$$\frac{d\tau}{d\log P} = \frac{\kappa P}{g} \ln 10. \quad (2.43)$$

At the infinite radius, the pressure is only due to radiation, thus  $P(\infty) = P_{\text{rad}} = \frac{1}{3}aT^4$  where  $a = 7.57 \times 10^{-15} \text{erg cm}^{-3} \text{K}^{-4}$  is the radiant density constant. We integrate Eq. 2.43 from the infinity, where  $\tau = 0$ , to the region where  $\tau = 2/3$  as the definition of the atmosphere. The run of temperature

with  $\tau$  is provided by the modified Eddington approximation for radiative transport,

$$T^4(\tau) = \frac{3}{4}T_{\text{eff}}^4(\tau + q(\tau)), \quad (2.44)$$

where  $q(\tau)$  is the Hopf function. The two equations Eqs. 2.42 and 2.44 can be integrated and provide  $T$  ( $=T_{\text{eff}}$ ) and  $P$  at  $r=R$ , remembering also that  $R^2=L/(4\pi \sigma T_{\text{eff}}^4)$ . Note that equation 2.44 may be substituted with more appropriate relations taken from suitable atmosphere models.

### 2.5.3 The envelope region

The envelope places in between the atmosphere and the inner structure. Therefore, its upper bound is at which  $\tau = 2/3$ , and the lower bound is set at the point where the mass  $m/M_{\text{tot}} = (1 - 10^{-5})$ . The latter definition prevents to have high temperature so that the ignition of nuclei does not occur in this region. Since the luminosity is kept constant there are only three physical quantities ( $r$ ,  $P$ ,  $m$ ) needed to be solved from the structure equations. Since the mass varies very little in this region, pressure is used as the independent variable since it varies monotonically with  $m$ . Thus, the structure equations of the envelope are,

$$\frac{\partial \ln r}{\partial \ln P} = -\frac{Pr}{G\rho M}, \quad (2.45)$$

$$\frac{\partial \ln M}{\partial \ln P} = -\frac{4\pi r^4 P}{GM^2}, \quad (2.46)$$

$$\frac{\partial \ln T}{\partial \ln P} = \min [\nabla_{\text{ad}}, \nabla_{\text{rad}}]. \quad (2.47)$$

The integration is performed starting from the external photosphere, from  $T$ ,  $P$ ,  $M$ , and  $R$  at  $\tau = 2/3$ , until  $m/M_{\text{tot}}$ . At this point, an iterative procedure matches the external solution with the internal one until one gets the solution. The treatment of radiative and convective envelopes are explicitly described in [Kippenhahn et al. \(1967\)](#). Figure. 2.1 shows the sketch of three regions in mass coordinate in PARSEC models.

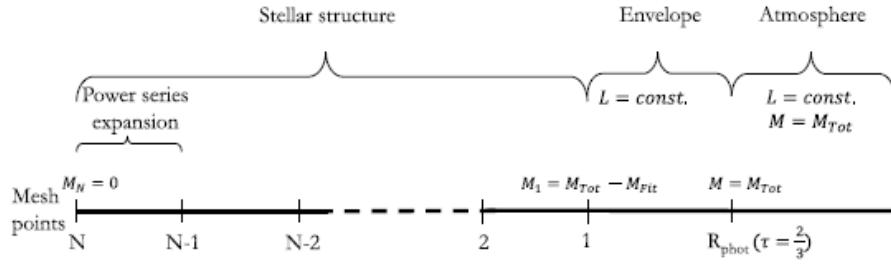


Figure 2.1: Sketch of three regions in PARSEC models: inner part, envelope, and atmosphere. The inner part directly connects to the central region from the mesh point mass  $M_1$ , the envelope is the inter-region between  $M_1$  and the innermost border of the atmosphere where  $\tau = 2/3$ , and forward to infinity is the atmosphere. In which,  $M_{\text{fit}}$  is chosen to be  $1 - 10^{-5}$ . The figure is adopted from [Costa \(2019\)](#).

# Chapter 3

## Stellar Model with Rotation

Rotation had been known to be one of the ingredients to explain many features from observations such as stellar population, (e.g., [Milone et al., 2017a](#); [Costa et al., 2019a](#)) or the enrichment of surface abundances (e.g., [Hunter et al., 2009](#); [Martins et al., 2015](#)). From a theoretical point of view, the impacts of rotation on stellar structure and evolution were successfully derived from many pioneering works (e.g., [Endal and Sofia, 1981](#); [Chaboyer and Zahn, 1992](#); [Zahn, 1992](#); [Meynet and Maeder, 1997](#)). In this chapter, I will focus on describing the equations of stellar structure for rotating-stars. The content of this chapter is mainly based on [Maeder \(2009\)](#). In Sect. 3.1, the basic assumptions which are used to study the rotating stars are summarised. The surface's properties of rotating stars are then shown in Sect. 3.2. The hydrostatic equation will be derived in Sect. 3.3. Next is the continuity equation will be re-derived in Sect. 3.4, and the energy conservation in Sect. 3.5. In Sect. 3.6, the transportation of energy in rotating-stars are discussed. A summary of derived structure equations will be shown in Sect. 3.7 for convenience, together with the calculation of the form factors that will be derived and shown in Sect. 3.8. Finally, Sect. 3.9 shows the changes of effective temperature along the co-latitude as a result of geometrical distortion in rotating stars.

### 3.1 Basic assumptions

The full scheme to study the effects of rotation would require a 3D simulation, however, under some assumptions, it is possible to cast these effects in

a 1D scheme. In particular, [Kippenhahn and Thomas \(1970\)](#) adopted four assumptions and developed a methodology to include the geometric distortion caused by rotation in the structure equations of stellar models. The four assumptions are:

1. The star is divided into shells which are delimited by equipotential surfaces (or isobars). The shells are not spherical as in the case of non-rotating models
2. In each shell, the angular velocity ( $\Omega$ ) has a cylindrical symmetry
3. The  $\Omega$  is constant along the latitude angle ( $\theta$ ) of the shells
4. The Roche approximation is used to define the shape of the surface of rotating stars.

These assumptions lead to a remarkable advantage to define the shape of isobars of a rotating star. We will see later that the system of structure equations for rotating stars remains the same as the non-rotating case but with only two “form factors” ( $f_P$  and  $f_T$ ) that are inserted to model the effects of rotation. They are introduced to take into account the mechanical and thermal distortion caused by rotation. As a first step, we should define the isobar and its properties, which will be presented in the next section.

## 3.2 The Roche model and stellar surface

In Roche model, all the mass is assumed to be concentrated in the central region where  $R = 0$ . There are two scenarios to describe an isobar, the so-called “baroclinic” scheme where the angular velocity  $\Omega$  and the total potential  $\Psi$  are constant, and the so-called “barotropic” scheme where the pressure  $P$  is constant over the stellar surface. In this thesis, calculations to define an isobar follow the “baroclinic” scenario. In this case, the total potential of rotating stars is written as

$$\Psi(R, \theta) = -\frac{GM}{R} - \frac{1}{2}\Omega^2 R^2 \sin^2 \theta = \text{const}, \quad (3.1)$$

where the first component is the gravitational potential, with  $M$  being the mass enclosed inside a sphere of radius  $R$ , and the second component is the potential caused by centrifugal acceleration.



The effective gravity is defined as,

$$\mathbf{g}_{\text{eff}} = \frac{1}{\rho} \nabla \mathbf{P} = -\nabla \Psi - R^2 \sin^2 \theta \Omega \nabla \Omega, \quad (3.2)$$

from Eq. 3.1 one can expand  $\mathbf{g}_{\text{eff}}$  vector in form of,

$$\mathbf{g}_{\text{eff}} = \left[ -\frac{GM}{R^2(\theta)} + \Omega^2 R(\theta) \sin^2 \theta \right] \mathbf{e}_r + [\Omega^2 R(\theta) \sin \theta \cos \theta] \mathbf{e}_\theta, \quad (3.3)$$

where  $\mathbf{e}_r$  and  $\mathbf{e}_\theta$  are the unity vectors in the radial and latitudinal directions. Thus, the modulus value of effective gravity  $g_{\text{eff}} = |\mathbf{g}_{\text{eff}}|$  is

$$g_{\text{eff}} = \left[ \left( -\frac{GM}{R^2(\theta)} + \Omega^2 R(\theta) \sin^2 \theta \right)^2 + (\Omega^2 R(\theta) \sin \theta \cos \theta)^2 \right]^{1/2}. \quad (3.4)$$

At the equator, the modulus of centrifugal force is balanced with the modulus of gravitational force. The so-called critical velocity (or break-up velocity,  $\Omega_{\text{crit}}$ ) is then defined as the surface angular velocity of the star at the point  $\theta = \pi/2$  (equator), where  $g_{\text{eff}} = 0$ . Therefore, from Eq. 3.4 it is written as,

$$\Omega_{\text{crit}} = \sqrt{\frac{GM}{R_{\text{e,crit}}^3}}, \quad (3.5)$$

where  $R_{\text{e,crit}}$  is the equatorial radius at the critical rotation.

At the pole, the centrifugal force is null, thus the equation of an isobar becomes,

$$\frac{GM}{R} + \frac{1}{2} \Omega^2 R^2 \sin^2 \theta = \frac{GM}{R_{\text{pol}}}. \quad (3.6)$$

If we consider a point at the equator, it should obey the relation above with the critical angular velocity and radius, therefore, we obtain a relationship between the equatorial radius and the polar radius,

$$\frac{R_{\text{e,crit}}}{R_{\text{pol}}} = \frac{3}{2}. \quad (3.7)$$

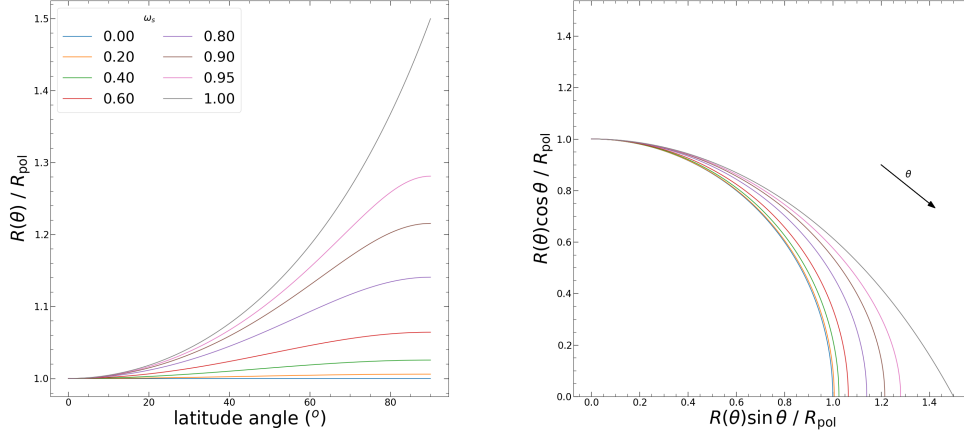


Figure 3.1: Shape of rotating stars' surface. *Left*: The variation of the radius ratio  $R(\theta)/R_{\text{pol}}$  with different latitude angles in degree unit. *Right*: The shape of a rotating star in 1D with many considered rotation rates ( $\omega$ ), the arrow implies the direction of  $\theta$  from pole-on ( $0^\circ$ ) to equator-on ( $90^\circ$ ).

The rotation rate  $\omega$  is then defined as the ratio of angular velocity and its critical value,

$$\omega^2 = \frac{\Omega^2}{\Omega_{\text{e,crit}}^2} = \frac{\Omega^2 R_{\text{e,crit}}^3}{GM} = \frac{27}{8} \frac{\Omega^2 R_{\text{pol}}^3}{GM}. \quad (3.8)$$

With this definition of  $\omega$ , the equation of an isobar can be rewritten as

$$\frac{1}{R/R_{\text{pol}}} + \frac{4}{27} \omega^2 \left( \frac{R}{R_{\text{pol}}} \right)^2 \sin^2 \theta - 1 = 0. \quad (3.9)$$

We can see that at a given  $\omega$  model, this equation is purely geometrical, i.e., its root  $(R/R_{\text{pol}})$  is the radii at a fixed latitude angle. For this purpose, the left panel of Fig. 3.1 shows the variation of  $R(\theta)/R_{\text{pol}}$  with  $\theta$  in many  $\omega$ -models. It is obvious that when the star rotates, it is stretched outwardly in terms of distance. The more we go to the equator, the more it is extended. This increases as increasing rotation rate. In order to provide a better illustration, the right panel of Fig. 3.1 shows the shape of the surface of many rotating models from zero to the critical one, at which the latitude angle varies from top-left down to bottom-right as in from the pole to equator.

In summary, we have obtained Eq. 3.9 which is the equation of stellar surfaces of rotating stars (or isobars). At a given rotation rate  $\omega$ , the equation gives a solution of radius  $R$  as a function of latitude angle  $R = R(\theta)$ , in another word, rotating stars lose their geometrical symmetry.

### 3.3 Hydrostatic equilibrium

As mentioned above, the individual shells have no longer spherical symmetry and thus any quantity that is not constant over an isobaric surface would be considered by means of a mean value. Inside an isobar with enclosed radius  $r_P$ , the corresponding volume is written as  $V_P = 4\pi/3r_P^3$ , and the mean value of a quantity  $q$  is computed as,

$$\langle q \rangle = \frac{1}{S_P} \int_{\Psi=\text{const}} q d\sigma. \quad (3.10)$$

Here,  $S_P$  is the surface over an isobar, and  $d\sigma$  is the element surface,

$$d\sigma = \frac{r^2 \sin \theta d\phi d\theta}{\cos \xi}, \quad (3.11)$$

with  $\phi$  being the longitude coordinate, and  $\xi$  an angle which is given by,

$$\cos \xi = \frac{\frac{1}{x^2} - \frac{8}{27}\omega^2 x \sin^2 \theta}{\sqrt{\left(-\frac{1}{x^2} + \frac{8}{27}\omega^2 x \sin^2 \theta\right)^2 + \left(\frac{8}{27}\omega^2 x \sin \theta \cos \theta\right)^2}}, \quad (3.12)$$

where  $x = R/R_{\text{pol}}$ , and we will come back to the definition of  $S_P$  and  $\xi$  in Sect. 3.8.1 while at the moment we temporarily adopt it.

From the Roche model, the effective gravity is expressed in the form of equipotential and angular velocity,

$$\mathbf{g}_{\text{eff}} = -\nabla \Psi - r^2 \sin^2 \theta \Omega \nabla \Omega. \quad (3.13)$$

Thus, the equation of hydrostatic equilibrium  $\nabla \mathbf{P} = \rho \mathbf{g}_{\text{eff}}$  becomes,

$$\nabla \mathbf{P} = -\rho (\nabla \Psi + r^2 \sin^2 \theta \Omega \nabla \Omega). \quad (3.14)$$

From this form we can see that vector  $\nabla \mathbf{P}$  must be parallel with both vectors  $\nabla \Psi$  and  $\nabla \Omega$ . This is likely because  $\Omega$  is constant on isobars and so do  $\Psi$ ,

which means that vector  $\nabla\Omega$  is parallel to vector  $\nabla\Psi$ , and hence Eq. 3.14 valid only if vector  $\nabla\mathbf{P}$  is parallel to them.

Since  $\nabla\Omega$  is parallel to  $\nabla\Psi$ , we can write

$$\nabla\Omega = -\alpha \nabla\Psi \quad \text{with} \quad \alpha = \left| \frac{d\Omega}{d\Psi} \right|. \quad (3.15)$$

From Eq. 3.13 the modulus of  $\mathbf{g}_{\text{eff}}$  is then simply written as,

$$g_{\text{eff}} = (1 - r^2 \sin^2 \theta \Omega \alpha) \frac{d\Psi}{dn}, \quad (3.16)$$

with  $dn \equiv dr_P$  being the average distance between two isobars. The hydrostatic equilibrium Eq. 3.14 then becomes,

$$\frac{dP}{dn} = -\rho (1 - r^2 \sin^2 \theta \Omega \alpha) \frac{d\Psi}{dn}. \quad (3.17)$$

The convenience of using the mass coordinate was already mentioned before, thus it is useful to express the mass  $M_P$  inside an isobar,

$$dM_P = \int_{\Psi=\text{const}} \rho \, dn \, d\sigma = d\Psi \int \rho \frac{(1 - r^2 \sin^2 \theta \Omega \alpha)}{g_{\text{eff}}} d\sigma \quad (3.18)$$

$$= \rho (1 - r^2 \sin^2 \theta \Omega \alpha) S_P < g_{\text{eff}}^{-1} > d\Psi. \quad (3.19)$$

In the second equality, we already used the relation Eq. 3.16. The last equality is obtained by using the definition of mean value Eq. 3.10 and the fact that  $\rho(1 - r^2 \sin^2 \theta \Omega \alpha)$  is constant on isobars. Thus, from Eq. 3.17, we obtain an equation of hydrostatic equilibrium in Lagrangian coordinate,

$$\frac{dP}{dM_P} = \frac{-1}{< g_{\text{eff}}^{-1} > S_P} = -\frac{GM_P}{4\pi r_P^4} f_P. \quad (3.20)$$

Here,  $f_P$  is the form factor over an isobaric surface which is defined as,

$$f_P = \frac{4\pi r_P^4}{GM_P S_P} \frac{1}{< g_{\text{eff}}^{-1} >}. \quad (3.21)$$

Therefore, from relation Eq. 3.20, we can see that apart from the form factor  $f_P$ , the equation of hydrostatic equilibrium in case of rotating model keeps the same form it has in the case of non-rotating stars. Moreover, it is obvious that in case of non-rotating, the effective gravity is a gradient of gravitational potential, hence  $f_P$  become unity which leads Eq. 3.20 to the classical hydrostatic equilibrium equation.

### 3.4 Continuity equation

The second equation we consider is the mass continuity equation. First, we need to consider the volume of a shell between two isobars which is defined as,

$$dV_P = \int_{\Psi=\text{const}} dn \, d\sigma = 4\pi r_P^2 dr_P. \quad (3.22)$$

By using Eq. 3.16 to express  $dn$ , and with the definition of the mean value (Eq. 3.10) we obtain the expression of  $dV_P$ ,

$$dV_P = d\Psi S_P [\langle g_{\text{eff}}^{-1} \rangle - \langle g_{\text{eff}}^{-1} r^2 \sin^2 \theta \rangle \Omega \alpha] = 4\pi r_P^2 dr_P. \quad (3.23)$$

Hence, we can get the continuity equation for shellular rotation by using the relation between  $d\Psi$  and  $dM_P$  in Eq. 3.19,

$$\frac{dr_P}{dM_P} = \frac{1}{4\pi r_P^2 \bar{\rho}}, \quad \text{with} \quad \bar{\rho} = \frac{\rho (1 - r^2 \sin^2 \theta \Omega \alpha) \langle g_{\text{eff}}^{-1} \rangle}{\langle g_{\text{eff}}^{-1} \rangle - \langle g_{\text{eff}}^{-1} r^2 \sin^2 \theta \rangle \Omega \alpha}. \quad (3.24)$$

We can see that  $\bar{\rho}$  is the average density of the shell between two isobars. Together, Eqs. 3.20 and 3.24 are the equations of hydrostatic equilibrium and mass conservation for shellular rotation stars.

### 3.5 Energy conservation

Similarly, we consider the net energy outflow from a shell between two isobars, which is given by,

$$dL_P = \int_{\Psi=\text{const}} \epsilon \, \rho \, dnd\sigma, \quad (3.25)$$

where  $\epsilon = \epsilon_{\text{nucl}} - \epsilon_{\nu} + \epsilon_{\text{grav}}$  is the total rate of energy production in the shell from nuclear reactions ( $\epsilon_{\text{nucl}}$ ), neutrino losses ( $\epsilon_{\nu}$ ) and gravitational energy ( $\epsilon_{\text{grav}}$ ). Using Eq. 3.16 and the condition that  $\rho(1 - r^2 \sin^2 \theta \Omega \alpha)$  is constant on an isobar, we obtain

$$dL_P = d\Psi \langle \frac{\epsilon}{g_{\text{eff}}} \rangle S_P \rho (1 - r^2 \sin^2 \theta \Omega \alpha). \quad (3.26)$$

Finally, from relation Eq. 3.19 we can deduce the equation of energy production in rotating stars in mass coordinate,

$$\frac{dL_P}{dM_P} = \frac{\langle \epsilon g_{\text{eff}}^{-1} \rangle}{\langle g_{\text{eff}}^{-1} \rangle}. \quad (3.27)$$

Because of the non-constancy of density and temperature on isobars, one can consider them as dependent variables. Hence, one can make an approximation for the energy conservation,

$$\frac{\langle (\epsilon_{\text{nucl}} - \epsilon_{\nu} + \epsilon_{\text{grav}}) g_{\text{eff}}^{-1} \rangle}{\langle g_{\text{eff}}^{-1} \rangle} \approx \epsilon_{\text{nucl}}(\bar{\rho}, \bar{T}) - \epsilon_{\nu}(\bar{\rho}, \bar{T}) + \epsilon_{\text{grav}}(\bar{\rho}, \bar{T}). \quad (3.28)$$

Therefore, one can rewrite Eq. 3.27,

$$\frac{dL_P}{dM_P} = \epsilon_{\text{nucl}} - \epsilon_{\nu} + \epsilon_{\text{grav}}, \quad (3.29)$$

in which the energy generation rates are now written with the average values of density and temperature.

## 3.6 Transport of energy

### 3.6.1 Radiative transfer

The radiative flux at a given point on the isobar is given by,

$$F = -\frac{4acT^3}{3\kappa\rho} \frac{dT}{dn} = -\frac{4acT^3}{3\kappa\rho} \frac{dT}{dM_P} \rho \langle g_{\text{eff}}^{-1} \rangle S_P g_{\text{eff}}, \quad (3.30)$$

in which we already used Eq. 3.16 to express  $dn$  and Eq. 3.19 to relate  $d\Psi$  and  $dM_P$  and finally using definition Eq. 3.10 to have the last equality of the equation above. Integrating the flux over the isobar, one obtains the energy transfer equation,

$$L_P = -\frac{4ac}{3} \langle g_{\text{eff}}^{-1} \rangle S_P^2 \left\langle \frac{T^3 g_{\text{eff}}}{\kappa} \frac{dT}{dM_P} \right\rangle. \quad (3.31)$$

Similarly, we can expand the last average term in the equation above as a function of the two dependent variables ( $\bar{\rho}$  and  $\bar{T}$ ) on an isobar, as we did for the energy conservation,

$$\left\langle \frac{T^3 g_{\text{eff}}}{\kappa} \frac{dT}{dM_P} \right\rangle \approx \frac{\bar{T}^3 \langle g_{\text{eff}} \rangle}{\kappa(\bar{\rho}, \bar{T})} \frac{d\bar{T}}{dM_P}. \quad (3.32)$$

Thus, one has from Eqs. 3.31 and 3.32,

$$\frac{d\bar{T}}{dM_P} = -\frac{3}{4ac} \frac{\kappa}{\bar{T}^3} \frac{L_P}{S_P^2} \frac{1}{<g_{\text{eff}}> <g_{\text{eff}}^{-1}>}. \quad (3.33)$$

with  $\kappa \equiv \kappa(\bar{\rho}, \bar{T})$ . Using the definition of radiative gradient in shellular rotation,  $\nabla_{\text{rad}} = \frac{3}{16\pi acG} \frac{\kappa L_P P}{M_P \bar{T}^4}$ , one can rewrite the equation above, such as

$$\frac{d\bar{T}}{dM_P} = -\frac{\bar{T}}{P} \frac{GM_P}{4\pi r_P^4} \nabla_{\text{rad}} \left( \frac{4\pi r_P^2}{S_P} \right)^2 \frac{1}{<g_{\text{eff}}> <g_{\text{eff}}^{-1}>}. \quad (3.34)$$

We can easily see that, apart from the last two terms in the expression above, the equation of radiative transfer is similar to the non-rotating model. By introducing the so-called form factor,

$$f_T = \left( \frac{4\pi r_P^2}{S_P} \right)^2 \frac{1}{<g_{\text{eff}}> <g_{\text{eff}}^{-1}>}, \quad (3.35)$$

the equation of radiative transfer of rotating stars is written as,

$$\frac{d \ln \bar{T}}{dM_P} = -\frac{GM_P}{4\pi r_P^4} \frac{1}{P} f_T \nabla_{\text{rad}}, \quad (3.36)$$

in which, we used  $d \ln \bar{T} = d\bar{T}/\bar{T}$ .

### 3.6.2 Convective transport

As once mentioned in Sect. 2.1, the energy can be transported by convection and can be rather complicated in its treatment. In this section, we examine the convective transport in the interior region of a star, where the temperature gradient is the adiabatic gradient. We then can write the average

$$<\nabla_{\text{ad}}> = <\frac{d \ln T}{d \ln P}> \approx \frac{d \ln \bar{T}}{d \ln P} = \nabla_{\text{ad}}(\bar{\rho}, \bar{T}). \quad (3.37)$$

Recalling the relation between  $dP$  and  $dM_P$  from Eq. 3.20, one obtains

$$\frac{d \ln \bar{T}}{dM_P} = -\frac{GM_P}{4\pi r_P^4} \frac{1}{P} f_P \nabla_{\text{ad}}, \quad (3.38)$$

with  $f_P$  being the form factor which was introduced in Eq. 3.21, and the adiabatic gradient being

$$\nabla_{\text{ad}} = \frac{P\delta}{\bar{T}\bar{\rho}c_P} \quad \text{with} \quad \delta = - \left( \frac{\partial \ln \bar{\rho}}{\partial \ln T} \right)_{P,\mu}. \quad (3.39)$$

Therefore, in general, the energy transport equation of rotating stars is written as,

$$\frac{d \ln \bar{T}}{dM_P} = - \frac{GM_P}{4\pi r_P^4} \frac{1}{P} f_P \min \left[ \nabla_{\text{ad}}, \nabla_{\text{rad}} \frac{f_T}{f_P} \right], \quad (3.40)$$

taking into account either radiative transport or convective transport of energy.

### 3.7 Stellar structure equations with rotation

We have re-derived the stellar structure equations for rotating stars in the sections above. For convenience to readers, I summarize those equations in this section. With the changes in dependent variables on an isobar (i.e.,  $\bar{\rho}, \bar{T}$ ) and the approximations, we rewrite the set of stellar structure equations for rotating stars,

$$\text{continuity equation: } \frac{\partial r_P}{\partial M_P} = \frac{1}{4\pi r_P^2 \bar{\rho}}, \quad (3.41)$$

$$\text{hydrostatic equilibrium: } \frac{\partial P}{\partial M_P} = - \frac{GM_P}{4\pi r_P^4} f_P, \quad (3.42)$$

$$\text{energy conservation: } \frac{\partial L_P}{\partial M_P} = \epsilon_{\text{nucl}} - \epsilon_{\nu} + \epsilon_{\text{grav}}, \quad (3.43)$$

$$\text{energy transfer: } \frac{\partial \ln \bar{T}}{\partial M_P} = - \frac{GM_P}{4\pi r_P^4} \frac{1}{P} f_P \min \left[ \nabla_{\text{ad}}, \nabla_{\text{rad}} \frac{f_T}{f_P} \right]. \quad (3.44)$$



with

$$f_P = \frac{4\pi r_P^4}{GM_P S_P} \frac{1}{\langle g_{\text{eff}}^{-1} \rangle}, \quad (3.45)$$

$$f_T = \left( \frac{4\pi r_P^2}{S_P} \right)^2 \frac{1}{\langle g_{\text{eff}} \rangle \langle g_{\text{eff}}^{-1} \rangle}, \quad (3.46)$$

$$\nabla_{\text{rad}} = \frac{3}{16\pi acG} \frac{\kappa L_P P}{M_P \bar{T}^4}, \quad (3.47)$$

$$\nabla_{\text{ad}} = \frac{P\delta}{\bar{T}\bar{\rho}c_P}, \quad (3.48)$$

where  $\delta = -\left(\frac{\partial \ln \bar{p}}{\partial \ln \bar{T}}\right)_{P,\mu}$  is the thermo-dynamical derivative. We should notice that a quantity such as  $\bar{x}$  represents the average value over a volume of the shell in between two neighboring isobars, while  $\langle x \rangle$  denotes the average value over a given isobar surface. The set of equations keeps the same form as the classical for non-rotating models (Eqs. 2.5 - 2.8, together with Eq. 2.9 in the convective zones). The only difference is the presence of the form factors ( $f_P$  and  $f_T$ ), describing the effects of rotation.

As mentioned in Chapter. 2, the star is divided in three regions, i.e., inner region, envelope, and atmosphere. We will see below that rotation impacts both outer regions (envelope and atmosphere). However, due to the boundary condition at the centre for angular velocity  $\left(\frac{d\Omega}{dr}\right)_c = 0$ , the structure equations at the centre can be adopted from non-rotating model.

### 3.7.1 Equations for stellar envelope

Provided that we use an envelope with a tiny mass, ( $m_{\text{envelope}}/M_{\text{tot}} \ll 1$ ), we may assume that the envelope rotates with an angular velocity equal to the outermost layer of the interior. Contrary to the mass, the pressure varies in a wide range of values in the envelope region and thus the latter is conveniently used as the independent variable in this part of the star. Using the relation between  $\partial P$  and  $\partial M_P$  in Eq. 3.42, one obtains the stellar structure equations

for the envelope which are,

$$\frac{\partial \ln r_P}{\partial \ln P} = -\frac{r_P P}{GM_P \bar{\rho}} \frac{1}{f_P}, \quad (3.49)$$

$$\frac{\partial \ln M_P}{\partial \ln P} = -\frac{4\pi r_P^4 P}{GM_P^2} \frac{1}{f_P}, \quad (3.50)$$

$$\frac{\partial \ln \bar{T}}{\partial \ln P} = \min \left[ \nabla_{\text{ad}}, \nabla_{\text{rad}} \frac{f_T}{f_P} \right]. \quad (3.51)$$

### 3.7.2 Equations for stellar atmosphere

In the atmosphere, the mass, the radius, and the luminosity are constant, thus only the equation of hydrostatic equilibrium and of energy transfer is needed to be considered. In this region, we suppose that  $\Omega$  is constant (independent on the depth of the atmosphere) and equal to the outermost of the envelope. In this case, one can clearly see that  $\alpha = |d\Omega/d\Psi| = 0$ , thus from Eqs. 3.17, 3.19 and 3.24 one has,

$$\frac{dP}{d\Psi} = -\rho, \quad (3.52)$$

$$\frac{d\Psi}{dM_P} = \frac{\rho^{-1}}{S_P < g_{\text{eff}}^{-1} >}, \quad (3.53)$$

$$\frac{dM_P}{dr_P} = 4\pi r_P^2 \rho. \quad (3.54)$$

Again we combine those three equations with the definition of optical depth  $d\tau_P = -\kappa \rho dr_P$ , and obtain the variation of pressure along the optical depth,

$$\frac{dP}{d\tau_P} = \frac{1}{\kappa} \frac{4\pi r_P^2}{S_P < g_{\text{eff}}^{-1} >}, \quad (3.55)$$

which can be transformed into,

$$\frac{d\tau_P}{d \log P} = \kappa \frac{S_P < g_{\text{eff}}^{-1} >}{4\pi r_P^2} P \ln 10. \quad (3.56)$$

Rotation also modifies the equation of radiative transport. One can write the radiative pressure variation in an average distance  $dn$ ,

$$\frac{dP_{\text{rad}}}{dn} = \frac{dP_{\text{rad}}}{dr_P} \frac{dr_P}{dM_P} \frac{dM_P}{d\Psi} \frac{d\Psi}{dn}. \quad (3.57)$$

Using relation in Eqs. 3.53, 3.54, and 3.16 with  $\alpha = 0$ , one obtains

$$\frac{dP_{\text{rad}}}{dn} = \frac{dP_{\text{rad}}}{dr_P} \frac{S_P < g_{\text{eff}}^{-1} >}{4\pi r_P^2} g_{\text{eff}}. \quad (3.58)$$

In the diffusive approximation, the local radiative pressure is written as

$$\frac{dP_{\text{rad}}}{dn} = -\frac{\kappa\rho}{c} F, \quad (3.59)$$

with  $c$  being the speed of light and  $F$  the energy flux. Therefore, we can basically deduce the term  $dP_{\text{rad}}/dr_P$  from Eq. 3.58. Furthermore, with the definition of optical depth above, we eventually obtain the relation,

$$\frac{dP_{\text{rad}}}{d\tau_P} = \frac{4\pi r_P^2}{S_P < g_{\text{eff}}^{-1} >} \frac{1}{c} \frac{F}{g}. \quad (3.60)$$

Integrating the derivative equation above from  $\tau_P$  to the surface where  $P \rightarrow 0$ , we get

$$P_{\text{rad}}(\tau_P) = \frac{F}{g_{\text{eff}}} \frac{1}{c} \left[ \frac{4\pi r_P^2}{S_P < g_{\text{eff}}^{-1} >} + q(\tau_P) g_{\text{eff}} \right], \quad (3.61)$$

where  $q(\tau)$  is the Hopf function. Then we apply the theorem of von Zeipel (1924a) which states that,

$$F = -\rho \frac{4acT^3}{3\kappa\rho} \frac{dT}{dM_P} \frac{dM_P}{dP} g_{\text{eff}}, \quad (3.62)$$

and use Eq. 3.33, and Eqs. 3.52 - 3.53, to get

$$\frac{F}{g_{\text{eff}}} = \frac{L}{S_P < g_{\text{eff}} >}. \quad (3.63)$$

Eventually, by using the expression of  $L = S_P \sigma T_{\text{eff}}^4$  and  $P_{\text{rad}} = \frac{4}{3} \frac{\sigma}{c} T^4$  in thermal equilibrium, one gets

$$T^4(\tau_P) = \frac{3}{4} T_{\text{eff}}^4 \left[ \frac{S_P}{4\pi r_P^2} f_T \tau_P + q(\tau_P) \frac{g_{\text{eff}}}{< g_{\text{eff}} >} \right]. \quad (3.64)$$

In the approximation of Roche model,  $g_{\text{eff}}$  is given by Eq. 3.4.

In summary, under the effects of rotation, the equations of stellar structure in the envelope are described by Eqs. 3.49 - 3.51, while Eqs. 3.56 and 3.64 express the structure of the atmosphere region of rotating stars. Besides that, at the centre, from the boundary condition, the radius is null and thus the angular momentum. Therefore, the structure equations are kept the same as in the classical non-rotating model.

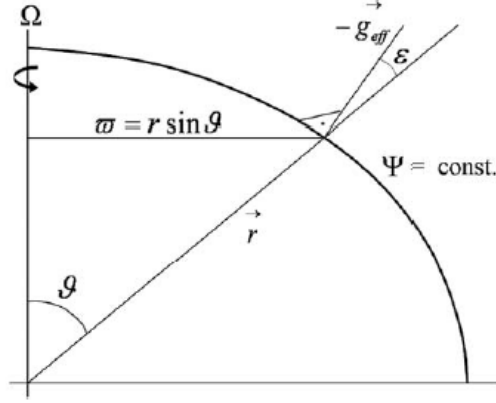


Figure 3.2: The angle  $\xi$  between the effective gravity and the radius on an isobar of rotating stars. The figure is adopted from [Maeder \(2009\)](#).

## 3.8 Calculation of the form factors

As demonstrated above, the rotation is characterised by the two form factors that appear in the structure equations. Therefore, evaluating these two factors is the next step to do. From Eqs. 3.45 and 3.46, in order to calculate  $f_P$ ,  $f_T$  we need to know the isobar surface ( $S_P$ ), the average effective gravity ( $\langle g_{\text{eff}} \rangle$ ), its inverse average ( $\langle g_{\text{eff}}^{-1} \rangle$ ) and the “volumetric” radius ( $r_P$ ).

### 3.8.1 Surface of an isobar

The surface of an isobar is calculated by integrating the element  $d\sigma$  over the whole surface,

$$S_P = \int_{\Psi=\text{const}} d\sigma, \quad \text{with} \quad d\sigma = \frac{r^2 \sin \theta \, d\phi d\theta}{\cos \xi}, \quad (3.65)$$

where  $r = r(\theta)$ , the radius, depends only on the latitude angle and  $\xi$  is the angle between effective gravity and radius ( $-\mathbf{g}_{\text{eff}}$  and  $\mathbf{r}$ ), which is defined as

$$\cos \xi = -\frac{\mathbf{g}_{\text{eff}} \cdot \mathbf{r}}{|\mathbf{g}_{\text{eff}}| |\mathbf{r}|}. \quad (3.66)$$

The angle  $\xi$  is zero only at the pole or equator as illustrated in Fig. 3.2. Inserting  $d\sigma$  we have,

$$S_P = 4\pi R_{\text{pol}}^2 \int_0^{\frac{\pi}{2}} \frac{x^2 \sin \theta}{\cos \xi} d\theta = 4\pi R_{\text{pol}}^2 S'. \quad (3.67)$$

Note that, in the first equality we already expanded the integral of  $d\phi$  from 0 to  $2\pi$ , taking into account the symmetry of two parts above and below the equator. We also used the notation  $x = x(\theta) = r(\theta)/R_{\text{pol}}$ . The dimensionless surface  $S'$  has been introduced in the equation above and is defined as,

$$S' = \int_0^{\frac{\pi}{2}} \frac{x^2 \sin \theta}{\cos \xi} d\theta. \quad (3.68)$$

In order to compute  $S_P$  we need to know the expression of  $\cos \xi$ . From Sect. 3.2 one already has the expression of the effective gravity both in vector and modulus forms. Therefore, we can easily insert Eqs. 3.3 and 3.4 into 3.66, which becomes

$$\cos \xi = \frac{\frac{GM}{R^2} - \Omega^2 R \sin^2 \theta}{\left[ \left( -\frac{GM}{R^2(\theta)} + \Omega^2 R(\theta) \sin^2 \theta \right)^2 + (\Omega^2 R(\theta) \sin \theta \cos \theta)^2 \right]^{1/2}}. \quad (3.69)$$

If we define  $x = R/R_{\text{pol}}$  and use the rotation rate  $\omega$  from Eq. 3.8, instead of the angular velocity  $\Omega$ , we can rewrite the equation above into

$$\cos \xi = \frac{\frac{1}{x^2} - \frac{8}{27} \omega^2 x \sin^2 \theta}{\left[ \left( -\frac{1}{x^2} + \frac{8}{27} \omega^2 x \sin^2 \theta \right)^2 + \left( \frac{8}{27} \omega^2 x \sin \theta \cos \theta \right)^2 \right]^{1/2}}. \quad (3.70)$$

As one can see,  $\cos \xi$  depends only on  $\omega$  and latitude angle  $\theta$  (since  $x \propto R(\theta)$ ). Therefore, the dimensionless  $S'$  in Eq. 3.68 depends only on rotation rate  $\omega$  eventually. To this purpose, Table. 3.1 lists the values of  $S'$  for different  $\omega$ . We now are able to calculate the isobar surface  $S_P$  from  $S'$  by multiplying it with the classical spherical surface, i.e.,  $4\pi R_{\text{pol}}^2$ .

### 3.8.2 Average effective gravity

From the definition of an average value we get

$$\langle g_{\text{eff}} \rangle = \frac{1}{S_P} \int_{\Psi=\text{const}} g_{\text{eff}} d\sigma = \frac{4\pi R_{\text{pol}}^2}{S_P} \int_0^{\frac{\pi}{2}} g_{\text{eff}} \frac{x^2 \sin^2 \theta}{\cos \xi} d\theta. \quad (3.71)$$

With the introduction of  $x$  and  $\omega$ , one should rewrite  $g_{\text{eff}}$  in Eq. 3.4 for convenience, which becomes

$$g_{\text{eff}} = \frac{GM}{R_{\text{pol}}^2} \left[ \left( -\frac{1}{x^2} + \frac{8}{27} \omega^2 x \sin^2 \theta \right)^2 + \left( \frac{8}{27} \omega^2 x \sin \theta \cos \theta \right)^2 \right]^{1/2}. \quad (3.72)$$

Using Eq. 3.67 for  $S_P$ , the average effective gravity becomes,

$$\langle g_{\text{eff}} \rangle = \frac{GM}{R_{\text{pol}}^2} \frac{1}{S'} \int_0^{\frac{\pi}{2}} g_{\text{eff}} \frac{x^2 \sin^2 \theta}{\cos \xi} d\theta. \quad (3.73)$$

If we do the same for the average of the inverse effective gravity, we should obtain

$$\langle g_{\text{eff}}^{-1} \rangle = \frac{GM}{R_{\text{pol}}^2} \frac{1}{S'} \int_0^{\frac{\pi}{2}} \frac{1}{g_{\text{eff}}} \frac{x^2 \sin^2 \theta}{\cos \xi} d\theta. \quad (3.74)$$

With  $S'$  from Table. 3.1 for different values of  $\omega$ , expression of  $\cos \xi$  from Eq. 3.70 and  $g_{\text{eff}}$  from Eq. 3.72, we are able to calculate the average of effective gravity as well as its inverse average on an isobar of rotating stars.

### 3.8.3 Volumetric radius

Recall again the definitions  $x = R/R_{\text{pol}}$  and  $\omega = \frac{27}{8} \frac{\Omega^2 R_{\text{pol}}^3}{GM}$ . One can rewrite the equation of an isobar (Eq. 3.9) in form of  $x$  and  $\omega$ , which is

$$\frac{4}{27} \omega^2 x^3 \sin^2 \theta - x + 1 = 0. \quad (3.75)$$

Clearly, this relation gives us an insight into the shape of the surface of a rotating star at a given rate  $\omega$ . Namely, by solving this third degree equation we obtain the radius as a function of latitude angle  $\theta$  and rotation rate  $\omega$ , i.e.,  $R = R_{\text{pol}} R'$  where  $R' = R'(\theta, \omega)$  is a dimensionless parameter obtained from the root of the equation above. It would be convenient to consider also the volume enclosed by it,  $V = V(\omega)$ , which is called volumetric volume and depends only on the rotation rate. By definition, we have

$$V = \int dR d\sigma = \int R_{\text{pol}} dR' \frac{(R_{\text{pol}} R')^2 \sin \theta d\phi d\theta}{\cos \xi} = \frac{4}{3} \pi R_{\text{pol}}^3 V', \quad (3.76)$$

with the dimensionless volume being

$$V' = 3 \int dR' \frac{R'^2 \sin \theta d\theta}{\cos \xi} = V'(\omega), \quad (3.77)$$

We can see that  $V'$  is a function of only  $\omega$  and its values are listed in Table. 3.1, for different values of  $\omega$ . On the other hand, we have  $V = \frac{4}{3}\pi r_P^3$ , namely we have

$$V = \frac{4}{3}\pi r_P^3 = \frac{4}{3}\pi R_{\text{pol}}^3 V', \quad (3.78)$$

or

$$r_P = R_{\text{pol}}(V')^{1/3}. \quad (3.79)$$

This important relation gives us a connection between the volumetric radius to the polar radius.

### 3.8.4 Computing the form factors

We have so far obtained all the quantities that are needed to compute  $f_P$  and  $f_T$ . They have been obtained by means of dimensionless quantities and the polar radius  $R_{\text{pol}}$  as showed in Eqs. 3.67, 3.73, 3.74 and 3.79. Therefore, at each time step during the evolution, one needs to derive and update the value for the polar radius. In order to do this, from Eq. 3.8, one needs at least to know the current  $\omega$ . For this purpose, one again needs a relation that links the physical quantities to the dimensionless quantities. We can find such a relation by combining Eqs. 3.8 and 3.78 which is

$$V'\omega^2 = \frac{27}{8} \frac{\Omega^2 r_P^3}{GM_P}. \quad (3.80)$$

The value of  $V'\omega^2$  is unique since  $V'$  depends only on  $\omega$ , and is listed in Table. 3.1.

In another word, at each time-step, for each shell that is identified by the mass  $M_P$ , enclosed inside a volumetric radius,  $r_P$ , and an angular velocity  $\Omega$ , one gets the specific  $\omega$  by using  $V'\omega^2$  from Eq. 3.80 and Table. 3.1. Once we know  $\omega$ , the dimensionless quantities can then be derived and thus the form factors can be calculated.

$\omega$	$S'$	$V'$	$f_P$	$f_T$	$V'\omega^2$
0.00	1.000	1.000	1.000	1.000	0.000
0.20	1.008	1.012	1.000	0.992	0.040
0.40	1.034	1.051	0.999	0.966	0.168
0.50	1.056	1.084	0.997	0.943	0.271
0.60	1.086	1.130	0.992	0.912	0.407
0.70	1.127	1.193	0.982	0.869	0.585
0.80	1.186	1.285	0.960	0.804	0.823
0.90	1.282	1.434	0.900	0.694	1.162
0.95	1.363	1.558	0.821	0.593	1.406
0.99	1.485	1.733	0.622	0.413	1.698
1.00	1.580	1.826	0.000	0.000	1.826

Table 3.1: The dimensionless quantities as function of rotation rate  $\omega$ . In which,  $S'$  is the surface,  $V'$  is volume,  $f_P$ ,  $f_T$  are the form factors and the product  $V'\omega^2$ .

### 3.9 The Von Zeipel theorem and the surface temperature

The Von Zeipel theorem defines a relationship between the radiative flux of a rotating star and the local effective gravity which is,

$$\mathbf{F} = -\frac{L}{4\pi GM^*} \mathbf{g}_{\text{eff}} \quad \text{with} \quad M^* = M \left( 1 - \frac{\Omega^2}{2\pi G \bar{\rho}_M} \right), \quad (3.81)$$

where  $\bar{\rho}_M$  is the average density of the star. The dimensionless quantity that multiplies the mass is indeed related to the product  $\omega^2 V'$ , namely

$$\frac{\Omega^2}{2\pi G \bar{\rho}_M} = \frac{(\omega^2 \Omega_{\text{crit}}^2) V}{2\pi G M_P} = \frac{\omega^2}{2\pi G M_P} \left( \frac{8}{27} \frac{G M_P}{R_{\text{pol}}^3} \right) \left( \frac{4}{3} \pi R_{\text{pol}}^3 V' \right) = \frac{16}{81} \omega^2 V'. \quad (3.82)$$

This means that, once we know  $\omega$ , we can get the dimensionless ratio by the dimensionless product  $(V'\omega^2)$  which is written in the last column of Table. 3.1.

On the other hand, since the total flux emitted from a star is proportional



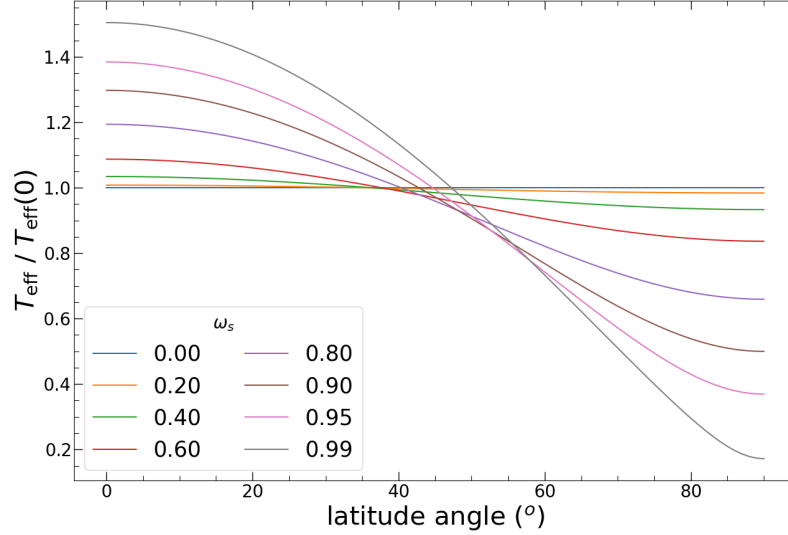


Figure 3.3: Ratio of effective temperature between rotating model and its non-rotating counterpart varies with the latitude angle in degree unit. Many rotation models are shown with different colors.

to its effective temperature at the surface (at fourth power), one can obtain

$$T_{\text{eff}}(\omega_s, \theta) = \left(1 - \frac{\Omega_s^2}{2\pi G \rho_M}\right)^{1/4} g_{\text{eff}}(\omega_s, \theta)^{1/4}. \quad (3.83)$$

It is clear that both  $T_{\text{eff}}$  and  $g_{\text{eff}}$  depend on both the rotation rate and the latitude angle. It is convenient to deduce a relation between the  $T_{\text{eff}}$  in case of rotation, and also its non-rotating counterpart ( $T_{\text{eff}}(0)$ ). We get

$$\frac{T_{\text{eff}}^4(\omega_s, \theta)}{T_{\text{eff}}^4(0)} = \left(1 - \frac{\Omega_s^2}{2\pi G \rho_M}\right)^{-1} \frac{g_{\text{eff}}(\omega_s, \theta)}{g_{\text{eff}}(0)}, \quad (3.84)$$

where  $g_{\text{eff}}(0) = GM/R_{\text{pol}}^2$ , is the effective gravity in case of non-rotating star. From Eq. 3.72 for  $g_{\text{eff}}$ , we have

$$\frac{T_{\text{eff}}^4(\omega_s, \theta)}{T_{\text{eff}}^4(0)} = \frac{\left[ \left(-\frac{1}{x^2} + \frac{8}{27}\omega_s^2 x \sin^2 \theta\right)^2 + \left(\frac{8}{27}\omega_s^2 x \sin \theta \cos \theta\right)^2 \right]^{1/2}}{\left(1 - \frac{\Omega_s^2}{2\pi G \rho_M}\right)} \quad (3.85)$$

Figure. 3.3 shows us the variation of surface temperature at different latitude angles from the pole ( $0^\circ$ ) to the equator ( $90^\circ$ ) for several rotation models. First, the blue line indicates the non-rotating model, i.e., the ratio is unity. Second, we can see how the effective temperature varies along the latitude angle, in the case of rotating stars. In particular, they become hotter in the polar region and cooler towards the equator. Third, the faster the star rotates the hotter it is at the pole, and vice versa at the equator.

We have proved that rotation changes the geometrical structure of a star. As a result, the effective temperature is not constant over the whole surface of a star, but instead,  $T_{\text{eff}}$  varies along the latitude angles. The faster a star rotates, the more distorted it becomes. This is called *geometrical distortion* effect that is caused by rotation in rotating models.

## Chapter 4

# Angular Momentum Transport

Besides the geometrical distortion, rotation also induces instabilities that causes a redistribution of chemical elements and of the angular momentum, throughout the star. Due to rotation, the mixing of chemical elements might occur also in radiative zones, something which doesn't occur in non-rotating models. Depending on rotation rate, this extra-mixing may have strong impact on the evolution of stars. It is well known that two main rotational instabilities may cause the extra-mixing:

- *Meridional circulation*: This instability is due to the thermal imbalance in rotating stars. The stellar material thus might make a macro motion from the poles to the equator, and hence induces a mixing throughout the star.
- *Shear instability*: The differences in rotation velocity between two neighborhood shells cause a turbulent mixing of chemical elements between layers. It is called shear instability in rotating stars.

Besides that, mass loss plays an important role in the transport of angular momentum since it is the main mechanism with which a star can lose its angular momentum after the zero-age-main-sequence (ZAMS). Therefore, this chapter will be dedicated to the angular momentum transport and mixing. In Sect. 4.1, the model of meridional circulation will be discussed in detail. Section. 4.2 is devoted to shear instability. The transport equation of angular momentum due to rotational instabilities is shown in Sect. 4.3. Next, the chemical mixing will be discussed in Sect. 4.4. In Sect. 4.5 we will discuss also how the angular velocity changes when we enter the domain of low-mass stars since it is acknowledged from the observation that

LMSs are slow- or even non-rotating stars. Empirical mass loss recipes for low- and intermediate-mass stars will be discussed in Sect. 4.6, while a new self-consistent formula from [Cranmer and Saar \(2011\)](#) will be discussed in Sect. 4.7.

## 4.1 Meridional circulation

The imbalance of temperature on the meridian plane of rotating stars generates a global circulation motion, the so-called meridional circulation. The problem of meridional circulation was first studied in [Eddington \(1926\)](#) and revisited over the years, in which a huge improvement was done by [Chaboyer and Zahn \(1992\)](#) and [Zahn \(1992\)](#). The solution is based on the assumption that the internal rotation depends essentially on the radii and little on the latitude, because of the existence of strong horizontal turbulence. One might then write,

$$\Omega(r, \theta) = \bar{\Omega}(r) + \hat{\Omega}(r, \theta), \quad \text{with} \quad \hat{\Omega} \ll \bar{\Omega}. \quad (4.1)$$

The horizontal average  $\bar{\Omega}$  is defined as the angular velocity of a shell that rotates like a solid body, and  $\hat{\Omega}$  expresses the differential rotation part. The main parameter that characterises meridional circulation is its velocity ( $\mathbf{U}$ ). In the second-order limit of Legendre polynomials, the meridional circulation velocity is given by

$$\mathbf{U} = U_2(r)P_2(\cos \theta)\mathbf{e}_r + V_2(r)\frac{dP_2(\cos \theta)}{d\theta}\mathbf{e}_\theta, \quad (4.2)$$

with  $U_2(r)$  is the amplitude of radial component,  $V_2(r)$  is of the horizontal component, and  $P_2(\cos \theta) = \frac{1}{2}(3\cos^2 \theta - 1)$ . If the anelastic approximation is applied, a relation between the radial and horizontal components of velocity  $\mathbf{U}$  can be deduced, which obeys

$$\frac{1}{r} \frac{d}{dr} [\rho r^2 U_2(r)] - 6\rho V_2(r) = 0. \quad (4.3)$$

The full derivation of Eq. 4.3 can be found in [Maeder \(2009\)](#). This implies that the horizontal component can be provided once we know  $U_2(r)$ .

On a given isobar at a surface level  $r$ , the velocity  $U_2(r)$  is calculated by

$$U_2(r) = \frac{P}{\bar{\rho} g c_P \bar{T} (\nabla_{\text{ad}} - \nabla + \frac{\phi}{\delta} \nabla_\mu)} \left[ \frac{L(r)}{M^*(r)} (E_\Omega + E_\mu) + \frac{c_P \bar{T}}{\delta} \frac{\partial \Theta}{\partial t} \right]. \quad (4.4)$$

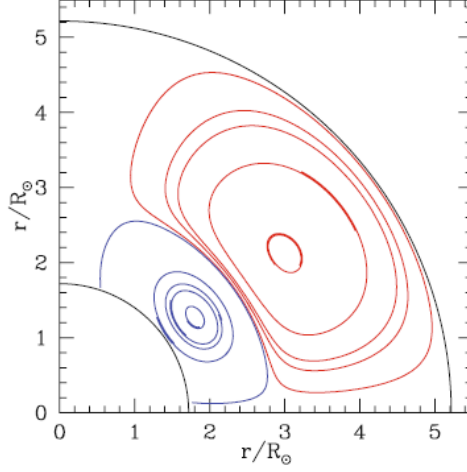


Figure 4.1: Circulation current of a rotating star in the middle of H-burning phase. Figure is adopted from [Maeder \(2009\)](#).

Here, the pressure  $P$ , average temperature  $\bar{T}$ , density  $\rho$ , effective gravity  $g$ , and luminosity  $L(r)$  are provided by the equations of stellar structure. The  $c_P$  is the specific heat at constant pressure,  $\nabla_{\text{ad}}$  and  $\nabla$  temperature gradients, the mean molecular weight gradient  $\nabla_\mu = \frac{d \ln \mu}{d \ln P}$ , thermodynamic derivatives  $\delta = \left( \frac{\partial \ln \rho}{\partial \ln T} \right)_{P, \mu}$  and  $\phi = \left( \frac{\partial \ln \rho}{\partial \ln \mu} \right)_{P, T}$ . The effective mass  $M^*$  is given in Eq. 3.81.

The density fluctuation,  $\Theta = \frac{\tilde{\rho}}{\bar{\rho}} = \frac{1}{3} \frac{r^2}{\bar{g}} \frac{d\Omega^2}{dr}$ , that is a measure of the differential rotation in the radial direction which is zero in case of uniform rotating.

The two terms  $E_\Omega$  and  $E_\mu$  depend on the distribution of  $\Omega$  and  $\mu$  respectively. In the case of uniform rotation, the term depending on  $\Omega$  is expressed as,

$$E_\Omega = 2 \left[ 1 - \frac{\bar{\Omega}^2}{2\pi G \bar{\rho}} - \frac{(\bar{\epsilon} + \bar{\epsilon}_{\text{grav}})}{\epsilon_m} \right] \frac{\tilde{g}}{\bar{g}}. \quad (4.5)$$

where  $\epsilon_m = L(r)/M(r)$  is the sum of nuclear and gravitational energy produced within the considered radius  $r$ , and  $\bar{\epsilon}$ ,  $\bar{\epsilon}_{\text{grav}}$  are the average energy production rate due to nuclear reaction and gravitational respectively,  $\tilde{g}/\bar{g}$  is the fluctuation of the mean effective gravity on an isobar. In general, the last two terms in the bracket are negligible and thus  $E_\Omega$  is positive, which means that the circulation goes up along the polar axis and moves inward on the equatorial plane, which transports the angular momentum inwardly,

as illustrated by the inner loop of Fig. 4.1. In contrast, in regions close to the surface where  $E_\Omega$  might become negative due to the increase of the term  $\overline{\Omega^2}/2\pi G\bar{\rho}$ . In this case, the circulation moves in the opposite direction which makes an outward transport of angular momentum (outer loop in Fig. 4.1).

The term depending on mean molecular weight  $\mu$ -variations is not zero only in regions where  $\mu$ -gradient is not zero. It is significant in regions around the convective core. The full expression of  $E_\mu$  can be found in Chapter. 11 of Maeder (2009), but not showing here due to the complex form of it.

In PARSEC code, there are three different approaches available for expressing  $U_2(r)$ :

- For solid rotation model, it is given by,

$$U_{\text{Kip}} = \frac{8}{3} k^2 \frac{L}{Mg} \frac{\gamma - 1}{\gamma} \frac{1}{\nabla_{\text{ad}} - \nabla} \left( 1 - \frac{\Omega^2}{2\pi G\bar{\rho}} \right), \quad (4.6)$$

where  $k^2 = \Omega^2 r_P^2 / GM$  is the local ratio of centrifugal acceleration to gravity, and  $\gamma = c_P / c_V$  is the specific heat ratio (see Kippenhahn et al., 2012);

- Including the correction by “stabilising” circulation from the molecular weight barrier, Heger et al. (2000) gives

$$U_{\text{Heg}} = \max(|U_{\text{Kip}}| - |V_\mu|, 0), \quad (4.7)$$

with  $V_\mu = \frac{H_P}{\tau_{\text{KH}}} \frac{\phi \nabla_\mu}{\delta(\nabla - \nabla_{\text{ad}})}$  is the molecular current,  $\tau_{\text{KH}}$  is the local Kelvin-Helmholtz timescale,  $\nabla_\mu = \frac{d \ln \mu}{d \ln P}$  is  $\mu$ -gradient;

- In the case of stationary and uniform rotation, Maeder (2009) and Potter et al. (2012) give an approximate form of Eq. 4.4 in regions with homogeneous composition, which is

$$U_{\text{Maed}} = \frac{8}{3} \frac{P}{\bar{\rho} \bar{g} c_P \bar{T}} \frac{L}{(\nabla_{\text{ad}} - \nabla + \frac{\phi}{\delta} \nabla_\mu)} \frac{1}{M^*} \left[ 1 - \frac{\overline{\Omega^2}}{2\pi G\bar{\rho}} - \frac{\bar{\epsilon} + \bar{\epsilon}_{\text{grav}}}{\epsilon_m} \right] \frac{\Omega^2 r_0^3}{GM}, \quad (4.8)$$

with  $r_0$  is the radius at which  $P_2(\cos \theta) = 0$ . This takes into account the molecular barrier and tends to zero both near the surface regions and at the centre.

The latter recipe is used in the new version PARSEC v2.0, i.e.,  $U_2 = U_{\text{Maed}}$ .

## 4.2 Shear instability

If two neighbouring layers rotate with different velocities, the velocities gradient between them may create a shear instability. The condition for shear instability is expressed by the Richardson criterion, which is defined as

$$Ri \equiv \frac{g}{\rho} \frac{d\rho/dz}{(dV/dz)^2} < \frac{1}{4} = Ri_{\text{crit}}, \quad (4.9)$$

with  $Ri_{\text{crit}} = 1/4$  is the critical Richardson number. The condition for shear instability to occur is the  $Ri$  must be smaller than its critical value. With further development on the expression of the Richardson number, the relative density along the horizontal direction  $d\rho/dz$  can then be expressed in terms of Brunt-Väisälä frequency, and thus Eq. 4.9 becomes,

$$Ri = \frac{N^2}{(dV/dz)^2} < Ri_{\text{crit}}. \quad (4.10)$$

In which, the Brunt-Väisälä frequency is contributed from thermal gradient and mean molecular weight gradient,

$$N^2 = N_T^2 + N_\mu^2 = \frac{g\delta}{H_P} \left( \nabla_{\text{int}} - \nabla + \frac{\phi}{\delta} \nabla_\mu \right), \quad (4.11)$$

with  $N_T^2 = \frac{g\delta}{H_P} (\nabla_{\text{int}} - \nabla)$ , and  $N_\mu^2 = \frac{g\phi}{H_P} \nabla_\mu$ . The  $H_P$  is the pressure scale height,  $g$  is effective gravity,  $\delta$ ,  $\phi$  are thermo-derivatives,  $\nabla_{\text{int}} = \frac{d}{d} \frac{\ln T_{\text{int}}}{\ln P}$ ,  $\nabla = \frac{d}{d} \frac{\ln T_{\text{ext}}}{\ln P}$  are the temperature gradients of the internal and external layers, correspondingly, and  $\nabla_\mu$  is  $\mu$ -gradient.

Combination of both effects by thermal diffusion and by horizontal turbulence. The diffusion coefficient by shear instability is given by

$$D_{\text{s.i.}} = \frac{(8/5) Ri_{\text{crit}} \left( r \frac{d\Omega}{dr} \right)^2}{\left[ N_{\text{T,ad}}^2 / (K + D_{\text{h}}) \right] + N_\mu^2 / D_{\text{h}}}, \quad (4.12)$$

where  $K = 4acT^3/3\kappa\rho^2c_P$  is the thermal diffusivity,  $D_{\text{h}} = |rU_2(r)|$  is the horizontal diffusion coefficient of the elements (Zahn, 1992),  $N_{\text{T,ad}}^2 = (g\delta/H_P)(\nabla_{\text{ad}} - \nabla)$  and  $N_\mu^2 = (g\phi/H_P)\nabla_\mu$ , (see also Talon and Zahn, 1997; Chieffi and Limongi, 2013, for more details).

### 4.3 Transport of angular momentum

In the presence of rotational instabilities, one needs to write down the equations describing the transport of angular momentum and the mixing of chemical elements. For angular momentum transportation, there are two different approaches. The first one is in which the transport of angular momentum obeys the advection-diffusion equation. In Lagrangian coordinates, the equation is given by

$$\rho \frac{\partial}{\partial t} (r^2 \Omega) = \frac{1}{5r^2} \frac{\partial}{\partial r} (\rho r^4 \Omega U(r)) + \frac{1}{r^2} \frac{\partial}{\partial r} \left( \rho D r^4 \frac{\partial \Omega}{\partial r} \right). \quad (4.13)$$

The first term in the right-handed side of the above equation represents the advection while the second term is for diffusion, with  $D$  is the total diffusion coefficient. This scheme is adopted in some stellar evolutionary codes, such as GENEC (Eggenberger et al., 2008), ROSE (Potter et al., 2012), and FRANEC (Chieffi and Limongi, 2013).

The second method, which is used in this version of PARSEC v2.0 code, in which the transport of angular momentum is treated as a purely diffusive process, the transport equation is thus simplified to,

$$\rho \frac{\partial (r^2 \Omega)}{\partial t} = \frac{1}{r^2} \frac{\partial}{\partial r} \left( \rho r^4 D \frac{\partial \Omega}{\partial r} \right), \quad (4.14)$$

where  $D$  is the total diffusion coefficient which represents many instabilities that transport the angular momentum. In this case, they are from the convective transfer, meridional circulation, and shear instability,

$$D = D_{\text{MLT}} + D_{\text{m.c.}} + D_{\text{s.i.}}. \quad (4.15)$$

The diffusion coefficient due to shear instability,  $D_{\text{s.i.}}$ , is given in Eq. 4.12. The  $D_{\text{m.c.}}$  is the coefficient that is caused by meridional circulation which is given by Chaboyer and Zahn (1992),

$$D_{\text{m.c.}} \simeq \frac{|r U_2(r)|^2}{30 D_{\text{h}}}. \quad (4.16)$$

The diffusion in convective zones is computed by the mixing-length-theory (Böhm-Vitense, 1958) with coefficient,

$$D_{\text{MLT}} = \frac{1}{3} v l_{\text{MLT}} \quad \text{with} \quad l_{\text{MLT}} = \alpha_{\text{MLT}} H_P. \quad (4.17)$$



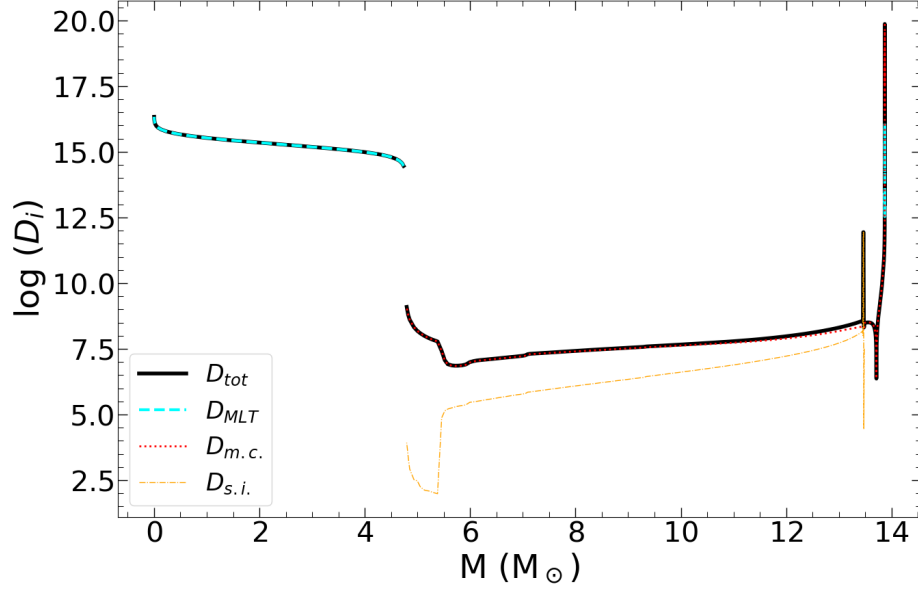


Figure 4.2: Distribution of diffusion coefficients that appear in Eq. 4.15 for a  $14M_\odot$  star at the stage where the current central hydrogen content  $X_c \approx 0.3$  during the MS. The model is computed with initial rotation rate  $\omega_i = 0.80$ , initial metallicity  $Z = 0.017$ ,  $Y = 0.279$ .

In the expressions above,  $D_h$  is the horizontal diffusion coefficient,  $U_2(r)$  is the radial velocity of meridional circulation,  $v$  is the velocity of bubbles that rise or sink in the convective regions and their mean free path  $l_{\text{MLT}}$ ,  $H_P$  is the pressure scale height, and  $\alpha_{\text{MLT}}$  is the MLT parameter.

Figure. 4.2 shows the internal distribution of the total diffusion coefficient ( $D_{\text{tot}}$ ), the diffusion coefficient in convective zones ( $D_{\text{MLT}}$ ), and the coefficients caused by meridional circulation ( $D_{\text{m.c.}}$ ) and shear instability ( $D_{\text{s.i.}}$ ), of a  $14M_\odot$  star. It is obvious that the  $D_{\text{MLT}}$  is non-zero only in the convective regions and in the overshooting regions, and is the dominant at the central. The contribution from rotational instabilities becomes important in the radiative regions. In particular, the meridional circulation coefficient is about 10 orders of magnitude larger than the shear instability coefficient in the inner part while in the outer part they tend to have equally impact.

## 4.4 Chemical mixing and the calibration of parameters

The equation of chemical mixing follows the form of Eq. 2.36 in Sect. 2.4. The extra mixing induced by rotational instabilities is contained in the total diffusion coefficient  $D_{\text{tot}}$  which is written by,

$$D_{\text{tot}} = D_{\text{MLT}} + f_c (D_{\text{s.i.}} + D_{\text{m.c.}}). \quad (4.18)$$

Here, the free parameter  $f_c$  was introduced to control the efficiency of rotational mixing which is needed to be calibrated so that it directly controls the speed of mixing without affecting the transport of angular momentum, (see Pinsonneault et al., 1989; Heger et al., 2000; Brott et al., 2011). The possible value of  $f_c$  ranges from 0 to 1, where  $f_c = 0$  implies that no material mixing caused by rotation and  $f_c = 1$  means that the processes that mix material would have the same efficiency on their transport of angular momentum.

Another free parameter is  $f_\mu$  that is multiplied to the gradient of molecular weight, namely,

$$\nabla_\mu^{\text{eff}} = f_\mu \times \nabla_\mu. \quad (4.19)$$

The introduction of  $f_\mu$  is necessary because it controls the molecular barrier “strength”. This is due to the fact that the inclusion of  $\nabla_\mu$  strongly inhibits the transport of chemical composition as implied in many works Bressan et al. (1981); Pinsonneault et al. (1989); Chaboyer et al. (1995); Meynet and Maeder (1997).

The calibration of these two parameters is still an open issue. The two parameters are compensated to each other in a way such that the factor  $f_\mu$  tends to inhibit the mixing process while  $f_c$  tends to enhance the mixing (see Costa et al., 2019b). Therefore, they render the calibration more difficult. Heger et al. (2000) proposed a method, in which the two parameters were calibrated to reproduce the ratio of surface nitrogen and helium abundances between the TAMS and the ZAMS for models from  $10 - 20 M_\odot$  with solar metallicity and an adopted ZAMS rotational velocity of  $\sim 200$  km/s. The results with  $f_c = 1/30$  and  $f_\mu = 0.05$  were claimed to be the best values of their calibration.

Another work was done by Brott et al. (2011), who used a sample containing B-stars in the LMC of the FLAMES survey to calibrate their models.

Table 4.1: Values of rotational mixing efficiency parameters,  $f_c$  and  $f_\mu$ .

$f_c$	$f_\mu$	Reference
0.033	0.05	<a href="#">Heger et al. (2000)</a>
0.0228	0.1	B11 <sup>1</sup> and Y06 <sup>2</sup>
0.17	0.45	<a href="#">Costa et al. (2019b)</a>

<sup>1</sup>B11 for [Brott et al. \(2011\)](#).<sup>2</sup>Y06 is for [Yoon et al. \(2006\)](#).

The models of  $13 M_\odot$  with various rotational velocities are performed. The trend of surface nitrogen abundances at the TAMS with projected rotational velocities is aimed to reproduce the trend from measurements. The resulted  $f_c = 0.0228$  was obtained, in combination with the adopted value of  $f_\mu = 0.1$  from [Yoon et al. \(2006\)](#) where the surface helium abundance was used for calibration.

In PARSEC v2.0, the calibration is done in three steps: i) first, the stars reported in [Brott et al. \(2011\)](#) are used to initialise the chemical partitions to compute the evolutionary models; ii) the overshooting parameter from convective core is calibrated by using the eclipsing binaries and are used in computing the evolutionary models as mentioned in Sect. 2.3.2; iii) the surface nitrogen abundances ratio between the TAMS and ZAMS is used to compare with the results of [Brott et al. \(2011\)](#). As a result,  $f_c = 0.17$  and  $f_\mu = 0.45$  are found as a preliminary calibration as claimed in [Costa et al. \(2019b\)](#). Table. 4.1 summaries the values of  $f_c$  and  $f_\mu$  in these three works, it should be mentioned that the adopted values from [Costa et al. \(2019b\)](#) are used throughout this project.

Besides that, it is also worthy to mention that the more complete solution for chemical mixing in rotating stars should take into account other processes that could possibly influence the stability of the medium such as the stabilizing or destabilizing effect of the distribution of angular momentum, radiative losses, etc... This more general model is already discussed in [Maeder et al. \(2013\)](#). However, those processes in general are not considered because the total diffusion coefficient already contains two free parameters that needed to be calibrated from observations.

It is also important to stress that the conservation of total angular momentum is checked at each time step. In PARSEC v2.0, the rotation is applied just before the star reaches the ZAMS. At first, the angular velocity ( $\Omega$ ) is

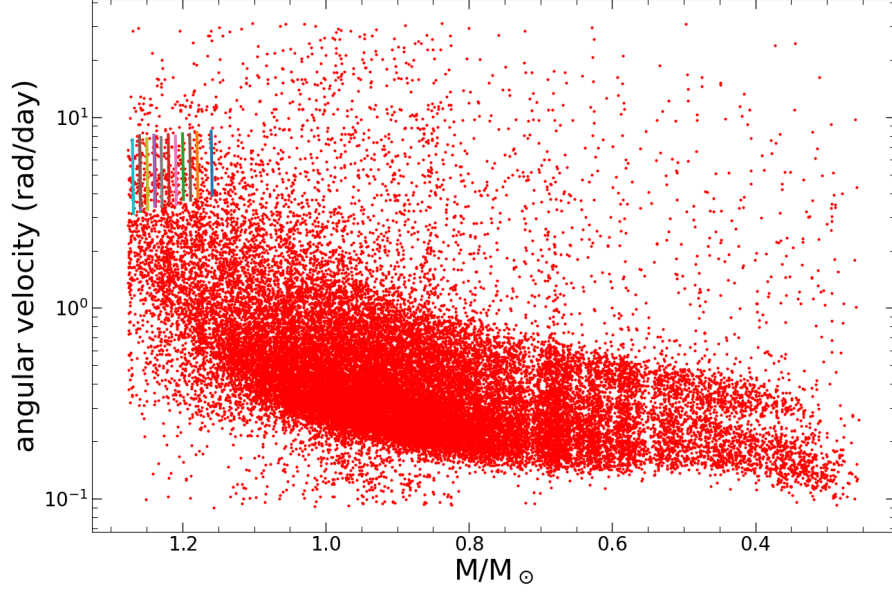


Figure 4.3: Distribution of angular momentum velocity (in rad/day) with stellar masses in the sample of [McQuillan et al. \(2014\)](#) (red dots). The angular momentum velocities of different mas-models that are computed with initial rotation rate  $\omega_i = 0.30$  from the ZAMS to the TAMS are shown by the solid lines.

assigned to the initial velocity which is provided by the initial rotation rate  $\omega = \Omega/\Omega_{\text{crit}}$  (Eq. 3.8) and it is kept constant in the whole star. After that, the angular velocity is let to evolve freely under the conservation of the total angular momentum, taking into account internal transport and losses of angular momentum from the star, e.g. by stellar winds.

## 4.5 The transition from non rotating to rotating, low-mass stars

Speaking of angular velocity, it is convenient for later discussions to briefly review the current status on the rotation rates of stars in the lower main

sequence. The analysis of [McQuillan et al. \(2014\)](#) aimed at deriving rotation periods in more than 34000 main-sequence stars from the *Kepler* mission, gives us an insightful look to the period-mass distribution. Figure. 4.3 shows the observed angular momentum velocity ( $\Omega$  in rad/day) against masses from the sample of [McQuillan et al. \(2014\)](#), in which to derive the angular velocity from the reported periods we use the formula  $\Omega = 2\pi/P$ . The trend of  $\Omega$  is rather obvious, namely, the angular velocity increases at increasing mass. In another word, low-mass stars are expected to rotate slowly or no-rotating at all.

For this reason, the initial rotation rate of a model of a given mass must be set with care. To be clearer at this point, in Fig. 4.3 the angular velocity of many models of mass smaller than  $1.27M_{\odot}$  with initial rotation rate  $\omega_i = 0.30$  during the evolution from ZAMS to TAMS are shown by the solid lines. There are a few things that we can take from this figure: i) the angular velocities from our rotating models are inside the trend of the observed data. ii) The smallest computed mass in this set of  $\omega_i = 0.30$  is  $1.16M_{\odot}$ . This cut-off is reasonable because at a given value of  $\omega_i$ , a smaller mass leads to a larger  $\Omega_{\text{crit}}$  due to strong dependence on  $R_{\text{pol}}$ . The angular velocity will thus be larger, falling outside the trend of observed data. iii) The models with lower  $\omega_i$  are expected to fall into the smaller mass range in the figure. However, we did not calculate models with values between  $\omega_i = 0$  and  $\omega_i = 0.30$  since, in that case, the effects of rotation will be negligible (for a detailed discussion see Chapter. 5).

Keeping this in mind, we now introduce a relation to set the maximum value of the initial rotation rate in the transition mass range  $M_{O1} - M_{O2}$ , describing the growth of the convective cores. We introduce a parameter,  $\omega_{\text{max}}$ , to control the desired maximum initial rotation rate for a given mass, which is written as

$$\omega_{\text{max}} = 0.99 \left( \frac{M_i - M_{O1}}{M_{O2} - M_{O1}} \right), \quad (4.20)$$

where  $M_{O1}$  is the largest initial mass of a star showing a vanishing convective core during the early hydrogen-burning phase, calculated without overshooting, and  $M_{O2} = M_{O1} + 0.3M_{\odot}$ . The initial rotation rate that can be applied to a given initial mass model must be smaller than the value of  $\omega_{\text{max}}$ . Since  $M_{O1}$  depends on metallicity, Table. 4.2 lists the values of  $\omega_{\text{max}}$  at each initial mass from  $M_{O1}$  to  $M_{O2}$  in six sets of metallicity that are studied in this project and will be described in Chapter. 5.

	Z= 0.017 M <sub>i</sub> /M <sub>⊙</sub>	Z= 0.014 M <sub>i</sub> /M <sub>⊙</sub>	Z= 0.01 M <sub>i</sub> /M <sub>⊙</sub>	Z= 0.008 M <sub>i</sub> /M <sub>⊙</sub>	Z= 0.006 M <sub>i</sub> /M <sub>⊙</sub>	Z= 0.004 M <sub>i</sub> /M <sub>⊙</sub>	ω <sub>max</sub>
M <sub>O1</sub>	1.18	1.16	1.14	1.14	1.09	1.06	0
	1.20	1.18	1.16	1.16	1.11	1.08	0.06
	1.22	1.20	1.18	1.18	1.13	1.10	0.13
	1.24	1.22	1.20	1.20	1.15	1.12	0.198
	1.26	1.24	1.22	1.22	1.17	1.14	0.264
	1.28	1.26	1.24	1.24	1.19	1.16	0.33
	1.30	1.28	1.26	1.26	1.21	1.18	0.396
	1.32	1.30	1.28	1.28	1.23	1.20	0.462
	1.34	1.32	1.30	1.30	1.25	1.22	0.528
	1.36	1.34	1.32	1.32	1.27	1.24	0.594
	1.38	1.36	1.34	1.34	1.29	1.26	0.66
	1.40	1.38	1.36	1.36	1.31	1.28	0.726
	1.42	1.40	1.38	1.38	1.33	1.30	0.792
	1.44	1.42	1.40	1.40	1.35	1.32	0.858
	1.46	1.44	1.42	1.42	1.37	1.34	0.924
M <sub>O2</sub>	1.48	1.46	1.44	1.44	1.39	1.36	0.99

Table 4.2: The values of ω<sub>max</sub> at different initial masses.

## 4.6 Mass loss

The mass loss process has a direct impact on the transport of angular momentum. In previous version of PARSEC as well as previous models from the same group (Girardi et al., 2000a; Bertelli et al., 2008), the mass loss of low-mass stars is applied only at the stage of isochrones calculation. This approximation is acceptable due to the fact that the RGB evolution of low-mass stars is very small affected by this process that, eventually, becomes important only very near the RGB-tip. Therefore, mass loss just causes a decrease in mass between RGB and the stage of ZAHB. This decrease is easily taken into account when interpolating the helium-burning tracks to calculate isochrones.

However, the inclusion of mass loss along the evolution of stars cannot be longer decoupled from the calculation of stellar evolution, in case of rotating stars. This is because mass-loss is the only way for the star to directly loose angular momentum. Furthermore, rotation may enhance mass loss due to the lower effective gravity caused by centrifugal forces. This may become a dramatic problem when the star is close to the critical velocity. Thus calculation of evolutionary tracks cannot be done without the inclusion of mass-loss. This is a big difference with respect to previous PARSEC and other Padova models.

In order to describe the enhancement of mass loss due to rotation, [Friend and Abbott \(1986\)](#) introduced an enhanced factor that depends on the escape velocity of the star at the surface. By fitting their numerical results, [Bjorkman and Cassinelli \(1993\)](#) provides the mass loss rate of a rotating star  $\dot{M}(\omega)$ , which is given by

$$\dot{M}(\omega) = \dot{M}(\omega = 0) \left(1 - \frac{v}{v_{\text{crit}}}\right)^{-\xi} \quad \text{with} \quad \xi = 0.43, \quad (4.21)$$

where  $v$  is surface tangential velocity. The critical tangential velocity at the surface of rotating stars (or break-up velocity) is usually defined as,

$$v_{\text{crit}}^2 = \frac{Gm}{r}(1 - \Gamma_e), \quad (4.22)$$

where  $G$ ,  $m$ ,  $r$  are the gravitational constant, mass, and radius in solar units and  $\Gamma_e$  is the Eddington factor. In general,  $\Gamma_e$  depends also on the angular momentum velocity, this dependence becomes more important in the extreme cases when the rotation rate is close to the critical value, (see [Maeder and Meynet, 2000](#), for more detailed discussions). However, in this project, we neglect this dependence of  $\Gamma_e$ , and this should be kept in mind as a caution. This dependence should be carefully tested in cases of extremely fast rotating stars and will be reserved for future projects.

The  $\dot{M}(\omega = 0)$  in Eq. 4.21 is the mass loss rate in case of classical non-rotating model. It is well known that the low mass stars loses mass in different way than intermediate-mass or even massive stars. Therefore, the next two subsections will describe them separately.

#### 4.6.1 Low-mass stars

The most widely used recipe for mass-loss in low-mass stars is the empirical law by [Reimers \(1975\)](#), which is

$$\dot{M}_{\text{Reimers}} = \eta \frac{LR}{M}, \quad (4.23)$$

where  $L$ ,  $R$  and  $M$  are luminosity, radius and mass in solar units, respectively. The parameter  $\eta$  represents the efficiency of the model which is generally calibrated against observations of the CMDs of globular clusters. Many calibrations had been presented over the years and gave a level to the uncertainty of  $\eta$ , for instance, [Renzini and Fusi Pecci \(1988\)](#) provided  $\eta = 0.35$ ,

or [Aaronson and Mould \(1982\)](#) gave  $\eta = 0.5 - 0.7$ , or [Miglio et al. \(2012\)](#) claimed  $\eta = 0.2$ .

A modification of the Reimers' law was done by [Schröder and Cuntz \(2005\)](#). There, the wind is assumed to result from the spillover of the extended chromosphere, and associated with the action of Alfvén waves. There are two new factors introduced to the standard formula of Reimers, one reflects the dependence of mechanical energy flux on effective temperature and the second one describes how the chromospheric height depends on gravity. The modified mass loss rate is written as,

$$\dot{M}_{\text{SC}} = \eta_1 \frac{LR}{M} \left( \frac{T_{\text{eff}}}{4000 \text{ K}} \right)^{3.5} \left( 1 + \frac{g_{\odot}}{4300 g} \right), \quad (4.24)$$

with  $T_{\text{eff}}$  is effective temperature in K, the stellar gravity  $g$  and the solar gravity  $g_{\odot}$  are in cgs units,  $\eta_1$  is a fitting parameter that is calibrated from observations. In which, the sonic point is used as a reference at which  $T_{\text{eff}} = 4000 \text{ K}$  and  $\log g = 0.8$  base on the calibration to the well-studied K supergiant  $\xi$ -Aurigea, (see [Schröder and Cuntz, 2005](#); [Baade et al., 1996](#)).

This modified formula of Schröder and Cuntz gives an improvement to a more physical picture of the original formula, and still contains a fitting parameter that needed to be calibrated from observation.

### 4.6.2 Intermediate-mass and massive stars

The mass loss becomes critical for our understanding of the evolution and fate of the intermediate-mass and massive stars in the Universe. During their evolution, the IMSs evolve towards the asymptotic giant branch where the mass loss becomes important and leads to either planetary nebula or type Ia supernovae explosion. The typical value of mass loss rate during the AGB phase of these stars is from  $\sim 10^{-8} - 10^{-4} M_{\odot}/\text{yr}$  ([Höfner and Olofsson, 2018](#); [Decin et al., 2020](#)).

In the case of massive stars, mass loss effects on their luminosity, burning lifetime, and effective temperature due to its high efficiency. It also has a crucial role in determining the type of resulting supernova explosion, depending on the strength of mass loss a red supergiant can evolve to the luminous-blue-variable phase or totally can avoid this phase (see review of [Smith, 2014](#)). Another example on the importance of mass loss to the fate of massive stars, consider a star of  $60 M_{\odot}$  with  $Z = 0.04$  either it remains intact and dies as



a  $\sim 25M_{\odot}$  black hole if its mass loss rate is about  $\sim 2$  times smaller than the rate at which it will die as a neutron star due to the evaporating of the envelope, see review of [Vink \(2022\)](#), (see also [Meynet et al., 1994a](#)).

In PARSEC model, the mass loss rate is adopted differently for different phases. Towards the supergiant phases ( $T_{\text{eff}} \leq 12000$  K), the mass loss rate provided by [de Jager et al. \(1988\)](#) is adopted. In the blue supergiant phase ( $T_{\text{eff}} \geq 12000$  K) or the luminous-blue-variables, the formula of [Vink et al. \(2001\)](#) is adopted. The formula from [Nugis and Lamers \(2000\)](#) is adopted for WR phases.

In principle, the mass-loss rates are expected to be smaller for stars of low metallicity. This dependency was pioneered by [Abbott and Lucy \(1985\)](#) and then persuaded by many works. In general, it is written as,

$$\dot{M} \propto Z^m, \quad (4.25)$$

with  $m$  ranging from 0.5 to 1. For example, [Leitherer et al. \(1992\)](#) gives a scale relation  $\dot{M} \propto Z^{0.8}$ , while [Vink et al. \(2001\)](#) gives  $m = 0.69$  for hot stars with  $T_{\text{eff}} \geq 25000$  K and  $m = 0.64$  for B-supergiants with  $T_{\text{eff}} \leq 25000$  K, or [Mokiem et al. \(2007\)](#) finds  $m = 0.83 \pm 0.16$  for O-and early B-type stars.

However, a later study of [Gräfener and Hamann \(2008\)](#) shows that the mass loss is strongly enhanced when stars approach the Eddington limit ( $\Gamma_e \rightarrow 1$ ). Therefore the dependence on  $\Gamma_e$  must be considered in the regions near the Humphrey-Davidson limit where  $\Gamma_e$  close to 1. Such dependency is also described in [Vink et al. \(2011\)](#), in which the mass loss rate becomes significantly enhanced when  $\Gamma_e > 0.7$ . Besides that, [Gräfener and Hamann \(2008\)](#) also shows that at low values of  $\Gamma_e$  the mass loss rate obeys the relation  $\dot{M} \propto (Z/Z_{\odot})^{0.85}$ , and as increasing  $\Gamma_e$  the metallicity dependence disappears. However, a more comprehensive analysis of the dependence of mass loss rate to both metallicity and  $\Gamma_e$  is still missing. A scaling relation is introduced to express this dependency of mass loss rate on  $\Gamma_e$  and  $Z$  in PARSEC models, which is given by

$$\dot{M} \propto \left( \frac{Z}{Z_{\odot}} \right)^{\alpha} \quad \text{with} \quad \alpha = 2.45 - 2.4 \times \Gamma_e, \quad (4.26)$$

where  $\Gamma_e$  is limited from 2/3 to 1. At low  $\Gamma_e$ , Eq. 4.26 follows the formulism of [Gräfener and Hamann \(2008\)](#), and at high- $\Gamma_e$  it becomes negligible.

In practise, in order to take into account the effect of  $\Gamma_e$ , the maximum value between the standard mass loss recipes and the one computed

by Eq. 4.26 multiplied with the mass loss rate from Vink et al. (2011) (say  $\dot{M}_{\Gamma_e}$ ) is assigned. Namely, towards the supergiant phases, the mass loss rate of de Jager et al. (1988) is compared with  $\dot{M}_{\Gamma_e}$  so that the larger value will be used. Similarly, in the region of blue-supergiant or luminous-blue-variable, the maximum value between the rate of Vink et al. (2001) and  $\dot{M}_{\Gamma_e}$  is adopted.

Finally, for numerical purposes, at each time step  $\Delta t$ , the new mass  $M_{\text{new}}$ , that is reduced by mass loss, is computed from the previous current mass  $M_{\text{old}}$ . Indeed, when  $\dot{M}$  is already defined, the new current mass is  $M_{\text{new}} = M_{\text{old}} - \dot{M}\Delta t$ .

## 4.7 Self-consistent physical mass loss rate

The mechanism responsible for producing mass loss in low-mass stars (cool, late-type) that described so far is basically the adoption from empirical formulas which include at least one calibrated parameter as we have seen in the section above. In this section, we will review the first theoretical model that expresses the mass loss mechanism directly from the star's fundamental properties. The material of this section is mainly from Cranmer and Saar (2011). The theoretical description is explicitly derived in Appendix A, while only a summary of important points is shown in this section.

### 4.7.1 Theoretical description

From the equation of energy conservation that is written in terms of the radiative energy loss and the total flux per cross-section area unit,

$$\frac{P^2}{4k_B^2 T^2} \Lambda(T) + \frac{1}{A} \frac{\partial}{\partial r} [A (F_C + F_M + F_W + F_A)] = 0, \quad (4.27)$$

in combination with the conservation of mass and momentum,

$$\rho u A = \text{constant}, \quad (4.28)$$

$$\rho u \frac{\partial u}{\partial r} = -\frac{\partial P}{\partial r} - \rho \frac{GM}{r^2} - \frac{\partial}{\partial r} \frac{\langle \delta B^2 \rangle}{8\pi}, \quad (4.29)$$

are the basic equations to derive the mass loss rate for cool, late-type stars (see Withbroe, 1988).

In the above formulas, the first term on the right-hand side of Eq. 4.27 is the expression of radiative energy loss, with  $k_B = 1.3807 \times 10^{-16} \text{ cm}^2 \text{gs}^{-2} \text{K}^{-1}$  is Boltzmann's constant,  $P$  is the pressure,  $T$  is temperature, and  $\Lambda(T)$  is the radiative loss function (see Cranmer et al. (2007)). In the second term, the total flux is contributed from four components, i.e., thermal conduction ( $F_C$ ), mechanical energy transport ( $F_M$ ), stellar wind ( $F_W$ ), and Alfvén wave ( $F_A$ ) (see Hammer (1982); Withbroe (1988)). The  $u$  is outflow speed and  $\langle \delta B^2 \rangle$  is the mean square wave magnetic field.

The model is divided into two scenarios: the outflow wind can be driven by gas pressure which corresponds to hot corona regions; or by wave pressure which corresponds to cool, extended chromosphere regions. We will discuss more details about these two driven-mechanisms in the next following sections.

### Hot coronal mass loss rate

Assume that we are considering a plasma fluid with a high gas pressure, this may cause an acceleration to produce a transition region (TR) from the base (cool chromosphere) to the hot corona region (illustrated in Figure. 4.4). As a consequence, the outflow speed in hot corona region is much larger than the Alfvén wave speed. More precisely, the Alfvén wave flux is expected to depend strongly on the gravity in such a way as Eq. 4.38, hence in the region of hot coronal the effect of Alfvén wave is negligible. The energy conservation law in Eq. 4.27 now becomes,

$$\frac{P^2}{4k_B^2 T^2} \Lambda(T) + \frac{1}{A} \frac{\partial}{\partial r} [A (F_C + F_M + F_W)] = 0. \quad (4.30)$$

By integrating the equation above for the region of hot coronal, i.e., from the transition region to the outflow part ( $R \rightarrow \infty$ ) and using the definition of mass loss rate  $\dot{M} = jA$ , with  $j$  is the mass flux and  $A$  is the cross-section area. The hot coronal mass loss rate is expressed in terms of the fluxes at the boundaries, which is

$$\dot{M} = \frac{A_{\text{TR}} (F_{M,\text{TR}} - F_C)}{V_{\text{esc}}^2}, \quad (4.31)$$

where  $V_{\text{esc}}$  is the escape velocity which is assumed to be the outflow speed at far distance,  $V_{\text{esc}} = u_{\infty} = \sqrt{\frac{2GM_*}{R_*}}$ , with  $M_*$ ,  $R_*$  are the mass and radius

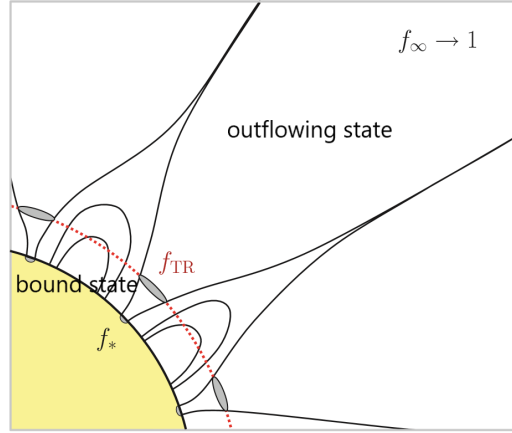


Figure 4.4: Illustration of transition region in cool star, the  $f_*$ ,  $f_{\text{TR}}$ ,  $f_\infty$  are the filling factors correspond to each regions.

at the outermost border of the photosphere. The cross-section area at the level of the transition region is  $A_{\text{TR}} = 4\pi R_{\text{TR}}^2 f_*^\theta$ , with the radius at the TR level approximately equal to the radius of the photosphere  $R_{\text{TR}} = R_*$ , the filling factor  $f_*$  which characterises for the geometrical of the fluid tube, and  $\theta$  is a dimensionless constant between 0 and 1 and is chosen to be 1/3, (see [Cranmer and Saar, 2011](#); [Kopp and Holzer, 1976](#)).

By definition, the mechanical energy flux is the flux of heat transferring between radiation and matter in corona zones. Thus, the mechanical flux at the TR level is given by

$$F_{\text{M,TR}} \equiv Q_{\text{TR}} R_* h \quad \text{with} \quad h = [0.5, 1.5]. \quad (4.32)$$

The heating rate at transition region,  $Q_{\text{TR}}$ , is computed by,

$$Q_{\text{TR}} = \left( \frac{\tilde{\alpha}_{\text{TR}} Q_*}{\tilde{\alpha}_*} \right)^{8/7} \left( \frac{m_H^2}{\rho_*^2 \Lambda_{\text{max}}} \right)^{1/7} f_*^{4(1-\theta)/7}, \quad (4.33)$$

with  $\theta = [0, 1]$ ,  $m_H$  is the hydrogen mass,  $\Lambda_{\text{max}}$  is the maximum of radiative loss function which depends on metallicity as given in [Cranmer and Saar \(2011\)](#),

$$\frac{\Lambda_{\text{max}}}{10^{-23} \text{erg cm}^3 \text{s}^{-1}} \approx 7.4 + 42 \left( \frac{Z}{Z_\odot} \right)^{1.13}, \quad (4.34)$$

$\tilde{\alpha}_* = 0.5$  and the  $\tilde{\alpha}_{\text{TR}}$  is computed by a relation,  $\tilde{\alpha} = 0.5 \frac{\mathcal{R}(1+\mathcal{R})\sqrt{2}}{(1+\mathcal{R}^2)^{3/2}}$ , with  $\mathcal{R} \approx (V_A - u_\infty)/(V_A + u_\infty)$ . In turn,  $V_A = B/(4\pi\rho)^{1/2}$  is the Alfvén speed and  $B$  is the magnetic field strength. The heating rate at the photosphere,  $Q_*$ , is computed through the Alfvén flux as shown in Appendix A.

The conductive flux at the inner corona is given by,

$$F_C = c_{\text{rad}} P_{\text{TR}} \quad \text{with} \quad c_{\text{rad}} \approx 14 \times 10^5 \sqrt{\frac{\Lambda_{\text{max}}(Z)}{\Lambda_{\text{max}}(Z_\odot)}}, \quad (4.35)$$

and  $P_{\text{TR}}$  is the pressure at the transition region.

### Cold-wave driven mass loss rate

In this scenario, a fluid tube in which the neutral and ion species move together as a whole and the temperature of all pieces is equal. Besides that, in a high density stellar atmosphere, the mechanical heating may balance with the radiative loss energy. Moreover, the contribution of conductive energy can be neglected if the outflow wind region is isothermal (see [Holzer et al., 1983](#)). In another word, the total flux now only has contribution from stellar wind and Alfvén wave, i.e.,  $F = F_W + F_A$ . In that case, the gas pressure can't be enough to drive a significant outflow, and the cooling wave starts to become a dominant.

From the definition of mass loss rate  $\dot{M} = jA = \rho u A$  is constant. Assume that the region is isothermal so that there should be a critical point where the temperature at this point doesn't change and thus we have,

$$\dot{M} = \rho_c u_c A_c. \quad (4.36)$$

Follow the derivation in Appendix A, we will see that the critical cross-section area  $A_c$  and outflow speed  $u_c$  are computed through the critical radius ( $r_c$ ), which are

$$A_c = 4\pi r_c^2 \quad \text{and} \quad u_c = \sqrt{\frac{1}{2} \frac{GM_*}{r_c}}, \quad (4.37)$$

where  $r_c \approx R_* \frac{7/4}{1+(v_{\perp*}/V_{\text{esc}})^2}$ , and the transverse velocity at the photosphere is computed through the Alfvén wave flux,  $v_{\perp*} = \sqrt{\frac{F_{A*}}{\rho_* V_{A*}}}$ . The form of Alfvén

wave flux is adopted from Musielak and Ulmschneider (2002) which is,

$$F_{A*} = F_0 \left( \frac{T_{\text{eff}}}{T_0} \right)^\eta \exp \left[ - \left( \frac{T_{\text{eff}}}{T_0} \right)^{25} \right], \quad (4.38)$$

where,

$$\frac{F_0}{10^9 [\text{erg.cm}^{-2}.\text{s}^{-1}]} = 5.724 \exp \left( - \frac{\log g}{11.48} \right), \quad (4.39)$$

$$\frac{T_0}{10^3 [\text{K}]} = 5.624 + 0.6002 \log g, \quad (4.40)$$

$$\eta = 6.774 + 0.5057 \log g, \quad (4.41)$$

$g$  is the gravitational acceleration. The Alfvén wave velocity at the photosphere is  $V_{A*} = B_*/(4\pi\rho_*)^{1/2}$ . The critical density of the plasma fluid is computed from the energy conservation of wave action condition  $\tilde{S} = \text{constant}$ . As a result, it is written as

$$\rho_c = 4\pi \left( \frac{\rho_* v_{\perp*}^2 V_{A*} A_*}{v_{\perp,c}^2 B_c A_c} \right)^2, \quad (4.42)$$

with the critical transverse velocity,  $v_{\perp,c} = 2u_c$ , and magnetic strength,  $B_c = \left( \frac{R_*}{r_c} \right)^2 f_* B_*$  with  $B_*$  is the magnetic strength at the photosphere.

### Combining the hot and cold mass loss rates

In order to express the contribution from both driven mechanisms, the total mass loss is the summation,

$$\dot{M} \approx \dot{M}_{\text{cold}} + \dot{M}_{\text{hot}} \exp(-4M_{A,\text{TR}}^2), \quad (4.43)$$

with  $\dot{M}_{\text{hot}}$  is given in Eq.4.31, and  $\dot{M}_{\text{cold}}$  is given in Eq.4.36. The Mach number at transition region,  $M_{A,\text{TR}} = u_{\text{TR}}/V_{A,\text{TR}}$  is introduced to control the efficiency of the hot coronal mass loss, due to the fact that there are stars that do not have corona. In which, the TR outflow speed is deduced from the hot coronal region through mass flux conservation which is,

$$u_{\text{TR}} = \frac{\dot{M}_{\text{hot}}}{4\pi R_*^2 f_{\text{TR}} \rho_{\text{TR}}}, \quad \text{with} \quad \rho_{\text{TR}} = \left[ \frac{\tilde{\alpha}_{\text{TR}} Q_* m_H^2}{\tilde{\alpha}_* \rho_*^{1/4} \Lambda_{\text{max}}} \right]^{4/7} f_*^{2(1-\theta)/7}. \quad (4.44)$$

The Alfvén speed at TR is computed by,

$$V_{A,TR} = \frac{B_{TR}}{\sqrt{4\pi\rho_{TR}}}, \quad (4.45)$$

where  $B_{TR} = f_*^{1-\theta} B_*$ , and  $B_* = 1.13 \sqrt{\frac{8\pi\rho_* k_B T_{eff}}{\mu m_H}}$  with the mean atomic weight  $\mu \approx \frac{7}{4} + \frac{1}{2} \tanh\left(\frac{3500-T_{eff}}{600}\right)$ .

To summarise, the total mass loss is computed by Eq. 4.43, where the contribution from hot corona regions is given in Eq. 4.31 while the contribution from cold-wave driven is from Eq. 4.36. All the quantities that contained in these two component mass loss rates are either computed from the fundamental properties of the considered star such as the mass, radius, density at the photosphere level, effective temperature, and the given metallicity, or the filling factor,  $f_*$ . Therefore, knowing  $f_*$  is necessary to proceed forwards.

### Filling factor determination

In PARSEC model,  $f_*$  is chosen to be the minimum limit of  $f(r)$  from [Cranmer and Saar \(2011\)](#), which is

$$f_* = \frac{0.5}{[1 + (x/0.16)^{2.6}]^{1.3}}, \quad (4.46)$$

where  $x \equiv Ro/Ro_\odot$ , and  $Ro \equiv P_{rot}/\tau_c$  which is called by Rossby number, used to describe the chromospheric flux ratio (see [Noyes et al., 1984](#), for more details), with the solar Rossby number  $Ro_\odot = 1.96$ .

The  $\tau_c$  appears in the Rossby number above is the convective turnover time (in days) which is computed by (see [Gunn et al., 1998](#)),

$$\tau_c = 314.24 \exp \left[ - \left( \frac{T_{eff}}{1952.5 \text{ K}} \right) - \left( \frac{T_{eff}}{6250 \text{ K}} \right)^{18} \right] + 0.002. \quad (4.47)$$

$P_{rot}$  is the rotation period. The rotation period in general depends on mass, radius, and time. We introduce an expression of  $P_{rot}(M, R, t)$  follows the power law in radius,

$$P_{rot}(M, R, t) = P_{MS}(M, t) \left( \frac{R}{R_\odot} \right)^\xi, \quad (4.48)$$

Table 4.3: Adopted coefficients.

Mamajek's formula		Sekiguchi's formula	
$a$	$0.407 \pm 0.021$	$t_0$	$-813.3175 \pm 42.5$
$b$	$0.325 \pm 0.024$	$t_1$	$684.4584 \pm 34.3$
$c$	$0.4095 \pm 0.010$	$t_2$	$-189.923 \pm 9.23$
$n$	$0.566 \pm 0.008$	$t_3$	$17.40875 \pm 0.827$
		$f_1$	$1.2136 \pm 0.038$
		$f_2$	$0.0209 \pm 0.0006$
		$d_1$	$-0.294 \pm 0.010$
		$g_1$	$-1.166 \pm 0.028$
		$e_1$	$0.3125 \pm 0.0076$

with  $\xi = 0.7$  by fitting the data from [Cranmer and Saar \(2011\)](#). The  $P_{\text{MS}}$  is the rotation period of stars at the MS phase. In PARSEC, there are two approaches to adopt  $P_{\text{MS}}$ . First, the constant value  $P_{\text{MS}} = 25$  days is adopted, based on the rotation period of the Sun (shown as FORM1 hereafter). The second way to obtain  $P_{\text{MS}}$  is doing calibration with the observed rotation period of MS stars that we find in literature (shown as FORM2 hereafter). This latter method will be described further below.

The dependence of  $P_{\text{MS}}$  on mass and age is adopted from [Mamajek and Hillenbrand \(2008\)](#) and [Sekiguchi and Fukugita \(2000\)](#) which is given by

$$P_{\text{MS}}(M, t) = P_{\text{MS}}(M)t^n \quad \text{with} \quad n = 0.566, \quad (4.49)$$

$t$  is the age in Myr. The mass-dependent component in Eq. 4.49 can be obtained by calibration with observed data. For this purpose, the simple polynomial function  $P_{\text{MS}}(M) = a_0 + a_1M + a_2M^2 + a_3M^3$  is used to fit the measured data from [McQuillan et al. \(2014\)](#), the details in deducing  $P_{\text{MS}}(M)$  will be shown below.

### Deducing the rotation period

We use the full sample of 34030 *KEPLER* MS stars in [McQuillan et al. \(2014\)](#) to produce the relation of  $P_{\text{MS}} \equiv P_{\text{MS}}(M)$ . First, the distribution of rotation



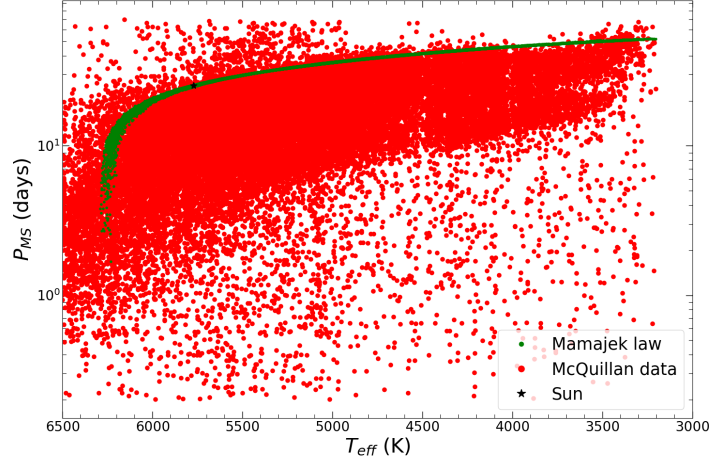


Figure 4.5: The sample of 34 000 MS stars of [McQuillan et al. \(2014\)](#) (red-dots), superimposed with the estimated period by using the formula of [Mamajek and Hillenbrand \(2008\)](#) (green-dots). The position of the Sun is shown by black-asterisk.

period is reproduced by adopting the theoretical formula from [Mamajek and Hillenbrand \(2008\)](#), which is written as

$$P_{\text{MS}}(B - V, t) = a [(B - V)_0 - c]^b t^n, \quad (4.50)$$

with coefficients  $a, b, c, n$  are given in Table. 4.3. In which, the colour  $(B - V)_0$  is converted to effective temperature by using the transformation form of [Sekiguchi and Fukugita \(2000\)](#),

$$\begin{aligned} (B - V)_0 = & t_0 + t_1 \log T_{\text{eff}} + t_2 (\log T_{\text{eff}})^2 + t_3 (\log T_{\text{eff}})^3 + f_1 [\text{Fe}/\text{H}] \\ & + f_2 [\text{Fe}/\text{H}]^2 + d_1 [\text{Fe}/\text{H}] \log T_{\text{eff}} + g_1 \log g + e_1 \log g \log T_{\text{eff}}. \end{aligned} \quad (4.51)$$

With the provided  $\log g$  and  $T_{\text{eff}}$  and the chosen  $[\text{Fe}/\text{H}] = 0$ , the estimated rotation period with solar age  $t = 4.65$  Gyr is shown by the green-dots in Fig. 4.5 overplotted with the data from [McQuillan et al. \(2014\)](#) in red-dots, the location of the Sun is shown by black-asterisk.

The second step, we interpolate the obtained theoretical distribution above by using the polynomial function with the variable is only  $T_{\text{eff}}$  and

so we get the relation  $P_{\text{MS}} = P_{\text{MS}}(T_{\text{eff}})$ . From this simple relation, we select a subsample that contains stars which are inside the range of  $P_{\text{MS}} \pm 2.0$  (days).

Then, the final step, from this subsample we perform a simple polynomial fit to the observed data with the variable is now the mass ( $M$ ) to obtain the relation  $P_{\text{MS}}(M)$ . As a result of the interpolation by using the function  $P_{\text{MS}} = a_0 + a_1M + a_2M^2 + a_3M^3$ , the coefficients  $a_i$  are,

$$\begin{aligned} a_0 &= 0.5666 \pm 0.0102, & a_1 &= -0.6668 \pm 0.0454, \\ a_2 &= 0.8944 \pm 0.0619, & a_3 &= -0.5674 \pm 0.0264. \end{aligned} \quad (4.52)$$

Therefore, to summary, the rotation period that is needed to calculate the filling factor, Eq. 4.48, can be computed either in two ways: one with the constant value of  $P_{\text{MS}} \approx 25$  days, or the deduced

$$P_{\text{MS}}(M, t) = P_{\text{MS}}(M)t^{0.566}, \quad P_{\text{MS}}(M) = a_1 + a_2M + a_3M^2 + a_4M^3, \quad (4.53)$$

with the interpolated coefficients  $a_i$  are listed in Eq. 4.52.

Figure. 4.6 shows the theoretical relation between  $\log \dot{M}$  and  $\log L$  of three selected models 0.9, 1.0 and 1.2 $M_{\odot}$  with  $Z = 0.017$  by using this self-consistent mass loss scheme over with the data taken from [Cranmer and Saar \(2011\)](#). The prediction by using both ways of  $P_{\text{MS}}$  as discussed above is shown with distinguished labels, namely, “FORM1” is by using the constant  $P_{\text{MS}}$  and “FORM2” is by using the deduced relation in Eq. 4.53. We find our model of 1 $M_{\odot}$  predicts very well the mass loss rate of the Sun in both cases. We find  $\dot{M} \approx 3.04 \cdot 10^{-14} M_{\odot}/\text{yr}$  by using the FORM1 scheme, while the FORM2 gives  $\dot{M} \approx 2.3 \cdot 10^{-14} M_{\odot}/\text{yr}$  against the observed value from [Cranmer and Saar \(2011\)](#),  $\dot{M} = (2.0 - 3.16) \cdot 10^{-14} M_{\odot}/\text{yr}$ . However, we should mention that more detailed calibrations should be done before we provide any further useful information on this subject as well as the computed tracks, and will be reported in the coming works.

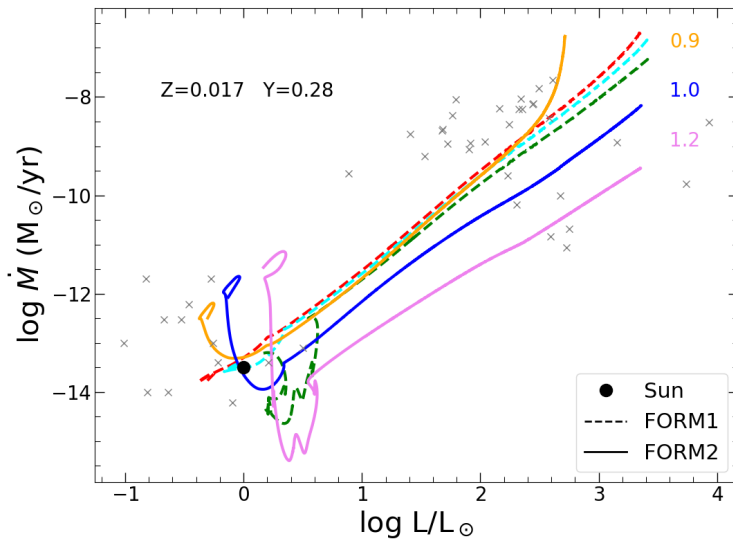


Figure 4.6: Mass loss rate as function of luminosity. The data is displayed in grey-crosses with the highlighted position of the Sun in black-dot. The relation from selected models of 0.9, 1.0 and 1.2 $M_{\odot}$  are shown in colour-lines.

# Chapter 5

## PARSEC V2.0: Stellar tracks with rotation

In this chapter, I will present the new comprehensive collection of stellar evolutionary tracks with the rotation that is computed with the PARSEC V2.0 code. For this purpose, calculations of rotating low- and intermediate-mass stellar models are intensively performed with this most updated version. The recent calibration of the extra mixing from overshooting and rotation is included in combination with several improvements in nuclear reaction network, treatment of convective mixing, mass loss, and other physical input parameters. This chapter is based on the paper [Nguyen et al. \(2022\)](#) and will be structured in four sections. Section 5.1 will show the motivations and aims that we want to achieve in this project. Section. 5.2 reviews the main input physics used in this present calculation. The particular attention is paid to differences with respect to the previous non-rotating models, given the important physical input changes. In Sect. 5.3, the effects of rotational mixing on the evolution of our new stellar models will be shown. The comparison of our current models with previous non-rotating ones as well as with other existing models in the literature will be discussed in Sect. 5.4.

### 5.1 Motivation and aims

The PAdova and tRieste Stellar Evolutionary Code (PARSEC) was first implemented in [Bressan et al. \(2012\)](#) and then used in several works aimed at producing large grids of stellar evolutionary tracks and isochrones. For

instance, [Chen et al. \(2014\)](#) extended the calculation to very low-mass star models, [Tang et al. \(2014\)](#) and [Chen et al. \(2015\)](#) pursued the calculation of massive stars up to  $350 M_{\odot}$ , and [Fu et al. \(2018\)](#) studied the evolution with  $\alpha$ -enhanced compositions. Extended sets of isochrones using PARSEC tracks were described in [Bressan et al. \(2012\)](#) and [Marigo et al. \(2017\)](#). More recently, a significant development was presented in [Costa et al. \(2019b\)](#), who included the effects of rotation in the new version of the code, PARSEC V2.0<sup>1</sup>.

As described in [von Zeipel \(1924a\)](#), [von Zeipel \(1924b\)](#), [Kippenhahn et al. \(1970\)](#), [Zahn \(1992\)](#), [Meynet and Maeder \(1997\)](#), [Chieffi and Limongi \(2013\)](#), and [Chieffi and Limongi \(2017\)](#), rotation might have a significant impact on the stellar structure induced by geometrical distortion, extra mixing, and enhanced mass-loss rates. Observational evidence regarding the large fractions of rapidly rotating stars among the Milky Way field stars (e.g. [Royer et al., 2007](#)) and in star clusters in Magellanic Clouds (e.g. [Dupree et al., 2017](#); [D’Antona et al., 2017](#)) suggests that rotation may indeed become an important driving agent for stellar evolution. Furthermore, it may be concurrent with other physical processes that drive extra mixing, such as convective overshooting (see e.g. [Jermyn et al., 2018](#); [Costa et al., 2019b](#)). The effect of extra mixing caused by overshooting from the unstable core was introduced a few decades ago (e.g. [Saslaw and Schwarzschild, 1965](#); [Maeder, 1975](#); [Roxburgh, 1978](#); [Bressan et al., 1981, 1986](#); [Bertelli et al., 1984, 1990b](#); [Bressan et al., 1993](#); [Meynet et al., 1994b](#); [Fagotto et al., 1994a,b](#); [Girardi et al., 2000b](#)) and is now incorporated into most libraries of stellar evolutionary tracks (e.g. [Demarque et al., 2004](#); [Pietrinferni et al., 2004](#); [Weiss and Schlattl, 2008](#); [Paxton et al., 2011, 2018](#); [Mowlavi et al., 2012](#); [Bressan et al., 2012](#); [Bossini et al., 2015](#); [Spada et al., 2017](#); [Hidalgo et al., 2018](#)). Many authors also suggest a variation in the overshooting efficiency, usually parameterised by the efficiency parameter  $\lambda_{\text{ov}}$ , with the initial mass (see e.g. [Pols et al., 1998](#)). Analysis of double-lined eclipsing binaries (DLEBs; [Claret and Torres, 2016, 2017, 2018, 2019](#)) supports a growing efficiency in the mass range  $\sim 1 - 1.7 M_{\odot}$  with a plateau in  $\lambda_{\text{ov}}$  above this range. However, the best fits of the DLEB parameters require a certain degree of stochasticity in some other important parameters, such as the mixing length scale, which in our opinion is difficult to accept, particularly in the case of binary components with the same mass. Indeed, [Costa et al. \(2019b\)](#) show that the observa-

---

<sup>1</sup>Stellar tracks and isochrones computed in this work are available at the following links: <http://stev.oapd.inaf.it/PARSEC> and <http://stev.oapd.inaf.it/cmd>, respectively.

tions of DLEBs could be well explained by the interplay between a ‘fixed’ overshooting efficiency and a varying initial rotational velocity. In fact, the latter also depends on environmental conditions. The results obtained by [Costa et al. \(2019b\)](#) can thus be considered an important step in the calibration of the efficiency of the overshooting phenomenon, at least in the domain of low- and intermediate-mass stars. This calibration has been subsequently supported by a combined analysis of Cepheids in the Large Magellanic Cloud (LMC) star cluster NGC1866 and the CMDs of its multiple stellar populations ([Costa et al., 2019a](#)).

Following these initial tests performed with the new code, we present in this chapter the new sets of evolutionary tracks and the corresponding isochrones in the next chapter for the PARSEC models with rotation. The initial mass range presented in this chapter goes from  $0.09 M_{\odot}$  to  $14 M_{\odot}$ . Models of more massive stars have already been computed for some particular purposes ([Spera et al., 2019](#); [Goswami et al., 2021](#); [Costa et al., 2021](#); [Goswami et al., 2022](#); [Costa et al., 2022](#)), but the full set including rotation is still in preparation and will be presented in a dedicated paper.

All the tracks start at the PMS phase and are terminated at a stage that depends on the initial mass: at ages largely exceeding the Hubble time; at the initial stages of the thermally pulsing asymptotic giant branch (TP-AGB); or at carbon exhaustion for more massive stars. The tracks are computed with an initial metal content ranging from  $Z = 0.004$  to  $0.017$  and with an initial He mass fraction that follows a linear enrichment law ([Bressan et al., 2012](#)). Tracks at lower metallicity are computed with an enhanced partition, and the details of these models with rotation will be presented in an upcoming paper. For every metallicity, we consider initial rotation rates from zero to the critical value. The theoretical isochrones are then derived and converted into several photometric systems which will be presented in Chapter 6.

## 5.2 Input physics

### 5.2.1 Solar metallicity, opacities, nuclear reactions, mixing length, equation of state

The exact abundance of elements heavier than  $^4\text{He}$  in the Sun is still known with some uncertainty. The early compilation by [Grevesse and Sauval \(1998\)](#), consisting of the abundances of 90 elements from lithium to uranium, yielded

the solar metallicity  $Z_{\odot} = 0.017$ . Later, [Asplund et al. \(2006\)](#) and [Asplund et al. \(2009\)](#) claimed lower values,  $Z_{\odot} = 0.0122$  and  $Z_{\odot} = 0.0134$ , respectively, or [Lodders et al. \(2009\)](#) with  $Z_{\odot} = 0.0141$ . Recent solar wind measurements give  $Z_{\odot} = 0.0196 \pm 0.0014$  ([von Steiger and Zurbuchen, 2016](#)). In this work, we adopt the solar-scaled mixtures by [Caffau et al. \(2011\)](#) where the current solar metallicity is  $Z_{\odot} = 0.01524$ , which is an intermediate value between those preferred by [Asplund et al. \(2009\)](#) and [von Steiger and Zurbuchen \(2016\)](#). Further extensions to other metallicity ranges with more suitable input physics, for example,  $\alpha$ -enhanced mixtures, will be provided in the forthcoming works.

The Rosseland mean opacities,  $\kappa_{\text{rad}}$ , are the same as those of PARSEC V1.2S. In the high temperature regime,  $4.2 \leq \log(T/K) \leq 8.7$ , the opacity tables are provided by the Opacity Project At Livermore (OPAL; see [Iglesias and Rogers, 1996](#)), while in the low temperature regime  $3.2 \leq \log(T/K) \leq 4.1$  we generate the opacity tables with the AESOPUS tool (see [Marigo and Aringer, 2009](#), for details). In the transition region  $4.1 \leq \log(T/K) \leq 4.2$ , the opacities are linearly interpolated between the OPAL and AESOPUS values. The contribution from conduction is computed following [Itoh et al. \(2008\)](#).

The transport of convective energy is described by the mixing length theory of [Böhm \(1958\)](#), adopting the value of mixing-length parameter  $\alpha_{\text{MLT}} = 1.74$  calibrated on the solar model by [Bressan et al. \(2012\)](#) (see also [Sonoi et al. 2019](#) for more calibrations). It is interesting, however, to note that the variation in  $\alpha_{\text{MLT}}$  for different stars has recently been remarked upon; for example, [Viani et al. \(2018\)](#) suggest a dependence of  $\alpha_{\text{MLT}}/\alpha_{\text{MLT}\odot}$  on gravity, effective temperature, and metallicity, while the study of [Song et al. \(2020\)](#) in FGK stars mainly focuses on the impact from metallicity. While these recent studies might be an inspiration for future works, at the moment we use the solar mixing-length parameter for all calculations,  $\alpha_{\text{MLT}} = \alpha_{\text{MLT}\odot} = 1.74$ . The EOS in PARSEC V2.0 is computed with the freely available FREEEOS code developed by A.W. Irwin<sup>2</sup>.

The nuclear reaction network, after the updates by [Fu et al. \(2018\)](#) and [Costa et al. \(2021\)](#), includes the p-p chains, the CNO tri-cycle, the Ne-Na, and Mg-Al chains,  $^{12}\text{C}$ ,  $^{16}\text{O}$  and  $^{20}\text{Ne}$  burning reactions, and the  $\alpha$ -capture reactions up to  $^{56}\text{Ni}$ , for a total of 72 different reactions tracing 32 isotopes:  $^1\text{H}$ ,  $\text{D}$ ,  $^3\text{He}$ ,  $^4\text{He}$ ,  $^7\text{Li}$ ,  $^7\text{Be}$ ,  $^{12}\text{C}$ ,  $^{13}\text{C}$ ,  $^{14}\text{N}$ ,  $^{15}\text{N}$ ,  $^{16}\text{O}$ ,  $^{17}\text{O}$ ,  $^{18}\text{O}$ ,  $^{19}\text{F}$ ,  $^{20}\text{Ne}$ ,  $^{21}\text{Ne}$ ,

---

<sup>2</sup><http://freeeos.sourceforge.net/>

$^{22}\text{Ne}$ ,  $^{23}\text{Na}$ ,  $^{24}\text{Mg}$ ,  $^{25}\text{Mg}$ ,  $^{26}\text{Mg}$ ,  $^{26}\text{Al}$ ,  $^{27}\text{Al}$ ,  $^{28}\text{Si}$ ,  $^{32}\text{S}$ ,  $^{36}\text{Ar}$ ,  $^{40}\text{Ca}$ ,  $^{44}\text{Ti}$ ,  $^{48}\text{Cr}$ ,  $^{52}\text{Fe}$ ,  $^{56}\text{Ni}$ , and  $^{60}\text{Zn}$ . We note that in the present calculations we do not go beyond the central carbon burning (but see [Costa et al., 2021](#), for massive stars).

### 5.2.2 Convective Overshooting

*Core overshooting (COV)*: The convective unstable region is well defined within the framework of the Schwarzschild criterion ([Schwarzschild, 1958](#)). However, in reality, the convective elements can travel up to a certain point beyond the border of the unstable region until their velocity drops to zero. This phenomenon is called overshooting. The determination of the edge of the true convective core was described in [Bressan et al. \(1981\)](#). In PARSEC, the overshooting parameter ( $\lambda_{\text{ov}}$ ) is taken across the unstable border; therefore, the COV length is  $l_{\text{ov}} \sim \frac{1}{2}\lambda_{\text{ov}}H_P$ , where  $H_P$  is the local pressure scale height.

*Envelope overshooting (EOV)*: The overshooting downwards from the base of the convective envelope has been invoked to explain the observations of the location of the red-giant-branch bump (RGBB) or the extension of blue loops in the CMD ([Alongi et al., 1991](#); [Cassisi et al., 2002](#); [Tang et al., 2014](#); [Fu et al., 2018](#)). Solar calibration with helioseismic data has been done by [Christensen-Dalsgaard et al. \(2011\)](#).

In PARSEC models, the treatment of overshoot from both the convective core and envelope are related to the initial masses. For this reason, we describe the values of overshooting parameters that we use in our calculations more completely in the next subsection.

### 5.2.3 Mass Range for Core and Envelope Overshooting

In a narrow interval of masses around  $1 M_{\odot}$ , there is a transition between stars that burn central hydrogen in a radiative core and those that burn hydrogen in a convective core due to the predominance of the CNO-cycle over the pp-cycle. Assessing the efficiency of COV in this mass range is a particularly delicate matter both theoretically (e.g. [Bertelli et al., 1986, 1990a](#); [Aparicio et al., 1990](#); [Ventura et al., 1998](#); [Mowlavi et al., 2012](#); [Higl et al., 2021](#)) and observationally (e.g. [Torres et al., 2014](#); [Claret and Torres, 2016, 2018](#); [Noll et al., 2021](#)). This happens because the inclusion of overshooting



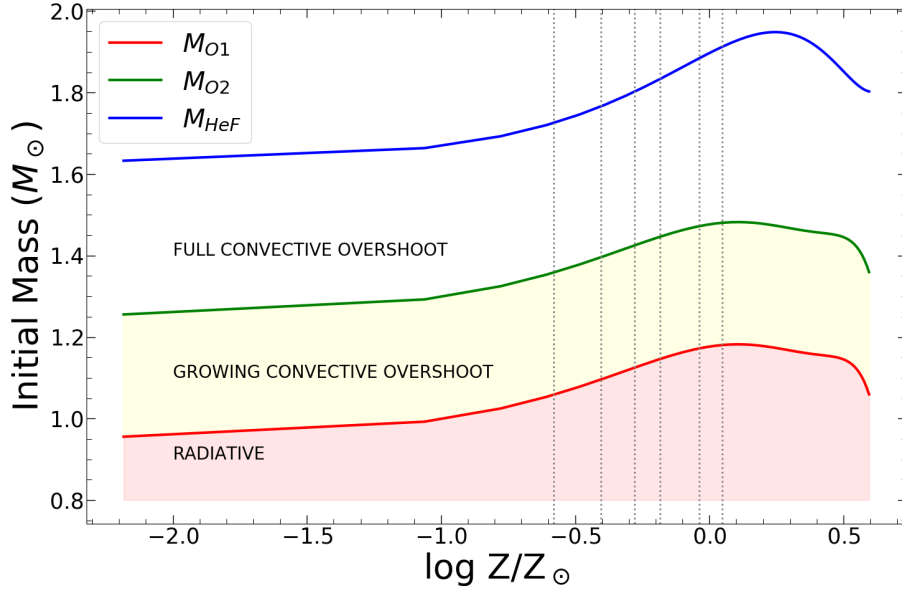


Figure 5.1: Transition masses ( $M_{O1}$ ,  $M_{O2}$ ,  $M_{HeF}$ ) as a function of metallicity in the case of no rotation. The red and green lines indicate  $M_{O1}$  and  $M_{O2}$ , respectively; The blue line indicates  $M_{HeF}$ . The red area indicates models with a radiative core without convective overshooting. The yellow area delineates the region of growing overshooting efficiency, while full overshooting efficiency occurs in the region above the green line. The vertical dotted grey lines mark the six computed initial metallicities. The solar metallicity is  $Z_{\odot} = 0.01524$ , from [Caffau et al. \(2011\)](#).

modifies the structure and the following evolution of the stars in an irreversible way. In fact, the smallest stars in this mass range reach the zero-age main sequence (ZAMS) with small convective cores that disappear as the central H-burning proceeds. If we apply an efficient overshooting to these models, the convective cores do not disappear, but instead tend to become larger and larger, producing a significantly different evolution. To avoid this behaviour, which is not favoured by observations ([Costa et al., 2019b](#); [Girardi et al., 2000a](#)), we define the limiting mass  $M_{O1}$  as the largest initial mass of a star showing a vanishing convective core during the early hydrogen-burning phase, calculated without overshooting. This mass depends on the initial chemical composition adopted. On the other hand, slightly above this mass

limit, observations favour an already well-developed overshooting efficiency, with  $\lambda_{\text{ov}} = \lambda_{\text{ov,max}}$ . This second mass limit is defined as  $M_{\text{O2}} = M_{\text{O1}} + 0.3M_{\odot}$ .

In PARSEC V2.0, we define an initial mass range where the transition from models with a radiative core to models with a fully grown convective core takes place,  $M_{\text{O1}} \leq M_i \leq M_{\text{O2}}$ . For initial masses  $M_i$  below  $M_{\text{O1}}$ , the core is stable against convection and energy is transported by radiation. For  $M_i$  between  $M_{\text{O1}}$  and  $M_{\text{O2}}$ , the overshooting parameter is let to increase linearly from  $\lambda_{\text{ov}} = 0$  up to a maximum value  $\lambda_{\text{ov,max}}$ , in order to have a smooth transition in the properties of the stars. For  $M_i \geq M_{\text{O2}}$ , the overshoot is applied with its maximum efficiency,  $\lambda_{\text{ov}} = \lambda_{\text{ov,max}} = 0.4$  following [Costa et al. \(2019b\)](#). This value corresponds to an overshooting length,  $l_{\text{ov}}$ , which extends about  $0.2 H_P$  above the Schwarzschild border.

As far as the envelope overshooting is concerned we recall that, for stars with mass  $M_i < M_{\text{O1}}$ , we adopted  $\Lambda_e = 0.5 H_P$ , as inspired by [Fu et al. \(2018\)](#); for stars with mass  $M_i > M_{\text{O2}}$ , we applied the maximum efficiency, as we did for COV; therefore,  $\Lambda_e = 0.7 H_P$ , as used in [Alongi et al. \(1991\)](#) and [Bressan et al. \(2012\)](#). In the transition region,  $\Lambda_e$  of a star is linearly interpolated between  $0.5 H_P$  and  $0.7 H_P$ . Table 5.1 shows the values of  $\lambda_{\text{ov}}$  and  $\Lambda_e$  adopted for each initial mass.

### 5.2.4 Rotation

With PARSEC V2.0 we compute evolutionary tracks of rotating stars using the methodology developed by [Kippenhahn and Thomas \(1970\)](#) and [Meynet and Maeder \(1997\)](#), implemented and described in [Costa et al. \(2019a\)](#) and [Costa et al. \(2019b\)](#). The basic quantity describing the effect of rotation in the stellar structure is the angular rotation rate,  $\omega$ , defined as

$$\omega = \frac{\Omega}{\Omega_c}, \quad \Omega_c = \left(\frac{2}{3}\right)^{3/2} \sqrt{\frac{GM}{R_{\text{pol}}^3}}, \quad (5.1)$$

where  $\Omega$  is the angular velocity,  $\Omega_c$  is the critical angular velocity (or breakup velocity), that is, the angular velocity at which the centrifugal force is equal to the effective gravity at the equator.  $G$  is the gravitational constant,  $M$  is the mass enclosed by  $R_{\text{pol}}$  that is the polar radius.

We considered a wide range of initial rotation rates, from non-rotating models ( $\omega_i = 0$ ) to models initially very near the critical breakup rotational velocity ( $\omega_i = 0.99$ ). It is commonly accepted that LMSs do not reach high

values of the rotational speed, compared to intermediate and high-mass stars. [McQuillan et al. \(2014\)](#) reports a sample of the rotation period of more than 34,000 MS stars. In their Figure 1, there is a clear trend for larger periods in smaller masses. This trend inevitably implies that stars with lower masses have lower initial rotational speeds.

On the other hand, rotation may reach high initial values for masses where convection is well developed ([Costa et al., 2019b](#)). For this reason, in analogy to what we did for the efficiency of convective COV, rotation was not considered for  $M_i \leq M_{O1}$  while, for  $M_i \geq M_{O2}$ , models were computed for the following initial rotation rates:  $\omega_i = 0.0, 0.30, 0.60, 0.80, 0.90, 0.95, 0.99$ . For stars with an initial mass in the range  $M_{O1} \leq M_i < M_{O2}$  we computed models with an initial rotation rate up to a maximum value of

$$\omega_{i,\max}(M) \equiv 0.99 \left( \frac{M - M_{O1}}{M_{O2} - M_{O1}} \right). \quad (5.2)$$

It is also important to mention that, in this version, the rotation is switched on a few models before the ZAMS phase. At this stage, the code computes the angular velocity  $\Omega$  that corresponds to the initial rotation rate  $\omega_i$  and assigns it to each shell of the star, forcing a solid body rotation. From the ZAMS on, the solid body rotation constraint is relaxed, and the stellar rotation evolves accordingly with the conservation and the transport of angular momentum.

### 5.2.5 Transport of angular momentum and chemical mixing

The transport of angular momentum is treated using the pure diffusive approximation ([Heger et al., 2000](#)), where the total diffusion coefficient comes from three components,

$$D = D_{\text{mix}} + D_{\text{s.i.}} + D_{\text{m.c.}}, \quad (5.3)$$

where  $D_{\text{mix}}$  is the diffusion coefficient in the convective zones. The last two terms are related to shear instability and meridional circulation. To compute the diffusion coefficient of the shear instability, we use the formula by [Talon and Zahn \(1997\)](#), which reads

$$D_{\text{s.i.}} = \frac{8}{5} \frac{\text{Ri}_c (rd\Omega_r/dr)^2}{N_T^2/(K + D_h) + N_\mu^2/D_h}, \quad (5.4)$$

where the Brunt-Väisälä frequency is split into  $N_T^2$  and  $N_\mu^2$ ,  $\text{Ri}_c = 1/4$  is the critical Richardson number,  $K$  is the thermal diffusivity, and  $D_h$  is the coefficient of horizontal turbulence.

When angular momentum transport is treated with the diffusive approach, the diffusion coefficient for the meridional circulation remains to be defined. Some authors define it as the product of circulation velocity and its typical length scale (Heger et al., 2000), while others use the same coefficient provided for chemical transport (Chieffi and Limongi, 2013). For the sake of simplicity, we decided to follow the latter approach. Therefore, we adopt the coefficient by Chaboyer and Zahn (1992), which reads

$$D_{\text{m.c.}} \simeq \frac{|rU|^2}{30D_h}, \quad (5.5)$$

where  $U$  is the radial component of the meridional circulation velocity (see also Maeder, 2009; Potter et al., 2012). It should be noted that, as discussed by Chaboyer and Zahn (1992) and Zahn (1992), this coefficient takes into account the net effect of the meridional current and horizontal diffusion for chemical species. A more detailed description of angular momentum transport should include meridional circulation as an advective process. However, due to the difficult numerical implementation of the advective-diffusive treatment, and the fact that the angular momentum redistribution goes in the direction of flattening  $\omega$  profiles during the MS phase (Chieffi and Limongi, 2013), we decided to use the simpler diffusive approach.

Future PARSEC versions will include the full advective-diffusive treatment for angular momentum transport. We refer to Costa et al. (2019b) for more details on the numerical implementation of rotation.

Another important difference of this new version, PARSEC V2.0, with respect to PARSEC V1.2S concerns chemical mixing. While in the latter version the gas was chemically homogenised within convective regions, in the present version we adopt a diffusive approach and solve a unique equation for chemical variation due to nuclear reactions, turbulent motions, molecular diffusion, and rotational mixing. The turbulent diffusion coefficient is calculated with the usual approximation  $D_T = \frac{1}{3}v_c l_c$  where the velocity of the eddies,  $v_c$ , and their mean free path,  $l_c$  are obtained from the mixing length theory (Böhm-Vitense, 1958).

We note that, while all the above processes can be treated at once, molecular diffusion can be switched off in models where the COV reaches its maximum efficiency (above  $M \geq M_{\text{O2}}$ ), because, in such models, the effects

of molecular diffusion become negligible with respect to turbulent diffusion and, eventually, rotational mixing. This allows a speed-up of the calculations without loss of generality. We discuss the effects brought by adopting either of the aforementioned mixing schemes later on.

### 5.2.6 Mass loss rates

The effects of mass loss in the evolution of low and IMSs have been extensively studied in many papers (e.g. [Reimers, 1975](#); [Bloeker, 1995](#); [Schröder and Cuntz, 2005](#); [Cranmer and Saar, 2011](#); [Rosenfield et al., 2014](#); [Kalirai et al., 2008](#); [Catalán et al., 2008](#); [Salaris et al., 2009](#)). In PARSEC models, as well as in previous models of the same group ([Girardi et al., 2000a](#); [Bertelli et al., 2008](#)), mass loss was not activated in the calculations of the low-mass tracks but only at the stage of isochrone calculations. This approximation has been tested in many different applications and has always been considered acceptable from our group. It derives from the fact that the RGB evolution of LMSs is just marginally affected by this process, which eventually becomes important only very near to the tip of the red-giant branch (TRGB). Therefore, mass loss just causes a decrease in mass between the RGB and the ‘zero-age horizontal branch’ (ZAHB) stage. This decrease was easily taken into account when interpolating the helium-burning tracks to prepare isochrones. This method allows a great flexibility (different mass-loss prescriptions can be tested without recomputing the evolutionary tracks) and speed-up at the level of isochrone calculation. In the more advanced phases of low and IMSs, typically from the early up to the end of the TP-AGB phase, mass-loss is one of the main processes driving the evolution and cannot be neglected. However, the evolution of stars in these phases is computed subsequently with the COLIBRI code ([Marigo et al., 2013](#)), where the most updated mass-loss rates are implemented.

With the inclusion of rotation, mass loss cannot be decoupled from evolution anymore and must be included in all evolutionary phases. This is because rotation may enhance the mass loss, affecting the evolutionary path of the star. This may become dramatic when the star is evolving in the proximity of the critical breakup velocity.

In this work, we apply the [Reimers \(1975\)](#) and [Reimers \(1977\)](#) law for

non-rotating LMSs, which is

$$\dot{M}(\omega = 0) = \eta \times 1.343 \times 10^{-5} \frac{L^{1.5}}{m T_{\text{eff}}^2}, \quad (5.6)$$

where  $\dot{M}$  is the mass-loss rate in  $M_{\odot}/\text{yr}$ ,  $L$  and  $m$  are the luminosity and mass in solar units, respectively, and  $T_{\text{eff}}$  is the effective temperature in K. The  $\eta$  is an efficiency coefficient that is generally calibrated against CMDs of globular clusters, for instance in [Renzini and Fusi Pecci \(1988\)](#) where the derived  $\eta$  is 0.35, or [Aaronson and Mould \(1982\)](#) who claimed that  $\eta = 0.5 - 0.7$  fits well their data of the red globular clusters in the Magellanic Clouds. In this work, we adopt  $\eta = 0.2$ , as more recently indicated from the asteroseismic analysis of the two old open clusters NGC 6791 and NGC 6819 by [Miglio et al. \(2012\)](#). As described in [Chen et al. \(2015\)](#), for non-rotating intermediate-mass and massive stars we adopt the mass-loss rate from [de Jager et al. \(1988\)](#) and [Vink et al. \(2001\)](#), respectively, both corrected by a factor that assumes the same dependence on the surface metallicity (i.e.  $\dot{M} \propto (Z/Z_{\odot})^{0.85} M_{\odot}/\text{yr}$ ).

In the case of rotating stars, the mass-loss rates are enhanced by a factor that depends on the surface tangential velocity,  $v$ , as expressed in [Costa et al. \(2019a\)](#) and [Costa et al. \(2019b\)](#). By numerically solving the fluid equations of a radiation-stellar wind model, [Friend and Abbott \(1986\)](#) yield a relation where the mass-loss rate of a rotating star is modified by a factor with respect to the mass loss of a non-rotating model, which is

$$\dot{M}(\omega) = \dot{M}(\omega = 0) \left( 1 - \frac{v}{v_{\text{crit}}} \right)^{-\xi}, \quad (5.7)$$

where  $\xi = 0.43$  is provided in [Bjorkman and Cassinelli \(1993\)](#) by fitting the numerical result of [Friend and Abbott \(1986\)](#).  $\dot{M}(\omega = 0)$  is the mass-loss rate in case of zero rotation and  $v_{\text{crit}}$  is the surface critical velocity, which is usually defined as ([Heger et al., 2000](#))

$$v_{\text{crit}}^2 = \frac{Gm}{r} (1 - \Gamma_e), \quad (5.8)$$

where  $G$ ,  $m$ , and  $r$  are the gravitational constant, mass, and radius in solar units, respectively, and  $\Gamma_e$  is the Eddington factor. In this recent work, the dependence of  $\Gamma_e$  with the angular velocity is neglected, instead, it should be considered for angular velocities near the critical one ([Maeder and Meynet, 2000](#)).

### 5.3 Evolutionary tracks

Before going into more detail on the analysis of our stellar evolutionary tracks, we summarise some of the main points on the adopted input physics. Firstly, we computed models with six initial metallicities:  $Z = 0.004, 0.006, 0.008, 0.01, 0.014, 0.017$ , which are relevant for the study of young and intermediate-age star clusters in the Milky Way disc and the Magellanic Clouds. The initial helium mass fraction follows the enrichment law:  $Y = Y_p + \frac{\Delta Y}{\Delta Z} Z$ , where  $Y_p = 0.2485$  is the primordial He abundance (Komatsu et al., 2011); the helium-to-metal enrichment ratio  $\Delta Y / \Delta Z = 1.78$  is based on the solar calibration in Bressan et al. (2012). More specifically, the corresponding initial He mass fraction is  $Y = 0.256, 0.259, 0.263, 0.267, 0.273, 0.279$ ; and the initial hydrogen abundance  $X = 0.740, 0.735, 0.729, 0.723, 0.713, 0.704$ .

Second, the initial rotation rate is parameterised by  $\omega_i$ : for each set of metallicity above, we compute models with rotation rates going from zero to very near the critical value,  $\omega_i = 0.00, 0.30, 0.60, 0.80, 0.90, 0.95, 0.99$ . The treatment of rotation rate for every single star in terms of mass is described in Sect. 5.2.4.

Third, the convective overshoot: we apply the overshoot from both the convective core and envelope in the calculations as described in Sects. 5.2.2 - 5.2.3.

Lastly, the mass intervals: For convenience, we describe the evolutionary tracks in three mass ranges: (i) VLMSs have initial masses  $M_i \lesssim M_{\text{vlm}}$ , where  $M_{\text{vlm}}$  is the smallest initial mass of a star that is able to ignite helium within the Hubble timescale. Stars with mass smaller than this limit spend their lifetime mainly on the hydrogen-burning phase; (ii) LMSs have initial masses between  $M_{\text{vlm}}$  and  $M_{\text{HeF}}$ , which includes  $M_{\text{O1}}$  and  $M_{\text{O2}}$  as mentioned above; and (iii) IMSs with  $M_i > M_{\text{HeF}}$ .  $M_{\text{HeF}}$  is defined as the transition mass between stars that develop an electron-degenerate core after the MS and hence develop an extended RGB with a He-flash at its tip, and those that do not, hence quietly igniting He-core burning in a non-degenerate core.

Figure 5.1 shows the dependence of  $M_{\text{O1}}$ ,  $M_{\text{O2}}$  and  $M_{\text{HeF}}$  as a function of metallicity, for non-rotating models. We also draw the six metallicities computed in this project. Table 5.1 lists the values of  $\lambda_{\text{ov}}$  and  $\Lambda_e$  adopted for each initial mass. Finally, the database of all stellar evolutionary tracks

Table 5.1: Values of COV and EOv parameters,  $\lambda_{\text{ov}}$  and  $\Lambda_e/H_p$ , respectively, which correspond to each initial mass,  $M_i/M_\odot$ , in six metallicities (Zs). The value of the transition masses,  $M_{\text{vlm}}$ ,  $M_{\text{O1}}$ , and  $M_{\text{O2}}$ , of each metallicity is also noted.

$\lambda_{\text{ov}}$	$\Lambda_e/H_p$	Z= 0.017	Z= 0.014	Z= 0.01	Z= 0.008	Z= 0.006	Z= 0.004	Note
		$M_i/M_\odot$	$M_i/M_\odot$	$M_i/M_\odot$	$M_i/M_\odot$	$M_i/M_\odot$	$M_i/M_\odot$	
0.000	0.000	< 0.80	< 0.80	< 0.75	< 0.75	< 0.70	< 0.70	$M_{\text{vlm}}$
0.000	0.500	< 1.18	< 1.16	< 1.14	< 1.14	< 1.09	< 1.06	
0.000	0.500	1.18	1.16	1.14	1.14	1.09	1.06	$M_{\text{O1}}$
0.027	0.513	1.20	1.18	1.16	1.16	1.11	1.08	
0.053	0.527	1.22	1.20	1.18	1.18	1.13	1.10	
0.080	0.540	1.24	1.22	1.20	1.20	1.15	1.12	
0.107	0.553	1.26	1.24	1.22	1.22	1.17	1.14	
0.133	0.567	1.28	1.26	1.24	1.24	1.19	1.16	
0.160	0.580	1.30	1.28	1.26	1.26	1.21	1.18	
0.187	0.593	1.32	1.30	1.28	1.28	1.23	1.20	
0.213	0.607	1.34	1.32	1.30	1.30	1.25	1.22	
0.240	0.620	1.36	1.34	1.32	1.32	1.27	1.24	
0.267	0.633	1.38	1.36	1.34	1.34	1.29	1.26	$M_{\text{O2}}$
0.293	0.647	1.40	1.38	1.36	1.36	1.31	1.28	
0.320	0.660	1.42	1.40	1.38	1.38	1.33	1.30	
0.347	0.673	1.44	1.42	1.40	1.40	1.35	1.32	
0.373	0.687	1.46	1.44	1.42	1.42	1.37	1.34	
0.400	0.700	1.48	1.46	1.44	1.44	1.39	1.36	
0.400	0.700	> 1.48	> 1.46	> 1.44	> 1.44	> 1.39	> 1.36	

that we produced in this work is available at <sup>3</sup>.

### 5.3.1 Very-low-mass stars

The PARSEC models for VLMSs ( $0.09 M_\odot \leq M_i \lesssim M_{\text{vlm}}$ ) were described in [Chen et al. \(2014\)](#) and successfully calibrated against the mass-radius relation of a sample of eclipsing binaries. For this purpose, the authors slightly modified the  $T - \tau$  relations provided by PHOENIX (BT-Settl) atmosphere models (see [Asplund et al., 2009](#); [Allard et al., 2012](#)). After this calibration, the corresponding isochrones were able to reproduce well the very low ZAMS of old globular clusters NGC 6397 and 47 Tuc, and of the open clusters M67 and Praesepe. These models were also adopted to fit *Gaia* DR2 CMD diagrams ([Gaia Collaboration, 2018a](#)). Here, we continue to use these very low-mass evolutionary tracks, referring to [Chen et al. \(2014\)](#) for all details.

<sup>3</sup><http://stev.oapd.inaf.it/PARSEC>



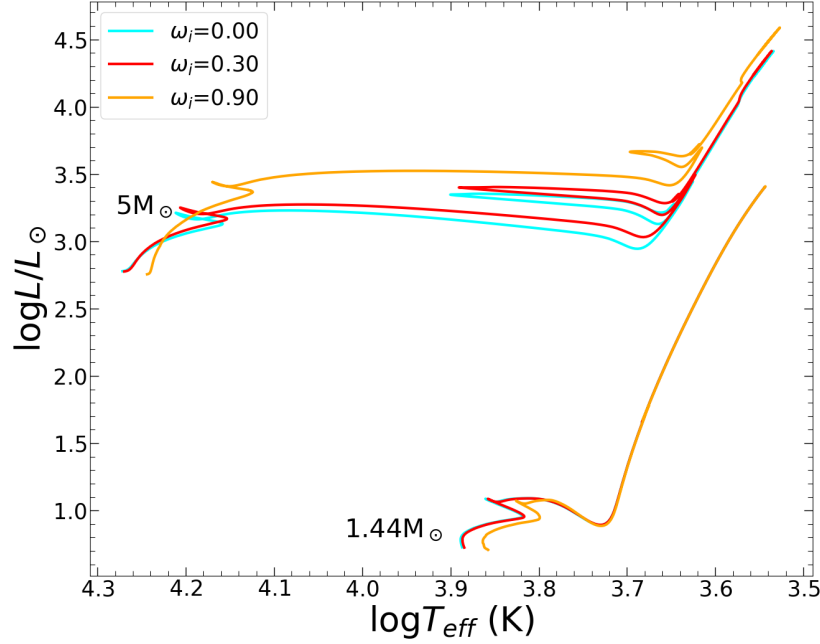


Figure 5.2: HRD of stars with initial masses of  $1.44 M_{\odot}$  and  $5 M_{\odot}$  with the composition  $Z = 0.008$ ,  $Y = 0.263$  for initial rotation rates  $\omega_i = 0.00$ ,  $0.30$ , and  $0.90$  (cyan, red, and orange lines, respectively). We do not plot the evolution of the PMS phase, for sake of clarity.

### 5.3.2 Low-mass stars

#### From the PMS to the tip of the RGB

We computed models of LMSs with initial masses in the interval from  $M_{\text{vlm}}$  to  $M_{\text{HeF}}$ . The mass step is  $0.05 M_{\odot}$  in the mass range from  $M_{\text{vlm}}$  to  $0.8 M_{\odot}$ ,  $0.02 M_{\odot}$  for the range from  $0.8 M_{\odot}$  to  $M_{\text{O2}}$ , and  $0.1 M_{\odot}$  for masses above  $M_{\text{O2}}$ . All the LMSs tracks begin from the PMS phase and end at the TRGB, where the star ignites its central He under strongly degenerate conditions (the so-called He flash).

Figure 5.2 shows the Hertzsprung-Russell diagram (HRD) of  $1.44 M_{\odot}$  stars with different initial rotation rates. It should be noted that, for rotating stars,  $T_{\text{eff}}$  is actually an average value over the isobaric surface; more

precisely it is the value that a non-rotating star with the same ‘volumetric radius’ would have to produce the same total luminosity. The volumetric radius is defined as the radius of a sphere with the same volume as that of a rotating star. The local effective temperature characterising different points at the surface of the star, instead, is a quantity that varies along the co-latitude angle ( $\theta = 0^\circ$  aligns with the rotation axis), becoming cooler towards the equator. This can be explained by the proportionality between  $T_{\text{eff}}^4$  and effective gravity  $g_{\text{eff}}$ , based on von Zeipel’s theorem (von Zeipel, 1924b; Espinosa Lara and Rieutord, 2007). In turn, the local effective gravity is reduced by the centrifugal force, which is higher for a higher rotation rate. Therefore, as we see in Fig. 5.2, the higher the rotation rate, the cooler the star is (by means of the average value) during the MS. In the post-MS phases, the conservation of angular momentum forces the surface angular velocity to drop down when the star expands, hence causing the star to evolve along the same path as non-rotating stars.

Another effect of rotation is that the faster the stars rotate, the longer they stay in the MS phase (Eggenberger et al., 2010; Ekström et al., 2012; Costa et al., 2019a). Fig. 5.3 shows the ratio of the MS duration between models with different  $\omega_i$  and their standard non-rotating counterparts,  $\omega_i = 0$ , as a function of the initial mass  $M_i$  and for  $Z = 0.01$ . We see that this ratio is higher than 1 for all rotating models and becomes higher as  $\omega_i$  increases. In the low-mass range ( $M \lesssim 1.8 M_\odot$ ) the ratio remains modest, while it increases significantly in the domain of intermediate-mass and massive stars. This is understandable because of the lower efficiency of rotational mixing in LMSs with respect to intermediate and massive ones, as will be discussed later in Sect. 5.3.3.

We also find that in the low-mass range, the size of the convective core does not depend significantly on  $\omega_i$ . This can be seen in Fig. 5.4 for the models of  $M_i = 1.44 M_\odot$  and  $Z = 0.017$ .

After the formation of the H-exhausted core, the star enters into the sub-giant phase and then ascends the RGB. Expansion of the envelope leads to a decrease in surface rotation velocity. This impact is illustrated in Fig. 5.5, where the equatorial tangential velocity drastically decreases after leaving the MS. The drop-down on rotation rate results in evolution as a non-rotating star, as already mentioned and as illustrated in the HRD of Fig. 5.2. We found that the luminosity at the TRGB phase is almost the same for any applied rotational rates (see also Ekström et al., 2012; Georgy et al., 2013).

For instance, the TRGB luminosity of the  $Z=0.004$ ,  $M_i = 1.36 M_\odot$  star

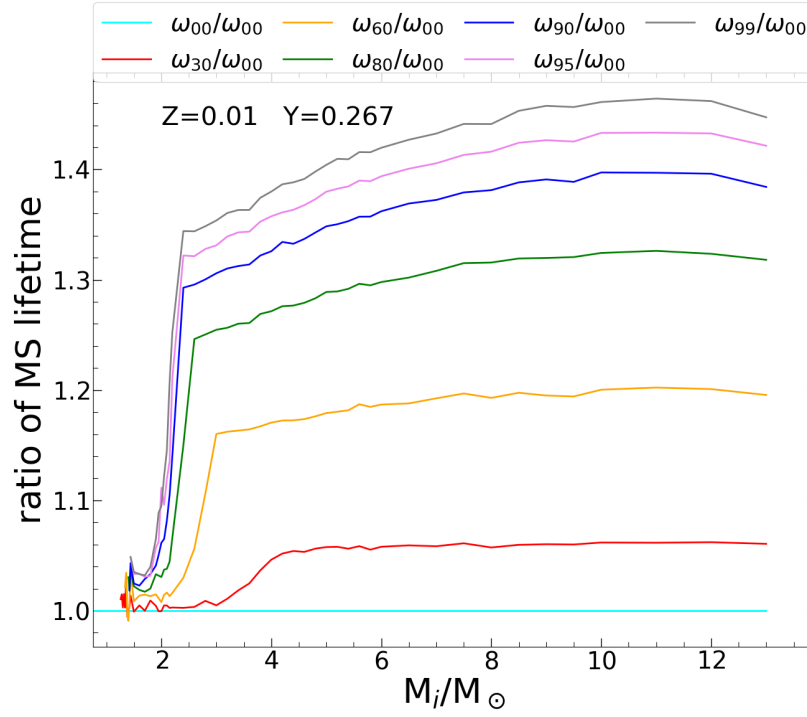


Figure 5.3: Ratio between the MS lifetimes of rotating and non-rotating models of the same mass, as a function of initial mass in the set  $Z = 0.01$ ,  $Y = 0.267$ . This lifetime is measured from the ZAMS until the exhaustion of the central H ( $X_c < 10^{-5}$ ). Different values of  $\omega_i$ , from 0 to 0.99, are considered, as indicated in the legend.

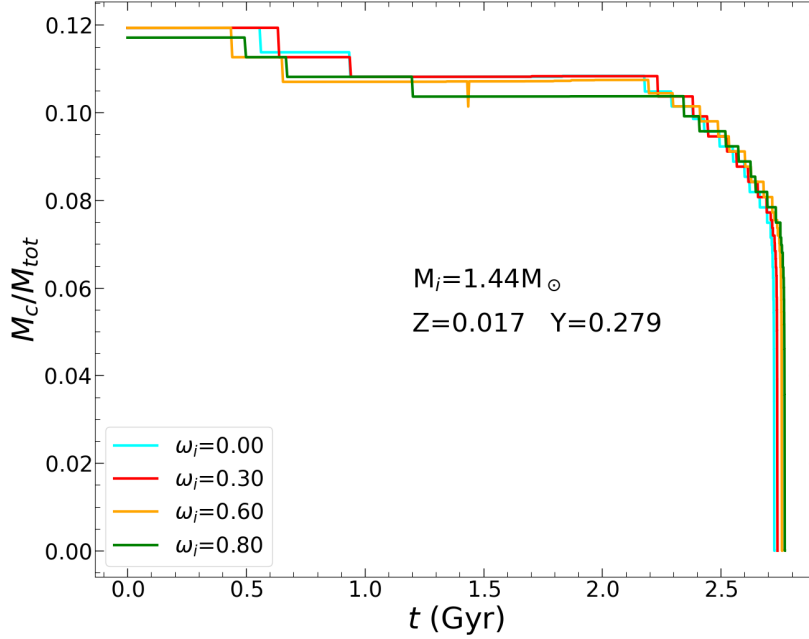


Figure 5.4: Time evolution of the mass of the convective core ( $M_c/M_{\text{tot}}$ ) during the H-burning phase for the model of  $M_i = 1.44 M_\odot$  and  $Z = 0.017$ .

is  $\log L/L_\odot = 3.38771$ ,  $3.38934$  and  $3.38919$  for the models with  $\omega_i = 0.00$ ,  $0.60$  and  $0.90$ , respectively. We see that the difference is less than  $0.0016$  dex in any case, and this is due to the slightly heavier He-core mass discussed above. In general, we found that the TRGB luminosity of our models with  $M \leq 1.5 M_\odot$  is about  $\log L/L_\odot \sim 3.385 - 3.420$ , depending on the initial metallicity. This result is important in the context of the TRGB method of distance determinations, and the recent ‘tension’ in the values of the Hubble constant  $H_0$  (see [Freedman et al., 2019, 2020](#), and references therein for more details).

On the other hand, we also checked the effect of rotation on the mass-loss rate. Fig. 5.6 shows the mass-loss rate of the  $1.39 M_\odot$  model with metallicity  $Z = 0.006$ , for three initial rotation rates,  $\omega_i = 0.00$ ,  $0.30$  and  $0.95$ . We plot  $\log \dot{M}$  from the ZAMS to the end of the RGB. As expected from equation (5.7), during the MS phase the star with higher rotation rates

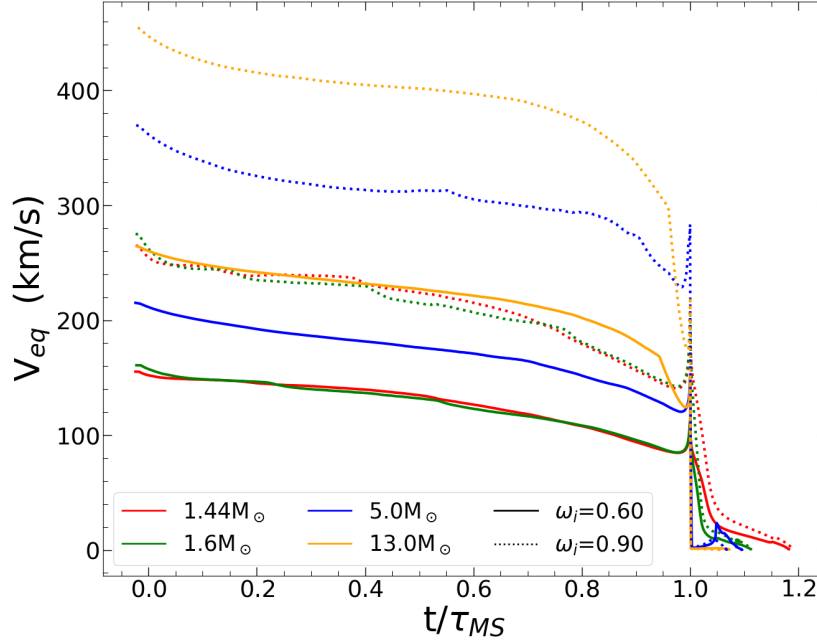


Figure 5.5: Evolution of surface tangential velocity at the equator,  $V_{eq}$ , versus the time,  $t$ , scaled to the MS duration,  $\tau_{MS}$ . The four selected mass models – 1.44  $M_{\odot}$  (red), 1.6  $M_{\odot}$  (green), 5  $M_{\odot}$  (blue), and 13  $M_{\odot}$  (orange) – are shown, with two initial rotation rates –  $\omega_i = 0.60$  (solid line) and  $\omega_i = 0.90$  (dotted line) – from the set with  $Z = 0.014$ ,  $Y = 0.273$ .

has higher mass-loss rates. However, in the RGB phase, because of the decline of the surface rotational velocity, it evolves as a non-rotating star but with a slightly older age. In general, stars lose their mass at a rate of about  $(0.6 - 6) \times 10^{-8} M_{\odot}/\text{yr}$  at the TRGB stage. This result is based on the Reimers law that we adopted in our models. Interesting alternative models for mass loss have been proposed (Cranmer et al., 2007; Cranmer and Saar, 2011), which will be the subject of other subsequent work. We note that during the stellar contraction phase just after the end of the MS, the tangential velocity may reach its critical value, at least for models with the highest initial rotation rates. This is the case for the model with  $\omega_i = 0.95$  shown in Fig. 5.6. In this case, the mass loss as provided by equation (5.7),

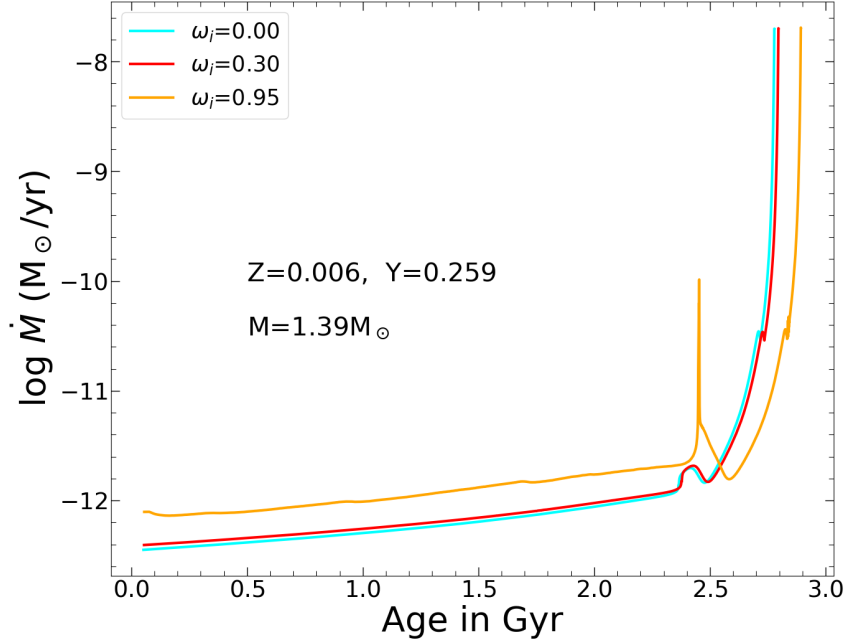


Figure 5.6: Mass-loss rate as a function of time of star  $M_i = 1.39 M_\odot$ ,  $Z = 0.006$  for three rotation rates,  $\omega_i = 0.00$ ,  $0.30$ , and  $0.95$  (cyan, red, and orange lines, respectively).

is enhanced by mechanical effects (Georgy et al., 2013; Costa et al., 2019a) as shown by the relative peak of about two orders of magnitude with respect to the other tracks, before entering the RGB phase.

Concerning the total mass lost on the RGB, we find that it is higher for the smaller initial masses. For non-rotating models of  $Z = 0.004$ , the stars with initial masses  $M_i = 0.9 M_\odot$ ,  $1.16 M_\odot$  and  $1.36 M_\odot$  lose about 11%, 6% and 4% of their initial mass, respectively. The total mass lost by the stars at the TRGB is illustrated in Fig. 5.7 for all six sets of metallicity and for two initial rotation rates,  $\omega_i = 0.00$  and  $0.95$  (the solid- and dashed-lines, respectively). From this figure, we also see that the key role in the total mass lost by the stars is taken, in decreasing order, by mass, metallicity, and rotation.

Figure 5.8 shows the difference in He-core mass at the TRGB between

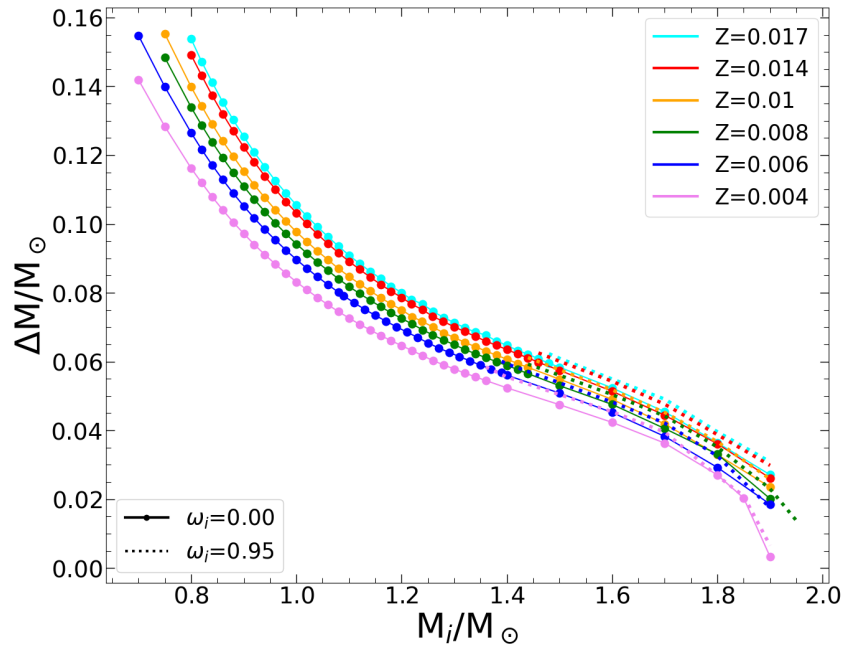


Figure 5.7: Total mass lost until the TRGB versus initial mass for six different metallicity sets. Solid and dashed lines represent models with  $\omega_i = 0.00$  and  $\omega_i = 0.95$ , respectively.

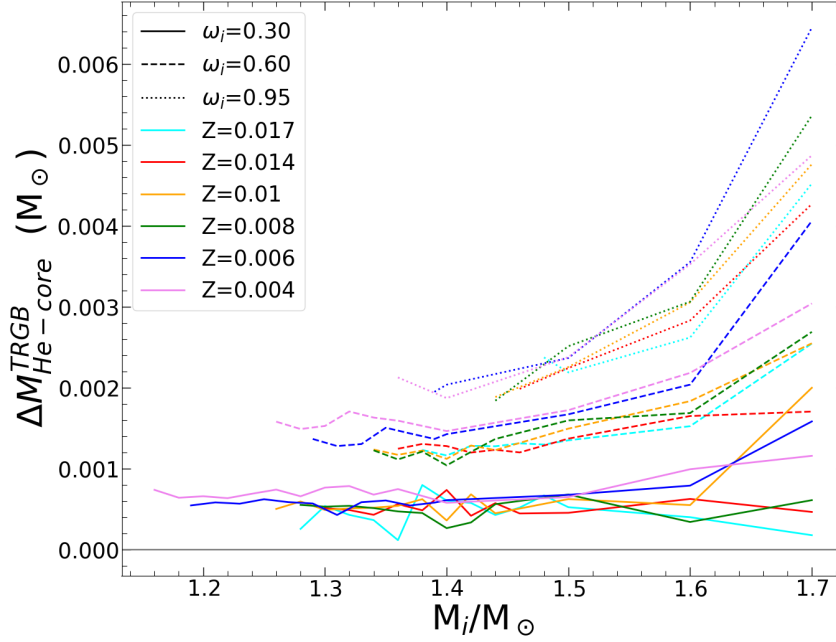


Figure 5.8: Difference in He-core mass at the TRGB phase between the rotating models and their non-rotating counterparts,  $\Delta M_{\text{He-core}}^{\text{TRGB}}$ . Three initial rotating rates are considered:  $\omega_i = 0.30, 0.60, 0.95$  (solid, dashed, and dotted line, respectively). The colours represent different initial metallicities. The solid grey line marks the reference line for  $\omega_i = 0$  models.

rotating models and their non-rotating counterparts, for three values of  $\omega_i = 0.30, 0.60, 0.95$  and for six metallicities. The higher the initial rotation rate, the larger the He-core mass the star has at the tip, at any metallicity. While the surface rotation at this stage is small even for the largest  $\omega_i$ , in the core it is still significant, as can be seen in Fig. 5.9. The larger the rotation, the less concentrated the core is, and a larger core mass is needed to reach the conditions for He ignition. At the larger initial masses, there is also a contribution of the more efficient rotational mixing during the MS phase. In general, the difference is  $\leq 0.006 M_\odot$ , depending on  $\omega_i$ . We note that these differences might affect the location of red clump stars in the HRD. This issue will be further investigated in a subsequent work.



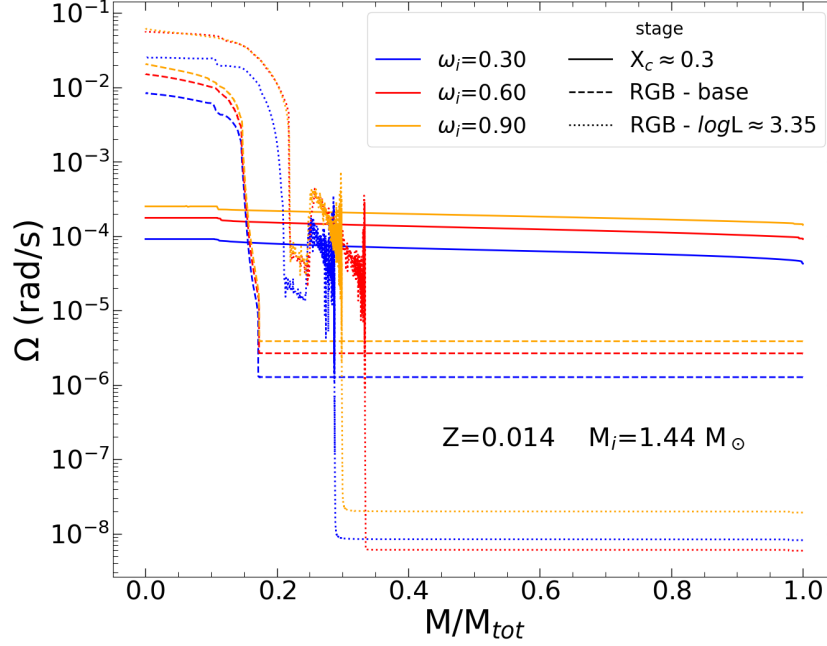


Figure 5.9: Internal distribution of angular velocity,  $\Omega$ . Three selected stages of models with  $Z = 0.014$ ,  $M_i = 1.44 M_\odot$  are presented: at which the central hydrogen  $X_c \approx 0.3$  during the MS (solid lines), at the base of the RGB phase (dashed lines), and near the TRGB with  $\log L \approx 3.35$  (dotted lines). The colours represent different selected initial rotation models.

### From the ZAHB to the TP-AGB

Low-mass stars develop an electron-degenerate core and climb the RGB until they undergo the He flash. The latter requires large amounts of CPU times to be computed in detail (see [Kippenhahn et al., 2012](#); [Mocák et al., 2008](#), for more details). Therefore, the computation of the evolutionary track is interrupted during the He-flash and restarted from a ZAHB model with the same He-core mass and surface chemical composition as the last RGB model. The initial ZAHB model is built following the method described in [Bressan et al. \(2012\)](#), taking into account the fraction of He that has been burned into carbon during the flash so that the degenerate core is lifted into a non-degenerate state. Then, the star is evolved along the horizontal branch and

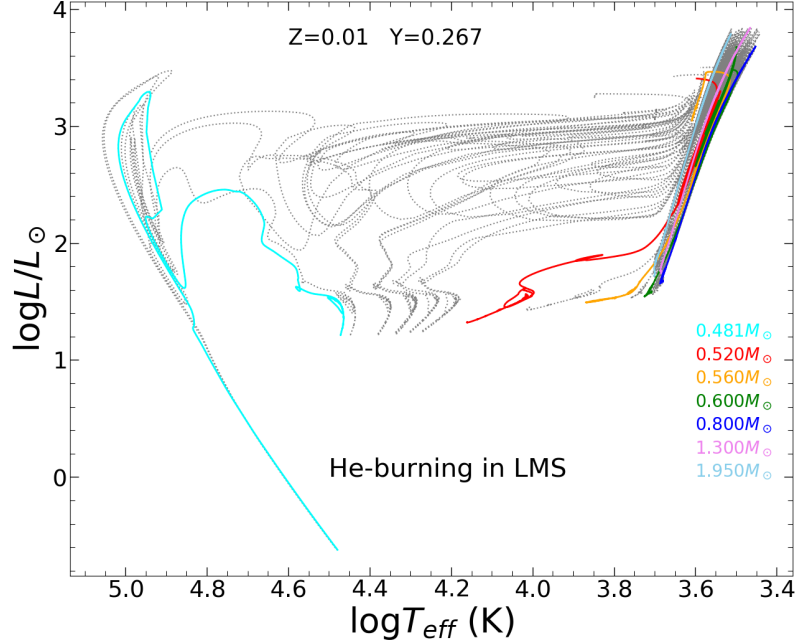


Figure 5.10: He-burning phase of LMSs in the set with  $Z = 0.01$ ,  $Y = 0.267$ . Tracks with ZAHB masses between  $0.481$  and  $1.95 M_{\odot}$  were computed in this case. A few of these tracks are marked with a different colour (with their mass in  $M_{\odot}$  indicated in the legend) for reference.

the evolution is terminated again after it experiences a few pulses of the TP-AGB phase. The evolutionary tracks in the HRD during the post-ZAHB phases of LMS are illustrated in Fig. 5.10, just for a single set of metallicity. Similar grids are available for all metallicities.

It is important to point out a few details in these calculations. First, rotation is turned off for the entire evolution beyond the ZAHB, simply because at those stages the rotational velocities have become small enough to not imply significant evolutionary effects.

Second, with respect to the previous version of PARSEC, the new tracks include mass loss starting from the ZAMS. Thus, for any given initial metallicity, we have different relations  $M_{\text{TRGB}}(M_i)$  for different  $\omega_i$ . These relations are merged to obtain a complete unique sequence of  $M_{\text{ZAHB}}(M_i)$ , with  $M_{\text{ZAHB}}^i$

spanning the range from the largest  $M_{\text{TRGB}}$  to the lowest value compatible with the thinnest envelope mass along the ZAHB sequence. We also pay attention to carefully sample the mass interval close to  $M_{\text{HeF}}$ . We then interpolate on the sequence of non-rotating models to obtain a unique complete  $M_{\text{core}}(M_{\text{ZAHB}}^i)$  relation, which is used to construct the ZAHB model sequence.

### 5.3.3 Intermediate-mass and massive stars

Intermediate-mass stars are defined as having masses larger than the  $M_{\text{HeF}}$  limit and smaller than the  $M_{\text{up}}$  threshold for C ignition in the core. Both limits depend on the initial metallicity and the rotation rate. Massive stars are computed up to  $14 M_{\odot}$ , leaving more massive stars to a dedicated paper, which is in preparation. Models with initial masses between  $M_{\text{HeF}}$  and  $2.2 M_{\odot}$  are computed with a mass step  $\Delta M_i = 0.05 M_{\odot}$ ; from  $2.2 M_{\odot}$  up to  $6 M_{\odot}$ ,  $\Delta M_i = 0.2 M_{\odot}$ ; up to  $10 M_{\odot}$ ,  $\Delta M_i = 0.5 M_{\odot}$  and  $\Delta M_i = 1 M_{\odot}$  above  $M_i = 10 M_{\odot}$ . All these tracks start on the PMS phase and are interrupted either after the first few thermal pulses along the AGB or after the ignition of carbon in the core. All evolutionary tracks in this mass range have been computed with the maximum overshooting efficiency, (i.e. with  $\lambda_{\text{ov}} = 0.4$  and  $\Lambda_e = 0.7 H_P$ ) and for all initial rotation rates from  $\omega_i = 0.00$  to  $0.99$  (Sect. 5.2.4). The mass-loss rates of rotating stars follow the description in Sect. 5.2.6, while the formulation of [de Jager et al. \(1988\)](#) was adopted for non-rotating models.

In Figure 5.2 we have already compared the evolution of a  $5 M_{\odot}$  model calculated with three different rotation rates,  $\omega_i = 0.0, 0.30, 0.90$ , with that of a  $1.44 M_{\odot}$  model with the same  $\omega_i$ . Rotation impacts the evolution of IMSs in a way different from the LMSs. At the beginning of the evolution, only the geometrical effects of rotation are visible: in both cases, the models that rotate faster are less luminous and cooler. As evolution proceeds, IMSs develop a convective core surrounded by a radiative envelope where the meridional circulation works efficiently. As a result, rotational mixing provides more fresh fuel to the central core, and hence a more massive core is built up (see Fig. 5.11). This causes the IMSs models that rotate faster to become more luminous and to increase their MS lifetimes significantly (as shown in Fig. 5.3). Due to the larger core masses, the higher luminosity is maintained during all post-MS evolutionary phases. In contrast, in low-mass models even in the case with the largest rotation rate, the growth of the core is never so high to make it more luminous than the non-rotating one. At

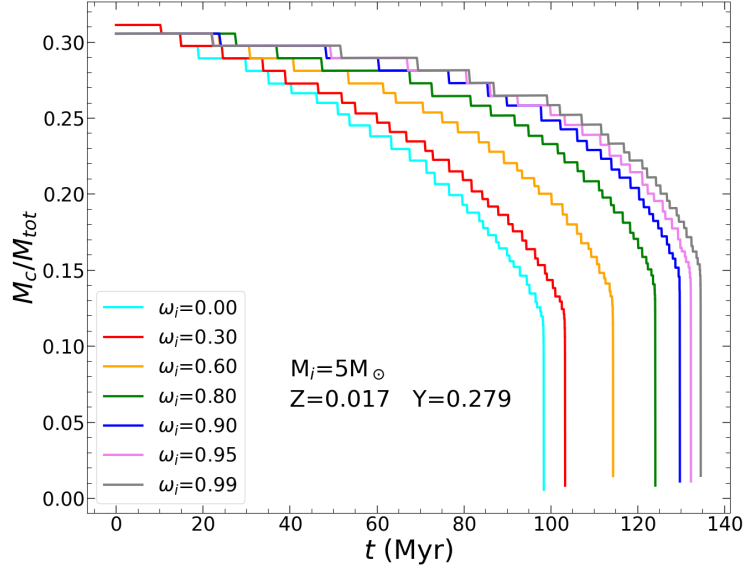


Figure 5.11: Evolution of the mass of the convective core ( $M_c/M_{tot}$ ) during the H-burning phase for the model of  $M_i = 5.0M_\odot$  and  $Z = 0.017$ .

lower masses, rotation affects the effective temperature more than the luminosity.

Another consequence of rotational mixing during the MS phase is the transport of nuclear-burned products from the central region to the surface. This effect does not occur in non-rotating stars until dredge-up events occur when the stars become red giants. In rotating stars, instead, significant mixing can occur at much earlier stages. The most evident effect of this mixing is an enhancement in the surface nitrogen and helium, followed by a depletion of both oxygen and carbon. Fig. 5.12 shows the evolution of He, C, N, O abundance, luminosity, effective temperature, and  $\omega$ , in three stars of mass  $3 M_\odot$ ,  $5 M_\odot$ , and  $9 M_\odot$ , for several initial rotation rates. The faster the star rotates on the MS, the more N and He appear at the surface, and the more C and O are depleted. The increase (decrease) in surface abundances develops gradually during the MS but suddenly jumps up (down) during the first dredge-up event that occurs after the end of the MS, when the star becomes a red giant. Afterward, rotational mixing is no longer efficient,

and the surface abundances remain constant until, eventually, the advent of the second dredge-up, which affects higher-mass IMSs, after the core-helium burning phase.

As can be seen in Figs. 5.2 and 5.12, the increased rotation rates on the MS also reduce the extension (in  $T_{\text{eff}}$ ) of the blue loop during the central He-burning phase. This is also an effect of the enhanced mixing caused by rotation (see the discussion of Costa et al., 2019a, and references therein).

The transition between LMSs and IMSs is set at a mass  $M_{\text{HeF}}$ , above which He ignition takes place quietly in a non-degenerate core. Fig. 5.14 shows the value of  $M_{\text{HeF}}$  as a function of initial rotation rates for the six metallicities computed in this project. The plot has a resolution of  $0.05 M_{\odot}$ , which is the mass separation between successive tracks computed around this mass range. First, lines of different colours illustrate the well-known dependence of  $M_{\text{HeF}}$  on the initial metallicity. Second, the dependence of  $M_{\text{HeF}}$  on the initial rotation rate. For instance, the  $Z = 0.004$  models have  $M_{\text{HeF}}$  values of either  $1.85 M_{\odot}$  or  $1.90 M_{\odot}$ , while those with  $Z = 0.017$  the values of  $2.00$  or  $2.05 M_{\odot}$ . We find that at increasing rotation rates, the value of  $M_{\text{HeF}}$  also tends to increase with respect to the non-rotating models. However, when the initial rotation rate increases to values close to the critical breakup velocity,  $M_{\text{HeF}}$  declines again, returning to the value of non-rotating stars. This behaviour of  $M_{\text{HeF}}$  cannot be discussed in much detail because all changes occur within the mass separation step of  $0.05 M_{\odot}$ . However, it is remarkable that rotation appears to have a limited impact on  $M_{\text{HeF}}$ .

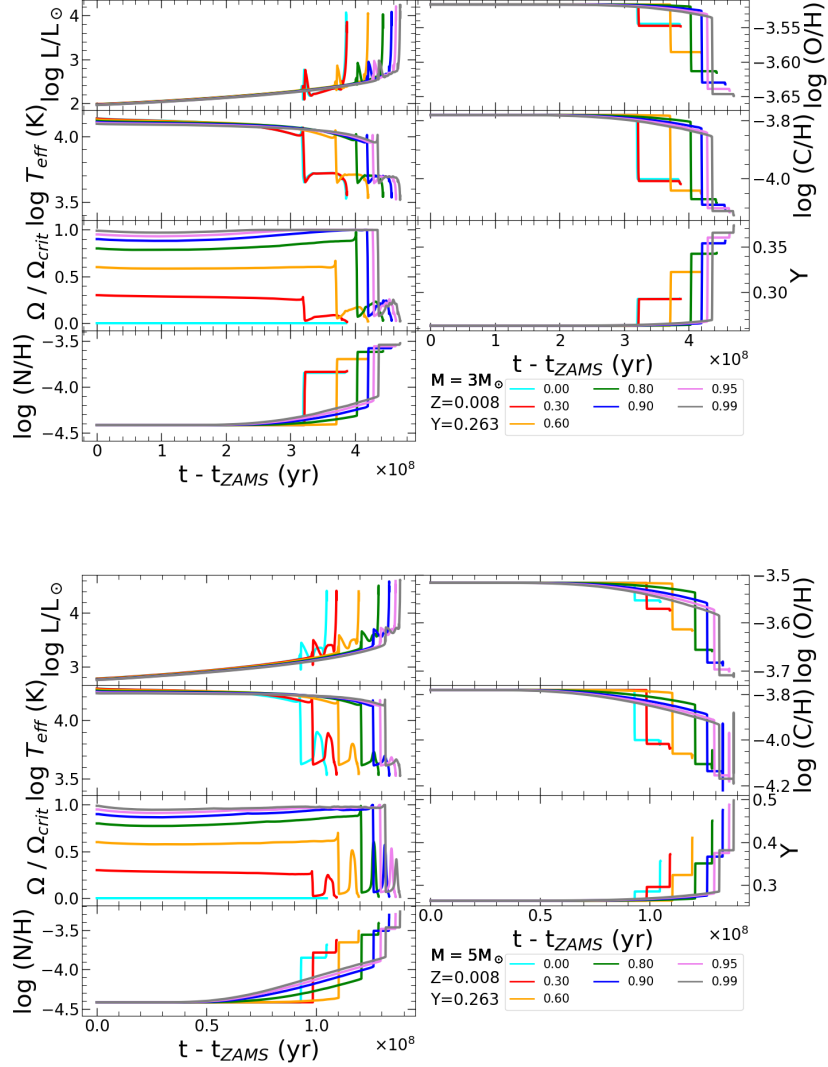


Figure 5.12: Evolution of  $\log L$ ,  $\log T_{\text{eff}}$ , rotation rate,  $\omega$ , and surface abundances of N, C, O, and He at the surface for many initial rotation rates from  $\omega_i = 0.00$  to  $0.99$  (from cyan to grey colours, respectively), for the cases of 3 and  $5 M_{\odot}$  stars (in the three sets of panels from top to bottom, respectively) with  $Z = 0.008$ ,  $Y = 0.263$ . The abundances of N, O, and C are by number and relative to the hydrogen abundance. For He, instead, we present the surface mass fraction  $Y$ .

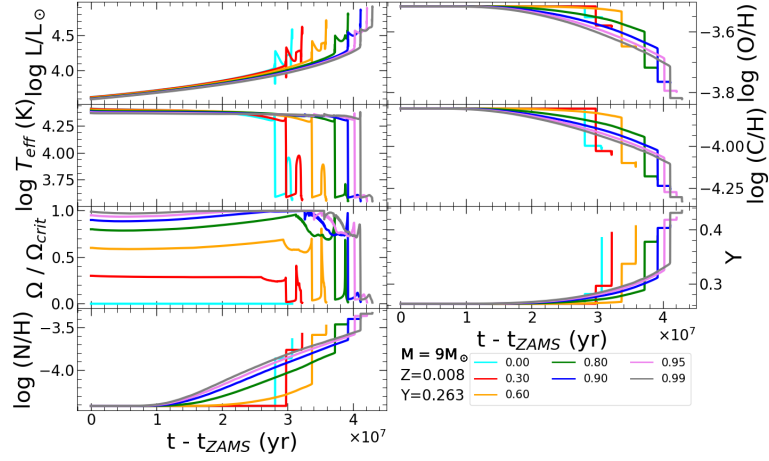


Figure 5.13: As in Figure. 5.12 but for the case of  $9M_{\odot}$  stars.

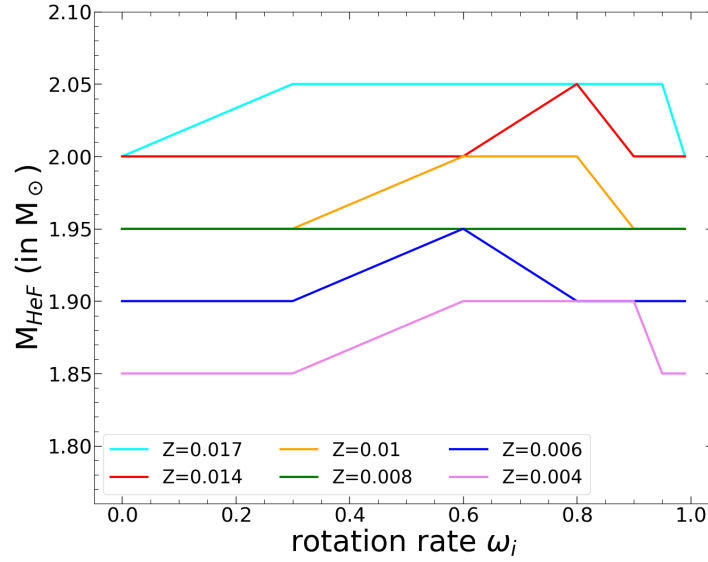


Figure 5.14: Maximum mass at which the star burns He in the central region under a strongly degenerative condition,  $M_{\text{HeF}}$ , versus the initial rotation rates. The colour refers to six computed metallicities in this work, as indicated in the legend.

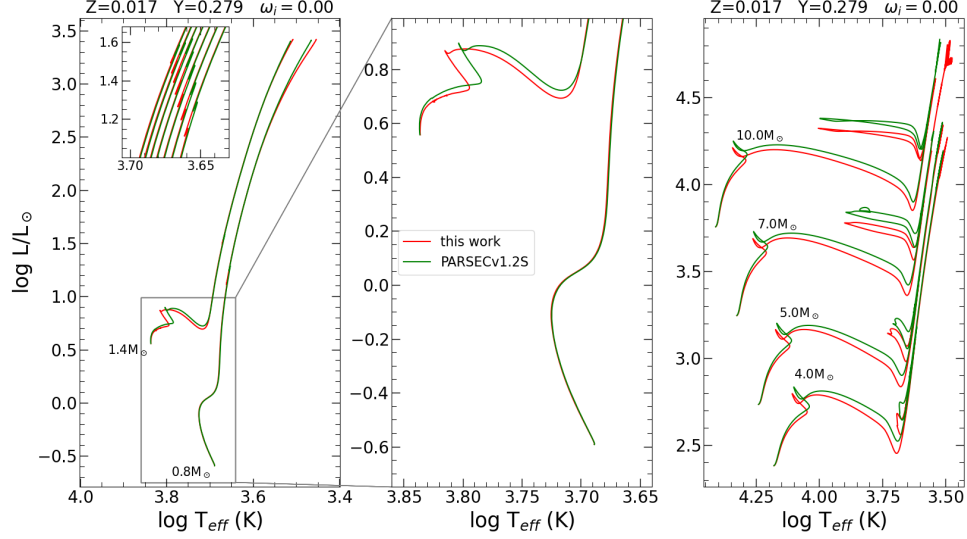


Figure 5.15: HRD comparing tracks between PARSEC v2.0 (this work, red lines) and the previous version (PARSEC v1.2S, green lines) for non-rotating stars of  $Z = 0.017$  and  $Y = 0.279$ . The left-hand panel shows the HRD of two LMSs with  $0.8$  and  $1.4 M_{\odot}$ . Their PMS phase is not shown, because it is essentially the same in the two versions. The inset details the region around the RGBB for tracks in the mass range  $0.8$  to  $1.4 M_{\odot}$  with a step of  $0.1 M_{\odot}$ . The middle panel zooms into the MS regions of the  $0.8$  and  $1.4 M_{\odot}$  tracks. The right panel instead compares intermediate-mass models for four different masses, as indicated.

## 5.4 Comparison with parsec V1.2S and other databases

In Figure 5.15 we show a comparison between the selected tracks calculated with the new version of the code, PARSEC V2.0, hereafter PS2, and with the older version, V1.2S, hereafter PS1. In both versions, we use the same initial chemical composition. In the leftmost panel, we show the case of a LMS with  $M_i = 0.8 M_{\odot}$ . Since this star does not possess a convective core during the H-burning phase, the HRD is the same for the two versions.

Instead, we recall that during the RGB evolution in the older version,



PS1, overshooting at the bottom of the convective envelope has not been considered in the mass range ( $\leq M_{O1}$ ), producing RGBBs that were too luminous with respect to the observed ones (Fu et al., 2018). To cope with this evident discrepancy, in the new version PS2, we include EOv in LMSs as described in Sects. 5.2.2 - 5.2.3. The effect of adding an extra mixing at the bottom of the convective envelope is highlighted in the inset of the left panel in Fig. 5.15, where the RGBBs of stars with masses  $0.8 M_{\odot} \leq M_i \leq 1.4 M_{\odot}$ , are shown.

However, in the mass range where stars develop a convective core in the MS (as in the case of  $M_i = 1.4 M_{\odot}$ ), COv and EOv are fully considered in both versions of the PARSEC code. In PS2, we adopt a smaller value of the maximum COv parameter  $\lambda_{ov,max} = 0.4$ , instead of the  $\lambda_{ov,max} = 0.5$  in PS1. Furthermore, in PS2 we adopt a diffusive treatment for convective mixing, where the diffusion equations are coupled with the nuclear reaction rates for all elements in the turbulent regions. In the PS1 version, the convective zones are ‘instantaneously’ homogenised at every time step. These differences already affect the MS phase of stars with convective cores (with  $M_i > M_{O1}$ ), as shown in the middle panel in Fig. 5.15. The PS2 track with  $1.4 M_{\odot}$  presents a hotter and slightly fainter MS phase, and a fainter sub-giant phase.

On the other hand, the RGB phase has the same slope in both versions of PARSEC tracks. The new tracks show a brighter and cooler TRGB. These differences in the TRGB are caused by the more massive He-core and the more extended envelope at the tip. This is mainly due to the different overshoot parameters used in PS2 and the fact that in this new calculation mass loss was implemented along the evolution while, in PS1, models were evolved at constant mass, and mass loss was applied at the stage of isochrone calculation only.

In Fig. 5.16 we compare the luminosity at the TRGB of the PS2 models with that of PS1, Bag of Stellar Tracks and Isochrones (BaSTI; Hidalgo et al. 2018), and MESA Isochrones and Stellar Tracks (MIST; Choi et al. 2016) evolutionary tracks. The latter two databases also include convective overshooting and diffusion in their models. We can see that PS2 predicts a quite constant TRGB luminosity and, generally, above the luminosity of other models shown in the plot. The difference between the new and old versions of PARSEC is about  $\sim 0.01 - 0.02$  dex. BaSTI gives an increased trend of TRGB luminosity with initial masses, which is in contrast with the trend from MIST. The PS2 TRGBs are  $\sim 0.04$  dex brighter than MIST.

The right-hand panel of Figure 5.15 shows the comparison between non-

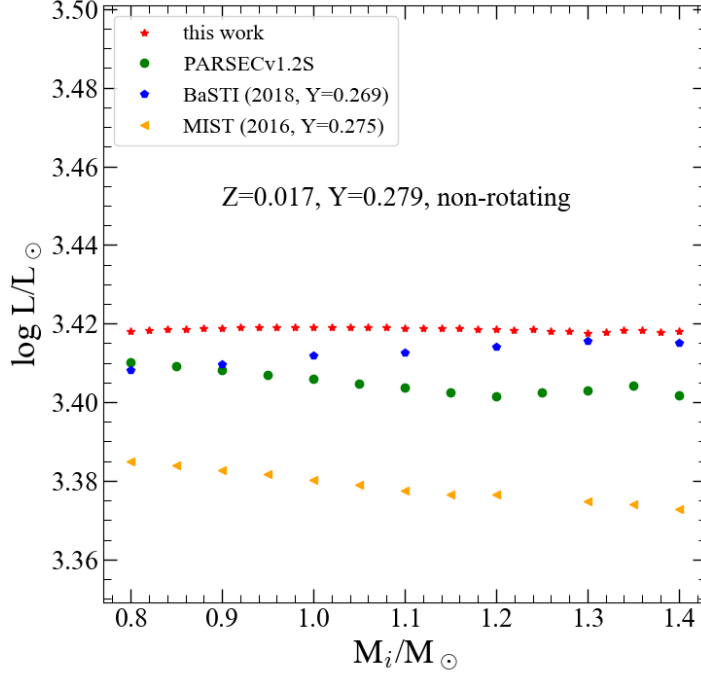


Figure 5.16: Luminosity at the TRGB as a function of initial mass for the tracks produced in this work (with  $\omega_i = 0$ ; red stars), in parsec v1.2S (green circles), and BaSTI (blue pentagons). The BaSTI tracks for a solar-scaled composition are taken from [Hidalgo et al. \(2018\)](#) with  $Z = 0.01721$ ,  $Y = 0.2695$ .

rotating models of IMSs of the two PARSEC code versions. In this case, the impact of the COV parameter is clear. The difference between PS1 and PS2’s tracks starts from the MS and continues up to the He-burning phase. In particular, the new tracks are less luminous than the previous ones, due to their smaller  $\lambda_{\text{ov,max}}$  value.

Recently, [Amard et al. \(2019\)](#) published grids of STAREVOL models in which rotation is included for masses from  $0.2 M_\odot$  to  $1.5 M_\odot$ . STAREVOL tracks are provided for three values of initial rotation rates,  $\omega_i = 0.20, 0.40$ , and  $0.60$ , while in this work we provide  $\omega_i = 0.30, 0.60, 0.80, 0.90, 0.95, 0.99$ . To facilitate the comparison, we perform a few PARSEC V2.0 calculations

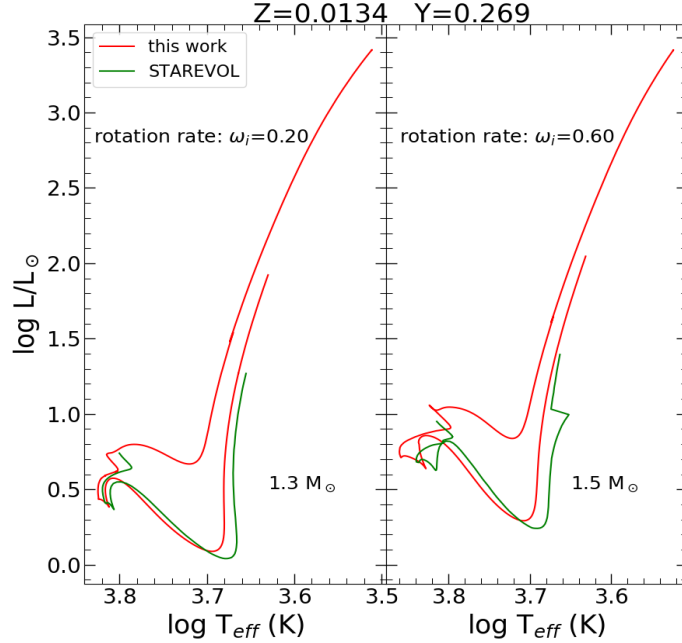


Figure 5.17: Comparison on HRD of rotating tracks between this work (red lines) and STAREVOL (green lines) with the same  $Z = 0.0134$  and  $Y = 0.269$ . Left-hand panel: Slow-rotating tracks with a  $\omega_i = 0.20$  and  $1.3 M_{\odot}$  star. Right-hand panel: Same as the left panel but with  $\omega_i = 0.60$  and  $M_i = 1.5 M_{\odot}$ .

with exactly the same initial composition ( $Z = 0.0134$  and  $Y = 0.269$ ) and the same initial rotation rate as STAREVOL. Fig. 5.17 compares the models of  $1.3 M_{\odot}$  and  $1.5 M_{\odot}$  produced by both PARSEC v2.0 (red line) and STAREVOL (green line). The differences between our and STAREVOL models are significant. First, the STAREVOL tracks evolve until the end of the MS phase, while our tracks extend up to the He flash. Second, for the same initial mass, rotation rate, and composition, our MS stars are hotter and brighter. This might be explained by the many differences in the input physical parameters between the two codes. For example, [Amard et al. \(2019\)](#) do not include overshooting in their calculations, while we consider it for both the convective core and the envelope. Third, there are differences in the implementation of rotation in each code, namely, STAREVOL implements

rotation from the PMS while we assign the rotation (and let it evolve) just before the ZAMS. It is also worth mentioning that there are other differences between the two codes; for example, they adopt the mixing-length parameter  $\alpha_{\text{MLT}} = 1.973$  and the nuclear reaction rates from the NACRE II database (Xu et al., 2013).

However, despite the differences listed above, the two codes give similar ages at the terminal-age-MS (TAMS). For instance, for the  $1.3 M_{\odot}$  star with  $\omega_i = 0.2$  PS2 gives 3.74 Gyr while STAREVOL gives 3.94 Gyr.

Another similarity is in the mass-loss rates: at the TAMS, the  $1.5 M_{\odot}$  star with  $\omega_i = 0.6$  loses its mass with a rate of  $\log \dot{M} = -11.70$  ( $M_{\odot}/\text{yr}$ ) in PS2 while STAREVOL gives  $\log \dot{M} = -11.62$  ( $M_{\odot}/\text{yr}$ ), even though the codes use different schemes for the mass-loss rate. In particular, we use the enhanced formula from the Reimers law with  $\eta = 0.2$  for rotating stars while STAREVOL uses the recipe of Cranmer and Saar (2011). However, we should note that at these early stages, mass loss does not play a crucial role yet.

## Chapter 6

# PARSEC V2.0: Isochrones with rotation

The main aim of this chapter is to present the isochrones of the corresponding stellar tracks that we computed and presented in Chapter. 5. This is the second part of the paper [Nguyen et al. \(2022\)](#). For producing isochrones, the most recent version of TRILEGAL code is used for this purpose ([Girardi et al., 2005](#); [Marigo et al., 2017](#)). The bolometric correction tables for rotating stars are explicitly presented in [Girardi et al. \(2019\)](#) and already implemented in the code (see also [Chen et al., 2019](#)). Several rotating isochrones are presented for different values of the inclination angle, to show the corresponding effects in the photometry.

This chapter will be divided into three sections. Section. 6.1 discusses the methodology of the interpolation to produce isochrones. Examples of these new obtained isochrones will be shown and analysed in this section, in which the effects of photometry changes due to rotation are consistently taken into account. Discussion and conclusions on this new collection of tracks and isochrones will be presented in Sect. 6.2. The quality of the new isochrones is preliminarily tested on two open clusters M67 and NGC6633. Finally, in Sect. 6.3 I will describe the web-interface dedicated to the new stellar tracks and isochrones.

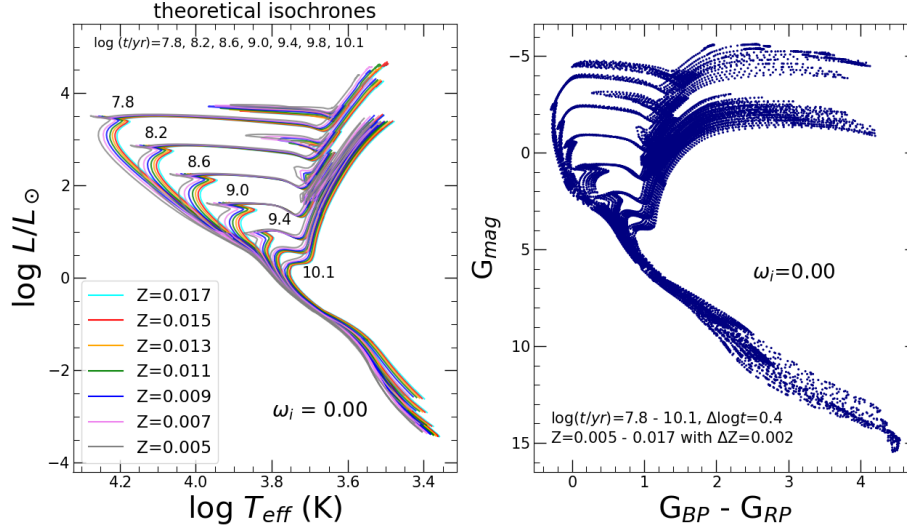


Figure 6.1: Theoretical isochrones calculated with the TRILEGAL code. Left-hand panel: Isochrones of non-rotating models for the ages  $\log(t/\text{yr}) = 7.8, 8.2, 8.6, 9.0, 9.4, 9.8, 10.1$  and seven different metallicities from 0.005 to 0.017 are shown in different colours, from grey to cyan, as indicated in the legend. Right-hand panel: Corresponding CMD in *Gaia* passbands of the theoretical isochrones shown in the left panel.

## 6.1 Production of isochrones

For all sets of evolutionary tracks described in the previous sections, we have constructed the corresponding isochrones. The initial phase begins from the PMS, and the final stage is either the beginning of the TP-AGB phase for low- and intermediate-mass models or the C-exhaustion for higher masses. As explained in Sect. 5.2.4, at a given initial metallicity and rotation rate, a certain number of low-mass models were not computed, due to our choice of decreasing  $\omega_{\text{max}}$  at decreasing  $M_i$ , in the transition towards LMSs (Eq. 5.2). While computing the isochrones, the missing tracks of a given  $\omega_i$  are replaced by the track with the nearest initial mass in the set of tracks with the same metallicity and with  $\omega_i$  immediately smaller. This ensures that the isochrones gradually shift from the required  $\omega_i$  to the non-rotating case in the mass interval between  $M_{O2}$  and  $M_{O1}$ .

After selecting all the stellar tracks in each set, based on the initial metal-

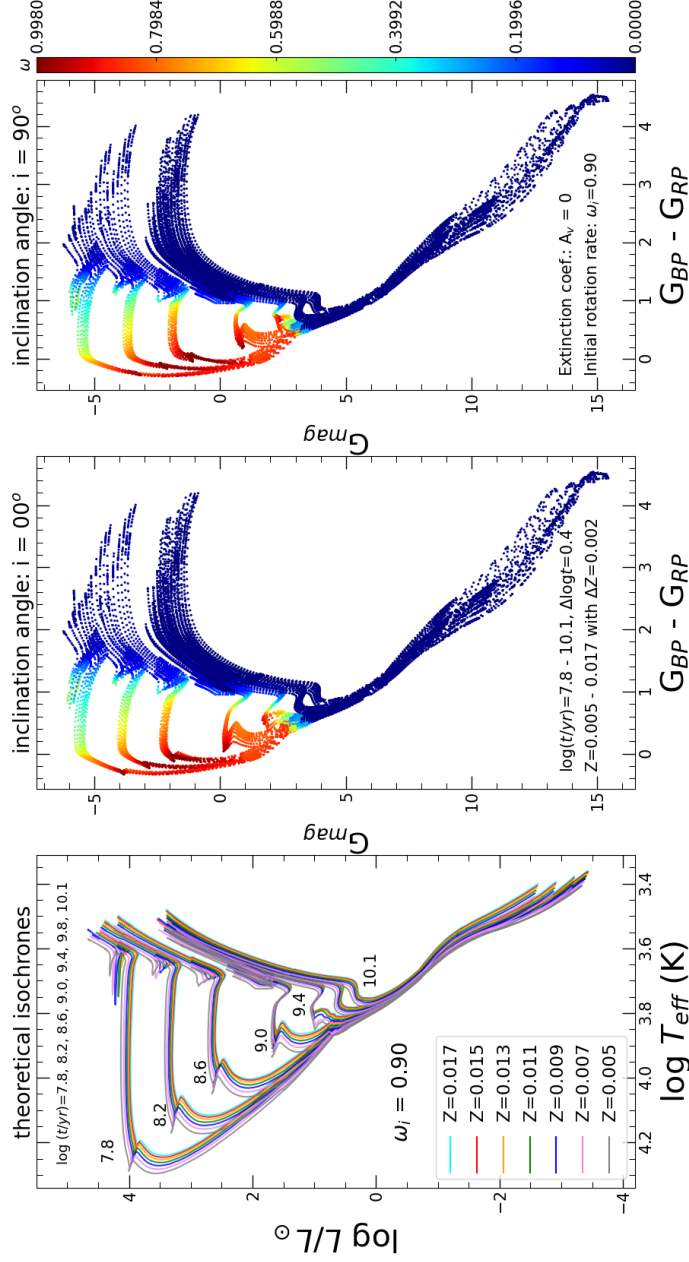


Figure 6.2: Theoretical isochrones calculated with the TRILEGAL code. Left-hand panel: Theoretical isochrones with the same parameter of  $\log t$ s and  $Z$ s as in Fig. 6.1 but for the  $\omega_i = 0.90$  set. Middle and right-hand panels: Corresponding CMD in the *Gaia*-passbands for two values of the inclination angle:  $i = 0^\circ$  (pole-on) and  $i = 90^\circ$  (equator-on). Changes in the rotation rate along the isochrones are indicated by the colour bar.

licity and rotation rate, the computation of isochrones proceeds through the following steps. First, the computed stellar evolutionary tracks in each set are homogeneously divided into phases separated by characteristic ‘equivalent evolutionary points’. Then, for a given age, the isochrone is constructed by interpolating all stellar properties between points of different initial mass but equivalent evolutionary stages. More details of the interpolation scheme can be found in Bertelli et al. (1990a) (see also Bertelli et al. 2008). In this work, the isochrones are produced by a recent version of the TRILEGAL code (Girardi et al., 2005; Marigo et al., 2017), which interpolates all the additional quantities needed to characterise rotating stars. Several isochrones have been produced with metallicity in the range from 0.004 to 0.017 in steps of 0.001 and ages in the range from 10 Myr to  $\sim 13$  Gyr at intervals of 0.05 in the scale log and for the seven sets of initial rotation rates from zero to  $\omega_i = 0.99$ . As an example, the left-hand panel of Fig. 6.1 shows the theoretical isochrones of non-rotating stars for selected ages and metallicities.

The theoretical isochrones provide the intrinsic properties of the stars, such as the luminosity, mean effective temperature, angular velocity, and radius at the pole and the equator. Then they are complemented with photometric magnitudes in several filters for comparison with observed CMDs. For non-rotating stars, this is usually done by using tables of bolometric corrections (BCs) as a function of effective temperature, surface gravity, and metallicity (see Girardi et al., 2002); eventually these tables also consider the interstellar extinction in a star-to-star basis, as in Girardi et al. (2008). The right-hand panel of Fig. 6.1 shows non-rotating isochrones in the *Gaia* passbands, corresponding to those shown in the left-hand panel, where *Gaia* EDR3 photometry is adopted (see Riello et al., 2021).

Bolometric correction tables for rotating stars have at least two more parameters than those for non-rotating stars: the rotation rate  $\omega$  and the inclination angle,  $i$ , of the line of sight with respect to the stellar rotation axes. Such BC tables are described in Girardi et al. (2019). They are already implemented in the YBC database<sup>1</sup> of BCs by Chen et al. (2019) and in the TRILEGAL code we use to produce the present isochrones. The left-hand panel of Fig. 6.2 shows some selected rotating isochrones. The two panels on the middle and right-hand side of Fig. 6.2 illustrate the result of applying the BCs to isochrones with rotation  $\omega_i$ , and how the photometry changes when observing rotating stars from  $i = 0^\circ$  (pole-on) and  $i = 90^\circ$  (equator-on). The

<sup>1</sup><http://stev.oapd.inaf.it/YBC/>



changes in the photometry are the most remarkable for the stars close to the upper MS, since they are the stars that still retain a large fraction of their initial rotational velocity.

For cool red giants, the BC tables for rotating stars do not cover the complete range of low effective temperatures that might be necessary to build the isochrones containing fast-rotating stars. For instance, for  $\omega = 0.9$  and  $\log g = 2$  the BC tables defined in [Girardi et al. \(2019\)](#) are limited to effective temperatures above  $\sim 4000$  K. Fortunately, inspection of our final isochrones reveals that this limitation is not a practical problem: it turns out that all giants with  $T_{\text{eff}}$  smaller than  $\sim 5000$  K are slow rotators, with  $\omega \lesssim 0.2$ . Since these slow rotators have nearly spherical configurations, we decide to apply the BC tables for non-rotating stars from [Chen et al. \(2019\)](#) (YBC) to all stars with  $T_{\text{eff}} < 5250$  K, for all values of  $\omega_i$ . This choice ensures a smooth behaviour of the colours, as can be appreciated in the middle and right panels of Fig. 6.2. To conclude this section, we stretch that the database of isochrones in several photometry systems is available at <sup>2</sup>.

## 6.2 Discussion and conclusions

We have presented a new library of evolutionary tracks with rotation for LMSs and IMSs produced with PARSEC V2.0. Masses from  $0.09 M_{\odot}$  to  $14 M_{\odot}$  and metallicities between  $Z=0.004$  and  $Z=0.017$  are considered, for seven values of the initial rotation rate in the range  $\omega_i = 0.00 - 0.99$ . The major differences between the last version of PARSEC, V2.0, and the previous one are: (i) the inclusion of rotation; (ii) the inclusion of mass loss along the evolution of all the stars because, for rotating models, it constitutes an important sink of angular momentum ([Friend and Abbott, 1986](#)); and (iii) the treatment of turbulent mixing as a diffusive process together with rotational mixing, nuclear processing, and molecular diffusion (for LMSs). In particular, concerning the last point, we recall that, to estimate the efficiency of overshooting from the convective core, we were guided by the work of [Costa et al. \(2019b\)](#), where the maximum COV parameter was calibrated in a well-studied sample of eclipsing binary systems ([Claret and Torres, 2018](#)), obtaining  $\lambda_{\text{ov}} = 0.4$ .

We also calculated the isochrones up to the beginning of the TP-AGB phase or up to the end of the central C-burning phase. Using the TRILEGAL

---

<sup>2</sup><http://stev.oapd.inaf.it/cmd>

code, they can be interpolated in metallicity between  $Z = 0.004$  and  $0.017$  and in the age range  $7.0 \leq \log(t/\text{yr}) \leq 10.1$ .

To illustrate some important consequences of the above differences, we show in Fig. 6.3 and Fig. 6.4 are two preliminary fits to the observed CMD of the open clusters M67 and NGC 6633, respectively. M67 (NGC 2682) is a well-known test bench for studying the internal physics of stellar models of LMSs with typical turnoff masses around  $1.2 M_{\odot}$ . In particular, its CMD was used to calibrate the efficiency of convective overshooting, due to the well-developed convective core in stars around its turnoff region. Furthermore, the cluster, together with other known open clusters, was also used to obtain the age-metallicity relation for the Milky Way disc stars (e.g. Viscasillas Vázquez et al., 2022). Its age has been repeatedly estimated over the years: Sarajedini et al. (2009) reported an age between 3.5 and 4.0 Gyr; from the asteroseismic properties of the giant and red clump stars, Stello et al. (2016) derived an age of the cluster of  $3.46 \pm 0.13$  Gyr; more recently, using the data from the *Gaia* Second Data Release (hereafter GDR2), Bossini et al. (2019) derived a distance modulus  $(m - M)_0 = 9.726$  mag, an interstellar extinction coefficient  $A_V = 0.115$  mag, and an age of  $3.639 \pm 0.017$  Gyr (see Arenou et al., 2018; Gaia Collaboration, 2018a,b,c, for more details about GDR2).

The M67 CMD, shown in Fig. 6.3, was obtained from the data provided by Cantat-Gaudin et al. (2018), who determined photometry, memberships, mean distances, and proper motions of stars in 1229 open clusters. It should be noted that the stars are limited to apparent  $G \lesssim 18$  mag to keep the photometric precision in *Gaia*'s passbands at the level of a few millimag (see Godoy-Rivera et al., 2021; Bossini et al., 2019; Evans et al., 2018, for more details). Also plotted in Fig. 6.3 are a number of our isochrones selected with the following criteria. Lines labeled PS2 indicate our best-fit PARSEC V2.0 isochrones. The fit was obtained by adopting the distance modulus obtained by Bossini et al. (2019),  $(m - M)_0 = 9.726$  mag, but correcting it for a zero-point offset of  $-30 \mu\text{arcsec}$  (Gaia Collaboration, 2018c). The final corrected distance modulus is  $(m - M)_0 = 9.69$  mag. For an initial composition of  $Z = 0.015$  ( $[\text{Fe}/\text{H}] \sim 0$ ),  $Y = 0.275$  (our corresponding He value), the best fit was obtained by adopting an extinction  $A_V = 0.1$  mag and an age of  $\log(t/\text{yr}) = 9.57$ . Plotted in the figure are both a non-rotating isochrone (dashed red line) and one for a slow rotation (solid red line). For both isochrones, we use the same best-fit parameters because the adopted low rotation only marginally affects the region above the cluster turnoff.

In the same figure, we also show the results we obtain using PARSEC

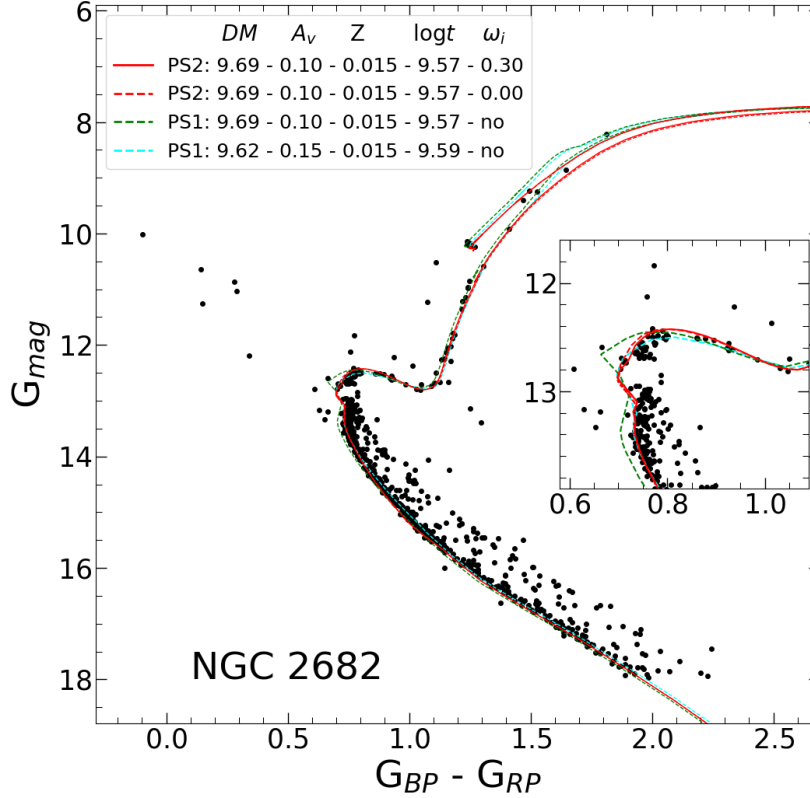


Figure 6.3: CMD of open cluster M67 (NGC 2682) from GDR2 data, overplotted with the isochrones that are produced in this work (solid and dashed red lines, labeled PS2) and those from the previous version, PARSEC V1.2S (dashed green and cyan lines, labeled PS1). The parameters of the isochrones,  $DM=(m-M)_0$ ,  $A_V$ ,  $Z$ ,  $\log t/yr$  and  $\omega_i$ , are displayed in the legend. The inset figure zooms into the turnoff region of this cluster.

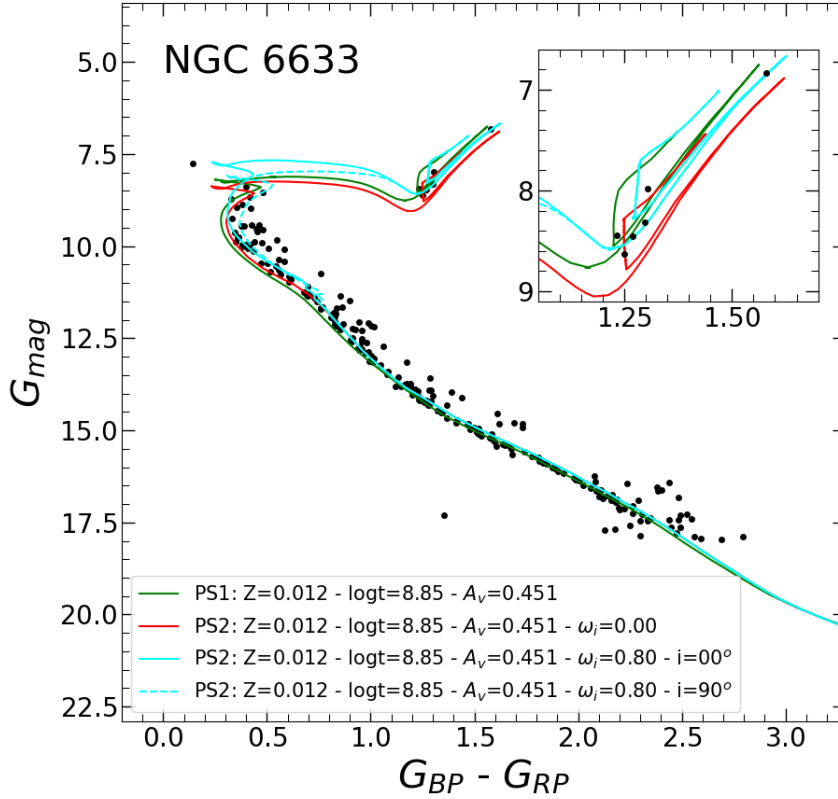


Figure 6.4: CMD of the open cluster NGC 6633 from GDR2. The displayed isochrones are for metallicity  $Z = 0.012$ ,  $\log(t/\text{yr}) = 8.85$ ,  $(m - M)_0 = 7.841$ , and  $A_V = 0.451$  mag. The red line represents the non-rotating case, and the two cyan lines are for rotating isochrones with the same  $\omega_i = 0.80$ , and inclination angles  $i = 0^\circ$  (solid line) and  $i = 90^\circ$  (dashed line). The green line is the isochrone obtained with PARSEC V1.2S assuming the same parameters of the previous non-rotating case.

V1.2S, labeled ‘PS1’. For the model represented by the dashed green line, we adopt the same fit parameters as the PS2 solutions. The inset in the figure is a zoomed-in look at the turnoff region to highlight the differences between the isochrones. We see that this PARSEC V1.2S isochrone has a more pronounced hook at the same fitting parameters. This is an evident feature of models computed with a larger COV parameter. Instead, the dashed cyan isochrone was drawn to reproduce the fit obtained with PS1 models, keeping only the metallicity fixed and letting the other parameters vary within reasonable uncertainties. For this second PS1 model, which runs almost on top of the PS2 isochrones, we adopted a slightly shorter distance modulus,  $(m - M)_0 = 9.62$ , a larger extinction,  $A_V = 0.15$  mag, and a 5% older age,  $\log(t/\text{yr}) = 9.59$ . We note that all four isochrones run almost superimposed onto one another in the sub-giant branch, which, being an almost horizontal feature in the CMD, is a robust indicator of the apparent distance. The new fitting parameters result from the need to diminish the hook extension that, with PARSEC V1.2S, can only be done by using a slightly older age for a fixed metallicity. The variation in the distance modulus and the attenuation almost compensate for each other, but the latter is also needed to improve the fitting of the colours of the turnoff region. The differences of the parameters between this fit and the PS2 ones should be representative of the differences obtained by using the new version of PARSEC instead of the previous V1.2S version in this age domain.

Recently, it has been shown that M67 harbours an interesting spectroscopic binary system located near the turnoff region, WOCS 11028, that challenges theoretical models (see [Sandquist et al., 2021](#), for a thorough discussion). Briefly, the mass of the primary component is estimated to be  $M_{\text{WOCSa}} = 1.222 \pm 0.006 M_\odot$ , while current predictions using different stellar evolution codes (including PARSEC V1.2S) give values that are lower by  $\delta m = 0.05 M_\odot$  (i.e. about  $8\sigma$  lower). We confirm that we also get the same result with the new version of PARSEC and leave this problem to a more exhaustive investigation using new PARSEC models with varying initial metallicity and He content (see also [Sandquist et al., 2021](#)).

Another object we present in this project as a preliminary check of the new models is the young open cluster NGC 6633, also present in the GDR2 catalogue. High-resolution spectroscopy for NGC6633 comes from the analysis by [Casamiquela et al. \(2021\)](#), who studied the age metallicity relation of the Milky Way using 47 open clusters observed with *Gaia*. [Bossini et al. \(2019\)](#) derived for NGC 6633  $(m - M)_0 = 7.866^{+0.024}_{-0.025}$  mag,  $\log(t/\text{yr}) = 8.888^{+0.006}_{-0.032}$ ,

and  $A_V = 0.451^{+0.025}_{-0.02}$  mag. With the same procedure used for M67, we fitted the CMD of NGC 6633 with the new isochrones, adopting  $Z = 0.012$ ,  $Y = 0.270$ ,  $A_V = 0.451$  mag, and distance modulus  $(m - M)_0 = 7.841$  mag, including a  $-30\mu\text{arcsec}$  offset in *Gaia* parallaxes, and the age of  $\log(t/\text{yr}) = 8.85$  (Fig. 6.4). Both non-rotating and rotating isochrones are displayed with values indicated in the corresponding labels. The lower MS is very well fitted, while the extended MS turnoff region is fully reproduced by rotating isochrones, also taking the effects of inclination angles into account, which, in this cluster, are clearly seen. Furthermore, the different rotational velocities in this cluster can also explain the particular feature visible near the red clump. Indeed, if only rotating models had been used, as needed by the fit of the turnoff region, it would have been difficult to explain the position of the three stars that clearly fall below the corresponding He clump, given the much shorter corresponding evolutionary lifetimes. They are instead fully compatible with the He clump of non-rotating models of similar age. Thus, even in NGC 6633 there are hints for the presence of at least one population of non-rotating stars and another of fast rotators, as in the case of the young LMC cluster NGC 1866 (Costa et al., 2019a).

### 6.3 Web-interfaces

This new collection of stellar evolutionary tracks and isochrones contains non-rotating and rotating models are stored in two dedicated web-interfaces. The first one is used for stellar tracks which can be found at: [http://stev.oapd.inaf.it/PARSEC/tracks\\_v2.html](http://stev.oapd.inaf.it/PARSEC/tracks_v2.html). Fig. 6.5 shows the front interface where the PARSEC V2.0 tracks are made available to download. The database is categorised by a combination of initial metallicity and rotation rate ( $Z, \omega$ ). With a desired  $(Z, \omega)$ , a set of tracks from  $0.09M_\odot$  up to  $14M_\odot$  can be downloaded directly from the page. Specifically, in case the user wants to have the tracks of all rotation rates from 0.0 to 0.99 with the same metallicity, they can get the set directly from the second column of the table, where the header appears as “ALL”. Note that in this site, the user can also download the tracks from previous version PARSEC V1.2S by going to the section “PARSEC V1.2S” (Fig. 6.6).

The second web-interface is dedicated for obtaining the corresponding isochrones, which can be visited at: [http://stev.oapd.inaf.it/cgi-bin/cmd\\_3.7](http://stev.oapd.inaf.it/cgi-bin/cmd_3.7). Fig. 6.7 shows the front page of this webpage where users can

## PARSEC

### PAdova TRieste Stellar Evolutionary Code

[HOME](#)
[STELLAR TRACKS](#)
[TOOLS](#)
[PAPERS](#)

#### STELLAR TRACKS DATABASE

This is the stellar tracks database of **PARSEC v2.0**.

Please cite the following papers if you use these tracks ([Costa et al. 2019a](#), [Costa et al. 2019b](#), [Nguyen et al. 2022](#)).

Detailed description of stellar tracks quantities are available [here](#).

[PARSEC V2.0](#)
[PARSEC V1.25](#)

#### PARSEC V2.0

Metallicity	All	$\Omega/\Omega_{\text{crit}} = 0.00$	$\Omega/\Omega_{\text{crit}} = 0.30$	$\Omega/\Omega_{\text{crit}} = 0.60$	$\Omega/\Omega_{\text{crit}} = 0.80$	$\Omega/\Omega_{\text{crit}} = 0.90$	$\Omega/\Omega_{\text{crit}} = 0.95$	$\Omega/\Omega_{\text{crit}} = 0.99$
0.004	<a href="#">GET</a>	<a href="#">GET</a>	<a href="#">GET</a>	<a href="#">GET</a>	<a href="#">GET</a>	<a href="#">GET</a>	<a href="#">GET</a>	<a href="#">GET</a>
0.006	<a href="#">GET</a>	<a href="#">GET</a>	<a href="#">GET</a>	<a href="#">GET</a>	<a href="#">GET</a>	<a href="#">GET</a>	<a href="#">GET</a>	<a href="#">GET</a>
0.008	<a href="#">GET</a>	<a href="#">GET</a>	<a href="#">GET</a>	<a href="#">GET</a>	<a href="#">GET</a>	<a href="#">GET</a>	<a href="#">GET</a>	<a href="#">GET</a>
0.01	<a href="#">GET</a>	<a href="#">GET</a>	<a href="#">GET</a>	<a href="#">GET</a>	<a href="#">GET</a>	<a href="#">GET</a>	<a href="#">GET</a>	<a href="#">GET</a>
0.014	<a href="#">GET</a>	<a href="#">GET</a>	<a href="#">GET</a>	<a href="#">GET</a>	<a href="#">GET</a>	<a href="#">GET</a>	<a href="#">GET</a>	<a href="#">GET</a>
0.017	<a href="#">GET</a>	<a href="#">GET</a>	<a href="#">GET</a>	<a href="#">GET</a>	<a href="#">GET</a>	<a href="#">GET</a>	<a href="#">GET</a>	<a href="#">GET</a>

Figure 6.5: Web-interface for stellar tracks that are presented in this work.

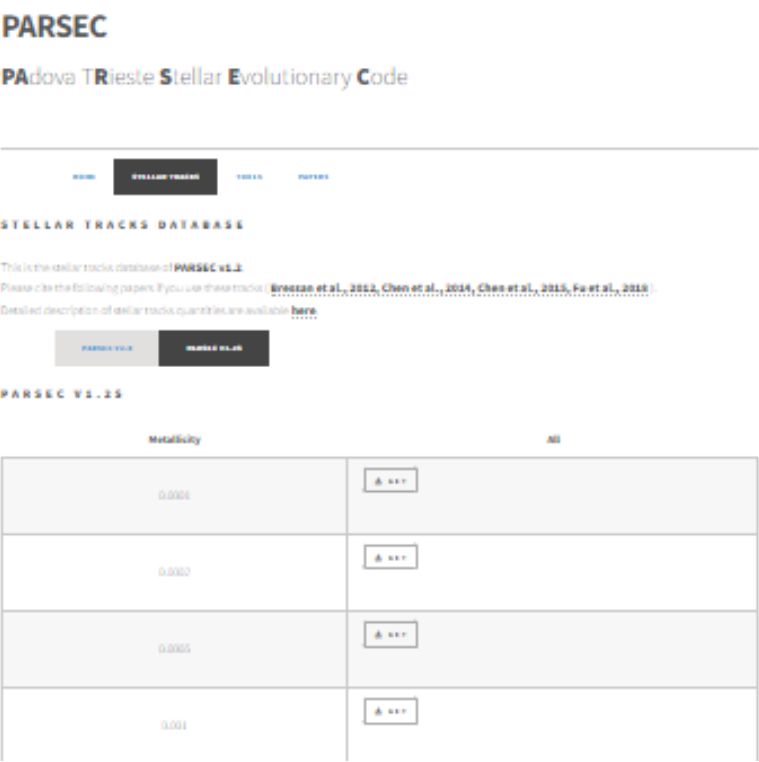


Figure 6.6: Stellar tracks from previous version PARSEC V1.2S.





Figure 6.7: Web-interface for isochrones.

obtain the desired isochrones. The first step is selecting the available stellar tracks from different versions of PARSEC code. Especially, with the option of PARSEC V2.0 the user can choose the desired initial rotation rate. The TP-AGB tracks that are computed by COLIBRI code is also available to choose as shown in Fig. 6.7a. The second step is choosing the photometry system and the BC tables as can be seen in Fig. 6.7b. A brief description for all the available photometry systems is made available to read on the side-line. And finally, the user should specify the initial mass function to use and the desired age and metallicity ranges. The age and metallicity can be declared in linear-scale or log-scale, from the initial value to the final value with a fine step as the user refers. The last action to do is to submit the request, as can be seen in Fig. 6.7c.

# Chapter 7

## Globular cluster M92

### 7.1 General background

The PARSEC stellar models have been widely used in the community since they were first published in [Bressan et al. \(2012\)](#). Many updates and improvements were provided over the years. For instance, [Chen et al. \(2014\)](#) extended the calculations to very-low-mass domain with the implementation of T- $\tau$  relation in the atmosphere model. The models of massive stars up to  $350M_{\odot}$  were provided in [Chen et al. \(2015\)](#), and [Fu et al. \(2018\)](#) studied the  $\alpha$ -enhanced stellar models with the calibration of GC 47Tuc. Most recently, rotation was implemented in the PARSEC code, [Costa et al. \(2019b\)](#). A large grid of stellar tracks and isochrones for several initial rotation rates were provided in [Nguyen et al. \(2022\)](#) with many updated input physics, e.g., mass loss is attached along the evolution of stars, the chemical mixing scheme, and the nuclear reaction networks. Moreover, the authors used solar-scaled mixtures from [Caffau et al. \(2011\)](#) for their calculations.

As a subsequent work to [Nguyen et al. \(2022\)](#), we would like to extend the calculations to the lower metallicity domain where  $\alpha$ -element abundances (i.e. of O, Ne, Mg, Si, S, Ar, Ca and Ti) may be different from the solar ones and may play an important role. The existence of  $\alpha$ -enhancement in globular clusters have been confirmed in many works (e.g., [Carney, 1996](#); [Pritzl et al., 2005](#); [Puzia et al., 2006](#); [Amarsi et al., 2019](#)). Besides that, it is well known that the solar-scaled mixtures can not be applied to all types of stars, therefore, including the  $\alpha$ -enhanced mixtures in calculations of stellar models becomes necessary, especially in studying stars in GCs, in the galactic

bulge (Gonzalez et al., 2011) or in the thick-disc (Ruchti et al., 2010).

For this purpose, we first use the GC M92 to calibrate our  $\alpha$ -enhanced models. One needs to know the chemical compositions of the cluster. This will be discussed in Sect. 7.2. The new opacity as well as the EOS tables are re-computed to complement with the new collected compositions. Since part of the work on M92 is devoted to the analysis of the main sequence stars that will be targeted by JWST observations, we will first present in Sect. 7.3 the input physics includes the calibration of the mass-radius relation performed with the new PARSEC v2.0 version, and the preliminary results on the computed tracks and isochrones, as well as the CMD fits with HST data of M92. A discussion on the next steps to do for this ongoing project will be presented in Sect. 7.4.

## 7.2 Chemical mixtures

The chemical abundances are usually given in literature as the absolute value scaled to the iron content and referred to the solar value, i.e.,  $[X/Fe] = \log(N_X/N_{Fe}) - \log(N_X/N_{Fe})_{\odot}$ , where  $N_X$  is the number distribution of an element  $X$ . In this project, we use the solar mixture from Caffau et al. (2011) to refer the standard solar abundances, with  $Z_{\odot} = 0.01524$ , for conversion from the original data. Other values can be found in Grevesse and Sauval (1998); Asplund et al. (2006); Lodders et al. (2009); Caffau et al. (2011) and von Steiger and Zurbuchen (2016).

The existence of multiple stellar populations in M92 has been investigated in many works. For example, Milone et al. (2017b) indicated that M92 hosts at least two populations: the first generation inherits the chemical properties from the molecular cloud from which it is formed; the second generation consists of stars that are enriched in nitrogen and depleted in oxygen, likely formed from the material processed by the first generation stars. Recently, Mészáros et al. (2020) investigates many chemical pieces of a large sample of stars in 31 globular clusters from the APOGEE survey. From the analysis of the distribution of aluminum abundance, they show a clear separation in the density histograms of Al and the Al-Mg anticorrelation maps which indicate an existence of two populations, that are separated by at least  $\sim 0.2$  dex in the  $[Al/Fe]$  abundance ratio. In particular, a population with enriched  $[Al/Fe]$  which is called second generation (SG), and a so-called first generation (FG) with  $[Al/Fe] < 0.3$  dex. In this project, we follow this procedure by

Table 7.1: Adopted chemical abundances of GC M92.

[el/Fe]	FG	SG	ref.
C	-0.3750	-0.2507	a
N	0.9523	1.0150	a
O	0.7852	0.5620	a
Ne	0.4000	0.4000	*
Na	0.0000	0.5000	c
Mg	0.3904	0.1675	a
Al	-0.1624	0.7502	a
Si	0.4450	0.5245	a
P	1.1800	1.1800	g
S	0.4000	0.4000	d
Ar	0.4000	0.4000	*
K	0.6520	0.6473	a
Ca	0.2800	0.3260	a
Sc	0.1600	0.1600	f
Ti	0.3000	0.3000	e
V	0.4800	0.4800	f
Cr	0.0000	0.0000	e
Mn	-0.2200	-0.2200	f
Co	0.2400	0.2400	f
Ni	-0.0500	-0.0500	e
Zn	0.1500	0.1500	e
Y	-0.0800	-0.0800	f
Zr	0.4700	0.4700	f
Ba	-0.2900	-0.2900	e
La	0.3100	0.3100	f
Ce	0.0920	-0.0680	a
Nd	0.3700	0.3700	f
Eu	0.5600	0.5600	f
Ho	0.8000	0.8000	f
Er	0.7700	0.7700	f

a: [Mészáros et al. \(2020\)](#)c: [Carretta et al. \(2009\)](#)d: [Kacharov et al. \(2015\)](#), NLTE analysise: [Bensby et al. \(2014\)](#)f: [Roederer and Sneden \(2011\)](#)g: [Hubrig et al. \(2009\)](#)

\*: estimated

setting  $[\text{Al}/\text{Fe}] = 0.3$  as a reference to separate the two generations in M92, and then derive the abundance of each chemical element in each group. The abundance of elements such as C, N, O, Mg, Al, Si, K, Ca, and Ce in the two generation groups are deduced from [Mészáros et al. \(2020\)](#), and listed in Table. 7.1. In order to be more complete in the abundances table for our purposes, the abundance of other elements is adopted from other works. For example, [Carretta et al. \(2009\)](#) provides the abundances of Na for 1958 RGB stars in 19 GCs from FLAMES/GIRAFFE spectra, in a wide range of metallicity  $-2.4 \leq [\text{Fe}/\text{H}] \leq 0.4$  dex. Sulphur is one of the members of the  $\alpha$ -element group, and there are very few measurements of  $[\text{S}/\text{Fe}]$  for stars in GCs, even nowadays. We adopt the mean value provided by [Kacharov et al. \(2015\)](#), where they derive the mean  $[\text{S}/\text{Fe}]$  in RGB stars of three GCs M4, M22, and M30. Since there is no evidence of difference  $[\text{S}/\text{Fe}]$  between two populations, we use the same value for both FG and SG. A similar situation holds for other elements such as Sc, Ti, V, Cr, Mn, Co, Ni, Zn, Y, Zr, Ba, La, Ce, Nd, Eu, Ho, Er; for those elements, we adopt the abundances provided by [Hubrig et al. \(2009\)](#), [Roederer and Sneden \(2011\)](#) and [Bensby et al. \(2014\)](#) and, when they are available, no different for both generations. The other two elements that belong to  $\alpha$ -element group are Ne and Ar, but since we are not able to find them in literature, we assume they have the same enhancement of S.

The iron abundance ( $[\text{Fe}/\text{H}]$ ) of the two generations is taken from [Mészáros et al. \(2020\)](#). In this work, there is only a slight difference, of  $\sim 0.048$  dex, between the FG and the SG. In particular, the FG has  $[\text{Fe}/\text{H}] = -2.2360$  dex, and the SG has  $[\text{Fe}/\text{H}] = -2.1885$  dex, in agreement with many other estimates in literature (e.g, [Zinn and West, 1984](#); [Carretta and Gratton, 1997](#)).

In this work, we consider that the  $\alpha$ -elements are O, Ne, Mg, Si, S, Ar, Ca, and Ti. With the adopted abundances listed in Table. 7.1 and the referred solar mixtures from [Caffau et al. \(2011\)](#), the  $[\alpha/\text{Fe}]$  ratio of the FG and SG are 0.715 and 0.524 dex correspondingly. The difference between the FG and SG in  $[\alpha/\text{Fe}]$  values are mainly driven by the different oxygen abundances. The corresponding metallicities in mass fraction of the two generations are then derived,  $Z_{\text{FG}} = 0.0005$  and  $Z_{\text{SG}} = 0.0003$ . It is important to emphasise that, at the moment, we follow the enrichment law to calculate the He abundance, which is

$$Y = Y_p + \frac{\Delta Y}{\Delta Z} Z \quad (7.1)$$

Table 7.2: Metallicity,  $[\alpha/\text{Fe}]$  ratio and helium abundance of M92.

	FG	SG
$[\text{Fe}/\text{H}]$	-2.2360	-2.1885
$[\alpha/\text{Fe}]$	0.7151	0.5241
$Z$	0.0005	0.0003
$Y$	0.250	0.250

where  $Y_p = 0.2485$  is the primordial He abundance (Komatsu et al., 2011) and the helium-to-metal enrichment ratio  $\frac{\Delta Y}{\Delta Z} = 1.78$  is based on the solar calibration in Bressan et al. (2012). Table. 7.2 summarises the values of metallicity in terms of both number and mass fraction for the FG and SG, as well as the  $[\alpha/\text{Fe}]$  ratio and He content, for convenience.

For this preliminary study, we will perform the calculations adopting only one single metallicity value,  $Z = 0.0003$ . The results of using both FG and SG chemical mixtures at this metallicity value will be shown and discussed below. The input physics that's used for these calculations will be described in Sect. 7.3.1. The checks on mass-radius relation will be shown in Sect. 7.3.2 for the sake of using  $T$ - $\tau$  relation in the atmosphere of stellar models of very low mass stars. In Sect. 7.3.3, we will show the preliminary computed tracks and isochrones. The fit to the observed CMD of M92 from HST data will be also shown in this section.

## 7.3 Calibration with M92

### 7.3.1 Input physics

The main difference of the input physics in this calculation with respect to the previous version of PARSEC v2.0 is the new adopted chemical mixtures and thus the  $\alpha$ -enhanced opacity tables. It is worth to note that rotation is not considered for M92.

As mentioned in Sect. 2.2 the opacity tables are necessarily recomputed due to the new adopted chemical mixtures of M92 for both generations. In the high temperature regime,  $4.2 \leq \log(T/\text{K}) \leq 8.7$ , the opacity tables are provided by the Opacity Project At Livermore (OPAL; see Iglesias and Rogers, 1996), while in the low temperature regime  $3.2 \leq \log(T/K) \leq 4.1$  the opacity tables are generated with the AESOPUS tool (see Marigo and

Aringer, 2009, for details). In the transition region  $4.1 \leq \log(T/K) \leq 4.2$ , the opacities are linearly interpolated between the OPAL and AESOPUS values. The contribution from conduction is computed following Itoh et al. (2008).

Figure 7.1 shows the distribution of  $\kappa_R$  in the case of FG and SG-mixtures in the plane of  $\log T$ - $\log R$ , and the comparison of  $\kappa_R$ -ratios between the FG, SG and the standard solar-mixtures. The “H-free” table ( $X = 0$ ) of metallicity  $Z = 0.0003$  is used to show in Fig. 7.1, while the case of “H-rich” tables is shown in Fig. 7.2.

It is also worth to note that the abundances of M92 that are listed in Table 7.1 have already been re-scaled to the solar values provided by Caffau et al. (2011).

We also keep using the most updated nuclear networks as we used in previous work (Nguyen et al., 2022). The nuclear networks include the p-p chains, the CNO tri-cycle, the Ne-Na, and Mg-Al chains,  $^{12}\text{C}$ ,  $^{16}\text{O}$  and  $^{20}\text{Ne}$  burning reactions, and the  $\alpha$ -capture reactions up to  $^{56}\text{Ni}$ , for a total of 72 different reactions tracing 32 isotopes:  $^1\text{H}$ ,  $\text{D}$ ,  $^3\text{He}$ ,  $^4\text{He}$ ,  $^7\text{Li}$ ,  $^7\text{Be}$ ,  $^{12}\text{C}$ ,  $^{13}\text{C}$ ,  $^{14}\text{N}$ ,  $^{15}\text{N}$ ,  $^{16}\text{O}$ ,  $^{17}\text{O}$ ,  $^{18}\text{O}$ ,  $^{19}\text{F}$ ,  $^{20}\text{Ne}$ ,  $^{21}\text{Ne}$ ,  $^{22}\text{Ne}$ ,  $^{23}\text{Na}$ ,  $^{24}\text{Mg}$ ,  $^{25}\text{Mg}$ ,  $^{26}\text{Mg}$ ,  $^{26}\text{Al}$ ,  $^{27}\text{Al}$ ,  $^{28}\text{Si}$ ,  $^{32}\text{S}$ ,  $^{36}\text{Ar}$ ,  $^{40}\text{Ca}$ ,  $^{44}\text{Ti}$ ,  $^{48}\text{Cr}$ ,  $^{52}\text{Fe}$ ,  $^{56}\text{Ni}$ , and  $^{60}\text{Zn}$ . The reaction rates and corresponding  $Q$  values are taken from JINA REACLIB database Cyburt et al. (2010).

We also adopt the standard mass loss rate by Reimers (1977) for our calculations, which is given by

$$\dot{M} = \eta \times 1.343 \times 10^{-5} \frac{L^{1.5}}{m T_{\text{eff}}^2}, \quad (7.2)$$

where  $\dot{M}$  is the mass-loss rate in  $\text{M}_{\odot}/\text{yr}$ ,  $L$  and  $m$  are the luminosity and mass in solar units, respectively, and  $T_{\text{eff}}$  is the effective temperature in K. The parameter  $\eta = 0.2$  is adopted from the asteroseismic analysis of the two old open clusters NGC 6791 and NGC 6819 by Miglio et al. (2012).

### 7.3.2 Mass-Radius relation

Concerning the very-low-mass models ( $< 0.75\text{M}_{\odot}$ ), Chen et al. (2014) use a realistic  $T$ - $\tau$  relation, provided  $T$ - $\tau$  relation from PHOENIX (BT-Settl) model atmosphere (Allard et al., 2012), to determine the boundary conditions. The  $T$ - $\tau$  relations in PHOENIX (BT-Settl) cover a wide range of  $\log T_{\text{eff}}/K = [2600, 700000]$  and  $\log g = [0.5, 6]$  ( $\text{cm/s}^2$ ).



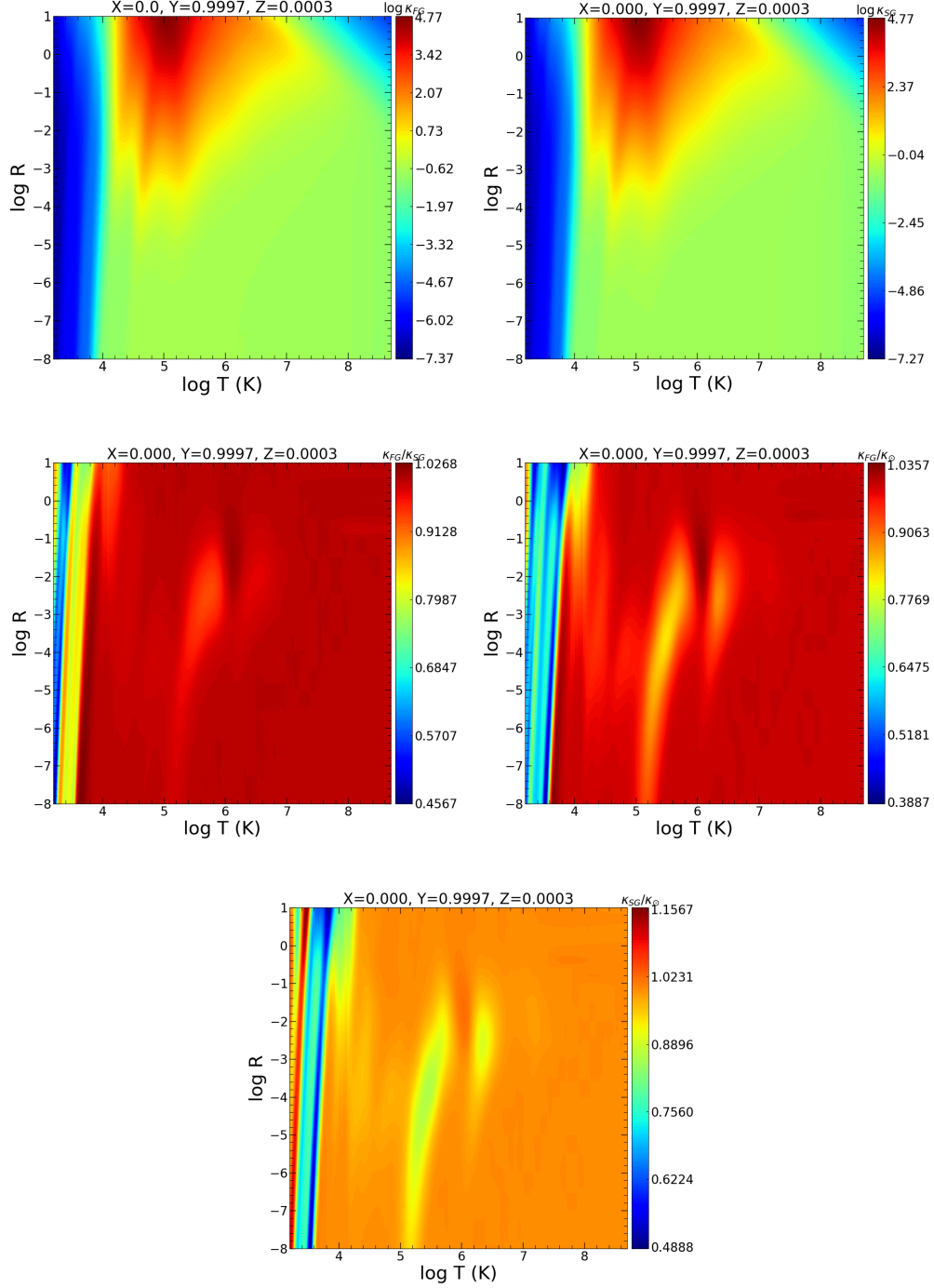


Figure 7.1: Maps of Rosseland mean opacities in the  $\log T$ - $\log R$  plane. The referenced metallicity  $Z = 0.0003$  of “H-free” tables are used to show in this figure. The top panels are the distribution map of  $\log \kappa_R$  in the case of FG and SG mixtures respectively, while the other three panels show the ratios of  $\kappa_R$  between different adopted mixtures, namely FG, SG and solar-scaled.

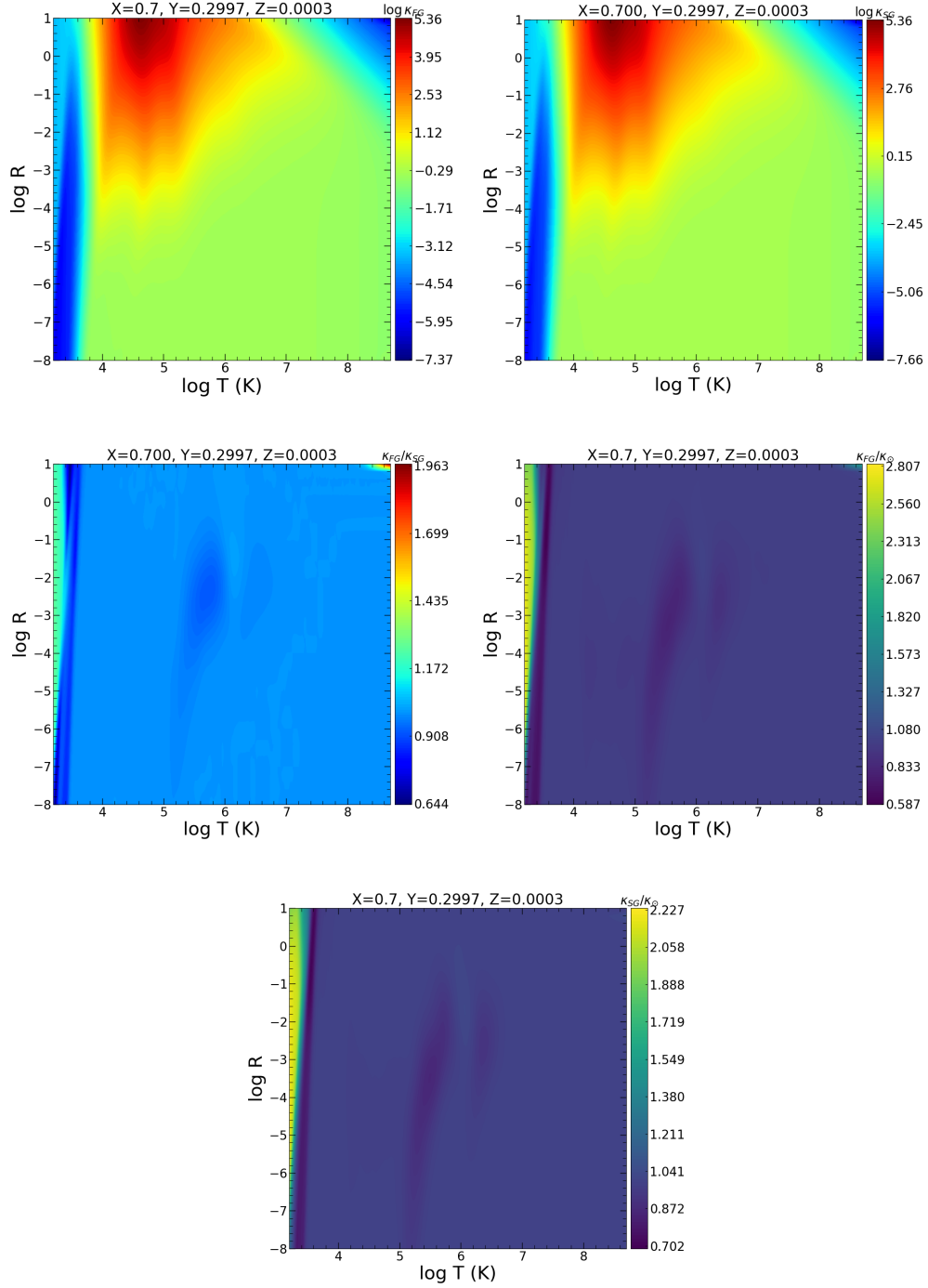


Figure 7.2: Maps of Rosseland mean opacities in the  $\log T$ - $\log R$  plane as shown in Fig. 7.1 but for “H-rich” tables where  $X = 0.7$ .

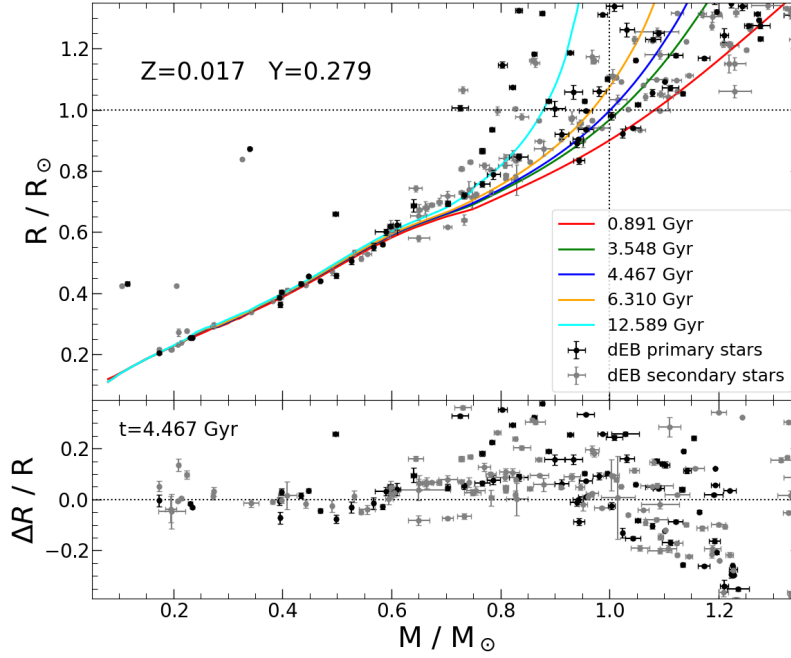


Figure 7.3: Mass-radius relation. The observed data is from DEBCat catalogue for the primary and secondary components with their errorbars are displayed by the filled-circles in black and grey colours. The superimposed isochrones in terms of  $M$  and  $R$  with several ages, the solar metallicity are shown in solid-lines. The bottom panel shows the differences between observed data and theoretical model of age 4.46 Gyr-isochrone.

Chen et al. (2014) calibrated the very low mass models against the observed mass-radius relation of the Detached Eclipsing Binary stars. To reproduce this relation they were forced to introduce a shift in the low temperature regime, namely,  $\Delta \log(T/T_{\text{eff}}) = 0$  at  $\log T_{\text{eff}} = 3.675$  linearly grows to  $\Delta \log(T/T_{\text{eff}}) = 0.06$  dex at  $\log T_{\text{eff}} = 3.5$ . The solar model calibration with these atmospheres gives  $\alpha_{\text{MLT}} = 1.77$ . With the new data of the Detached Eclipsing Binary stars (DEBCat; Southworth, 2017), we first re-check the mass-radius relation by adopting the models with  $T$ - $\tau$  relation as described above. For this purpose, we recompute the very-low-mass models following the same procedure as Chen et al. (2014), adopting  $\alpha_{\text{MLT}} = 1.77$ , with the initial metallicity  $Z = 0.017$ . Figure. 7.3 shows the isochrones with several

ages spanning from  $\sim 1$  Gyr to  $\sim 12.5$  Gyr, superimpose with the observed data from DEBCat catalogue. We can clearly see that over the range from  $0.1$  to  $0.6M_{\odot}$ , the theoretical relation fits very well the observed data. In the higher mass domain,  $\gtrsim 0.75M_{\odot}$  the radii are sensitive to stellar age and thus tend to spread a wide range of values. In the transition region from  $\sim 0.6 - 0.75M_{\odot}$ , the three stars that fall below the isochrones become difficult to explain with the current model, while the upper stars can be explained with the older age relation. However, if we expect these stars to have similar age to the Sun, the prediction from current models is not able to fit the data. Obviously, more detailed checks should be done in the future to understand better this region. One possibility could be that we neglect rotation, since these stars are binaries. However here we keep using the model that was carefully studied in [Chen et al. \(2014\)](#) to obtain the first preliminary models for the case of GC M92.

### 7.3.3 Preliminary track and isochrones fitting

We perform a calculation for a set of very low mass stars from  $0.08M_{\odot}$  up to  $0.72M_{\odot}$  with a step mass of  $0.02M_{\odot}$ , using the  $T-\tau$  relation as described above with  $\alpha_{\text{MLT}} = 1.77$ . Then, we add to the set the higher masses from  $0.74$  up to  $0.84M_{\odot}$  using the parameter  $\alpha_{\text{MLT}} = 1.74$  without the modification of  $T-\tau$  relation, and similar to a set of models with masses from  $1.75M_{\odot}$  to  $2.2M_{\odot}$  with the step of  $0.5M_{\odot}$ . We do not compute the mass models in the transition region at the moment because they are not needed for ages as old as those expected for M92 and because we are focusing on the lower-MS part of M92. The calculation for horizontal-branch models is also done for the sake of producing complete isochrones.

Figure. 7.4 shows the computed tracks, divided into three panels which correspond to the very low mass, the low mass, and the HB tracks, for both sets of chemical mixtures (i.e., FG and SG correspond to the top and bottom panels). At the moment, we present only one metallicity  $Z = 0.0003$  to have a first test on our models. More complete and detailed models will be presented in a forthcoming paper. All the tracks begin from the PMS (dotted-lines). At first, there is no nuclear reactions are allowed to occur and the models are fully convective and homogeneous in chemical compositions. The stars then evolve along the contraction during the PMS phase. Determining the ZAMS point is important since it marks the beginning of the central H-burning phase, this point is defined to be the location of the model when

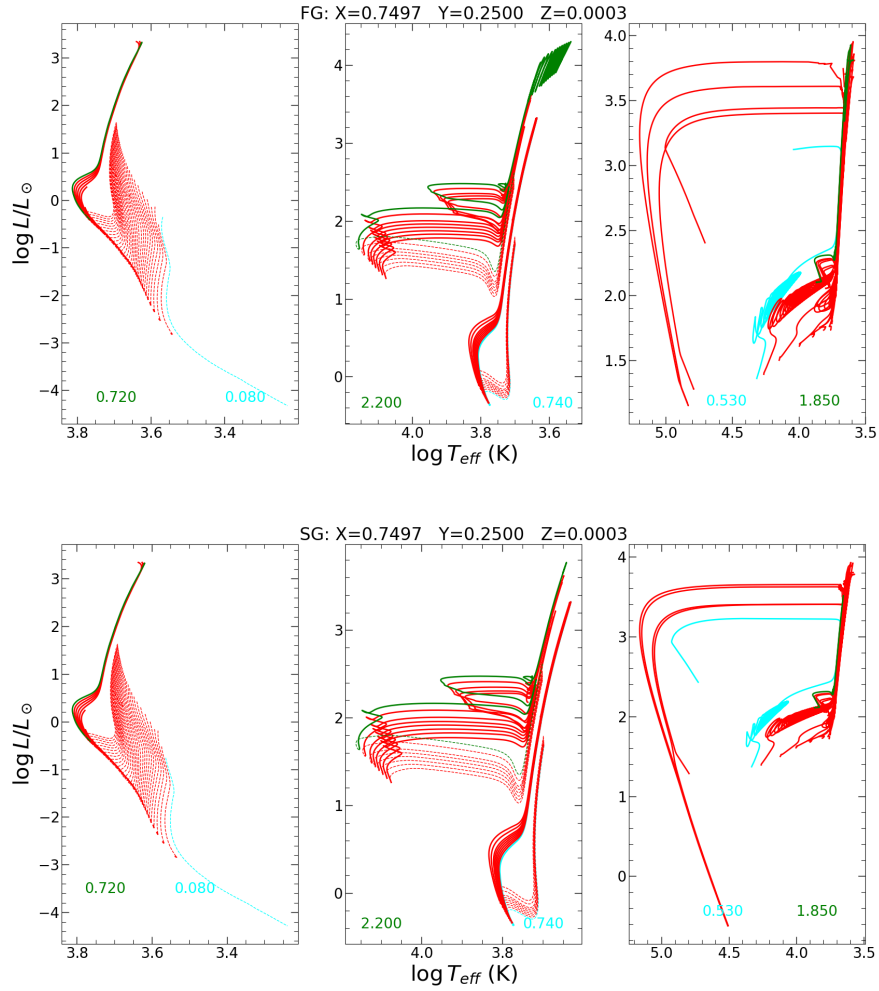


Figure 7.4: HRD of computed tracks by using the chemical mixtures of the FG (top-panel) and of the SG (bottom-panel) with the same value of metallicity  $Z = 0.0003$ .

the evolutionary speed in the HRD abruptly drops (i.e., a decrease by more than two orders of magnitude in a very short time). As we can see in the left panel of Fig. 7.4 low mass stars spend a very long time to burning hydrogen in the centre and the models are forced to stop at an age of about 30 Gyr.

Low-mass-stars with masses  $\gtrsim 0.7M_{\odot}$ , after burning the central-H, experience a strong envelope expansion and evolve along the subgiant phase before climbing along the RGB. Eventually, they reach the condition of degeneration in the He-core and undergo the so-called He-flash. The computation of this phase is rather expensive in CPU time. Therefore, the calculations of LMSs are stopped at the early stage of the He-flash. The He-burning phase of LMSs is then restarted from a suitable ZAHB model with the same core mass and surface chemical compositions as when they left the tip of the RGB phase. The evolution of He-burning phase of these stars is shown in the right panel of Fig. 7.4. As we can see in the middle panel of Fig. 7.4 the evolution of some IMSs up to  $2.2M_{\odot}$ . These stars do not reach the degenerate condition in the central core but are able to burn He in a stable way, that leads to the appearance of the blue bloop. These stars are forced to stop at the first few models of the thermal pulse asymptotic giant branch (TP-AGB) in the PARSEC code. A subsequent calculation for low-mass and IMSs at more advanced phases, especially from the early to the end of TP-AGB phase, can be achieved with the COLIBRI code (Marigo et al., 2013).

The next step is to produce the isochrones from the computed tracks. Though we should emphasise that due to the limitation in time there would be more checks and works to be operated after this thesis. However, at the moment we are able to show at least the first look to the CMD of M92 in the Hubble Space Telescope (HST) data.

The isochrones are produced in the way as described in previous works (e.g., Bressan et al., 2012; Nguyen et al., 2022). First, briefly summary, the computed stellar evolutionary tracks are homogeneously divided into phases separated by a few characteristic ‘equivalent evolutionary points’. Then, for a given age, the isochrone is constructed by interpolating all stellar properties between points of different initial masses but equivalent evolutionary stages. The bolometric correction is taken from the YBC database<sup>1</sup>, where we use the *HST/ACS WFC* filter (Siriani et al., 2005) to convert our theoretical isochrones to the photometric magnitudes for the CMD fitting purpose below.

Globular cluster M92 is among the oldest clusters in the galactic stellar

---

<sup>1</sup><http://stev.oapd.inaf.it/YBC/>

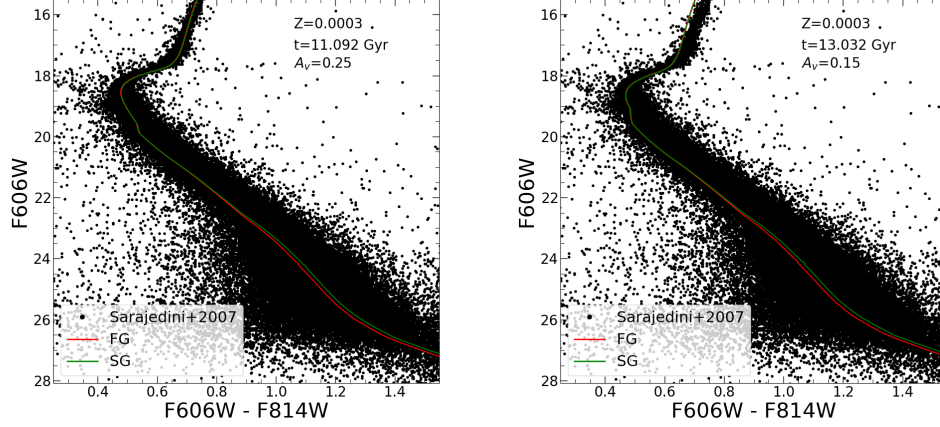


Figure 7.5: Colour-magnitude diagram of GC M92. The data is taken from Sarajedini et al. (2007), superimposed by the selected isochrones with  $Z = 0.0003$  and distance modulus  $(m - M)_0 = 14.65$  mag. The isochrones with age  $t = 11.09$  Gyr is shown in the left panel, while the isochrone with  $t = 13.03$  Gyr is in the right panel. The color lines represent for either the FG or the SG.

system. For instance, VandenBerg et al. (2002) derived an age of  $13.5 \pm 1.5$  Gyr, while Paust et al. (2007) found an age of  $14.2 \pm 1.2$  Gyr by comparing the theoretical and observed luminosity function. A lower age was found by Di Cecco et al. (2010), which is about  $11 \pm 1.5$  Gyr. Or recently Nardiello et al. (2022) use the JWST data to compare with the theoretical isochrones taken from BaSTI-IAC database (Pietrinferni et al., 2021), and find a well-fit by the isochrone of 13 Gyr. They also determine the distance modulus for M92, they find  $(m - M)_0 = 14.65 \pm 0.07$  mag. This result is in agreement with the literature, for example, Carretta et al. (2000) gives  $(m - M)_0 = 14.72 \pm 0.07$  including binary correction, or Sollima et al. (2006) bases on the near-infrared period-luminosity relation of RR Lyrae stars gives  $(m - M)_0 = 14.65 \pm 0.1$  mag.

For the benefit of fitting the observed CMD of M92, we adopt here the distance modulus  $(m - M)_0 = 14.65$  mag to our isochrones. Fig. 7.5 shows the observed HST data of M92 from Sarajedini et al. (2007). It should be noted that we use the formulation and coefficients from Sirianni et al. (2005) to transform the original ground-base data ( $VI$ -magnitudes) to the

WFC VEGAMAG photometric system. The isochrones with an age of 11.09 Gyr and 13.03 Gyr are used to do the fit. The extinction coefficient  $A_V$  is chosen so that to obtain a good-fit to the observed data. We can see that the age and  $A_V$  are compensate to each others, i.e., if we use the younger age isochrone, the value of  $A_V$  is higher than the one that with older age. However, with the first preliminary check we at least can see that the cluster might have an age between 11 – 13 Gyr with the possibly extinction value from 0.15 – 0.25 mag. More detail and careful consideration in the sense of model computation would be carried on in future, while this results should be emphasised as preliminary checks on our current models.

Focusing on the low-MS, the difference in  $[\alpha/\text{Fe}]$  values does not fully help us to explain the broad extension in the  $F606W - F814W$  colour of M92. Interestingly, [Milone et al. \(2017b\)](#) suggested a difference in He content between the two populations, namely, the second generation is enriched in helium content while the first generation inherits the original compositions from the molecular cloud that labours them. Indeed, this was already shown in [Fu et al. \(2018\)](#) for the case of GC 47Tuc. More detailed and carefully tests on this aspect would be a part of this project and will be updated after this thesis.

## 7.4 Preliminary conclusions, remarks and next steps

We have presented our first preliminary results on the comparison of the new  $\alpha$ -enhanced tracks with GC M92. For this purpose, we use the most updated version of PARSEC code to perform the calculations. A preparatory work has been done to collect the chemical abundances of the cluster. This is not an easy task since the stars are very old, and it is not clear if their observed abundances are the initial abundances from which the star cluster formed. There is evidence of multiple populations but, even in that case, it is not possible to assess the previous statement. Sedimentation effects and convective dredge-up may have acted to change the observed abundances, besides the effects already known. In any case, we searched for as many chemical elements, as possible for the sake of completeness, from carbon, nitrogen, oxygen to erbium. The selection of 31 elements is shown in Table. 7.1 with the abundances that scaled to the adopted solar-abundances, for the FG and



SG of M92. As a result, we found the metallicity of the two populations which are  $[\text{Fe}/\text{H}] = -2.2360$  and  $-2.1885$  correspond to the FG and SG, as well as the  $\alpha$ -iron ratio,  $[\alpha/\text{Fe}] = 0.7151$  and  $0.5241$ , respectively.

The opacity tables are then calculated with respect to these mixtures of M92 for both FG and SG (see Sect. 7.3.1).

Based on the mass-radius relation, we perform a calculation of the solar model with this new version of the code. Especially at the very-low-mass regime, it was concluded by [Chen et al. \(2014\)](#) that a modification of the theoretical  $T$ - $\tau$  relation is needed to explain the very-low-mass region of the observed relation. However, we recognise that also in the mass range from  $\sim 0.6 - 0.75 M_{\odot}$  the theoretical relation may not be appropriate to fit the new observed data. At the moment, we don't know yet what is needed to explain the observed data in this regime, but we could think of rotation. Although, we are using data from detached eclipsing binaries where stars should not be affected by rotation. However, the stars could have been interacting in the past and the effects of rotation could be visible also now. Another possibility could be to consider the magnetic field within the star, which again calls for future work to be done. Pragmatically we could see if a small revision of the  $T$ - $\tau$  relation that we use now can cure this discrepancy.

In spite of this limitation on the M-R relation in the region from  $0.6 - 0.75 M_{\odot}$ , we may make a first look to the CMD of M92. Especially, we pay attention to the low-MS part of the cluster which, supposedly, harbours multiple stellar populations. We performed the calculations using both the adopted FG and SG-mixtures with the initial total metallicity  $Z = 0.0003$  and  $Y = 0.25$ . This choice of  $(Z, Y)$  combination is based on the enrichment law,  $Y = 0.2485 + 1.78 \times Z$ , as usually done in PARSEC models. The computed mass range in this set is from  $0.08 M_{\odot}$  up to  $1.0 M_{\odot}$ .

Roughly, we find the age of M92 could be between  $11 - 13$  Gyr with a variation of extinction coefficient  $A_V = 0.15 - 0.25$ . Though we can see there is a separation between the two generation-isochrones at the low-MS part, this is not enough to explain the widely broad colour range of the observed data. We find that it could be due to the He content as suggested in [Milone et al. \(2017b\)](#), while in our calculations we use a unique value  $Y = 0.25$ , for both generations.

More details will be obtained from the comparison of the models with the Discretionary Early Release Science (ERS program 1334) that targeted the lower main sequence of M92 ([Boyer et al., 2022](#)).

PI: Daniel Weisz, University of California - Berkeley, Investigators. Ti-

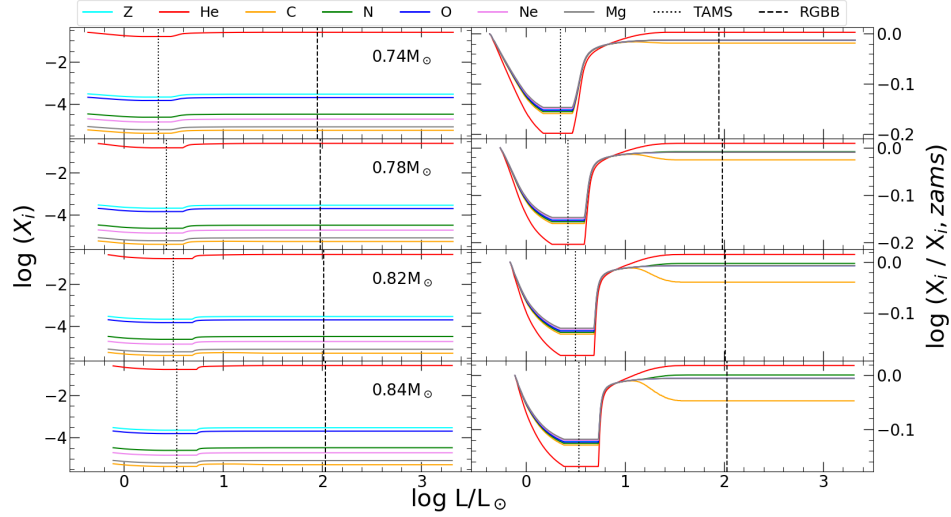


Figure 7.6: Evolution of surface chemical abundances from the ZAMS to the tip of RGB phase. *Left panel:* The variation of current surface He, C, N, O, Ne, Mg, and metallicity Z of four selected stars with masses from  $0.74 - 0.84 M_{\odot}$  in the set of FG-mixtures ( $Z=0.0003$ ). *Right panel:* The variation of surface abundances normalised to their initial values (taken at the ZAMS).

tle: The Resolved Stellar Populations Early Release Science Allocation: 27.5 hours allocation (program Completed).

After the calibration with M92, a new collection of stellar evolutionary tracks and isochrones with  $\alpha$ -enhanced mixtures for several initial metallicities with detailed descriptions will be delivered to the community.

We finally conclude this chapter by comparing the initial surface abundances adopted for this cluster with those predicted by our calculations in different evolutionary phases. This latter could represent the observed ones, allowing us to get a posterior evaluation of the possible evolutionary corrections to be applied to observed abundances in old stars. Figure. 7.6 shows the changes of surface abundances from the ZAMS up to the tip of RGB phase of four selected models, with initial mass ranging from  $M_i = 0.75 M_{\odot}$  to  $M_i = 0.85 M_{\odot}$ . These models have been selected because they are representative of the upper main sequence of the globular cluster M92, which is

known to have an age of about  $\sim 11 - 13$  Gyr.

Despite the significant change during the MS due to the diffusion process, the surface abundances tend to be re-homogenised when stars reach the RGB, when the first dredge-up event begins. A factor of changing with respect to their initial abundance is clearly seen in the left-panel of Fig. 7.6, different for different elements. The absolute value of this factor is also different in different mass models. I plan to carry out this work in more detail in my future career.

# Chapter 8

## Conclusion

In order to conclude this thesis, a short summary of the works that I have done during my PhD will be presented in this chapter. Producing the new collection of stellar evolutionary tracks and corresponding isochrones with rotation is the main target of my PhD thesis. Essentially, I focus on the low- and intermediate-mass range, however including also a range of massive stars. For this purpose, first, after the introduction in Chapter. 1, I summarised the standard classical model of spherical symmetry stellar structure and evolution in Chapter. 2. Then, in Chapter. 3, I describe the structure equations of stars under the impact of rotation, from the theoretical point of view. The effect of geometrical distortions that leads to the redistribution of effective temperature along the latitude angle is clearly shown. They are due to the changes of surface gravity caused by centrifugal forces in rotating models. In Chapter. 4, I discuss the transport of angular momentum and the mixing of chemical elements in rotating stars. The pure diffusive scheme is adopted to solve the transport equation of angular momentum. The chemical mixing is also described by the pure diffusive scheme. The total diffusive coefficient is the sum of all processes that are at work. Namely, in the convective zones turbulent diffusion, and in the regions where the two rotational instabilities actively work, i.e., meridional circulation and shear instability. The calibration of these two parameters is necessary before any calculations and is done in PARSEC V2.0 ([Costa et al., 2019b](#)). Another process that directly impacts the transport of angular momentum is mass loss. It becomes even more important due to the enhancement in the case of rotating stars. Many adopted empirical formulas from literature are available, but I have also considered a self-consistent mass loss rate from [Cranmer and Saar](#)

(2011) that I plan to apply in the future to low-mass stars.

In Chapter. 5, I present the new collection of stellar tracks that are computed with rotation by using the PARSEC V2.0 code. The effects of rotation are carefully studied for both cases of low-mass and intermediate-mass stars. In the HRD, we find that rotating stars tend to be cooler and more luminous with respect to their non-rotating counterparts, an effect that is due to the loss of spherical symmetry and due to the extra mixing caused by rotation. Besides that, the stars spend a longer time in the MS phase and build a heavier He-core in the post-MS phases. The angular velocity of the He-cores slowly increases after the TAMS. However, their rotation rates are rather modest. We also find the enhancement of the CNO-cycle products at the surface in the case of intermediate-mass/massive stars. In Chapter. 6, I present the corresponding isochrones. The isochrones are constructed using the TRILEGAL code, and are complemented with photometric magnitudes in many filter systems. The BC tables for rotating stars take into account several inclination angles. To show the result of our new models we compare them with the Gaia CM diagrams of two open clusters, M67 and NGC 6633. We find that our new isochrone reproduces very well the hook feature of M67 as well as the “global” fitting of the cluster, with an age of  $\sim 3.72$  Gyrs for  $[\text{Fe}/\text{H}] \sim 0$ ,  $(m - M)_0 = 9.69$  and  $A_V = 0.1$  mag. We find a hint of at least two populations that are harboured in the cluster NGC 6633. In particular, one population with fast rotating stars that can explain the extended MS turn-off region, while the second population is composed of non-rotating stars that is used to explain the location of the three stars at the He-clump. To provide our new models to the community, we developed a web-interface for tracks at <sup>1</sup> and at <sup>2</sup> for isochrones. A detailed description of these two interfaces and the corresponding databases is presented in this chapter.

In Chapter. 7, I present my ongoing projects on the calculation of  $\alpha$ -enhanced mixtures for the study of GCs, galactic bulge, and the Milky Way thick disc. The detailed chemical abundances of GC M92 for both FG and SG are carefully collected from literature. The new opacity tables as well as the EOS tables are updated with these new chemical compositions. At the moment, we focus on the very-low-mass range and do a first preliminary comparison using the metallicity  $Z = 0.0003$  for both FG- and SG-mixtures. We suspect that the He-content may play a role to explain the broadness of

---

<sup>1</sup>[http://stev.oapd.inaf.it/PARSEC/tracks\\_v2.html](http://stev.oapd.inaf.it/PARSEC/tracks_v2.html)

<sup>2</sup>[http://stev.oapd.inaf.it/cgi-bin/cmd\\_3.7](http://stev.oapd.inaf.it/cgi-bin/cmd_3.7)

the lower main sequence of M92. We also focus on the mass-radius relation, since we are dealing with the VLM stars. We see that the calibrated  $T$ - $\tau$  relation (Chen et al., 2014) is good to explain the observed data below  $\sim 0.6M_{\odot}$ , while in the region between  $\sim 0.6-0.75M_{\odot}$  there is still a mismatch between the models and the observed data. Rotation and/or magnetic fields could play a role in this aspect. However, we need to carefully study these effects before we can draw any firm conclusions on this subject.

# Appendix A

## Self-consistence mass loss rate

*Mass Loss* is a process refers to the fact that the stars lose their material during their evolution, study the mass loss rate can help us understand the final state of stars in their evolution. Let us start from the definition of mass and energy's conservation law of a spherical symmetry star,

$$\frac{\partial r}{\partial m} = \frac{1}{4\pi r^2 \rho} \quad (\text{A.1})$$

$$\frac{\partial L}{\partial m} = \epsilon - T \frac{\partial S}{\partial t} \quad (\text{A.2})$$

with  $r$  is radius of the sphere in [cm];  $m$  is the mass (in [g]) corresponds to a sphere of radius  $r$ ;  $\rho$  is the correspond density in [ $\text{g cm}^{-3}$ ];  $L$  is the luminosity in [ $\text{erg s}^{-1}$ ];  $\epsilon$  is the energy generated rate which is in unit of [ $\text{erg s}^{-1} \text{ g}^{-1}$ ];  $T$  is the temperature in K;  $S$  is the entropy which characterizes for the thermodynamic state of the system in [ $\text{erg K}^{-1} \text{ g}^{-1}$ ].

Using the definition of total flux  $F = L/4\pi r^2$  which is the energy received per unit area (in [ $\text{erg cm}^{-2} \text{ s}^{-1}$ ]) and substitute Eq. A.1 to Eq. A.2 we would obtain a relation,

$$\frac{1}{\rho} \frac{1}{4\pi r^2} \frac{\partial 4\pi r^2 F}{\partial r} = \epsilon - T \frac{\partial S}{\partial t}. \quad (\text{A.3})$$

Now, we consider a single fluid of pure hydrogen plasma which is assumed in a steady state. As a consequence of this assumption, the entropy term would be vanished in the right hand side of Eq. A.3. For convenience of latter calculations, we denote  $A = 4\pi r^2$  is the cross-section area of the fluid, and

hence Eq. A.3 becomes

$$-\rho\epsilon + \frac{1}{A} \frac{\partial(AF)}{\partial r} = 0. \quad (\text{A.4})$$

Note, the term  $-\rho\epsilon$  in the right-hand side of Eq. A.4 is called by the radiative energy loss which is in unit of  $[erg.cm^{-3}.s^{-1}]$ . The radiative energy loss is written as

$$-\rho\epsilon = N^2 \Lambda(T) = \frac{P^2}{4k_B^2 T^2} \Lambda(T). \quad (\text{A.5})$$

In which,  $N$  is the total number density in the fully ionized system;  $P = 2Nk_B T$  is the gas pressure, the number 2 is due to the fact that there are 2 particles considered ( $e^-, p$ ); and  $\Lambda(T)$  is the radiative loss function (see Cranmer et al. (2007)).

The total energy flux is now described as a sum of contribution due to thermal conduction ( $F_C$ ), mechanical energy transport ( $F_M$ ), stellar wind ( $F_W$ ) and Alfvén wave ( $F_A$ ) (see Hammer, 1982; Withbroe, 1988),

$$F = F_C + F_M + F_W + F_A. \quad (\text{A.6})$$

For latter conveniences we rewrite the energy conservation law,

$$\frac{P^2}{4k_B^2 T^2} \Lambda(T) + \frac{1}{A} \frac{\partial}{\partial r} [A (F_C + F_M + F_W + F_A)] = 0. \quad (\text{A.7})$$

In combine with the conservation of mass and momentum (see Withbroe, 1988),

$$\rho u A = constant, \quad (\text{A.8})$$

$$\rho u \frac{du}{dr} = -\frac{dP}{dr} - \rho \frac{GM}{r^2} - \frac{d}{dr} \frac{\langle \delta B^2 \rangle}{8\pi}, \quad (\text{A.9})$$

the three equations, Eq. A.7-A.9, are the basic equations for deducing the mass loss rate of cool stars, which will be described in more details in the following sections.

The model of cool-star mass loss was studied in Cranmer and Saar (2011), in which the authors analyse the winds in two scenarios. The outflow wind can be driven by gas pressure or wave pressure which corresponds to a hot corona and cool, extended chromosphere regions. We will discuss in more details about both these mechanisms in the next following sections.



## A.1 Hot coronal Mass Loss

In this section we are considering a plasma fluid with a high gas pressure, this may cause an acceleration to produce a transition region (TR) from the base (cool chromosphere) to the hot corona region (the illustration of this phenomenon is showing in Fig. 4.4). As a consequence, the outflow speed in hot corona region is much larger than the Alfvén wave speed. More precisely, the Alfvén wave flux is expected to depend strongly on the gravity (Eq. A.54), (see also Cranmer and Saar, 2011), hence in the region of hot coronal, the effect of Alfvén wave is negligible. The energy conservation law in Eq. A.7 now becomes,

$$\frac{P^2}{4k_B^2 T^2} \Lambda(T) + \frac{1}{A} \frac{\partial}{\partial r} [A(F_C + F_M + F_W)] = 0. \quad (\text{A.10})$$

Now, we will consider one by one the energy fluxes in Eq. A.10 above. First, the energy flux driven by stellar winds. It is a sum of kinetic energy flux and potential energy flux (see Cranmer and Saar, 2011; Hammer, 1982), which is

$$F_W = j \left( \frac{u^2}{2} - \frac{GM}{r} \right), \quad (\text{A.11})$$

in which,  $j = \rho u$  is the mass flux in unit of  $[\text{g cm}^{-2} \text{ s}^{-1}]$  and  $u$  is the outflow speed in  $\text{cm s}^{-1}$ .

Due to the inward direction of conductive energy flux, it is more convenience that we replace  $F_C$  to  $-F_C$ , knowing that  $F_C$  now is understood as the magnitude of conductive flux. The energy conservation equation is now becomes,

$$\frac{P^2}{4k_B^2 T^2} \Lambda(T) + \frac{1}{A} \frac{\partial}{\partial r} \left\{ A \left[ F_M - F_C + j \left( \frac{u^2}{2} - \frac{GM}{r} \right) \right] \right\} = 0. \quad (\text{A.12})$$

By integrating the equation above from TR region to  $r \rightarrow \infty$  and have in mind the assumption that the radiative loss energy is balanced with both the energy transported toward the stellar surface by thermal conduction and the energy deposited by the mechanical energy from the far distanced hot corona layers (see Withbroe, 1988). This lead us to a relation,

$$A_{TR} (F_{M,TR} - F_C) - (jA)_{TR} \frac{GM_*}{R_*} = (jA)_\infty \frac{u_\infty^2}{2}. \quad (\text{A.13})$$

Note that, in the expression above the kinetic energy at TR is assumably negligible, but a dominant at large distances. Besides, if the corona is a low corona, the transition region could be considered as a thin area. As a consequence, the mass and radius at TR are the stellar mass and radius,  $M_{TR} = M_*$ ,  $R_{TR} = R_*$ .

By the definition of conservation of mass,  $jA$  is a constant. The mass loss rate is defined as  $\dot{M} \equiv jA$  so that it obeys Eq. A.13,

$$A_{TR}(F_{M,TR} - F_C) = \dot{M} \left( \frac{u_\infty^2}{2} + \frac{GM_*}{R_*} \right). \quad (\text{A.14})$$

In the study of [Cranmer and Saar \(2011\)](#), they assumed the outflow speed at far distance is equal to the escape velocity, which is

$$u_\infty = V_{esc} = \sqrt{\frac{2GM_*}{R_*}}. \quad (\text{A.15})$$

Thus, the mass loss rate is now written as,

$$\dot{M} = \frac{A_{TR}(F_{M,TR} - F_C)}{V_{esc}^2}. \quad (\text{A.16})$$

The expression of mechanical flux and conductive flux will be discussed in the following subsections due to their complexities. Besides, it's worth to mention about the cross-section area  $A$ . As introduced before that the area  $A = 4\pi r^2$ , however, this classical definition can not be able to describe the cross-section area of a complexity plasma fluid. The cross-section area is now defined as,

$$A = 4\pi r^2 f(r), \quad (\text{A.17})$$

where  $f(r)$  is called by the filling factor which characterizes for the geometrical of the fluid tube, which is a dimensionless factor and tends to increase with height to a completely symmetry shape of fluid at  $\infty$ , by definition  $f_\infty = 1$ . As shown in Fig. 4.4, the filling factor at transition region is falling somewhere in between it's value at the photosphere and at the far distance,  $f_* < f_{TR} < f_\infty$ . In [Cranmer and Saar \(2011\)](#), the filling factor at TR is assumed to relate to photosphere filling factor  $f_*$  by a power law that  $f_{TR} = f_*^\theta$ , with  $\theta$  is a dimensionless constant between 0 and 1. In this project  $\theta$  is chosen to be 1/3. (see also [Kopp and Holzer \(1976\)](#))

### A.1.1 Mechanical energy flux

The mechanical energy flux is the flux of heat transferring between radiation and matter in corona regions. In the special case, in which the heat rate  $Q \propto r^{-\beta}$  and  $A \propto r^\gamma$ , with  $\beta, \gamma$  are constant and will be compressed into the scaling factor  $h$  as a single variable, [Cranmer and Saar \(2011\)](#). Formally,  $Q$  is computed by

$$Q = \frac{1}{A} \frac{\partial(AF)}{\partial r} = \frac{\tilde{\alpha} \rho v_\perp^3}{\lambda_\perp}, \quad (\text{A.18})$$

thus we can deduce the mechanical flux from this relation by integrating both sides of the equation above from the base of TR to infinity. In static atmosphere model that the mechanical heating energy is negligible, thus the mechanical flux at TR is computed by

$$(AF_M)_{TR} = \int_{R_*}^{\infty} Q(r) A(r) dr. \quad (\text{A.19})$$

Using the expression of  $Q$  and  $A$  above with an assumption that  $Q(\infty) \ll Q_{TR}$ , we finally get the expression of TR mechanical flux,

$$F_{M,TR} \equiv Q_{TR} R_* h. \quad (\text{A.20})$$

where,  $h = 1/|\beta - \gamma - 1| = [0.5, 1.5]$  is a dimensionless scaling factor;  $Q_{TR}$  denote for the heating rate at TR. The transverse velocity  $v_\perp \propto \rho^{-1/4}$  at near the photosphere and the effective correlation length  $\lambda_\perp \propto A^{1/2} \propto B^{-1/2}$ . Then, taking the ratio between heating rate at TR and at photosphere, we would have

$$\frac{Q_{TR}}{Q_*} = \frac{\tilde{\alpha}_{TR}}{\tilde{\alpha}_*} \left( \frac{\rho_{TR}}{\rho_*} \right)^{1/4} \left( \frac{B_{TR}}{B_*} \right)^{1/2}. \quad (\text{A.21})$$

Besides that, from the relation between  $A$  and  $B$ , we get a relation of magnetic field strength ratio with the filling factor ratio, which is

$$\frac{B_{TR}}{B_*} = \frac{A_*}{A_{TR}} = \frac{f_*}{f_{TR}} = f_*^{1-\theta}. \quad (\text{A.22})$$

Making another assumption that the heating rate at TR is equal to the maximum of radiative cooling function  $Q_{cool}$  (see [Cranmer et al. \(2007\)](#)), that is written as,

$$Q_{TR} = \max |Q_{cool}| = \frac{\rho_{TR}^2 \Lambda_{max}}{m_H^2}. \quad (\text{A.23})$$

From this relation we could be able to deduce the density at TR by inserting  $Q_{TR}$  in Eq. A.21 into Eq. A.23, as a result the stellar density at TR is obtained as

$$\rho_{TR} = \left[ \frac{\tilde{\alpha}_{TR} Q_* m_H^2}{\tilde{\alpha}_* \rho_*^{1/4} \Lambda_{max}} \right]^{4/7} f_*^{2(1-\theta)/7}. \quad (\text{A.24})$$

And then, put  $\rho_{TR}$  above back into Eq. A.21 in combine with Eq. A.22 we can obtain the expression of heating rate at TR,

$$Q_{TR} = \left( \frac{\tilde{\alpha}_{TR} Q_*}{\tilde{\alpha}_*} \right)^{8/7} \left( \frac{m_H^2}{\rho_*^2 \Lambda_{max}} \right)^{1/7} f_*^{4(1-\theta)/7}, \quad (\text{A.25})$$

in which  $\theta = [0, 1]$ ;  $m_H = 1.67333 \times 10^{-24}$  (g) is hydrogen mass;  $\Lambda_{max}$  is the maximum of radiative loss function which depends on metallicity as given in [Cranmer and Saar \(2011\)](#),

$$\frac{\Lambda_{max}}{10^{-23} \text{erg cm}^3 \text{s}^{-1}} \approx 7.4 + 42 \left( \frac{Z}{Z_\odot} \right)^{1.13}. \quad (\text{A.26})$$

$\tilde{\alpha}_* = 0.5$  and the  $\tilde{\alpha}_{TR}$  is computed by a relation,

$$\tilde{\alpha} = \alpha_0 \frac{\mathcal{R}(1 + \mathcal{R})\sqrt{2}}{(1 + \mathcal{R}^2)^{3/2}}, \quad (\text{A.27})$$

$\tilde{\alpha}$  is the efficiency factor which depends on the effective reflection coefficient  $\mathcal{R}$ , in turns,  $\mathcal{R}$  describes for the fact that stars create upward waves give rise to the downward waves as a reflection. The chosen  $\alpha_0 = 0.5$  is based on the turbulent transport model of [Breech et al. \(2009\)](#),

$$\mathcal{R} \approx (V_A - u_\infty)/(V_A + u_\infty), \quad (\text{A.28})$$

where  $V_A = B/(4\pi\rho)^{1/2}$  is the Alfvén speed and  $B$  denote for the magnetic field strength; and  $u_\infty$  is the asymptotic outflow speed in a coronal wind which is assumed to be equal to escape velocity  $u_\infty = V_{esc}$  as mentioned above.

The heating rate at photosphere,  $Q_*$ , is computed by

$$Q_* = \frac{\tilde{\alpha}_* \rho_* v_{\perp*}^3}{\lambda_{\perp*}}, \quad (\text{A.29})$$

where  $\lambda_{\perp*} = \lambda_{\perp\odot} (H_*/H_\odot)$  is an effective correlation length for the largest eddies in the turbulent cascade which called by perpendicular length scale.

The solar values are  $\lambda_{\perp\odot} = 300$  km and  $H_{\odot} = 139$  km, (see [Cranmer and Saar, 2011](#)). The transverse velocity amplitude of Alfvén wave in the photosphere,  $v_{\perp*}$  is determined by the energy flux  $F_{A*}$ ,

$$v_{\perp*} = \sqrt{\frac{F_{A*}}{\rho_* V_{A*}}} \quad (\text{A.30})$$

see more details in section. [A.2](#)

### A.1.2 Conductive energy flux

In the inner corona, the conductive energy flux is given by (see [Hammer \(1982\)](#))

$$F_C = -\kappa \frac{dT}{dr} \quad (\text{A.31})$$

with thermal conductivity,

$$\kappa = (1.89 \times 10^{-5} \text{ erg.cm}^{-1}.\text{s}^{-1}.\text{K}^{-7/2}) \frac{T^{5/2}}{\ln \Lambda(T)}. \quad (\text{A.32})$$

As mentioned in [Withbroe \(1988\)](#), for a static atmosphere with a negligible mechanical heating energy, one can consider the thermal conduction energy is balanced by the radiative energy loss. Therefore, Eq. [A.10](#) is now reduced to

$$\frac{1}{A} \frac{\partial}{\partial r} (AF_C) = -\frac{P^2}{4k_B^2 T^2} \Lambda(T) \quad \text{or} \quad -\frac{4k_B^2 T^2}{P^2} \frac{1}{\Lambda(T)} \partial(AF_C) = A \partial r. \quad (\text{A.33})$$

Assume that we are in a low corona so that the TR cross-section area is very thin, thus the equation above can be reduced to a simpler form,

$$-\frac{4k_B^2 T^2}{P^2} \frac{1}{\Lambda(T)} dF_C = dr. \quad (\text{A.34})$$

Substituting  $dr$  above to Eq. [A.31](#), we have

$$-\frac{4k_B^2 T^2}{P^2} \frac{1}{\Lambda(T)} F_C dF_C = -\kappa dT \quad \text{or} \quad F_C dF_C = \frac{\kappa P^2}{4k_B^2 T^2} \Lambda(T) dT. \quad (\text{A.35})$$

Now, integrate both sides of the equation above we will obtain,

$$\frac{1}{2} [F_C^2(T_0) - F_C^2(T_{TR})] = \int_{T_{TR}}^{T_0} \frac{\kappa P^2}{4k_B^2 T^2} \Lambda(T) dT \quad (\text{A.36})$$

$$= -1.89 \times 10^{-5} \frac{P^2}{4k_B^2} \int_{T_0}^{T_{TR}} \frac{\Lambda T^{1/2}}{\ln \Lambda} dT, \quad (\text{A.37})$$

where  $T_0$  is the temperature at cool photosphere and  $T_{TR}$  is the temperature at TR. We also assume that the conductive flux at the TR is much higher than at the photosphere  $F_C(T_{TR}) \gg F_C(T_0)$ , and thus we have

$$F_C = \left( \sqrt{\frac{1.89 \times 10^{-5}}{2k_B^2} \int_{T_0}^{T_{TR}} \frac{\Lambda T^{1/2}}{\ln \Lambda} dT} \right) P_{TR} = c_{rad} P_{TR}, \quad (\text{A.38})$$

where  $c_{rad}$  is a constant (in unit of speed  $cm/s$ ) which is expressed in [Cranmer and Saar \(2011\)](#),

$$c_{rad} \approx 14 \times 10^5 \sqrt{\frac{\Lambda_{max}(Z)}{\Lambda_{max}(Z_\odot)}}; \quad (\text{A.39})$$

and  $P_{TR} = (2\rho_{TR}/m_H)k_B T_{TR}$  is the pressure at the TR,  $\Lambda_{max}$  is in Eq. [A.26](#). Besides,  $T_{TR} = 2 \times 10^5$  K and the TR density is given in Eq. [A.24](#),

$$\rho_{TR} = \left[ \frac{\tilde{\alpha}_{TR} Q_* m_H^2}{\tilde{\alpha}_* \rho_*^{1/4} \Lambda_{max}} \right]^{4/7} f_*^{2(1-\theta)/7}. \quad (\text{A.40})$$

## A.2 Cold-wave driven Mass Loss

In this section, we will consider one fluid in which the neutral and ion species move together as a whole and the temperature of all pieces are equal. Besides that, in a high density stellar atmosphere, the mechanical heating may balance with the radiative loss energy and thus the total energy flux is now contributed only from stellar wind, thermal conduction and Alfvén wave,  $F = F_W + F_C + F_A$  (see [Cranmer and Saar \(2011\)](#)). However, the contribution of conductive energy can be neglected according to [Holzer et al. \(1983\)](#) by considering the isothermal outflow wind model, thus the conductive energy flux is ignorable in case of cold-wave wind. In that case, the gas pressure can't be enough to drive a significant outflow, and the cooling wave starts to become a dominant.

Rewrite the conservation of mass and momentum in Eq. A.8 and Eq. A.9,

$$\rho u A = \text{constant}, \quad (\text{A.41})$$

$$\rho u \frac{du}{dr} = -\rho \frac{dv_T^2}{dr} + \frac{\rho}{2} \frac{dV_{esc}^2}{dr} - \frac{d}{dr} \left( \frac{\langle \delta B^2 \rangle}{8\pi} \right), \quad (\text{A.42})$$

where  $v_T^2 = P/\rho$  is thermal speed,  $P$  is gas pressure and  $\langle \delta B^2 \rangle$  is the mean square wave magnetic field which related to mean square velocity field  $\langle \delta v^2 \rangle$  through energy density  $\xi$ ,

$$\xi = \frac{\langle \delta B^2 \rangle}{4\pi} = \rho \langle \delta v^2 \rangle. \quad (\text{A.43})$$

Since we are considering the simplest case of cold-wave driven wind which is based on the condition that  $v_T^2 \ll \langle \delta v^2 \rangle$  and  $M_A \ll 1$ . Therefore, to obtain the equation of motion of this flow we will insert  $\langle \delta B^2 \rangle$  from Eq. A.43 into Eq. A.42, simplify  $\rho$  in both sides and apply the two conditions of cold wave, as a result we will get an equation

$$\frac{d}{dr} (u^2 - \langle \delta v^2 \rangle - V_{esc}^2) = 0. \quad (\text{A.44})$$

Now, from the definition of mass loss rate  $\dot{M} = \rho u A = \text{constant}$  and we assume that the region is isothermal so that exists a critical point where the temperature at this point doesn't change and thus we have,

$$\dot{M} = \rho_c u_c A_c. \quad (\text{A.45})$$

First of all, in order to determine the critical density  $\rho_c$  we base on the energy conservation of wave action, which is,

$$\tilde{S} \equiv \rho v_{\perp}^2 V_A A = \text{constant} \quad \text{or} \quad \rho_c = \frac{\rho_* v_{\perp*}^2 V_{A*} A_*}{v_{\perp,c}^2 V_{A,c} A_c}, \quad (\text{A.46})$$

thus the critical radius would be the first parameter that we must know. From the equation of motion Eq. A.44, we have

$$u_c^2 - \langle \delta v_c^2 \rangle - V_{esc,c}^2 = u_0^2 - \langle \delta v_0^2 \rangle - V_{esc,0}^2 = -V_{esc,0}^2 \left( 1 + \frac{\langle \delta v_0^2 \rangle - u_0^2}{V_{esc,0}^2} \right). \quad (\text{A.47})$$

Besides that, from [Hammer \(1982\)](#) we know that at the critical point we would have two equations,

$$\begin{aligned} u_c^2 - \frac{1}{4}\langle\delta v_c^2\rangle &= 0, \\ \langle\delta v_c^2\rangle - \frac{V_{esc,c}^2}{\beta} &= 0. \end{aligned} \tag{A.48}$$

where  $\beta = (r/2A)(dA/dr)$ . Therefore, we can reduce the left-hand side of Eq. A.47 to only  $V_{esc,c}^2$  by using the relation in Eq. A.48, we will have the final relation as

$$-V_{esc,c}^2 \left(1 + \frac{3}{4}\frac{1}{\beta}\right) = -V_{esc,0}^2 \left(1 + \frac{\langle\delta v_0^2\rangle - u_0^2}{V_{esc,0}^2}\right), \tag{A.49}$$

or,

$$\frac{r_c}{R_*} = \left(1 + \frac{3}{4}\frac{1}{\beta}\right) \bigg/ \left(1 + \frac{\langle\delta v_0^2\rangle - u_0^2}{V_{esc,0}^2}\right); \tag{A.50}$$

if the flow is spherical symmetric, i.e.,  $\beta = 1$ ; and assume that the outflow speed at photosphere is very small  $u_0 \ll 1$ , thus we have the relation of critical radius and photosphere radius which as follows

$$\frac{r_c}{R_*} \approx \frac{7/4}{1 + (v_{\perp*}/V_{esc})^2} \tag{A.51}$$

with  $v_{\perp*}^2 \equiv \langle\delta v_0^2\rangle$  is the transverse velocity at the photosphere.

Starting from the Alfvén wave energy flux,

$$F_A = \xi V_A = \rho \langle\delta v^2\rangle V_A \tag{A.52}$$

with  $\xi$  is taken from Eq. A.43. Therefore, the transverse velocity at photosphere can be computed by,

$$v_{\perp*} = \sqrt{\frac{F_{A*}}{\rho_* V_{A*}}}. \tag{A.53}$$

In turn, the Alfvén wave energy flux at photosphere is given in [Cranmer and Saar \(2011\)](#), in which they utilized the model of [Musielak and Ulmschneider \(2002\)](#) with a mixing length  $\alpha = 2$ , and  $B = 0.85B_{eq}$  to get the analytic fit,

$$F_{A*} = F_0 \left(\frac{T_{eff}}{T_0}\right)^\eta \exp \left[ - \left(\frac{T_{eff}}{T_0}\right)^{25} \right], \tag{A.54}$$



where,

$$\frac{F_0}{10^9[erg.cm^{-2}.s^{-1}]} = 5.724 \exp\left(-\frac{\log g}{11.48}\right), \quad (A.55)$$

$$\frac{T_0}{10^3[K]} = 5.624 + 0.6002 \log g, \quad (A.56)$$

$$\eta = 6.774 + 0.5057 \log g, \quad (A.57)$$

$\log g = 0, 1, 2, 3, 4, 5$  are the gravitational acceleration.

Therefore, the critical cross-section area is determined through  $A_c = 4\pi r_c^2$  by considering that the flowing fluid is symmetry at the critical point. For the Alfvén wave velocities, we use the assumption of magnetic flux conservation,  $BA = \text{constant}$ , so that  $\langle \delta B^2/4\pi \rangle = B^2/4\pi$  and  $\langle \delta v^2 \rangle = V_A^2$ , then put those onto Eq. A.43 and we will get

$$V_A = \frac{B}{(4\pi\rho)^{1/2}}. \quad (A.58)$$

Using Eq. A.58 for both photosphere region and critical point we will obtain the  $V_{A,*}$  and  $V_{A,c}$  in Eq. A.46. The magnetic field strength at photosphere is given in Cranmer and Saar (2011) which is,

$$B_* = 1.13 B_{eq} = 1.13 \sqrt{\frac{8\pi\rho_* k_B T_{eff}}{\mu m_H}}, \quad (A.59)$$

with  $\mu$  is the mean atomic weight which is computed through effective temperature  $T_{eff}$ ,

$$\mu \approx \frac{7}{4} + \frac{1}{2} \tanh\left(\frac{3500 - T_{eff}}{600}\right), \quad (A.60)$$

and the magnetic field strength at critical point is computed from the magnetic flux conservation that,

$$B_* A_* = B_c A_c \quad \text{or} \quad B_c = \left(\frac{R_*}{r_c}\right)^2 f_* B_*. \quad (A.61)$$

The final parameter that we need to know in order to determine the critical density is the transverse velocity at this point,  $v_{\perp,c}$ . As pointed out

in [Holzer et al. \(1983\)](#) that the flow speed at critical point is a sound speed modified by Alfvén waves

$$v_s^2 = v_T^2 + \frac{1}{4} \left( \frac{1 + 3M_A}{1 + M_A} \right) \langle \delta v^2 \rangle, \quad (\text{A.62})$$

hence, apply for cold-wave driven wind (i.e.,  $v_T^2 \ll \langle \delta v^2 \rangle$  and  $M_A \ll 1$ ) we would have the transverse velocity at critical point is

$$v_{\perp,c} = 2u_c. \quad (\text{A.63})$$

Finally, it is obvious from Eq. [A.48](#) with  $\beta = 1$  that,

$$u_c = \sqrt{\frac{1}{4} V_{esc,c}^2} = \sqrt{\frac{1}{2} \frac{GM_*}{r_c}}. \quad (\text{A.64})$$

Due to the appearance of  $\rho_c$  while computing  $V_{A,c}$  we should rewritten the formula of  $\rho_c$  in Eq. [A.46](#), such that

$$\rho_c = 4\pi \left( \frac{\rho_* v_{\perp*}^2 V_{A*} A_*}{v_{\perp,c}^2 B_c A_c} \right)^2. \quad (\text{A.65})$$

### A.3 Combining hot and cold mass loss rate

The total mass loss rate is the sum from both contributions, i.e., hot coronal and cold-wave driven. However, based on a fact that there are stars that has no corona, thus the total mass loss is expressed in the form as,

$$\dot{M} = \dot{M}_{cold} + \dot{M}_{hot} \exp(-4M_{A,TR}^2), \quad (\text{A.66})$$

where the  $\dot{M}_{hot}$  is given in Eq. [A.16](#);  $\dot{M}_{cold}$  is given in Eq. [A.45](#) and the TR Mach number,  $M_{A,TR} = u_{TR}/V_{A,TR}$ .

The TR outflow speed is deduced from the hot coronal region through the mass flux conservation which is,

$$u_{TR} = \frac{\dot{M}_{hot}}{4\pi R_*^2 f_{TR} \rho_{TR}}. \quad (\text{A.67})$$

In the expression above, the filling factor at TR is assumed to be  $f_{TR} = f_*^\theta$ ; and the TR density is given in Eq. A.24,

$$\rho_{TR} = \left[ \frac{\tilde{\alpha}_{TR} Q_* m_H^2}{\tilde{\alpha}_* \rho_*^{1/4} \Lambda_{max}} \right]^{4/7} f_*^{2(1-\theta)/7}, \quad (\text{A.68})$$

all the parameters in the expression above are described in section. A.1.1

The Alfvén speed at TR is computed by,

$$V_{A,TR} = \frac{B_{TR}}{\sqrt{4\pi\rho_{TR}}}, \quad (\text{A.69})$$

where  $B_{TR}$  is given in Eq. A.22,  $B_{TR} = f_*^{1-\theta} B_*$ ; and in turn,  $B_*$  is computed by Eq. A.59.

# Bibliography

- M. Aaronson and J. Mould. The extended giant branches of intermediate age globular clusters in the Magellanic Clouds. II. *ApJS*, 48:161–184, February 1982. doi: 10.1086/190773.
- D. C. Abbott and L. B. Lucy. Multiline transfer and the dynamics of stellar winds. *ApJ*, 288:679–693, January 1985. doi: 10.1086/162834.
- Helmut A. Abt, Frederic H. Chaffee, and Graham Suffolk. Rotational Velocities of AP Stars. *ApJ*, 175:779, August 1972. doi: 10.1086/151598.
- Eric G. Adelberger, Sam M. Austin, John N. Bahcall, A. B. Balantekin, Gilles Bogaert, Lowell S. Brown, Lothar Buchmann, F. Edward Cecil, Arthur E. Champagne, Ludwig de Braekeleer, Charles A. Duba, Steven R. Elliott, Stuart J. Freedman, Moshe Gai, G. Goldring, Christopher R. Gould, Andrei Gruzinov, Wick C. Haxton, Karsten M. Heeger, Ernest Henley, Calvin W. Johnson, Marc Kamionkowski, Ralph W. Kavanagh, Steven E. Koonin, Kuniharu Kubodera, Karlheinz Langanke, Tohru Motobayashi, Vijay Pandharipande, Peter Parker, R. G. Robertson, Claus Rolfs, R. F. Sawyer, N. Shaviv, T. D. Shoppa, K. A. Snover, Erik Swanson, Robert E. Tribble, Sylvaine Turck-Chièze, and John F. Wilkerson. Solar fusion cross sections. *Reviews of Modern Physics*, 70(4):1265–1291, October 1998. doi: 10.1103/RevModPhys.70.1265.
- D. R. Alexander and J. W. Ferguson. Low-Temperature Rosseland Opacities. *ApJ*, 437:879, December 1994. doi: 10.1086/175039.
- F. Allard, D. Homeier, and B. Freytag. Models of very-low-mass stars, brown dwarfs and exoplanets. *Philosophical Transactions of the Royal Society of London Series A*, 370(1968):2765–2777, June 2012. doi: 10.1098/rsta.2011.0269.
- M. Alongi, G. Bertelli, A. Bressan, and C. Chiosi. Effects of envelope overshoot on stellar models. *A&A*, 244:95, April 1991.

- L. Amard, A. Palacios, C. Charbonnel, F. Gallet, C. Georgy, N. Lagarde, and L. Siess. First grids of low-mass stellar models and isochrones with self-consistent treatment of rotation. From 0.2 to 1.5  $M_{\odot}$  at seven metallicities from PMS to TAMS. *A&A*, 631:A77, November 2019. doi: 10.1051/0004-6361/201935160.
- A. M. Amarsi, P. E. Nissen, and Á. Skúladóttir. Carbon, oxygen, and iron abundances in disk and halo stars. Implications of 3D non-LTE spectral line formation. *A&A*, 630:A104, October 2019. doi: 10.1051/0004-6361/201936265.
- A. Aparicio, G. Bertelli, C. Chiosi, and J. M. Garcia-Pelayo. CCD UBV<sub>R</sub> photometry of the old rich open cluster King 2 : comparison with theoretical models. *A&A*, 240:262, December 1990.
- F. Arenou, X. Luri, C. Babusiaux, C. Fabricius, A. Helmi, T. Muraveva, A. C. Robin, F. Spoto, A. Vallenari, T. Antoja, T. Cantat-Gaudin, C. Jordi, N. Leclerc, C. Reylé, M. Romero-Gómez, I. C. Shih, S. Soria, C. Barache, D. Bossini, A. Bragaglia, M. A. Breddels, M. Fabrizio, S. Lambert, P. M. Marrese, D. Massari, A. Moitinho, N. Robichon, L. Ruiz-Dern, R. Sordo, J. Veljanoski, L. Eyer, G. Jasiewicz, E. Pancino, C. Soubiran, A. Spagna, P. Tanga, C. Turon, and C. Zurbach. Gaia Data Release 2. Catalogue validation. *A&A*, 616:A17, August 2018. doi: 10.1051/0004-6361/201833234.
- Martin Asplund, Nicolas Grevesse, and A. Jacques Sauval. The solar chemical composition. *Nucl. Phys. A*, 777:1–4, October 2006. doi: 10.1016/j.nuclphysa.2005.06.010.
- Martin Asplund, Nicolas Grevesse, A. Jacques Sauval, and Pat Scott. The Chemical Composition of the Sun. *ARA&A*, 47(1):481–522, September 2009. doi: 10.1146/annurev.astro.46.060407.145222.
- Robert Baade, Thomas Kirsch, Dieter Reimers, Frank Toussaint, Philip D. Bennett, Alexander Brown, and Graham M. Harper. The Wind Outflow of zeta Aurigae: A Model Revision Using Hubble Space Telescope Spectra. *ApJ*, 466: 979, August 1996. doi: 10.1086/177569.
- J. N. Bahcall and M. H. Pinsonneault. Helium Diffusion in the Sun. *ApJ*, 395: L119, August 1992. doi: 10.1086/186502.
- D. Bemmerer, F. Confortola, H. Costantini, A. Formicola, Gy. Gyürky, R. Bonetti, C. Brogini, P. Corvisiero, Z. Elekes, Zs. Fülöp, G. Gervino, A. Guglielmetti, C. Gustavino, G. Imbriani, M. Junker, M. Laubenstein, A. Lemut, B. Limata, V. Lozza, M. Marta, R. Menegazzo, P. Prati, V. Roca, C. Rolfs,

- C. Rossi Alvarez, E. Somorjai, O. Straniero, F. Strieder, F. Terrasi, and H. P. Trautvetter. Activation Measurement of the  $\text{He3}(\alpha, \gamma)\text{Be7}$  Cross Section at Low Energy. *Phys. Rev. Lett.*, 97(12):122502, September 2006. doi: 10.1103/PhysRevLett.97.122502.
- T. Bensby, S. Feltzing, and M. S. Oey. Exploring the Milky Way stellar disk. A detailed elemental abundance study of 714 F and G dwarf stars in the solar neighbourhood. *A&A*, 562:A71, February 2014. doi: 10.1051/0004-6361/201322631.
- G. Bertelli, A. G. Bressan, and C. Chiosi. The HR diagram of massive stars : widening of the main sequence band and WR formation. *A&A*, 130:279–293, January 1984.
- G. Bertelli, A. Bressan, C. Chiosi, and K. Angerer. Evolutionary models for low and intermediate mass stars with convective overshooting. *A&AS*, 66:191–234, November 1986.
- G. Bertelli, R. Betto, A. Bressan, C. Chiosi, E. Nasi, and A. Vallenari. Theoretical isochrones with convective overshoot. *A&AS*, 85:845–853, October 1990a.
- G. Bertelli, R. Betto, A. Bressan, C. Chiosi, E. Nasi, and A. Vallenari. Theoretical isochrones with convective overshoot. *A&AS*, 85:845–853, October 1990b.
- G. Bertelli, L. Girardi, P. Marigo, and E. Nasi. Scaled solar tracks and isochrones in a large region of the Z-Y plane. I. From the ZAMS to the TP-AGB end for 0.15-2.5  $\{M\}_{\odot}$  stars. *A&A*, 484(3):815–830, June 2008. doi: 10.1051/0004-6361:20079165.
- J. E. Bjorkman and J. P. Cassinelli. Equatorial Disk Formation around Rotating Stars Due to Ram Pressure Confinement by the Stellar Wind. *ApJ*, 409:429, May 1993. doi: 10.1086/172676.
- T. Bloeker. Stellar evolution of low and intermediate-mass stars. I. Mass loss on the AGB and its consequences for stellar evolution. *A&A*, 297:727, May 1995.
- K. H. Böhm. Über die Größe der Konvektionselemente in Schichten mit variablem Temperaturgradienten. Mit 2 Textabbildungen. *ZAp*, 46:245, January 1958.
- E. Böhm-Vitense. Über die Wasserstoffkonvektionszone in Sternen verschiedener Effektivtemperaturen und Leuchtkräfte. Mit 5 Textabbildungen. *ZAp*, 46:108, January 1958.

- D. Bossini, A. Miglio, M. Salaris, M. Vrad, S. Cassisi, B. Mosser, J. Montalbán, L. Girardi, A. Noels, A. Bressan, A. Pietrinferni, and J. Tayar. Kepler red-clump stars in the field and in open clusters: constraints on core mixing. *MNRAS*, 469(4):4718–4725, August 2017. doi: 10.1093/mnras/stx1135.
- D. Bossini, A. Vallenari, A. Bragaglia, T. Cantat-Gaudin, R. Sordo, L. Balaguer-Núñez, C. Jordi, A. Moitinho, C. Soubiran, L. Casamiquela, R. Carrera, and U. Heiter. Age determination for 269 Gaia DR2 open clusters. *A&A*, 623:A108, March 2019. doi: 10.1051/0004-6361/201834693.
- Diego Bossini, Andrea Miglio, Maurizio Salaris, Adriano Pietrinferni, Josefina Montalbán, Alessandro Bressan, Arlette Noels, Santi Cassisi, Léo Girardi, and Paola Marigo. Uncertainties on near-core mixing in red-clump stars: effects on the period spacing and on the luminosity of the AGB bump. *MNRAS*, 453(3): 2290–2301, November 2015. doi: 10.1093/mnras/stv1738.
- Martha L. Boyer, Jay Anderson, Mario Gennaro, Marla Geha, Kristen B. Wingfield McQuinn, Erik Tollerud, Matteo Correnti, Max J. Brenner Newman, Roger E. Cohen, Nitya Kallivayalil, Rachel Beaton, Andrew A. Cole, Andrew Dolphin, Jason S. Kalirai, Karin M. Sandstrom, Alessandro Savino, Evan D. Skillman, Daniel R. Weisz, and Benjamin F. Williams. The JWST Resolved Stellar Populations Early Release Science Program. I. NIRCам Flux Calibration. *Research Notes of the American Astronomical Society*, 6(9):191, September 2022. doi: 10.3847/2515-5172/ac923a.
- B. Breech, W. H. Matthaeus, S. R. Cranmer, J. C. Kasper, and S. Oughton. Electron and proton heating by solar wind turbulence. *Journal of Geophysical Research (Space Physics)*, 114(A9):A09103, Sep 2009. doi: 10.1029/2009JA014354.
- A. Bressan, G. Bertelli, and C. Chiosi. Evolution of low mass stars with convective overshooting. *Mem. Soc. Astron. Italiana*, 57:411–426, 1986.
- A. Bressan, F. Fagotto, G. Bertelli, and C. Chiosi. Evolutionary Sequences of Stellar Models with New Radiative Opacities. II.  $Z = 0.02$ . *A&AS*, 100:647, September 1993.
- A. G. Bressan, C. Chiosi, and G. Bertelli. Mass loss and overshooting in massive stars. *A&A*, 102(1):25–30, September 1981.
- Alessandro Bressan, Paola Marigo, Léo. Girardi, Bernardo Salasnich, Claudia Dal Cero, Stefano Rubele, and Ambra Nanni. PARSEC: stellar tracks and isochrones with the PAdova and TRieste Stellar Evolution Code. *MNRAS*, 427(1):127–145, November 2012. doi: 10.1111/j.1365-2966.2012.21948.x.

- I. Brott, S. E. de Mink, M. Cantiello, N. Langer, A. de Koter, C. J. Evans, I. Hunter, C. Trundle, and J. S. Vink. Rotating massive main-sequence stars. I. Grids of evolutionary models and isochrones. *A&A*, 530:A115, June 2011. doi: 10.1051/0004-6361/201016113.
- E. Caffau, H. G. Ludwig, M. Steffen, B. Freytag, and P. Bonifacio. Solar Chemical Abundances Determined with a CO5BOLD 3D Model Atmosphere. *Sol. Phys.*, 268(2):255–269, February 2011. doi: 10.1007/s11207-010-9541-4.
- T. Cantat-Gaudin, C. Jordi, A. Vallenari, A. Bragaglia, L. Balaguer-Núñez, C. Soubiran, D. Bossini, A. Moitinho, A. Castro-Ginard, A. Krone-Martins, L. Casamiquela, R. Sordo, and R. Carrera. A Gaia DR2 view of the open cluster population in the Milky Way. *A&A*, 618:A93, October 2018. doi: 10.1051/0004-6361/201833476.
- Bruce W. Carney. The Constancy of  $[\alpha/\text{Fe}]$  in Globular Clusters of Differing  $[\text{Fe}/\text{H}]$  and Age. *PASP*, 108:900, October 1996. doi: 10.1086/133811.
- E. Carretta and R. G. Gratton. Abundances for globular cluster giants. I. Homogeneous metallicities for 24 clusters. *A&AS*, 121:95–112, January 1997. doi: 10.1051/aas:1997116.
- E. Carretta, A. Bragaglia, R. G. Gratton, S. Lucatello, G. Catanzaro, F. Leone, M. Bellazzini, R. Claudi, V. D’Orazi, Y. Momany, S. Ortolani, E. Pancino, G. Piotto, A. Recio-Blanco, and E. Sabbi. Na-O anticorrelation and HB. VII. The chemical composition of first and second-generation stars in 15 globular clusters from GIRAFFE spectra. *A&A*, 505(1):117–138, October 2009. doi: 10.1051/0004-6361/200912096.
- Eugenio Carretta, Raffaele G. Gratton, Gisella Clementini, and Flavio Fusi Pecci. Distances, Ages, and Epoch of Formation of Globular Clusters. *ApJ*, 533(1): 215–235, April 2000. doi: 10.1086/308629.
- L. Casamiquela, C. Soubiran, P. Jofré, C. Chiappini, N. Lagarde, Y. Tarricq, R. Carrera, C. Jordi, L. Balaguer-Núñez, J. Carbajo-Hijarrubia, and S. Blanco-Cuaresma. Abundance-age relations with red clump stars in open clusters. *A&A*, 652:A25, August 2021. doi: 10.1051/0004-6361/202039951.
- Santi Cassisi, Maurizio Salaris, and Giuseppe Bono. The Shape of the Red Giant Branch Bump as a Diagnostic of Partial Mixing Processes in Low-Mass Stars. *ApJ*, 565(2):1231–1238, February 2002. doi: 10.1086/324695.



- S. Catalán, J. Isern, E. García-Berro, and I. Ribas. The initial-final mass relationship of white dwarfs revisited: effect on the luminosity function and mass distribution. *MNRAS*, 387(4):1693–1706, July 2008. doi: 10.1111/j.1365-2966.2008.13356.x.
- B. Chaboyer and J. P. Zahn. Effect of horizontal turbulent diffusion on transport by meridional circulation. *A&A*, 253:173–177, January 1992.
- Brian Chaboyer and Yong-Cheol Kim. The OPAL Equation of State and Low-Metallicity Isochrones. *ApJ*, 454:767, December 1995. doi: 10.1086/176529.
- Brian Chaboyer, P. Demarque, and M. H. Pinsonneault. Stellar Models with Microscopic Diffusion and Rotational Mixing. I. Application to the Sun. *ApJ*, 441:865, March 1995. doi: 10.1086/175408.
- Yang Chen, Léo Girardi, Alessandro Bressan, Paola Marigo, Mauro Barbieri, and Xu Kong. Improving PARSEC models for very low mass stars. *MNRAS*, 444(3):2525–2543, November 2014. doi: 10.1093/mnras/stu1605.
- Yang Chen, Alessandro Bressan, Léo Girardi, Paola Marigo, Xu Kong, and Antonio Lanza. PARSEC evolutionary tracks of massive stars up to  $350 M_{\odot}$  at metallicities  $0.0001 \leq Z \leq 0.04$ . *MNRAS*, 452(1):1068–1080, September 2015. doi: 10.1093/mnras/stv1281.
- Yang Chen, Léo Girardi, Xiaoting Fu, Alessandro Bressan, Bernhard Aringer, Piero Dal Tio, Giada Pastorelli, Paola Marigo, Guglielmo Costa, and Xing Zhang. YBC: a stellar bolometric corrections database with variable extinction coefficients. Application to PARSEC isochrones. *A&A*, 632:A105, December 2019. doi: 10.1051/0004-6361/201936612.
- Alessandro Chieffi and Marco Limongi. Pre-supernova Evolution of Rotating Solar Metallicity Stars in the Mass Range  $13\text{--}120 M_{\odot}$  and their Explosive Yields. *ApJ*, 764(1):21, February 2013. doi: 10.1088/0004-637X/764/1/21.
- Alessandro Chieffi and Marco Limongi. The Synthesis of  $^{44}\text{Ti}$  and  $^{56}\text{Ni}$  in Massive Stars. *ApJ*, 836(1):79, February 2017. doi: 10.3847/1538-4357/836/1/79.
- Jieun Choi, Aaron Dotter, Charlie Conroy, Matteo Cantiello, Bill Paxton, and Benjamin D. Johnson. MESA Isochrones and Stellar Tracks (MIST). I. Solar-scaled Models. *ApJ*, 823(2):102, June 2016. doi: 10.3847/0004-637X/823/2/102.

- J. Christensen-Dalsgaard, M. J. P. F. G. Monteiro, M. Rempel, and M. J. Thompson. A more realistic representation of overshoot at the base of the solar convective envelope as seen by helioseismology. *MNRAS*, 414(2):1158–1174, June 2011. doi: 10.1111/j.1365-2966.2011.18460.x.
- A. Claret and G. Torres. The dependence of convective core overshooting on stellar mass. *A&A*, 592:A15, July 2016. doi: 10.1051/0004-6361/201628779.
- Antonio Claret and Guillermo Torres. The Dependence of Convective Core Overshooting on Stellar Mass: A Semi-empirical Determination Using the Diffusive Approach with Two Different Element Mixtures. *ApJ*, 849(1):18, November 2017. doi: 10.3847/1538-4357/aa8770.
- Antonio Claret and Guillermo Torres. The Dependence of Convective Core Overshooting on Stellar Mass: Additional Binary Systems and Improved Calibration. *ApJ*, 859(2):100, June 2018. doi: 10.3847/1538-4357/aabd35.
- Antonio Claret and Guillermo Torres. The Dependence of Convective Core Overshooting on Stellar Mass: Reality Check and Additional Evidence. *ApJ*, 876(2):134, May 2019. doi: 10.3847/1538-4357/ab1589.
- Thomas Constantino and Isabelle Baraffe. Significant uncertainties from calibrating overshooting with eclipsing binary systems. *A&A*, 618:A177, October 2018. doi: 10.1051/0004-6361/201833568.
- Guglielmo Costa. Evolution of rotating stars with parsec: implementation and comparison with observations, 2019.
- Guglielmo Costa, Léo Girardi, Alessandro Bressan, Yang Chen, Paul Goudfrooij, Paola Marigo, Thaíse S. Rodrigues, and Antonio Lanza. Multiple stellar populations in NGC 1866. New clues from Cepheids and colour-magnitude diagram. *A&A*, 631:A128, November 2019a. doi: 10.1051/0004-6361/201936409.
- Guglielmo Costa, Léo Girardi, Alessandro Bressan, Paola Marigo, Thaíse S. Rodrigues, Yang Chen, Antonio Lanza, and Paul Goudfrooij. Mixing by overshooting and rotation in intermediate-mass stars. *MNRAS*, 485(4):4641–4657, June 2019b. doi: 10.1093/mnras/stz728.
- Guglielmo Costa, Alessandro Bressan, Michela Mapelli, Paola Marigo, Giuliano Iorio, and Mario Spera. Formation of GW190521 from stellar evolution: the impact of the hydrogen-rich envelope, dredge-up, and  $^{12}\text{C}(\alpha, \gamma)^{16}\text{O}$  rate on the pair-instability black hole mass gap. *MNRAS*, 501(3):4514–4533, March 2021. doi: 10.1093/mnras/staa3916.

- Guglielmo Costa, Alessandro Ballone, Michela Mapelli, and Alessandro Bressan. Formation of black holes in the pair-instability mass gap: evolution of a post-collision star. *arXiv e-prints*, art. arXiv:2204.03492, April 2022.
- Steven R. Cranmer and Steven H. Saar. Testing a Predictive Theoretical Model for the Mass Loss Rates of Cool Stars. *ApJ*, 741(1):54, November 2011. doi: 10.1088/0004-637X/741/1/54.
- Steven R. Cranmer, Adriaan A. van Ballegooijen, and Richard J. Edgar. Self-consistent Coronal Heating and Solar Wind Acceleration from Anisotropic Magnetohydrodynamic Turbulence. *apjs*, 171(2):520–551, Aug 2007. doi: 10.1086/518001.
- Paul A. Crowther, Olivier Schnurr, Raphael Hirschi, Norhasliza Yusof, Richard J. Parker, Simon P. Goodwin, and Hasan Abu Kassim. The R136 star cluster hosts several stars whose individual masses greatly exceed the accepted  $150M_{\text{stellar}}$  stellar mass limit. *MNRAS*, 408(2):731–751, October 2010. doi: 10.1111/j.1365-2966.2010.17167.x.
- Richard H. Cyburt, A. Matthew Amthor, Ryan Ferguson, Zach Meisel, Karl Smith, Scott Warren, Alexander Heger, R. D. Hoffman, Thomas Rauscher, Alexander Sakharuk, Hendrik Schatz, F. K. Thielemann, and Michael Wiescher. The JINA REACLIB Database: Its Recent Updates and Impact on Type-I X-ray Bursts. *ApJS*, 189(1):240–252, July 2010. doi: 10.1088/0067-0049/189/1/240.
- L. da Silva, L. Girardi, L. Pasquini, J. Setiawan, O. von der L  he, J. R. de Medeiros, A. Hatzes, M. P. D  llinger, and A. Weiss. Basic physical parameters of a selected sample of evolved stars. *A&A*, 458(2):609–623, November 2006. doi: 10.1051/0004-6361:20065105.
- Francesca D’Antona, Antonino P. Milone, Marco Tailo, Paolo Ventura, Enrico Vesperini, and Marcella di Criscienzo. Stars caught in the braking stage in young Magellanic Cloud clusters. *Nature Astronomy*, 1:0186, August 2017. doi: 10.1038/s41550-017-0186.
- C. de Jager, H. Nieuwenhuijzen, and K. A. van der Hucht. Mass loss rates in the Hertzsprung-Russell diagram. *A&AS*, 72:259–289, February 1988.
- L. Decin, M. Montarg  s, A. M. S. Richards, C. A. Gottlieb, W. Homan, I. McDonald, I. El Mellah, T. Danilovich, S. H. J. Wallstr  m, A. Zijlstra, A. Baudry, J. Bolte, E. Cannon, E. De Beck, F. De Ceuster, A. de Koter, J. De Ridder, S. Etoka, D. Gobrecht, M. Gray, F. Herpin, M. J  ste, E. Lagadec, P. Kervella,

- T. Khouri, K. Menten, T. J. Millar, H. S. P. Müller, J. M. C. Plane, R. Sahai, H. Sana, M. Van de Sande, L. B. F. M. Waters, K. T. Wong, and J. Yates. (Sub)stellar companions shape the winds of evolved stars. *Science*, 369(6510): 1497–1500, September 2020. doi: 10.1126/science.abb1229.
- Pierre Demarque, Jong-Hak Woo, Yong-Cheol Kim, and Sukyoung K. Yi. Y<sup>2</sup> Isochrones with an Improved Core Overshoot Treatment. *ApJS*, 155(2):667–674, December 2004. doi: 10.1086/424966.
- H. E. Dewitt, H. C. Graboske, and M. S. Cooper. Screening Factors for Nuclear Reactions. I. General Theory. *ApJ*, 181:439–456, April 1973. doi: 10.1086/152061.
- A. Di Cecco, R. Becucci, G. Bono, M. Monelli, P. B. Stetson, S. Degl’Innocenti, P. G. Prada Moroni, M. Nonino, A. Weiss, R. Buonanno, A. Calamida, F. Caputo, C. E. Corsi, I. Ferraro, G. Iannicola, L. Pulone, M. Romaniello, and A. R. Walker. On the Absolute Age of the Globular Cluster M92. *PASP*, 122(895): 991, September 2010. doi: 10.1086/656017.
- Aaron Dotter, Brian Chaboyer, Darko Jevremović, Veselin Kostov, E. Baron, and Jason W. Ferguson. The Dartmouth Stellar Evolution Database. *ApJS*, 178(1): 89–101, September 2008. doi: 10.1086/589654.
- A. K. Dupree, A. Dotter, C. I. Johnson, A. F. Marino, A. P. Milone, III Bailey, J. I., J. D. Crane, M. Mateo, and E. W. Olszewski. NGC 1866: First Spectroscopic Detection of Fast-rotating Stars in a Young LMC Cluster. *ApJ*, 846(1):L1, September 2017. doi: 10.3847/2041-8213/aa85dd.
- A. S. Eddington. *The Internal Constitution of the Stars*. 1926.
- P. Eggenberger, G. Meynet, A. Maeder, R. Hirschi, C. Charbonnel, S. Talon, and S. Ekström. The Geneva stellar evolution code. *Ap&SS*, 316(1-4):43–54, August 2008. doi: 10.1007/s10509-007-9511-y.
- P. Eggenberger, A. Miglio, J. Montalbán, O. Moreira, A. Noels, G. Meynet, and A. Maeder. Effects of rotation on the evolution and asteroseismic properties of red giants. *A&A*, 509:A72, January 2010. doi: 10.1051/0004-6361/200912897.
- S. Ekström, C. Georgy, P. Eggenberger, G. Meynet, N. Mowlavi, A. Wyttenbach, A. Granada, T. Decressin, R. Hirschi, U. Frischknecht, C. Charbonnel, and A. Maeder. Grids of stellar models with rotation. I. Models from 0.8 to 120 M<sub>⊙</sub> at solar metallicity (Z = 0.014). *A&A*, 537:A146, January 2012. doi: 10.1051/0004-6361/201117751.

- A. S. Endal and S. Sofia. Rotation in solar-type stars. I - Evolutionary models for the spin-down of the sun. *ApJ*, 243:625–640, January 1981. doi: 10.1086/158628.
- F. Espinosa Lara and M. Rieutord. The dynamics of a fully radiative rapidly rotating star enclosed within a spherical box. *A&A*, 470(3):1013–1022, August 2007. doi: 10.1051/0004-6361:20077263.
- D. W. Evans, M. Riello, F. De Angeli, J. M. Carrasco, P. Montegriffo, C. Fabricius, C. Jordi, L. Palaversa, C. Diener, G. Busso, C. Cacciari, F. van Leeuwen, P. W. Burgess, M. Davidson, D. L. Harrison, S. T. Hodgkin, E. Pancino, P. J. Richards, G. Altavilla, L. Balaguer-Núñez, M. A. Barstow, M. Bellazzini, A. G. A. Brown, M. Castellani, G. Cocozza, F. De Luise, A. Delgado, C. Ducourant, S. Galleti, G. Gilmore, G. Giuffrida, B. Holl, A. Kewley, S. E. Koposov, S. Marinoni, P. M. Marrese, P. J. Osborne, A. Piersimoni, J. Portell, L. Pulone, S. Ragaini, N. Sanna, D. Terrett, N. A. Walton, T. Wevers, and Ł. Wyrzykowski. Gaia Data Release 2. Photometric content and validation. *A&A*, 616:A4, August 2018. doi: 10.1051/0004-6361/201832756.
- F. Fagotto, A. Bressan, G. Bertelli, and C. Chiosi. Evolutionary sequences of stellar models with new radiative opacities. III.  $Z=0.0004$  and  $Z=0.05$ . *A&AS*, 104:365–376, April 1994a.
- F. Fagotto, A. Bressan, G. Bertelli, and C. Chiosi. Evolutionary sequences of stellar models with new radiative opacities. IV.  $Z=0.004$  and  $Z=0.008$ . *A&AS*, 105:29–38, May 1994b.
- Jason W. Ferguson, David R. Alexander, France Allard, Travis Barman, Julia G. Bodnarik, Peter H. Hauschildt, Amanda Heffner-Wong, and Akemi Tamanai. Low-Temperature Opacities. *ApJ*, 623(1):585–596, April 2005. doi: 10.1086/428642.
- Wendy L. Freedman, Barry F. Madore, Dylan Hatt, Taylor J. Hoyt, In Sung Jang, Rachael L. Beaton, Christopher R. Burns, Myung Gyoon Lee, Andrew J. Monson, Jillian R. Neeley, M. M. Phillips, Jeffrey A. Rich, and Mark Seibert. The Carnegie-Chicago Hubble Program. VIII. An Independent Determination of the Hubble Constant Based on the Tip of the Red Giant Branch. *ApJ*, 882(1):34, September 2019. doi: 10.3847/1538-4357/ab2f73.
- Wendy L. Freedman, Barry F. Madore, Taylor Hoyt, In Sung Jang, Rachael Beaton, Myung Gyoon Lee, Andrew Monson, Jill Neeley, and Jeffrey Rich. Calibration of the Tip of the Red Giant Branch. *ApJ*, 891(1):57, March 2020. doi: 10.3847/1538-4357/ab7339.

- David B. Friend and David C. Abbott. The Theory of Radiatively Driven Stellar Winds. III. Wind Models with Finite Disk Correction and Rotation. *ApJ*, 311: 701, December 1986. doi: 10.1086/164809.
- Xiaoting Fu, Alessandro Bressan, Paolo Molaro, and Paola Marigo. Lithium evolution in metal-poor stars: from pre-main sequence to the Spite plateau. *MNRAS*, 452(3):3256–3265, September 2015. doi: 10.1093/mnras/stv1384.
- Xiaoting Fu, Alessandro Bressan, Paola Marigo, Léo Girardi, Josefina Montalbán, Yang Chen, and Ambra Nanni. New PARSEC data base of  $\alpha$ -enhanced stellar evolutionary tracks and isochrones - I. Calibration with 47 Tuc (NGC 104) and the improvement on RGB bump. *MNRAS*, 476(1):496–511, May 2018. doi: 10.1093/mnras/sty235.
- (Babusiaux, C., et al.) Gaia Collaboration. Gaia Data Release 2. Observational Hertzsprung-Russell diagrams. *A&A*, 616:A10, August 2018a. doi: 10.1051/0004-6361/201832843.
- (Brown, A. G. A., et al.) Gaia Collaboration. Gaia Data Release 2. Summary of the contents and survey properties. *A&A*, 616:A1, August 2018b. doi: 10.1051/0004-6361/201833051.
- (Lindgren, L., et al.) Gaia Collaboration. Gaia Data Release 2. The astrometric solution. *A&A*, 616:A2, August 2018c. doi: 10.1051/0004-6361/201832727.
- C. Georgy, S. Ekström, P. Eggenberger, G. Meynet, L. Haemmerlé, A. Maeder, A. Granada, J. H. Groh, R. Hirschi, N. Mowlavi, N. Yusof, C. Charbonnel, T. Decressin, and F. Barblan. Grids of stellar models with rotation. III. Models from 0.8 to 120  $M_{\odot}$  at a metallicity  $Z = 0.002$ . *A&A*, 558:A103, October 2013. doi: 10.1051/0004-6361/201322178.
- L. Girardi, A. Bressan, G. Bertelli, and C. Chiosi. Evolutionary tracks and isochrones for low- and intermediate-mass stars: From 0.15 to 7  $M_{sun}$ , and from  $Z=0.0004$  to 0.03. *A&AS*, 141:371–383, February 2000a. doi: 10.1051/aas:2000126.
- L. Girardi, A. Bressan, G. Bertelli, and C. Chiosi. Evolutionary tracks and isochrones for low- and intermediate-mass stars: From 0.15 to 7  $M_{sun}$ , and from  $Z=0.0004$  to 0.03. *A&AS*, 141:371–383, February 2000b. doi: 10.1051/aas:2000126.

- L. Girardi, G. Bertelli, A. Bressan, C. Chiosi, M. A. T. Groenewegen, P. Marigo, B. Salasnich, and A. Weiss. Theoretical isochrones in several photometric systems. I. Johnson-Cousins-Glass, HST/WFPC2, HST/NICMOS, Washington, and ESO Imaging Survey filter sets. *A&A*, 391:195–212, August 2002. doi: 10.1051/0004-6361:20020612.
- L. Girardi, M. A. T. Groenewegen, E. Hatziminaoglou, and L. da Costa. Star counts in the Galaxy. Simulating from very deep to very shallow photometric surveys with the TRILEGAL code. *A&A*, 436(3):895–915, June 2005. doi: 10.1051/0004-6361:20042352.
- Léo Girardi, Julianne Dalcanton, Benjamin Williams, Roelof de Jong, Carme Gallart, Matteo Monelli, Martin A. T. Groenewegen, Jon A. Holtzman, Knut A. G. Olsen, Anil C. Seth, Daniel R. Weisz, and ANGST/ANGRRR Collaboration. Revised Bolometric Corrections and Interstellar Extinction Coefficients for the ACS and WFPC2 Photometric Systems. *PASP*, 120(867):583, May 2008. doi: 10.1086/588526.
- Léo Girardi, Guglielmo Costa, Yang Chen, Paul Goudfrooij, Alessandro Bressan, Paola Marigo, and Andrea Bellini. On the photometric signature of fast rotators. *MNRAS*, 488(1):696–705, September 2019. doi: 10.1093/mnras/stz1767.
- Diego Godoy-Rivera, Marc H. Pinsonneault, and Luisa M. Rebull. Stellar Rotation in the Gaia Era: Revised Open Clusters’ Sequences. *ApJS*, 257(2):46, December 2021. doi: 10.3847/1538-4365/ac2058.
- O. A. Gonzalez, M. Rejkuba, M. Zoccali, V. Hill, G. Battaglia, C. Babusiaux, D. Minniti, B. Barbuy, A. Alves-Brito, A. Renzini, A. Gomez, and S. Ortolani. Alpha element abundances and gradients in the Milky Way bulge from FLAMES-GIRAFFE spectra of 650 K giants. *A&A*, 530:A54, June 2011. doi: 10.1051/0004-6361/201116548.
- S. Goswami, A. Slemer, P. Marigo, A. Bressan, L. Silva, M. Spera, L. Boco, V. Grisoni, L. Pantoni, and A. Lapi. The effects of the initial mass function on Galactic chemical enrichment. *A&A*, 650:A203, June 2021. doi: 10.1051/0004-6361/202039842.
- S. Goswami, L. Silva, A. Bressan, V. Grisoni, G. Costa, P. Marigo, G. L. Granato, A. Lapi, and M. Spera. Impact of very massive stars on the chemical evolution of extremely metal-poor galaxies. *A&A*, 663:A1, July 2022. doi: 10.1051/0004-6361/202142031.

- H. C. Graboske, H. E. Dewitt, A. S. Grossman, and M. S. Cooper. Screening Factors for Nuclear Reactions. II. Intermediate Screen-Ing and Astrophysical Applications. *ApJ*, 181:457–474, April 1973. doi: 10.1086/152062.
- G. Gräfener and W. R. Hamann. Mass loss from late-type WN stars and its Z-dependence. Very massive stars approaching the Eddington limit. *A&A*, 482(3): 945–960, May 2008. doi: 10.1051/0004-6361:20066176.
- N. Grevesse and A. J. Sauval. Standard Solar Composition. *Space Sci. Rev.*, 85: 161–174, May 1998. doi: 10.1023/A:1005161325181.
- A. G. Gunn, C. K. Mitrou, and J. G. Doyle. On the rotation-activity correlation for active binary stars. *mnras*, 296(1):150–164, May 1998. doi: 10.1046/j.1365-8711.1998.01347.x.
- R. Hammer. Energy balance of stellar coronae. I - Methods and examples. II - Effect of coronal heating. *apj*, 259:767–791, Aug 1982. doi: 10.1086/160213.
- A. Heger, N. Langer, and S. E. Woosley. Presupernova Evolution of Rotating Massive Stars. I. Numerical Method and Evolution of the Internal Stellar Structure. *ApJ*, 528(1):368–396, January 2000. doi: 10.1086/308158.
- L. G. Henyey, J. E. Forbes, and N. L. Gould. A New Method of Automatic Computation of Stellar Evolution. *ApJ*, 139:306, January 1964. doi: 10.1086/147754.
- Sebastian L. Hidalgo, Adriano Pietrinferni, Santi Cassisi, Maurizio Salaris, Alessio Mucciarelli, Alessandro Savino, Antonio Aparicio, Victor Silva Aguirre, and Kuldeep Verma. The Updated BaSTI Stellar Evolution Models and Isochrones. I. Solar-scaled Calculations. *ApJ*, 856(2):125, April 2018. doi: 10.3847/1538-4357/aab158.
- J. Higl, L. Siess, A. Weiss, and H. Ritter. An analysis of the TZ Fornacis binary system. *A&A*, 617:A36, September 2018. doi: 10.1051/0004-6361/201833112.
- J. Higl, E. Müller, and A. Weiss. Calibrating core overshooting parameters with two-dimensional hydrodynamical simulations. *A&A*, 646:A133, February 2021. doi: 10.1051/0004-6361/202039532.
- Susanne Höfner and Hans Olofsson. Mass loss of stars on the asymptotic giant branch. Mechanisms, models and measurements. *A&A Rev.*, 26(1):1, January 2018. doi: 10.1007/s00159-017-0106-5.



- T. E. Holzer, T. Fla, and E. Leer. Alfven waves in stellar winds. *apj*, 275:808–835, Dec 1983. doi: 10.1086/161576.
- S. Hubrig, F. Castelli, G. de Silva, J. F. González, Y. Momany, M. Netopil, and S. Moehler. A high-resolution study of isotopic composition and chemical abundances of blue horizontal branch stars in the globular clusters NGC 6397 and NGC 6752. *A&A*, 499(3):865–878, June 2009. doi: 10.1051/0004-6361/200911721.
- I. Hunter, I. Brott, N. Langer, D. J. Lennon, P. L. Dufton, I. D. Howarth, R. S. I. Ryans, C. Trundle, C. J. Evans, A. de Koter, and S. J. Smartt. The VLT-FLAMES survey of massive stars: constraints on stellar evolution from the chemical compositions of rapidly rotating Galactic and Magellanic Cloud B-type stars. *A&A*, 496(3):841–853, March 2009. doi: 10.1051/0004-6361/200809925.
- Carlos A. Iglesias and Forrest J. Rogers. Updated Opal Opacities. *ApJ*, 464:943, June 1996. doi: 10.1086/177381.
- Alan W. Irwin. FreeEOS: Equation of State for stellar interiors calculations. Astrophysics Source Code Library, record ascl:1211.002, November 2012.
- Naoki Itoh, Shinsuke Uchida, Yu Sakamoto, Yasuharu Kohyama, and Satoshi Nozawa. The Second Born Corrections to the Electrical and Thermal Conductivities of Dense Matter in the Liquid Metal Phase. *ApJ*, 677(1):495–502, April 2008. doi: 10.1086/529367.
- Adam S. Jermyn, Christopher A. Tout, and Shashikumar M. Chitre. Enhanced rotational mixing in the radiative zones of massive stars. *MNRAS*, 480(4):5427–5446, November 2018. doi: 10.1093/mnras/sty1831.
- N. Kacharov, A. Koch, E. Caffau, and L. Sbordone. Galactic evolution of sulphur as traced by globular clusters. *A&A*, 577:A18, May 2015. doi: 10.1051/0004-6361/201425058.
- Jasonjot S. Kalirai, Brad M. S. Hansen, Daniel D. Kelson, David B. Reitzel, R. Michael Rich, and Harvey B. Richer. The Initial-Final Mass Relation: Direct Constraints at the Low-Mass End. *ApJ*, 676(1):594–609, March 2008. doi: 10.1086/527028.
- S. C. Keller and P. R. Wood. Bump Cepheids in the Magellanic Clouds: Metallicities, the Distances to the LMC and SMC, and the Pulsation-Evolution Mass Discrepancy. *ApJ*, 642(2):834–841, May 2006. doi: 10.1086/501115.

- R. Kippenhahn and H. C. Thomas. A Simple Method for the Solution of the Stellar Structure Equations Including Rotation and Tidal Forces. In Arne Slettebak, editor, *IAU Colloq. 4: Stellar Rotation*, page 20, January 1970.
- R. Kippenhahn, A. Weigert, and Emmi Hofmeister. Methods for Calculating Stellar Evolution. *Methods in Computational Physics*, 7:129–190, January 1967.
- R. Kippenhahn, E. Meyer-Hofmeister, and H. C. Thomas. Rotation in Evolving Stars. *A&A*, 5:155, March 1970.
- Rudolf Kippenhahn, Alfred Weigert, and Achim Weiss. *Stellar Structure and Evolution*. 2012. doi: 10.1007/978-3-642-30304-3.
- Rudolf Kippenhahn, Alfred Weigert, and Achim Weiss. *Stellar Structure and Evolution*. 2013. doi: 10.1007/978-3-642-30304-3.
- E. Komatsu, K. M. Smith, J. Dunkley, C. L. Bennett, B. Gold, G. Hinshaw, N. Jarosik, D. Larson, M. R. Nolta, L. Page, D. N. Spergel, M. Halpern, R. S. Hill, A. Kogut, M. Limon, S. S. Meyer, N. Odegard, G. S. Tucker, J. L. Weiland, E. Wollack, and E. L. Wright. Seven-year Wilkinson Microwave Anisotropy Probe (WMAP) Observations: Cosmological Interpretation. *ApJS*, 192(2):18, February 2011. doi: 10.1088/0067-0049/192/2/18.
- R. A. Kopp and T. E. Holzer. Dynamics of coronal hole regions. I. Steady polytropic flows with multiple critical points. *solphys*, 49(1):43–56, Jul 1976. doi: 10.1007/BF00221484.
- Claus Leitherer, Carmelle Robert, and Laurent Drissen. Deposition of Mass, Momentum, and Energy by Massive Stars into the Interstellar Medium. *ApJ*, 401: 596, December 1992. doi: 10.1086/172089.
- K. Lodders, H. Palme, and H. P. Gail. Abundances of the Elements in the Solar System. *Landolt B&ouml;rnsstein*, 4B:712, January 2009. doi: 10.1007/978-3-540-88055-4\_34.
- J. MacDonald and D. J. Mullan. Precision modelling of M dwarf stars: the magnetic components of CM Draconis. *MNRAS*, 421(4):3084–3101, April 2012. doi: 10.1111/j.1365-2966.2012.20531.x.
- A. Maeder. Stellar evolution III: the overshooting from convective cores. *A&A*, 40(3):303–310, May 1975.

- A. Maeder and G. Meynet. Stellar evolution with rotation. VI. The Eddington and Omega -limits, the rotational mass loss for OB and LBV stars. *A&A*, 361: 159–166, September 2000.
- A. Maeder, G. Meynet, N. Lagarde, and C. Charbonnel. The thermohaline, Richardson, Rayleigh-Taylor, Solberg-Høiland, and GSF criteria in rotating stars. *A&A*, 553:A1, May 2013. doi: 10.1051/0004-6361/201220936.
- André Maeder. *Physics, Formation and Evolution of Rotating Stars*. 2009. doi: 10.1007/978-3-540-76949-1.
- Eric E. Mamajek and Lynne A. Hillenbrand. Improved Age Estimation for Solar-Type Dwarfs Using Activity-Rotation Diagnostics. *apj*, 687(2):1264–1293, Nov 2008. doi: 10.1086/591785.
- P. Marigo and B. Aringer. Low-temperature gas opacity. *ÆSOPUS*: a versatile and quick computational tool. *A&A*, 508(3):1539–1569, December 2009. doi: 10.1051/0004-6361/200912598.
- P. Marigo, L. Girardi, C. Chiosi, and P. R. Wood. Zero-metallicity stars. I. Evolution at constant mass. *A&A*, 371:152–173, May 2001. doi: 10.1051/0004-6361:20010309.
- Paola Marigo, Alessandro Bressan, Ambra Nanni, Léo Girardi, and Maria Letizia Pumo. Evolution of thermally pulsing asymptotic giant branch stars - I. The COLIBRI code. *MNRAS*, 434(1):488–526, September 2013. doi: 10.1093/mnras/stt1034.
- Paola Marigo, Léo Girardi, Alessandro Bressan, Philip Rosenfield, Bernhard Aringer, Yang Chen, Marco Dussin, Ambra Nanni, Giada Pastorelli, Thaíse S. Rodrigues, Michele Trabucchi, Sara Bladh, Julianne Dalcanton, Martin A. T. Groenewegen, Josefina Montalbán, and Peter R. Wood. A New Generation of PARSEC-COLIBRI Stellar Isochrones Including the TP-AGB Phase. *ApJ*, 835(1):77, January 2017. doi: 10.3847/1538-4357/835/1/77.
- F. Martins, A. Hervé, J. C. Bouret, W. Marcolino, G. A. Wade, C. Neiner, E. Alecian, J. Grunhut, and V. Petit. The MiMeS survey of magnetism in massive stars: CNO surface abundances of Galactic O stars. *A&A*, 575:A34, March 2015. doi: 10.1051/0004-6361/201425173.
- A. McQuillan, T. Mazeh, and S. Aigrain. Rotation Periods of 34,030 Kepler Main-sequence Stars: The Full Autocorrelation Sample. *apjs*, 211(2):24, Apr 2014. doi: 10.1088/0067-0049/211/2/24.

- Szabolcs Mészáros, Thomas Masseron, D. A. García-Hernández, Carlos Allende Prieto, Timothy C. Beers, Dmitry Bizyaev, Drew Chojnowski, Roger E. Cohen, Katia Cunha, Flavia Dell’Agli, Garrett Ebelke, José G. Fernández-Trincado, Peter Frinchaboy, Doug Geisler, Sten Hasselquist, Fred Hearty, Jon Holtzman, Jennifer Johnson, Richard R. Lane, Ivan Lacerna, Penelopé Longa-Peña, Steven R. Majewski, Sarah L. Martell, Dante Minniti, David Nataf, David L. Nidever, Kaike Pan, Ricardo P. Schiavon, Matthew Shetrone, Verne V. Smith, Jennifer S. Sobek, Guy S. Stringfellow, László Szigeti, Baitian Tang, John C. Wilson, and Olga Zamora. Homogeneous analysis of globular clusters from the APOGEE survey with the BACCHUS code - II. The Southern clusters and overview. *MNRAS*, 492(2):1641–1670, February 2020. doi: 10.1093/mnras/stz3496.
- G. Meynet and A. Maeder. Stellar evolution with rotation. I. The computational method and the inhibiting effect of the  $\mu$ -gradient. *A&A*, 321:465–476, May 1997.
- G. Meynet, A. Maeder, G. Schaller, D. Schaerer, and C. Charbonnel. Grids of massive stars with high mass loss rates. V. From 12 to 120  $M_{\text{sun}}$  at  $Z=0.001$ , 0.004, 0.008, 0.020 and 0.040. *A&AS*, 103:97–105, January 1994a.
- G. Meynet, A. Maeder, G. Schaller, D. Schaerer, and C. Charbonnel. Grids of massive stars with high mass loss rates. V. From 12 to 120  $M_{\text{sun}}$  at  $Z=0.001$ , 0.004, 0.008, 0.020 and 0.040. *A&AS*, 103:97–105, January 1994b.
- A. Miglio, K. Brogaard, D. Stello, W. J. Chaplin, F. D’Antona, J. Montalbán, S. Basu, A. Bressan, F. Grundahl, M. Pinsonneault, A. M. Serenelli, Y. Elsworth, S. Hekker, T. Kallinger, B. Mosser, P. Ventura, A. Bonanno, A. Noels, V. Silva Aguirre, R. Szabo, J. Li, S. McCauliff, C. K. Middour, and H. Kjeldsen. Asteroseismology of old open clusters with Kepler: direct estimate of the integrated red giant branch mass-loss in NGC 6791 and 6819. *MNRAS*, 419(3):2077–2088, January 2012. doi: 10.1111/j.1365-2966.2011.19859.x.
- A. P. Milone, A. F. Marino, F. D’Antona, L. R. Bedin, G. Piotto, H. Jerjen, J. Anderson, A. Dotter, M. di Criscienzo, and E. P. Lagioia. Multiple stellar populations in Magellanic Cloud clusters - V. The split main sequence of the young cluster NGC 1866. *MNRAS*, 465(4):4363–4374, March 2017a. doi: 10.1093/mnras/stw2965.
- A. P. Milone, G. Piotto, A. Renzini, A. F. Marino, L. R. Bedin, E. Vesperini, F. D’Antona, D. Nardiello, J. Anderson, I. R. King, D. Yong, A. Bellini, A. Aparicio, B. Barbuy, T. M. Brown, S. Cassisi, S. Ortolani, M. Salaris, A. Sarajedini, and R. P. van der Marel. The Hubble Space Telescope UV Legacy Survey

- of Galactic globular clusters - IX. The Atlas of multiple stellar populations. *MNRAS*, 464(3):3636–3656, January 2017b. doi: 10.1093/mnras/stw2531.
- M. Mocák, E. Müller, A. Weiss, and K. Kifonidis. The core helium flash revisited. I. One and two-dimensional hydrodynamic simulations. *A&A*, 490(1):265–277, October 2008. doi: 10.1051/0004-6361:200810169.
- M. R. Mokiem, A. de Koter, J. S. Vink, J. Puls, C. J. Evans, S. J. Smartt, P. A. Crowther, A. Herrero, N. Langer, D. J. Lennon, F. Najarro, and M. R. Villamariz. The empirical metallicity dependence of the mass-loss rate of O- and early B-type stars. *A&A*, 473(2):603–614, October 2007. doi: 10.1051/0004-6361:20077545.
- A. Mora, B. Merín, E. Solano, B. Montesinos, D. de Winter, C. Eiroa, R. Ferlet, C. A. Grady, J. K. Davies, L. F. Miranda, R. D. Oudmaijer, J. Palacios, A. Quirrenbach, A. W. Harris, H. Rauer, A. Collier Cameron, H. J. Deeg, F. Garzón, A. Penny, J. Schneider, Y. Tsapras, and P. R. Wesselius. EXPORT: Spectral classification and projected rotational velocities of Vega-type and pre-main sequence stars. *A&A*, 378:116–131, October 2001. doi: 10.1051/0004-6361:20011098.
- N. Mowlavi, P. Eggenberger, G. Meynet, S. Ekström, C. Georgy, A. Maeder, C. Charbonnel, and L. Eyer. Stellar mass and age determinations . I. Grids of stellar models from  $Z = 0.006$  to  $0.04$  and  $M = 0.5$  to  $3.5 M_{\odot}$ . *A&A*, 541:A41, May 2012. doi: 10.1051/0004-6361/201117749.
- Z. E. Musielak and P. Ulmschneider. Excitation of transverse magnetic tube waves in stellar convection zones. II. Wave energy spectra and fluxes. *aap*, 386:606–614, May 2002. doi: 10.1051/0004-6361:20011834.
- D. Nardiello, L. R. Bedin, A. Burgasser, M. Salaris, S. Cassisi, M. Griggio, and M. Scalco. Photometry and astrometry with JWST - I. NIRCам point spread functions and the first JWST colour-magnitude diagrams of a globular cluster. *MNRAS*, 517(1):484–497, November 2022. doi: 10.1093/mnras/stac2659.
- C. T. Nguyen, G. Costa, L. Girardi, G. Volpato, A. Bressan, Y. Chen, P. Marigo, X. Fu, and P. Goudfrooij. PARSEC V2.0: Stellar tracks and isochrones of low- and intermediate-mass stars with rotation. *A&A*, 665:A126, September 2022. doi: 10.1051/0004-6361/202244166.
- A. Noll, S. Deheuvels, and J. Ballot. Probing core overshooting using subgiant asteroseismology: The case of KIC10273246. *A&A*, 647:A187, March 2021. doi: 10.1051/0004-6361/202040055.

- R. W. Noyes, L. W. Hartmann, S. L. Baliunas, D. K. Duncan, and A. H. Vaughan. Rotation, convection, and magnetic activity in lower main-sequence stars. *apj*, 279:763–777, Apr 1984. doi: 10.1086/161945.
- T. Nugis and H. J. G. L. M. Lamers. Mass-loss rates of Wolf-Rayet stars as a function of stellar parameters. *A&A*, 360:227–244, August 2000.
- J. B. Oke and Jesse L. Greenstein. The Rotational Velocities of - - and G-Type Giant Stars. *ApJ*, 120:384, November 1954. doi: 10.1086/145929.
- Nathaniel E. Q. Paust, Brian Chaboyer, and Ata Sarajedini. BVI Photometry and the Luminosity Functions of the Globular Cluster M92. *AJ*, 133(6):2787–2798, June 2007. doi: 10.1086/513511.
- Bill Paxton, Lars Bildsten, Aaron Dotter, Falk Herwig, Pierre Lesaffre, and Frank Timmes. Modules for Experiments in Stellar Astrophysics (MESA). *ApJS*, 192(1):3, January 2011. doi: 10.1088/0067-0049/192/1/3.
- Bill Paxton, Josiah Schwab, Evan B. Bauer, Lars Bildsten, Sergei Blinnikov, Paul Duffell, R. Farmer, Jared A. Goldberg, Pablo Marchant, Elena Sorokina, Anne Thoul, Richard H. D. Townsend, and F. X. Timmes. Modules for Experiments in Stellar Astrophysics (MESA): Convective Boundaries, Element Diffusion, and Massive Star Explosions. *ApJS*, 234(2):34, February 2018. doi: 10.3847/1538-4365/aaa5a8.
- Adriano Pietrinferni, Santi Cassisi, Maurizio Salaris, and Fiorella Castelli. A Large Stellar Evolution Database for Population Synthesis Studies. I. Scaled Solar Models and Isochrones. *ApJ*, 612(1):168–190, September 2004. doi: 10.1086/422498.
- Adriano Pietrinferni, Sebastian Hidalgo, Santi Cassisi, Maurizio Salaris, Alessandro Savino, Alessio Mucciarelli, Kuldeep Verma, Victor Silva Aguirre, Antonio Aparicio, and Jason W. Ferguson. Updated BaSTI Stellar Evolution Models and Isochrones. II.  $\alpha$ -enhanced Calculations. *ApJ*, 908(1):102, February 2021. doi: 10.3847/1538-4357/abd4d5.
- M. H. Pinsonneault, Steven D. Kawaler, S. Sofia, and P. Demarque. Evolutionary Models of the Rotating Sun. *ApJ*, 338:424, March 1989. doi: 10.1086/167210.
- Onno R. Pols, Christopher A. Tout, Peter P. Eggleton, and Zhanwen Han. Approximate input physics for stellar modelling. *MNRAS*, 274(3):964–974, June 1995. doi: 10.1093/mnras/274.3.964.

- Onno R. Pols, Klaus-Peter Schröder, Jarrod R. Hurley, Christopher A. Tout, and Peter P. Eggleton. Stellar evolution models for  $Z = 0.0001$  to  $0.03$ . MNRAS, 298(2):525–536, August 1998. doi: 10.1046/j.1365-8711.1998.01658.x.
- Adrian T. Potter, Christopher A. Tout, and John J. Eldridge. Towards a unified model of stellar rotation. MNRAS, 419(1):748–759, January 2012. doi: 10.1111/j.1365-2966.2011.19737.x.
- Barton J. Pritzl, Kim A. Venn, and Mike Irwin. A Comparison of Elemental Abundance Ratios in Globular Clusters, Field Stars, and Dwarf Spheroidal Galaxies. AJ, 130(5):2140–2165, November 2005. doi: 10.1086/432911.
- Thomas H. Puzia, Markus Kissler-Patig, and Paul Goudfrooij. Extremely  $\alpha$ -Enriched Globular Clusters in Early-Type Galaxies: A Step toward the Dawn of Stellar Populations? ApJ, 648(1):383–388, September 2006. doi: 10.1086/505679.
- D. Reimers. Circumstellar absorption lines and mass loss from red giants. *Memoires of the Societe Royale des Sciences de Liege*, 8:369–382, January 1975.
- D. Reimers. On the absolute scale of mass-loss in red giants. I. Circumstellar absorption lines in the spectrum of the visual companion of  $\alpha^1$ Her. A&A, 61:217–224, October 1977.
- Alvio Renzini and Flavio Fusi Pecci. Tests of evolutionary sequences using color-magnitude diagrams of globular clusters. ARA&A, 26:199–244, January 1988. doi: 10.1146/annurev.aa.26.090188.001215.
- M. Riello, F. de Angeli, D. W. Evans, P. Montegriffo, J. M. Carrasco, G. Busso, L. Palaversa, P. Burgess, C. Diener, M. Davidson, N. Rowell, C. Fabricius, C. Jordi, M. Bellazzini, E. Pancino, D. L. Harrison, C. Cacciari, F. van Leeuwen, N. C. Hambly, S. T. Hodgkin, P. J. Osborne, G. Altavilla, M. A. Barstow, A. G. A. Brown, M. Castellani, S. Cowell, F. de Luise, G. Gilmore, G. Giuffrida, S. Hidalgo, G. Holland, S. Marinoni, C. Pagani, A. M. Piersimoni, L. Pulone, S. Ragaini, M. Rainer, P. J. Richards, N. Sanna, N. A. Walton, M. Weiler, and A. Yoldas. VizieR Online Data Catalog: Gaia Early Data Release 3 photometric passbands (Riello+, 2021). *VizieR Online Data Catalog*, art. J/A+A/649/A3, January 2021.
- Tha  se S. Rodrigues, L  o Girardi, Andrea Miglio, Diego Bossini, Jo Bovy, Courtney Epstein, Marc H. Pinsonneault, Dennis Stello, Gail Zasowski, Carlos Allende Prieto, William J. Chaplin, Saskia Hekker, Jennifer A. Johnson, Szabolcs

- Mészáros, Benoît Mosser, Friedrich Anders, Sarbani Basu, Timothy C. Beers, Cristina Chiappini, Luiz A. N. da Costa, Yvonne Elsworth, Rafael A. García, Ana E. García Pérez, Fred R. Hearty, Marcio A. G. Maia, Steven R. Majewski, Savita Mathur, Josefina Montalbán, David L. Nidever, Basilio Santiago, Mathias Schultheis, Aldo Serenelli, and Matthew Shetrone. Bayesian distances and extinctions for giants observed by Kepler and APOGEE. *MNRAS*, 445(3): 2758–2776, December 2014. doi: 10.1093/mnras/stu1907.
- Thaíse S. Rodrigues, Diego Bossini, Andrea Miglio, Léo Girardi, Josefina Montalbán, Arlette Noels, Michele Trabucchi, Hugo Rodrigues Coelho, and Paola Marigo. Determining stellar parameters of asteroseismic targets: going beyond the use of scaling relations. *MNRAS*, 467(2):1433–1448, May 2017. doi: 10.1093/mnras/stx120.
- Ian U. Roederer and Christopher Sneden. Heavy-element Dispersion in the Metal-poor Globular Cluster M92. *AJ*, 142(1):22, July 2011. doi: 10.1088/0004-6256/142/1/22.
- F. J. Rogers and A. Nayfonov. Updated and Expanded OPAL Equation-of-State Tables: Implications for Helioseismology. *ApJ*, 576(2):1064–1074, September 2002. doi: 10.1086/341894.
- Philip Rosenfield, Paola Marigo, Léo Girardi, Julianne J. Dalcanton, Alessandro Bressan, Marco Gullieuszik, Daniel Weisz, Benjamin F. Williams, Andrew Dolphin, and Bernhard Aringer. Evolution of Thermally Pulsing Asymptotic Giant Branch Stars. IV. Constraining Mass loss and Lifetimes of Low Mass, Low Metallicity AGB Stars. *ApJ*, 790(1):22, July 2014. doi: 10.1088/0004-637X/790/1/22.
- Philip Rosenfield, Léo Girardi, Benjamin F. Williams, L. Clifton Johnson, Andrew Dolphin, Alessandro Bressan, Daniel Weisz, Julianne J. Dalcanton, Morgan Fouesneau, and Jason Kalirai. A New Approach to Convective Core Overshooting: Probabilistic Constraints from Color-Magnitude Diagrams of LMC Clusters. *ApJ*, 841(2):69, June 2017. doi: 10.3847/1538-4357/aa70a2.
- I. W. Roxburgh. Convection and stellar structure. *A&A*, 65(2):281–285, April 1978.
- F. Royer, J. Zorec, and A. E. Gómez. Rotational velocities of A-type stars. III. Velocity distributions. *A&A*, 463(2):671–682, February 2007. doi: 10.1051/0004-6361:20065224.
- G. R. Ruchti, J. P. Fulbright, R. F. G. Wyse, G. F. Gilmore, O. Bienaymé, J. Binney, J. Bland-Hawthorn, R. Campbell, K. C. Freeman, B. K. Gibson, E. K.



- Grebel, A. Helmi, U. Munari, J. F. Navarro, Q. A. Parker, W. Reid, G. M. Seabroke, A. Siebert, A. Siviero, M. Steinmetz, F. G. Watson, M. Williams, and T. Zwitter. Origins of the Thick Disk as Traced by the Alpha Elements of Metal-poor Giant Stars Selected from Rave. *ApJ*, 721(2):L92–L96, October 2010. doi: 10.1088/2041-8205/721/2/L92.
- Maurizio Salaris, Aldo Serenelli, Achim Weiss, and Marcelo Miller Bertolami. Semi-empirical White Dwarf Initial-Final Mass Relationships: A Thorough Analysis of Systematic Uncertainties Due to Stellar Evolution Models. *ApJ*, 692(2):1013–1032, February 2009. doi: 10.1088/0004-637X/692/2/1013.
- Eric L. Sandquist, David W. Latham, Robert D. Mathieu, Emily Leiner, Andrew Vanderburg, Dennis Stello, Jerome A. Orosz, Luigi R. Bedin, Mattia Libralato, Luca Malavolta, and Domenico Nardiello. The K2 M67 Study: Precise Mass for a Turnoff Star in the Old Open Cluster M67. *AJ*, 161(2):59, February 2021. doi: 10.3847/1538-3881/abca8d.
- Ata Sarajedini, Luigi R. Bedin, Brian Chaboyer, Aaron Dotter, Michael Siegel, Jay Anderson, Antonio Aparicio, Ivan King, Steven Majewski, A. Marín-Franch, Giampaolo Piotto, I. Neill Reid, and Alfred Rosenberg. The ACS Survey of Galactic Globular Clusters. I. Overview and Clusters without Previous Hubble Space Telescope Photometry. *AJ*, 133(4):1658–1672, April 2007. doi: 10.1086/511979.
- Ata Sarajedini, Aaron Dotter, and Allison Kirkpatrick. Deep 2MASS Photometry of M67 and Calibration of the Main-Sequence J -  $K_S$  Color Difference as an Age Indicator. *ApJ*, 698(2):1872–1878, June 2009. doi: 10.1088/0004-637X/698/2/1872.
- W. C. Saslaw and M. Schwarzschild. Overshooting from Stellar Convective Cores. *ApJ*, 142:1468, November 1965. doi: 10.1086/148430.
- D. Saumon, G. Chabrier, and H. M. van Horn. An Equation of State for Low-Mass Stars and Giant Planets. *ApJS*, 99:713, August 1995. doi: 10.1086/192204.
- K. P. Schröder and M. Cuntz. A New Version of Reimers’ Law of Mass Loss Based on a Physical Approach. *ApJ*, 630(1):L73–L76, September 2005. doi: 10.1086/491579.
- M. Schwarzschild, R. Howard, and R. Härm. Inhomogeneous Stellar Models. V. a. Solar Model with Convective Envelope and Inhomogeneous Interior. *ApJ*, 125:233, January 1957. doi: 10.1086/146297.

- Martin Schwarzschild. *Structure and evolution of the stars*. Princeton, Princeton University Press, 1958., 1958.
- Maki Sekiguchi and Masataka Fukugita. A Study of the B-V Color-Temperature Relation. *aj*, 120(2):1072–1084, Aug 2000. doi: 10.1086/301490.
- G. Shajn and O. Struve. On the rotation of the stars. *MNRAS*, 89:222–239, January 1929. doi: 10.1093/mnras/89.3.222.
- M. Sirianni, M. J. Jee, N. Benítez, J. P. Blakeslee, A. R. Martel, G. Meurer, M. Clampin, G. De Marchi, H. C. Ford, R. Gilliland, G. F. Hartig, G. D. Illingworth, J. Mack, and W. J. McCann. The Photometric Performance and Calibration of the Hubble Space Telescope Advanced Camera for Surveys. *PASP*, 117(836):1049–1112, October 2005. doi: 10.1086/444553.
- Nathan Smith. Mass Loss: Its Effect on the Evolution and Fate of High-Mass Stars. *ARA&A*, 52:487–528, August 2014. doi: 10.1146/annurev-astro-081913-040025.
- A. Sollima, C. Cacciari, and E. Valenti. The RR Lyrae period-K-luminosity relation for globular clusters: an observational approach. *MNRAS*, 372(4):1675–1680, November 2006. doi: 10.1111/j.1365-2966.2006.10962.x.
- N. Song, S. Alexeeva, T. Sitnova, L. Wang, F. Grupp, and G. Zhao. Impact of the convective mixing-length parameter  $\alpha$  on stellar metallicity. *A&A*, 635:A176, March 2020. doi: 10.1051/0004-6361/201937110.
- T. Sonoi, H. G. Ludwig, M. A. Dupret, J. Montalbán, R. Samadi, K. Belkacem, E. Caffau, and M. J. Goupil. Calibration of mixing-length parameter  $\alpha$  for MLT and FST models by matching with CO<sup>5</sup>BOLD models. *A&A*, 621:A84, January 2019. doi: 10.1051/0004-6361/201833495.
- J. Southworth. VizieR Online Data Catalog: The DEBCat detached eclipsing binary catalogue (Southworth, 2015). *VizieR Online Data Catalog*, art. V/152, November 2017.
- F. Spada, P. Demarque, Y. C. Kim, T. S. Boyajian, and J. M. Brewer. The Yale-Potsdam Stellar Isochrones. *ApJ*, 838(2):161, April 2017. doi: 10.3847/1538-4357/aa661d.
- Mario Spera, Michela Mapelli, Nicola Giacobbo, Alessandro A. Trani, Alessandro Bressan, and Guglielmo Costa. Merging black hole binaries with the SEVN code. *MNRAS*, 485(1):889–907, May 2019. doi: 10.1093/mnras/stz359.

- Dennis Stello, Andrew Vanderburg, Luca Casagrande, Ron Gilliland, Victor Silva Aguirre, Eric Sandquist, Emily Leiner, Robert Mathieu, and David R. Soderblom. The K2 M67 Study: Revisiting Old Friends with K2 Reveals Oscillating Red Giants in the Open Cluster M67. *ApJ*, 832(2):133, December 2016. doi: 10.3847/0004-637X/832/2/133.
- S. Talon and J. P. Zahn. Anisotropic diffusion and shear instabilities. *A&A*, 317: 749–751, February 1997.
- Jing Tang, Alessandro Bressan, Philip Rosenfield, Alessandra Slemmer, Paola Marigo, Léo Girardi, and Luciana Bianchi. New PARSEC evolutionary tracks of massive stars at low metallicity: testing canonical stellar evolution in nearby star-forming dwarf galaxies. *MNRAS*, 445(4):4287–4305, December 2014. doi: 10.1093/mnras/stu2029.
- E. Tognelli, P. G. Prada Moroni, and S. Degl’Innocenti. The Pisa pre-main sequence tracks and isochrones. A database covering a wide range of  $Z$ ,  $Y$ , mass, and age values. *A&A*, 533:A109, September 2011. doi: 10.1051/0004-6361/200913913.
- Guillermo Torres, Luiz Paulo R. Vaz, Claud H. Sandberg Lacy, and Antonio Claret. Absolute Properties of the Eclipsing Binary System AQ Serpentis: A Stringent Test of Convective Core Overshooting in Stellar Evolution Models. *AJ*, 147(2):36, February 2014. doi: 10.1088/0004-6256/147/2/36.
- Don A. Vandenberg, O. Richard, G. Michaud, and J. Richer. Models of Metal-poor Stars with Gravitational Settling and Radiative Accelerations. II. The Age of the Oldest Stars. *ApJ*, 571(1):487–500, May 2002. doi: 10.1086/339895.
- Paolo Ventura, Anna Zeppieri, Italo Mazzitelli, and Francesca D’Antona. Full spectrum of turbulence convective mixing: I. theoretical main sequences and turn-off for  $0.6 / 15 M_{\odot}$ . *A&A*, 334:953–968, June 1998.
- Lucas S. Viani, Sarbani Basu, M. Joel Ong J., Ana Bonaca, and William J. Chaplin. Investigating the Metallicity-Mixing-length Relation. *ApJ*, 858(1):28, May 2018. doi: 10.3847/1538-4357/aab7eb.
- Jorick S. Vink. Very massive stars: a metallicity-dependent upper-mass limit, slow winds, and the self-enrichment of globular clusters. *A&A*, 615:A119, July 2018. doi: 10.1051/0004-6361/201832773.
- Jorick S. Vink. Theory and Diagnostics of Hot Star Mass Loss. *ARA&A*, 60: 203–246, August 2022. doi: 10.1146/annurev-astro-052920-094949.

- Jorick S. Vink, A. de Koter, and H. J. G. L. M. Lamers. Mass-loss predictions for O and B stars as a function of metallicity. *A&A*, 369:574–588, April 2001. doi: 10.1051/0004-6361:20010127.
- Jorick S. Vink, L. E. Muijres, B. Anthonisse, A. de Koter, G. Gräfener, and N. Langer. Wind modelling of very massive stars up to 300 solar masses. *A&A*, 531:A132, July 2011. doi: 10.1051/0004-6361/201116614.
- C. Viscasillas Vázquez, L. Magrini, G. Casali, G. Tautvaišienė, L. Spina, M. Van der Swaelmen, S. Randich, T. Bensby, A. Bragaglia, E. Friel, S. Feltzing, G. G. Sacco, A. Turchi, F. Jiménez-Esteban, V. D’Orazi, E. Delgado-Mena, Š. Mikolaitis, A. Drazdauskas, R. Minkevičiūtė, E. Stonkutė, V. Bagdonas, D. Montes, G. Guiglion, M. Baratella, H. M. Tabernero, G. Gilmore, E. Alfaro, P. Francois, A. Korn, R. Smiljanic, M. Bergemann, E. Franciosini, A. Gonneau, A. Hourihane, C. C. Worley, and S. Zaggia. The Gaia-ESO survey: Age-chemical-clock relations spatially resolved in the Galactic disc. *A&A*, 660:A135, April 2022. doi: 10.1051/0004-6361/202142937.
- R. von Steiger and T. H. Zurbuchen. Solar Metallicity Derived from in situ Solar Wind Composition. *ApJ*, 816(1):13, January 2016. doi: 10.3847/0004-637X/816/1/13.
- H. von Zeipel. The radiative equilibrium of a rotating system of gaseous masses. *MNRAS*, 84:665–683, June 1924a. doi: 10.1093/mnras/84.9.665.
- H. von Zeipel. The radiative equilibrium of a slightly oblate rotating star. *MNRAS*, 84:684–701, June 1924b. doi: 10.1093/mnras/84.9.684.
- Achim Weiss and Helmut Schlattl. GARSTEC—the Garching Stellar Evolution Code. The direct descendant of the legendary Kippenhahn code. *Ap&SS*, 316 (1-4):99–106, August 2008. doi: 10.1007/s10509-007-9606-5.
- George L. Withbroe. The Temperature Structure, Mass, and Energy Flow in the Corona and Inner Solar Wind. *apj*, 325:442, Feb 1988. doi: 10.1086/166015.
- Jong-Hak Woo, Carme Gallart, Pierre Demarque, Sukyoung Yi, and Manuela Zoccali. Testing Intermediate-Age Stellar Evolution Models with VLT Photometry of Large Magellanic Cloud Clusters. II. Analysis with the Yale Models. *AJ*, 125 (2):754–769, February 2003. doi: 10.1086/345959.
- Y. Xu, S. Goriely, A. Jorissen, G. L. Chen, and M. Arnould. Databases and tools for nuclear astrophysics applications. BRUSsels Nuclear LIBrary (BRUSLIB), Nuclear Astrophysics Compilation of REactions II (NACRE II) and Nuclear

- NETwork GENerator (NETGEN). *A&A*, 549:A106, January 2013. doi: 10.1051/0004-6361/201220537.
- S. C. Yoon, N. Langer, and C. Norman. Single star progenitors of long gamma-ray bursts. I. Model grids and redshift dependent GRB rate. *A&A*, 460(1):199–208, December 2006. doi: 10.1051/0004-6361:20065912.
- J. P. Zahn. Circulation and turbulence in rotating stars. *A&A*, 265:115–132, November 1992.
- R. Zinn and M. J. West. The globular cluster system of the Galaxy. III. Measurements of radial velocity and metallicity for 60 clusters and a compilation of metallicities for 121 clusters. *ApJS*, 55:45–66, May 1984. doi: 10.1086/190947.